TKK Dissertations 102
Espoo 2008

STRAIN-BASED APPROACH TO FATIGUE STRENGTH ASSESSMENT OF LASER-WELDED JOINTS

Doctoral Dissertation

Heikki Remes

Helsinki University of Technology
Faculty of Engineering and Architecture
Department of Applied Mechanics

TKK Dissertations 102
Espoo 2008

STRAIN-BASED APPROACH TO FATIGUE STRENGTH ASSESSMENT OF LASER-WELDED JOINTS

Doctoral Dissertation

Heikki Remes

Dissertation for the degree of Doctor of Science in Technology to be presented with due permission of the Faculty of Engineering and Architecture for public examination and debate in Auditorium K216 at Helsinki University of Technology (Espoo, Finland) on the 7th of March, 2008, at 12 noon.

Helsinki University of Technology
Faculty of Engineering and Architecture
Department of Applied Mechanics

Teknillinen korkeakoulu
Insinööritieteiden ja arkkitehtuurin tiedekunta
Sovelletun mekaniikan laitos

Distribution:
Helsinki University of Technology
Faculty of Engineering and Architecture
Department of Applied Mechanics
P.O. Box 5300
FI - 02015 TKK
FINLAND
URL: http://www.tkk.fi/Yksikot/Laiva/
Tel. +358-9-451 3501
Fax +358-9-451 4173
E-mail: leila.silonsaari@tkk.fi

ISBN 978-951-22-9189-2
ISBN 978-951-22-9190-8 (PDF)
ISSN 1795-2239
ISSN 1795-4584 (PDF)
URL: http://lib.tkk.fi/Diss/2008/isbn9789512291908/

TKK-DISS-2416

Yliopistopaino
Helsinki 2008

ABSTRACT OF DOCTORAL DISSERTATION	HELSINKI UNIVERSITY OF TECHNOLOGY P.O. BOX 1000, FI-02015 TKK http://www.tkk.fi

Author Heikki Remes

Name of the dissertation
Strain-Based Approach to Fatigue Strength Assessment of Laser-Welded Joints

Manuscript submitted 03.05.2007	Manuscript revised 05.11.2007

Date of the defence 07.03.2008

☒ Monograph	☐ Article dissertation (summary + original articles)

Faculty	Faculty of Engineering and Architecture
Department	Department of Applied Mechanics
Field of research	Naval Architecture
Opponent(s)	Professor Wolfgang Fricke, Professor Gary Marquis
Supervisor	Professor Petri Varsta
Instructor	Professor Petri Varsta

New laser-based welding technology leads to differences in the geometrical and mechanical properties of welded joints as compared to those encountered in conventional arc-welded joints. The present work concentrates on the effects of these properties on the fatigue resistance of steel butt joints welded using laser-based methods. The investigation exploited both experimental and theoretical methods.

In laser-based joints, the mechanical properties within the joint varied strongly, affecting notch stresses and strains. Therefore, the response analysis based on Neuber's rule requires a separate structural and local approach. The structural analysis, based on the stress-strain curve of parent material, gives the loading for the weld notch. This is applied to the local analysis, where the stress-strain curve of the heat-affected zone (HAZ) is used.

The initiation life of macro cracks of laser-based joints was observed to form an essential part of the total fatigue life, suggesting that the mechanical properties of the material in the weld notch have a strong influence on fatigue resistance. The strain-based approach was applied with several discrete growth steps to model the propagation of short cracks up to the length of a macro crack in the weld notch. Within each step, the number of load cycles causing the increase of fracture was calculated with the Coffin-Manson formula. The length of a discrete growth step, which describes the damage zone, was based on the multiple of the averaged grain size of the HAZ material. This growth length also defines the averaging distance of effective notch stresses and strains. The approach was validated with the results of fatigue tests, using welded miniature and plate specimens.

The new theoretical approach with several discrete growth steps was especially relevant to laser-based joints with fine-grained microstructure in the HAZ. The short crack modelling was required to attain reliable predictions for the fatigue resistance of welded butt joints when the life of the macro crack initiation constituted a significant portion of the total fatigue life or the initiation life varied as the function of the applied stress range. The outcome of this important result explained the increase of the slope of *S-N* curves from the generally accepted value of 3.0 for arc-welded joints up to values above 10 for laser-based joints.

The main reason for the differences in the initiation process of fatigue crack between the laser-based and arc-welded joints was the dissimilar grain size in the HAZ. The average grain size of the laser-based joints was about seven times smaller than that of the arc-welded joint. The other parameters causing the difference were the hardness of the weld materials and the weld size, which affected the joint stiffness, and thus the notch stresses and strains.

Keywords fatigue, macro crack initiation, strain-based approach, weld notch, butt joint, laser hybrid welding

ISBN (printed)	978-951-22-9189-2	ISSN (printed)	1795-2239
ISBN (pdf)	978-951-22-9190-8	ISSN (pdf)	1795-4584
Language	English	Number of pages	153 p.

Publisher Helsinki University of Technology, Department of Applied Mechanics

Print distribution Helsinki University of Technology, Department of Applied Mechanics

☒ The dissertation can be read at http://lib.tkk.fi/Diss/2008/isbn9789512291908/

VÄITÖSKIRJAN TIIVISTELMÄ	TEKNILLINEN KORKEAKOULU PL 1000, 02015 TKK http://www.tkk.fi

Tekijä Heikki Remes

Väitöskirjan nimi
Laserhitsatun liitoksen väsymislujuuden arviointi venymämenetelmällä

Käsikirjoituksen päivämäärä 03.05.2007	Korjatun käsikirjoituksen päivämäärä 05.11.2007

Väitöstilaisuuden ajankohta 07.03.2008

☒ Monografia	☐ Yhdistelmäväitöskirja (yhteenveto + erillisartikkelit)

Tiedekunta	Insinööritieteiden ja arkkitehtuurin tiedekunta
Laitos	Sovelletun mekaniikan laitos
Tutkimusala	Laivanrakennustekniikka
Vastaväittäjä(t)	Professori Wolfgang Fricke, Professori Gary Marquis
Työn valvoja	Professori Petri Varsta
Työn ohjaaja	Professori Petri Varsta

Laserhitsaus aiheuttaa hitsausliitokselle perinteiseen kaarihitsaukseen verrattuna erilaiset geometriset ja mekaaniset ominaisuudet. Tässä työssä on selvitetty näiden ominaisuuksien vaikutusta laser- ja laserhybridihitsatun päittäisliitoksen väsymislujuuteen. Tutkimuksessa on hyödynnetty sekä kokeellisia että teoreettisia menetelmiä.

Laser- ja hybridihitsatun liitoksen materiaaliominaisuudet muuttuvat voimakkaasti hitsiliitoksessa, mikä vaikuttaa reunaloven jännityksiin ja venymiin. Tämän johdosta Neuberin malliin perustuva vasteen laskenta edellyttää erillistä rakenteellista ja paikallista analyysiä. Rakenteellisessa analyysissä käytetään perusmateriaalin jännitys-venymäkäyrää ja tuloksena on hitsin reunaloveen kohdistuva kuormitus. Tämän perusteella suoritetaan paikallisanalyysi käyttäen muutosvyöhykkeen jännitys-venymäkäyrää.

Väsytyskuormituksessa makrosärön ydintymiseen kuluneen ajan havaittiin laser- ja hybridihitsatuille liitoksille muodostavan oleellisen osan liitoksen väsymisiästä, jolloin reunaloven materiaaliominaisuuksilla on merkittävä vaikutus väsymislujuuteen. Lyhyiden säröjen kasvun kuvaamiseen käytettiin venymämenetelmää ja usean diskreetin kasvuaskeleen mallia. Yhden diskreetin kasvuaskeleen kesto laskettiin Coffin-Manson yhtälöstä. Vaurioalueen kokoa kuvaava askelmitta määräytyi hitsin muutosvyöhykkeen keskimääräisen kidekoon monikerran perusteella. Tämä askelmitta määrittää myös pituuden tehollisen lovijännityksen ja -venymen keskiarvoistukselle. Kehitetty laskentamenetelmä validoitiin väsytyskokeiden tulosten avulla, joissa koekappaleet sisälsivät eri hitsimateriaalista valmistetut sauvat ja päittäisliitokset.

Uusi teoreettinen laskentamenetelmä sisältäen diskreettisen särön kasvumallin osoittautui toimivaksi erityisesti laser- ja hybridihitseillä, joilla muutosvyöhykkeen mikrorakenne oli hienorakenteinen. Lyhyen särön kasvun mallintaminen oli edellytys luotettavan väsymislujuusennusteen saamiseksi liitoksille, kun makrosärön ydintymisaika muodosti merkittävän osan liitoksen väsymisiästä. Vastaava havainto tehtiin tapauksissa, joissa makrosärön ydintymisaika suhteessa koko väsymisikään muuttui käytetyn jännityksen vaihteluvälin funktiona. Tämän merkittävän tuloksen avulla pystyttiin selittämään *S*-*N*-käyrän kulmakertoimen muutos laser- ja hybridihitsatuille liitoksille yleisesti hyväksytystä arvosta 3.0 arvoon 10 tai jopa yli sen.

Pääasiallisin syy laser- ja kaarihitsatun liitoksen väsymissärön ydintymisprosessin eroavuuteen oli muutosvyöhykkeen erilainen kidekoko. Keskimääräinen kidekoko laser- ja hybridihitsatuille liitoksille oli noin seitsemäsosa kaarihitsatun vastaavasta kidekoosta. Muita tekijöitä, jotka aiheuttivat väsymislujuuksien eroavuutta, olivat hitsimateriaalin kovuus ja hitsin koko. Jälkimmäinen vaikutti liitoksen jäykkyyteen ja siten lovijännityksiin ja -venymiin.

Asiasanat väsyminen, makrosärön ydintyminen, venymämenetelmä, reunalovi, päittäisliitos, laserhybridihitsaus

ISBN (painettu)	978-951-22-9189-2	ISSN (painettu)	1795-2239
ISBN (pdf)	978-951-22-9190-8	ISSN (pdf)	1795-4584
Kieli	Englanti	Sivumäärä	153 s.

Julkaisija Teknillinen korkeakoulu, Sovelletun mekaniikan laitos

Painetun väitöskirjan jakelu Teknillinen korkeakoulu, Sovelletun mekaniikan laitos

☒ Luettavissa verkossa osoitteessa http://lib.tkk.fi/Diss/2008/isbn9789512291908/

PREFACE

Since the late 1980s, laser-welded structures have been investigated in the Ship Laboratory of Helsinki University of Technology (TKK). The experiments have shown unexpected differences in fatigue between the laser- and arc-welded structures, underlining the challenge of fatigue design. This has been the main motivation for my thesis, which aims towards a better understanding of fatigue behaviour of laser-welded joints.

I am grateful to my supervisor, Professor Petri Varsta, for all his encouragement and guidance. Many discussions between us during the course of this work were of essential importance. The good working atmosphere and resources he provided ensured a proper research environment and allowed me to concentrate on my research. I would like to also thank my colleagues, Jani Romanoff, Hendrik Naar, Alan Klanac, Kristjan Tabri, and Sören Ehlers, for their support and encouragement. Thanks are also due to the staff of the Ship Laboratory, as well as to Mikko Jutila, for their kind assistance. I also wish to express my gratitude to the pre-examiners of this work, Professor Gary Marquis and Dr. Timo Mikkola, for their valuable and constructive criticism.

The research presented in this thesis was initiated within the framework of the research project “Fatigue strength modelling of laser welded joints”. The project was funded by the Finnish Academy. The project LAPROMAT, which was funded by the European Commission, provided funding for the experimental work. This financial support is gratefully acknowledged. I am also grateful to the project manager, Dr. Pentti Kujala, for his guidance and support. The working period during which I performed fatigue testing at the Institute of Fundamental Technological Research in Poland was very fruitful. I am grateful to Professor Lech Dietrich and Dr. Grzegorz Socha for their encouragement and guidance. Our discussions enhanced my commitment to research. Ruukki, Force Technology, Meyer Werft and Aker Yards Finland are also gratefully acknowledged for their assistance and cooperation in producing the welded plate samples. Special appreciation is also due to Risto Laitinen from Ruukki, Jens Klaestrup Kristensen and Mr. Jakob Weldingh from Force Technology, Guido Pethan from Meyer Werft, and Kari Laiho from Aker Yards. I would like to thank also Frank Roland for the coordination between Meyer Werft and TKK.

Finally, I would like to thank my family and friends for their support during this period of my life.

Helsinki, October 2007 Heikki Remes

TABLE OF CONTENTS

APPENDIXES

NOMENCLATURE

Symbols

A	area
A_5	failure strain
A^2	value of Anderson-Darling test
a	depth of surface crack
a_o	material characteristic length
b	fatigue strength exponent
c	fatigue ductility exponent
C	crack growth rate coefficient
d	average grain size
D	notch depth, value of Kolmogorov-Smirnov test
D_1 , D_2	notch depth measured from surface of plate, weld profile
e	axial misalignment, eccentricity
E	modulus of elasticity
E_{CH}	chord modulus
E_T	tangent modulus
F	force, geometrical parameter of weld and crack
h	weld height
H_l , H_r	vertical distance between centre line of specimen and left or right ends
I	moment of inertia
k_m	stress magnification factor due to misalignments
k_m^*	modified stress magnification factor
$k_{m,e}$, $k_{m,\alpha}$	stress magnification factor due to axial, angular misalignment
k_n	stress magnification factor due to short crack growth
K	stress intensity factor
K'	cyclic strain-hardening coefficient
K_c	fracture toughness
K_t	linear elastic stress concentration factor
ΔK	range of stress intensity factor
l	length of surface crack
L	length
m	slope of S-N curve
M	moment
M_{per}	permanent plastic moment
n	crack growth rate exponent, number of growth step
n'	cyclic strain-hardening exponent
N	number of load cycles
N_{in}	initiation life for step n of short crack growth
P	probability

P_{cm}	carbon equivalent
P_{swt}	damage parameter
R	load ratio
s	scatter factor
t	plate thickness
y	distance from neutral axis
x, y, z	Cartesian coordinate system
w	weld width
α	angular misalignment
β	notch opening angle
$\Delta\sigma_0$	fatigue strength at 2 million load cycles for smooth specimen
ε	normal strain
$\varepsilon_f^{'}$	fatigue ductility coefficient
ε_{sf}	structural strain due to axial force
$\varepsilon_{\mathrm{sm}}$	structural strain due to moment
γ	notch flank angle
ν	Poisson's ratio
λ_e , λ_α	parameters defining the influence of boundary condition
Λ_f , Λ_m	load proportion factor for force and moment
θ	weld flank angle
ρ	notch root radius
σ	normal stress
$\sigma_f^{'}$	fatigue strength coefficient
σ_{nom}	nominal stress
σ_{sb}	secondary bending stress
σ_u	tensile strength
σ_y	yield stress

Subscripts

1, 2	directions of principal stresses and strains
I	fracture mode I
a	amplitude
c	critical
e	effective
el	elastic
eq	equivalent
f	failure
hs	hot-spot
i	initiation
ie	inelastic
ln	local notch

m	mean, macro
max	maximum
mea	measured
min	minimum
p	propagation
p(%)	probability level in percent
pl	elasto-plastic
pre	predicted
r	weld root
s	short, structural
t	weld toe
th	threshold
tot	total
x, y, z	directions x, y, z

Modifier

Δ	range
f( )	function

Abbreviations

ACPD	alternating current potential drop
ASTM	American Society for Testing and Materials
BS	British Standard
CEV	carbon equivalent value
FAT	fatigue class, characteristic fatigue strength at 2 million cycles
FE	finite element
FEA	finite element analysis
FEM	finite element method
HAZ	heat affected zone
HV, HB	Vickers and Brinell hardness
Hybrid	laser combined arc, welding method
Hybrid LF	Hybrid welding method, where laser beam travels in front of MAG torch
Hybrid MF	Hybrid welding method, where MAG torch travels in front of laser beam
Laser	Laser welding without wire material
MTS	material testing system
PM	parent material
PPCC	probability plot correlation coefficient
SAW	submerged arc welding
SSC	cyclic stress-strain curve
TZ	transition zone
WM	weld metal
WN	weld notch

ORIGINAL FEATURES

Previous investigations show that the laser-based joints can have significantly different fatigue strength compared to the arc-welded joints. Up to now, the physical explanation for the difference in fatigue resistance between the laser-based and arc-welded joints has been lacking. This thesis provides an improved understanding of the fatigue damage process in the laser-based joints, focusing especially on the influence of mechanical properties on macro crack initiation. The present results are also directed towards the modelling and predicting of fatigue strength of welded steel joints. The following features of this thesis are believed to be original:

1. Experimental investigation of the geometrical dimensions and mechanical properties of the weld notch and their influence on the macro crack initiation and propagation life for butt joints welded by laser-based methods. The study revealed the significance of the macro crack initiation period for the total fatigue life as well as the significant effect of mechanical properties on the fatigue strength of the joint.

2. The nonlinear FE analysis of stresses and strains in a laser hybrid welded joint considering the effect of HAZ with strongly varying strength properties. The main features needed for a simplified response approach were drawn from this analysis and clarified. Material elasto-plastic behaviour, both in base plate and in weld notch, should be considered.

3. Two-step approach to estimate the notch stresses and strains of the laser-welded joints. This approach covers differences in the stress-strain behaviour of material zones in the welded joint. It is able to describe the elasto-plastic stresses and strains with sufficient accuracy under full or partial yielding of a cross-section.

4. Development of a theoretical approach to macro crack initiation based on the discrete growth of short cracks. This approach is based on the stress and strain effective in the fatigue analysis, taking into account material microstructure and hardness. The approach enables modelling of the initiation process of a macro

crack in welded steel joints with varying geometrical and mechanical properties.

5. Statistical analysis of the parameters describing the geometry of welded butt joints to define the critical geometry in relation to fatigue. This analysis is based on the relation between the weld's geometrical dimensions and stress concentration factor. The analysis reveals the difference in the stress concentration factor between the laser-based and arc-welded joints caused by a differing size of weld bead.

6. The approach to estimate the fatigue resistance of laser-welded joints based on the effective notch strain and on critical weld geometry. The approach gives the theoretical basis for macro crack initiation, thus making it possible to improve the fatigue life prediction for both laser-based and arc-welded joints.

1 INTRODUCTION

1.1 General

During the past few decades, the shipbuilding industry has shown increasing interest in laser welding; in fact, the first installations have already been supplied to shipyards (Kahl 2000; Müller and Koczera 2003; Roland *et al.* 2004; Herbert 2004). Hybrid welding, i.e. laser combined with gas-shielded metal arc welding, is expected to become especially widespread. Hybrid welding offers special advantages, such as low welding distortions, high productivity and easy automation, over arc welding. Additionally, this new welding method opens opportunities for the design of light weight structures. However, the welding process of laser-based welding differs from that of arc welding. Laser welding causes localised heat input with narrow weld and heat-affected zones, inducing hardness distribution with strong variation, see Figure 1.

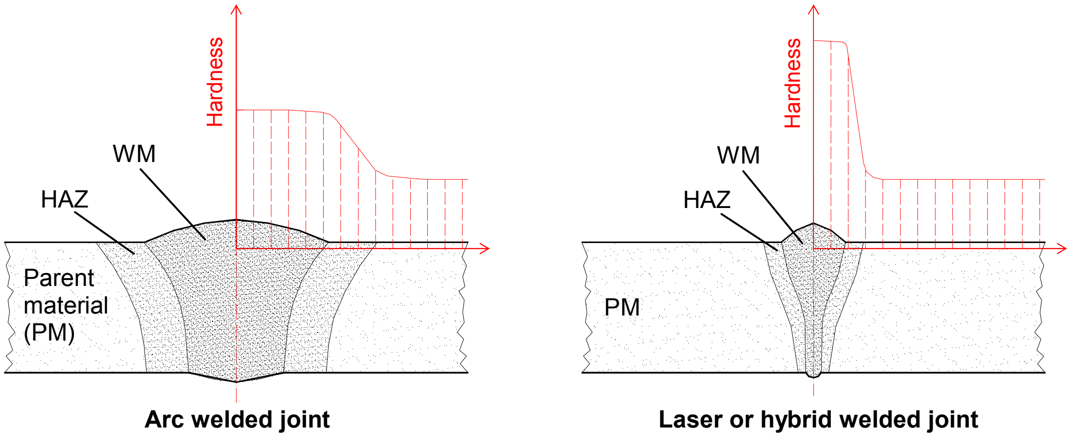

Figure 1: Material zones of joints welded respectively by arc and laser methods: parent material (PM) with weld materials consisting of heat-affected zone (HAZ) and weld metal (WM).

Structural design of passenger ships aims at decreasing light ship weight and lowering the centre of gravity without reducing the reliability of the hull girder. This requires combined and deep knowledge of loads, responses and strengths. Today, most fractures in ship structures are due to fatigue. Fatigue is a progressive process and damage is accumulated during several millions of load cycles. This damage is often initiated from weld discontinuities; therefore, the mechanical and geometrical properties of welded joints have a strong influence on the fatigue. Fatigue failure in the time scale is composed of crack initiation, propagation and of the final fracture when the crack grows to a critical size. This complexity of the damage process implies special challenges for the fatigue design of the structures.

Motions of a ship in waves induce cyclic primary stresses in the hull girder, which define the nominal stress range, $\Delta\sigma_{nom}$, in fatigue assessment. Figure 2 presents the vertical distribution of the nominal stress due to the longitudinal bending of the hull girder of passenger ships. A special feature in welded ship structures is that the nominal stress is also influenced by fabrication methods. Therefore, the nominal stress can exceed the material yield strength. Geometrical discontinuities in welded structures cause increases in the structural stress σ_s (Hobbacher 2007). The weld of a joint induces the local notch stress σ_{ln} and strain ε_{ln}, which define the response for the fatigue analysis. In the following text, the notch stress and strain are used without subscripts when there is no danger of misinterpretation. Fatigue resistance is defined by the fatigue capacity and the slope of the *S*-*N* curve.

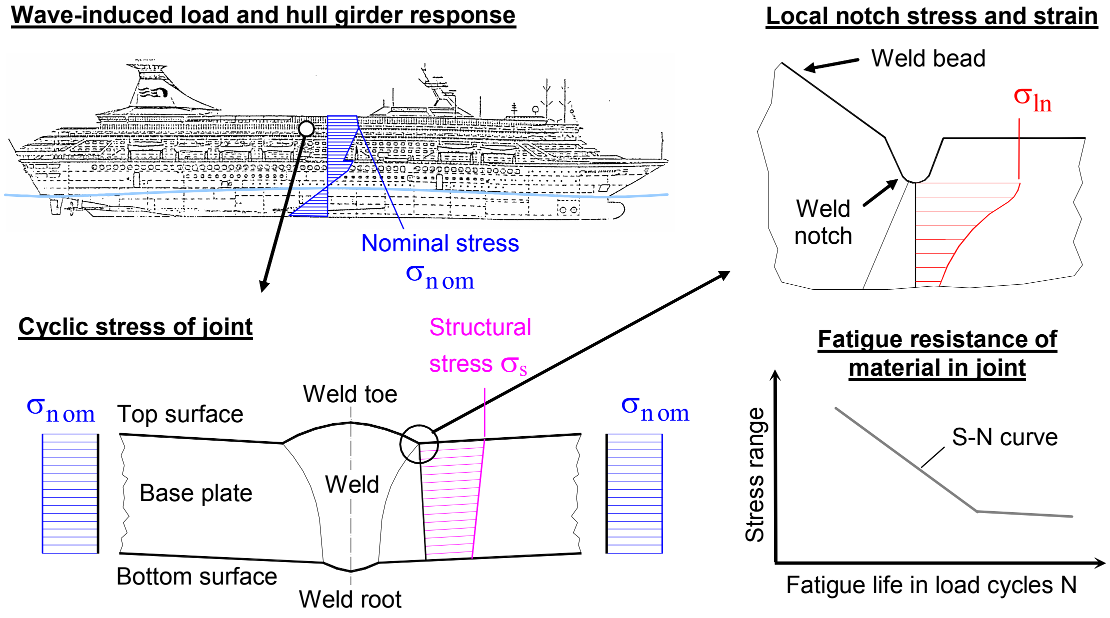

Figure 2: Fatigue assessment of a welded joint.

The design for fatigue of a welded joint is based on the cumulative damage theory and on the nominal, structural or notch stress approaches, depending on the level of structural analysis. Consequently, the fatigue resistance is described with the experimental *S*-*N* curves that include different degrees of information about the geometry and material properties of welded joints. The existing experimental database of the *S-N* curves covers different arc-welded joints. Knowledge of the *S-N* curves for the fatigue design of joints welded by laser-based methods is mainly limited to the level of the nominal stress approach, see, for instance, Kujala *et al.* (1999), Laitinen *et al.* (1999), Meyer Werft (2000), and Weldingh and Kristensen (2003). However, previous investigations have revealed that the *S-N* curves of laser-based joints and arc-welded joints can differ significantly. The slope value of *S-N* curves equal to 3 is commonly used for arc-welded joints. As for laser-welded joints, the slope value has been observed to reach up to a value of 10 (Laitinen *et al.* 1999). Additionally, significantly higher fatigue strength has been reported for laser-based joints compared to those of arc-welded joints (Ring and Dahl 1994; Weldingh and Kristensen 2003). The physical explanations for these discrepancies are still quite obscure.

1.2 State of art

Studies of the fatigue resistance of welded joints strongly rely on experiments. This is mainly due to the extremely local phenomenon of the process of fatigue damage. However, the codes for practical fatigue design require information concerning the parameters that affect the fatigue process, derived from theoretical models.

According to present knowledge, the fatigue damage process is divided into different stages (Cui 2002). Macro crack initiation includes short crack nucleation, the growth of short cracks up to the threshold length $l_{s,th}$ and the propagation of short cracks up to the threshold length of the macro crack $l_{m,th}$. The initiation is followed by the phase of macro crack propagation up to the final failure of the structure. The length $l_{s,th}$ is the smallest crack size that has a stable and measurable crack growth rate. This crack length is observed to be about three times the grain size of the material (Tokaji *et al.* 1986; Miller 1987; Goto 1994; Kawagoishi *et al.* 2000).

Different theoretical experiment-based models exist to describe the macro crack initiation. To describe this stage, the Paris law (Paris and Erdogan 1963) has been applied with an increased crack length by a constant value related to material properties (El Haddad *et al.* 1979). Nisitani (1981) has proposed a separate model based on the mechanical parameters of short crack propagation from $l_{s,th}$ up to $l_{m,th}$. Recently, it was shown that the model of short crack propagation based on the Paris Law should also include the crack closure effect (Hou and Charng 1997; Newman *et al.* 1999; Peeker and Niemi 1999). Notch tip plasticity, three-dimensionality of the stress state and the size of the damage zone are important issues there. However, it is questionable whether the idea based on the individual crack length can be used, as several short cracks normally exist in the damage process. Zhixue (2001) suggests that the total area of short cracks is the most descriptive parameter. Socha (2003; 2004) shows that the damage process of short cracks can also be described by the change of inelastic strains. Murakami and Miller (2005) report that the cumulative damage model based on the Coffin-Manson equation (Coffin 1954; Manson 1954) can be used to estimate short crack propagation. A comprehensive review of different damage models was given by Fatemi and Yang (1998).

According to Lawrence *et al.* (1978), in the strain-based approach to welded joints, the macro crack initiation is described by the Coffin-Manson equation. This initiation phase is followed by the macro crack propagation, which is normally modelled with the Paris law. The stress-based approaches (Radaj 1990) aim to determine the endurance limit of welded joints. However, these approaches can also be used to explain the damage process from the crack nucleation up to the final failure, assuming that the slope of the S-N curve m is independent from the structural detail and obtains a specific value. This approach is only valid if the period of the short crack nucleation and propagation is negligible. Then the Paris law gives $m = 3$.

Damage models for fatigue rely primarily on experimental investigations. Experiments are carried out to determine material parameters and validate theoretical models. In fatigue experiments, the smallest detectable damage depends on the measuring technique and on the applied test specimens. In the case of a finely polished surface, the replica technique has been frequently applied to the microscopic study of cracks (Murakami and Miller 2005). The crack length of 10 μm on the surface of a specimen is detectable, but the measurement of the crack depth is not possible using this technique. Alternatively, extensometers or strain gauges with advanced data processing have been successfully applied. With the transverse extensometer, it is possible to measure damage at an early stage of fatigue (Socha 2003). The strain gauge or the extensometer with the compliance method (Anderson 2005) is applied to monitor the surface crack propagation with the measuring accuracy of 80 μm (Cai and Shin 2005). Surface roughness of welded joints and material inhomogeneity will influence the accuracy of this method. In the case of welded joints, a crack length of 0.3 mm - 0.5 mm can be observed by strain gauges or the ACPD (alternating current potential drop) method (Bell *et al.* 1989; Otegui *et al.* 1991; Ring and Dahl 1994). Thus, this size of crack length corresponds more to that of a macro crack, and therefore the phase of the macro crack initiation is difficult to observe. Consequently, the fatigue experiments of welded joints usually aim to observe the final failure and the total fatigue life required to determine the *S-N* curve.

The influence of the weld geometry on the fatigue strength of laser-based joints has been investigated with the help of the stress-based approach. Ring and Dahl (1994) have studied laser-welded butt joints and have found that the laser weld has about a 50% higher fatigue strength than that of the conventional arc weld due to better weld geometry. This fact has been supported by other studies dealing with butt and cruciform joints (Weichel and Petershagen 1995; Caccese *et al.* 2006) and with laser stake welded joints (Kujala *et al.* 1999). Additionally, Weichel and Petershagen (1995) report that the fatigue strength of the laser joints is influenced by the welding energy and by the carbon content of parent material, which affect the microstructure of the weld. High and localised welding energy can also cause the strength overmatching of weld. Kristensen (1996) indicates that this overmatching may protect the weld notch against plastic deformations, thus causing an increase of fatigue life. This problem was investigated by Dahl and Reinhold (1996) using the strain-based approach. However, the correlation between experimental and computational results was not satisfactory. This may be the result of poor geometrical modelling of the weld notch. Thus, further investigations that take into account the actual notch shape are needed to draw clear conclusions as to the effect of geometrical and material parameters on the fatigue resistance.

The influence of weld notch shape on the fatigue resistance has been studied for arc-welded joints, while similar studies for laser-based joints are still in their infancy.

Bell *et al.* (1989) have experimentally investigated the significance of the undercut of weld toe on the fatigue of T-joints. They observe that the depth of the undercut can significantly reduce the fatigue life. Janosch and Debiez (1998) have reported the same results with the help of experimental and computational studies. A systematic analysis of the influence of weld notch shape was presented by Gosch and Petershagen (1997). They illustrate the effect of the undercut shape using the notch stress approach. The notch depth D and the root radius ρ are mentioned as the most significant parameters, see Figure 3. The effect of a sharp undercut, i.e. a crack-like notch, has been analysed using the crack propagation approach (Petershagen 1986; Nguyen and Wahab 1995; 1996; 1998; Wahab and Alam 2004). These studies show that weld imperfections on the surface are more critical than internal ones. However, it should be noticed that the applied crack propagation approach ignores the period of the macro crack initiation.

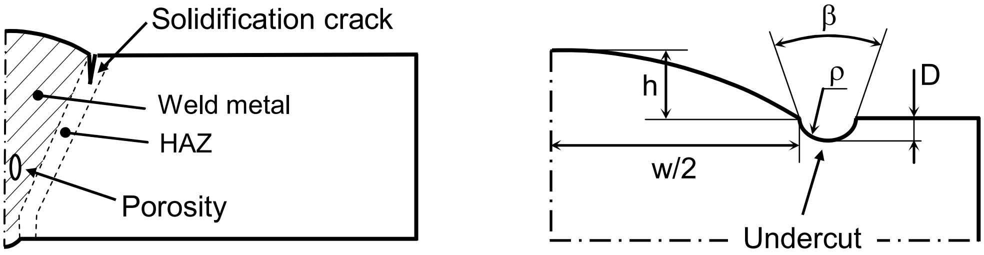

Figure 3: Different imperfections in the weld according to Wahab and Alam (2004) and the weld geometry according to Gosch and Petershagen (1997)

The notch stress approach has given promising results for the fatigue strength at the endurance limit of laser-welded joints (Ring and Dahl 1994; Weichel and Petershagen 1995). However, the slope of the *S-N* curve still stays unclear, and thus requires additional modelling of the macro crack initiation life. The strain-based approach is usually applied to model the macro crack initiation, where the influence of the mean stress is taken into account, see Morrow (1965) and Smith *et al.* (1970). The first application of the strain-based approach for welded joints was described by Mattos and Lawrence (1977). However, in the case of welded joints, the fatigue coefficients of the Coffin-Manson equation can be especially difficult to determine, and thus the hardness-based estimation was suggested (Lawrence *et al.* 1981). Recently, this approach has been observed to give satisfactory results for different parent materials (Roessle and

Fatemi 2000; Lee and Song 2006), but its applicability to laser-based joints needs validation.

The notch stress and strain inside the elasto-plastic range are usually determined using the Neuber rule (1961) or Glinka's approach (1985) to simplify the analyses. These closed-form solutions are well known. They are used in several applications focused on welded structures, as reviewed by Radaj and Sonsino (1998). The influence of different material zones in arc-welded joints has been studied by Fricke *et al.* (1996) and Heo *et al.* (2004). They suggest that the applied stress-strain curve should be based on that of the weld or on the mean value between the weld and HAZ.

In the case of welded joints with sharp notches, it is necessary to define the effective stress and strain for fatigue. This is due to the high value of their gradients related to the scale of grain size. Lawrence *et al.* (Mattos and Lawrence 1977; Lawrence *et al.* 1978) suggest a combined stress- and strain-based approach, where the stress concentration factor in Neuber's rule is replaced by the fatigue notch factor from Peterson's semi-empirical formula (1959). An idea of fictitious radius equal to the specific size (Neuber 1968) was further developed for welded joints by Radaj (1990) and applied in the strain-based approach, for example, by Fricke *et al.* (1996). These approaches have been originally developed for the notch stress approach. In the literature, several approaches to determine the effective stress have been presented, see Yao *et al.* (1995). There, the effective stress is obtained by averaging the stress inside a certain volume (Taylor 1999). The use of these in the strain-based approach can be challenged, because the estimation of the fatigue life given by this combination of the approaches leads to unsatisfactory results (Dahl and Reinhold 1996; Radaj *et al.* 1998).

Since the first application of the strain-based approach for welded joints (Mattos and Lawrence 1977), different damage models (Radaj and Sonsino 1998) have been proposed that include, for example, the effect of multiaxial loading (Sonsino 1995). However, little attention has been paid to the short crack propagation using the strain-based approach.

1.3 Scope of work

Previous investigations have been unable to explain the differences in fatigue resistance between laser-based and arc-welded joints. Therefore, one goal of the present study was to complement existing knowledge of fatigue damage in laser-based joints. These joints included both laser and hybrid welds.

The present investigation focused on the influence of the weld geometry and mechanical properties on fatigue due to the welding process. The fatigue resistance of different material zones in welded joints was investigated by weld materials testing. Welded joints were additionally tested to study the effect of the weld geometry. To describe the influence of notch geometry and material properties on fatigue resistance, the development of a new theoretical approach was required. In this approach, the non-linear behaviour of the stresses and strains in the weld in particular was assumed to have an important effect on short crack growth. The application of the new theory concentrated on butt joints welded by the laser-based methods. Additionally, arc-welded joints were included as a reference. This basic type of butt-welded joint made it possible to concentrate on the effect of the weld notch itself, and thus to avoid the problem caused by the complicated structural stress. However, in the case of butt joints, this response also included the influence of joint misalignments.

1.4 Outline of work

The present investigation comprises both an experimental and a theoretical study, see Figure 4. The experimental work presented in Chapter 2 consists of the measurement of joints and fatigue testing. The measurements of joints covered their geometrical dimensions and mechanical properties. The fatigue experiments included the tests of weld materials without the effect of the weld geometry and the tests of welded joints, which included both material and geometrical effects. The tests of the weld materials were carried out using miniature specimens, and thus these tests will be referred to as miniature tests. Correspondingly, the tests of welded joints using plate specimens are referred to as joint tests. These experimental investigations aimed to study the correlation between fatigue strength and joint parameters. These measurements also made it possible to validate the new theoretical fatigue model. In the fatigue tests, advanced measuring techniques based on the change of the inelastic strain (Socha 2003) and on the compliance method were applied to observe the damage process.

In the theoretical analysis, first a preliminary study of notch stresses and strains in a welded joint with different material zones was conducted using the non-linear FEM (Finite Element Method) to reveal the influence of material inhomogeneity. This analysis, presented in Chapter 3, formed a basis to develop a simplified response method based on the linear elastic FEM and Neuber's rule. This and the new theoretical approach to macro crack initiation are given in Chapter 4. This approach, based on material hardness and averaged grain size, was validated with the data from the miniature tests. Chapters 5 and 6 provide the statistical analysis of weld dimensions and their effect on the notch stresses, which, in turn, was applied to determine the critical weld geometry. With the help of this geometry, the actual stress concentration factor for the fatigue analysis was determined. This is covered in Chapter 7, complemented by the new theoretical approach to estimate the fatigue resistance of welded butt joints. The results of the approach were validated with the experimental results.

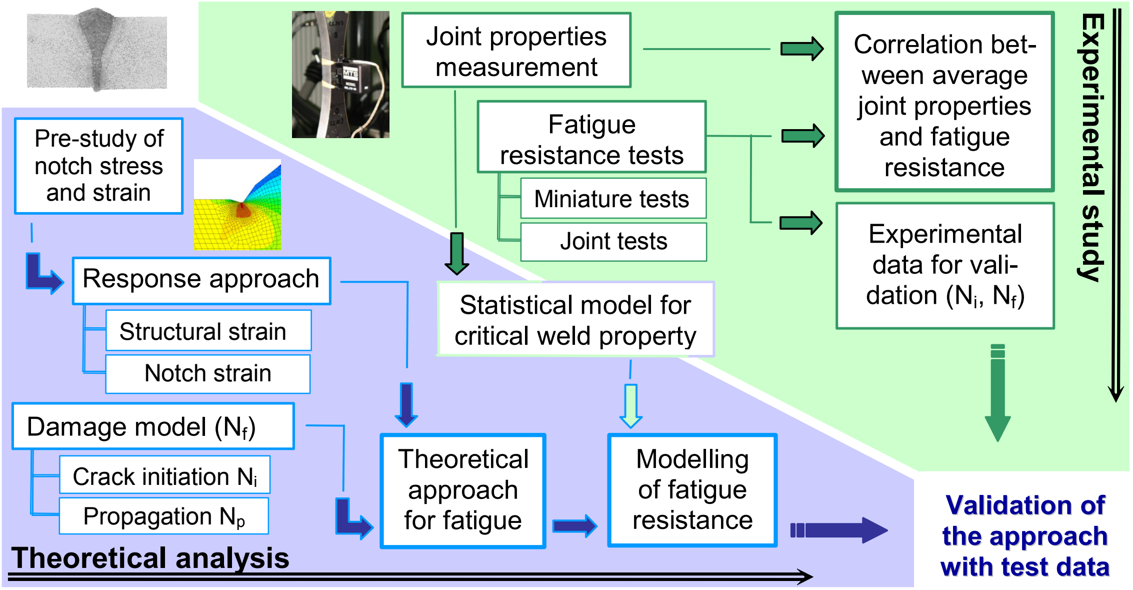

Figure 4: Flow chart of investigation.

2 EXPERIMENTAL WORK

2.1 Objectives

The experimental study aimed to reveal the main parameters that affect the fatigue resistance of welded butt joints. The focus was on the hybrid laser welds. Furthermore, the laser and arc welds were also studied for comparison. Figure 5 presents the general contents of the experimental investigation. The work was divided into three main tasks: the geometrical dimensions of the joints, their mechanical properties and fatigue resistance.

The non-destructive replica technique was applied to define the geometrical dimensions of the weld and weld notch. The mechanical testing included the measurements of the Vickers hardness (HV) profiles as well as the monotonic and cyclic stress-strain curves (SSC) for the weld materials using the miniature test specimens. The fatigue tests included separate tests for weld materials and for welded joints. Weld material tests with the miniature test specimens gave the initiation life of the macro crack for different weld materials. The pre-fabricated micro notched specimens were used for validation. The tests of the welded joints gave the initiation life of the macro crack and the fatigue strength. In the present work, the main results of the investigations are presented and discussed. Their further details can be found in Remes and Socha (2003), Remes (2003), Tamminen and Remes (2003), and Gribenberg (2003).

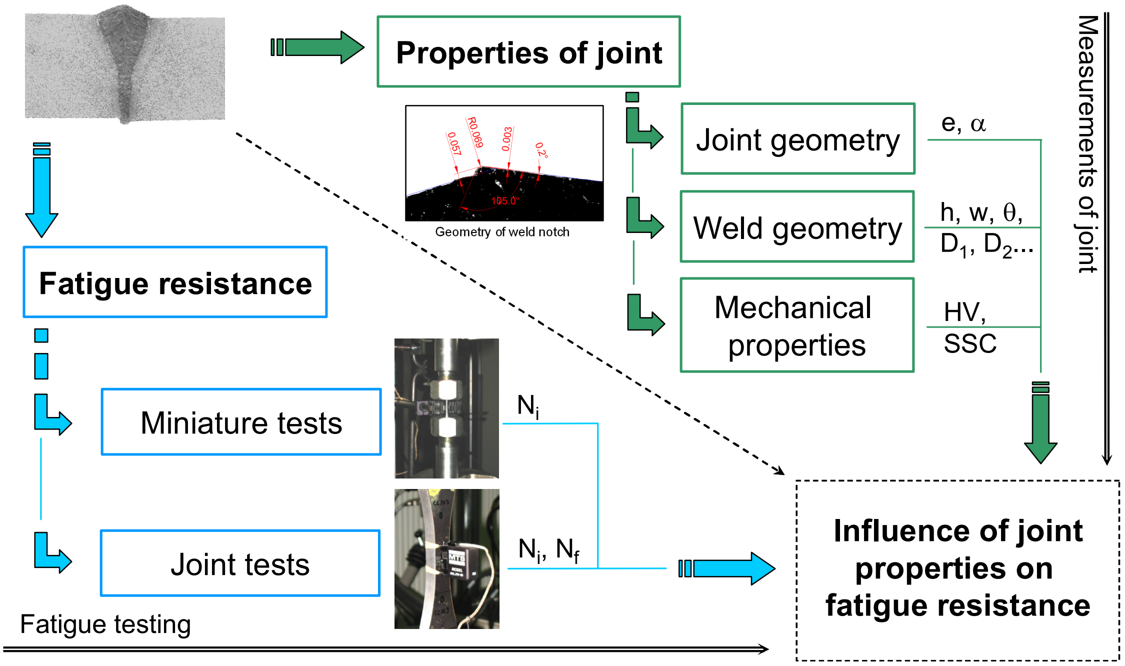

Figure 5: Layout of experimental investigations.

2.2 Fabrication of test specimens

2.2.1 Welded plates

The thickness of the welded plates was 12 mm and the steel material was RAEX S275 LASER, the chemical composition of which is shown in Table 1. This parent material fulfils the requirements for the chemical composition presented in the guidelines of Classification Societies (1996; 2006). Some values of the mechanical properties for the base plates are shown in Table 2.

Table 1: Chemical composition (wt %) of the RAEX S275 LASER steel

Chemical	C	Si	Mn	P	S	Al	Nb	V	Ti	CEV	P_{cm}
wt %	0.08	0.014	1.39	0.008	0.004	0.028	0.003	0.006	0.001	0.32	0.15

Table 2: Mechanical properties of the base plate

Steel Type	Grade	σ_y [MPa]	σ_u [MPa]	A_5 [%]
RAEX S275 LASER	L 24 D	285	438	34 [1]

[1] The value according to the certificate produced by the steel manufacturer

One-side welding with full penetration was used to manufacture the plates for the test specimens. Table 3 shows the welding methods and the producers. Two hybrid welding methods, $C0_2$-laser combined with MAG, were used, see Figure 6. In the Hybrid LF welding, the laser beam was travelling in front of the MAG torch. An opposite welding order was used in the case of the Hybrid MF method, where the MAG torch travelled in front of the laser beam. Laser-welded plates were produced using the $C0_2$-laser without filler material. The submerged arc welding (SAW) was carried out using the one-side welding method.

Table 3: Description of welded plates with welding methods

Abbreviation	Description of the welding method	Producer
Hybrid LF	CO_2-Laser combined MAG welding, Laser travels first	Force Technology
Hybrid MF	CO_2-Laser combined MAG welding, MAG travels first	Meyer Werft
Laser	CO_2-Laser welding without filler material	Force Technology
SAW	Submerged arc welding using two wires	Aker Yards Finland

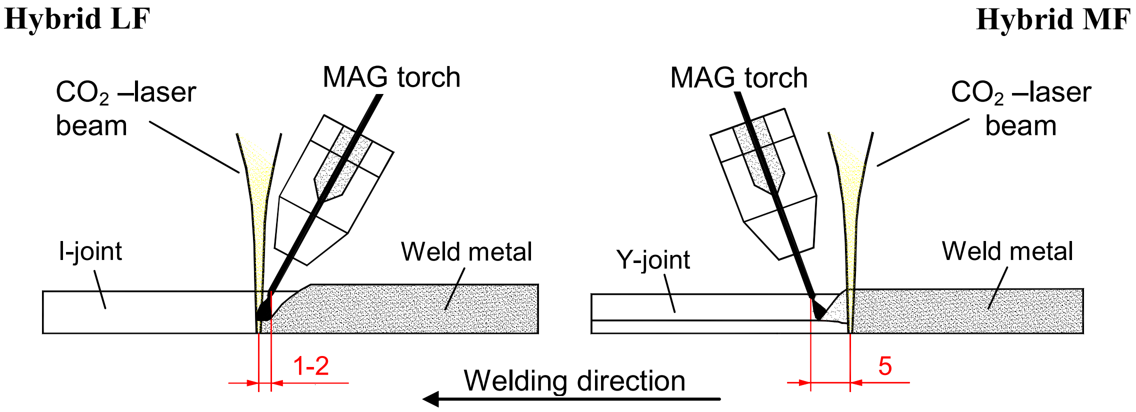

Figure 6: Arrangements of hybrid welding.

The laser and hybrid welding were performed in the Welding Laboratory of the FORCE Technology and in Meyer Werft Shipyard. The edges of the plates were milled. I-type groove shape was used for the Laser and for the Hybrid LF welding. For the Hybrid MF welding, the groove shape was Y-type. Before welding, the parts of the plate were tack welded to ensure zero air gaps in the joints. In the FORCE Technology Hybrid LF, welding was performed with Rofin-Sinar SR 170 17 kW CO_2-laser and ESAB ARISTO 500 MAG equipment. Shielding gas was a mixture of helium, argon and oxygen. The filler wire was ESAB 12.51 with a diameter of 1 mm. Laser welding was carried out with the help of the Rofin-Sinar equipment; helium was used as shielding gas. The Hybrid MF welding was performed using Trumpf TLF 1200 10 kW CO_2-laser and Fronius TPS 450 MIG equipment. The filler wire was Hoesch Weko 4 with a diameter of 1.2 mm. Shielding gas was helium. Table 4 gives welding parameters for the Laser, Hybrid LF and Hybrid MF welding.

Table 4: Laser and hybrid welding parameters

Welding method		Laser	Hybrid LF	Hybrid MF
Travel speed	m/min	1.0	1.4	1.5
Laser: Power	kW	11.0	14.0	10.0
MAG: Current	A	-	193	420
Voltage	V	-	21.4	40.6
Wire speed	m/min	-	6.9	16.2

The submerged arc welding was performed in the panel production line of Aker Yards in Turku Shipyard. One-side welding with two wires was applied. The watercooled Cu-backing rod was used on the root side. During welding, the plates were clamped using vacuums. The travel speed was 0.65 m/min, while for the two wires the current was 831 A and 504 A, and the voltage 32 V and 35 V.

2.2.2 Test specimens

Test specimens were manufactured from the welded plates, see Figure 7. Two different types of test specimens were used: a miniature and a welded-plate test specimen. All the test specimens had an hourglass shape to localize the damage process to the narrowest cross-section of the specimen. In the miniature specimens, this cross-section was varied between the different material zones: parent material, HAZ and weld metal. The welded plates were milled to clean the surfaces so that the different material zones could be seen and marked for machining. After that, cut slices were turn-milled and, finally, the miniature specimens were polished. The welded-plate test specimens were water-cut from the welded plate. Then, the side surfaces were milled and sharp corners were ground.

Figure 8 presents the dimensions of the miniature specimens. The length of the specimen was 40 mm and the minimum diameter of the cross-section was 4 mm. The radius of the hourglass was 20 mm. The notched miniature specimens had a micro notch with 0.05 mm depth and 0.02 mm radius.

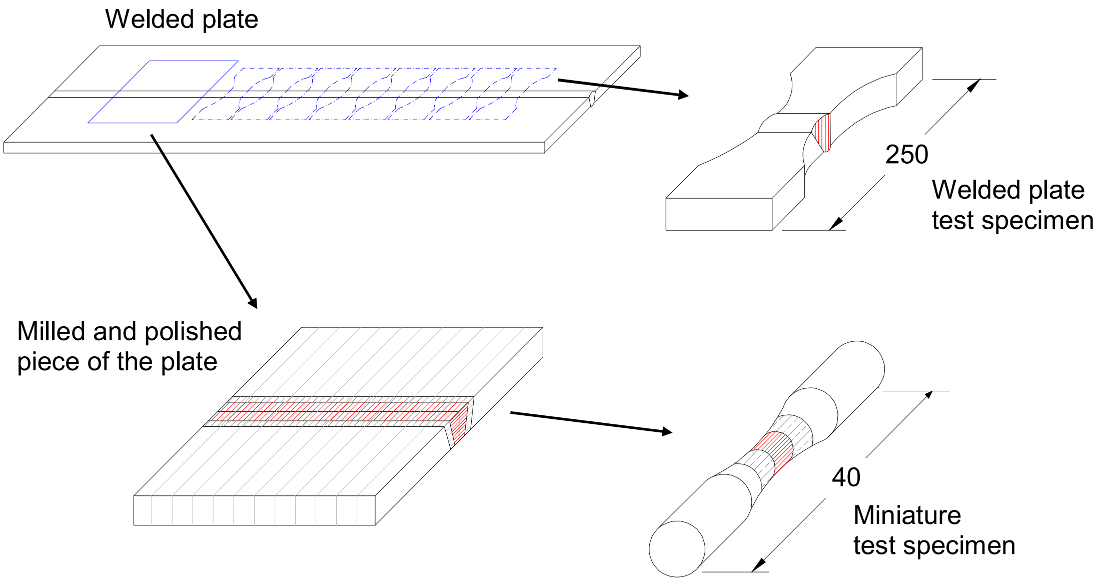

Figure 7: Manufacturing the test specimens.

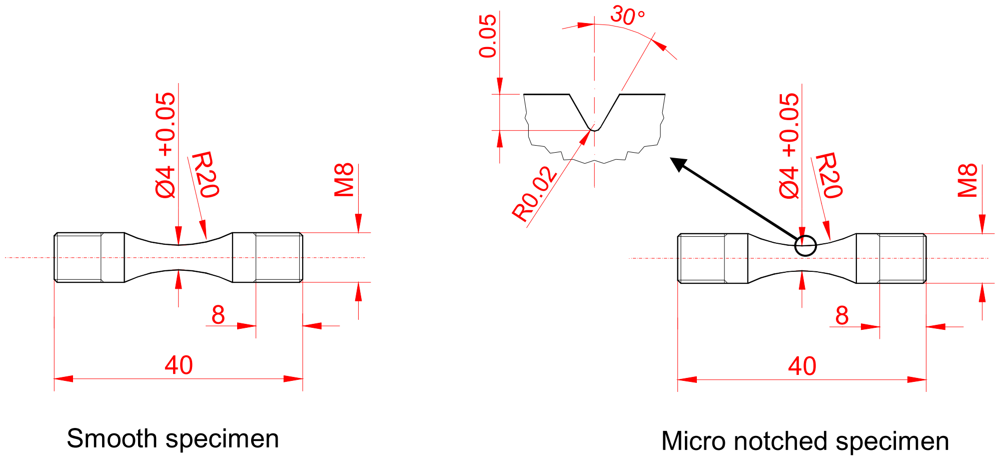

Figure 8: Geometry of a smooth (left) and a notched (right) miniature test specimen.

The geometry of the welded-plate specimens is presented in Figure 9. The width of the narrowest cross-section was limited to 20 mm because of the available maximum 100 kN load of the test equipment. The specimen length was 250 mm and the radius of the hourglass was 160 mm. Two different types of welded-plate specimens were used. Type A was without any modifications. The ends of the Type B specimen were machined to eliminate the bending moment during gripping. Type B was used in the case of high angular misalignment.

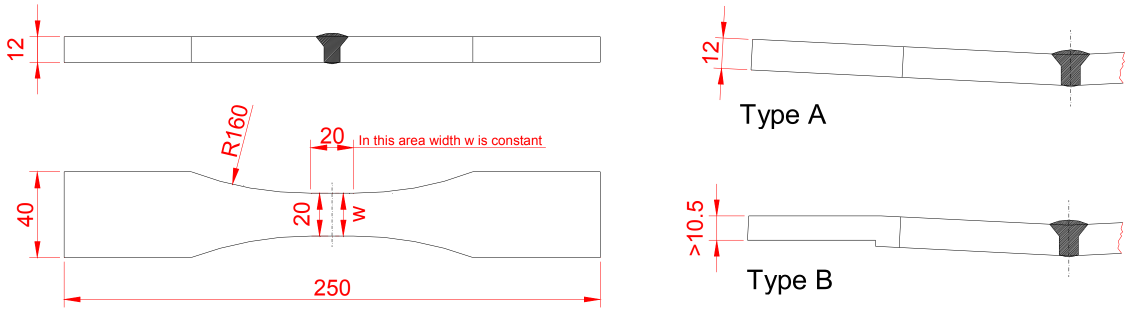

Figure 9: Geometry of welded-plate specimens for Type A and B.

2.3 Definition of geometrical dimensions of a butt joint

Descriptive geometrical dimensions of welded butt joints are required further on in the study. An introduction to the geometrical definitions is given by Yung and Lawrence (1985) and Gosch and Petershagen (1997), but for laser welds there exist additional requirements. The geometrical dimensions were selected to cover those that affect stresses and strains in the locations of the joint critical to macro crack initiation or propagation. Special emphasis was put on the shape of the weld notch.

The geometrical dimensions of the welded butt joint were categorized into three groups: the misalignments of the joint, the dimensions of the weld bead and the weld notch. The misalignments included the axial misalignment e and the angular misalignment α, see Figure 10. The axial misalignment represents the eccentricity of welded plates. The geometrical dimensions of the weld and weld notch are given in Figure 11. The geometry of the weld is defined with three different geometrical dimensions: the weld width w, the height of weld h and the flank angle of weld θ. Subscripts t and r refer to the weld toe and root side, respectively. Five additional dimensions were used to describe the geometry of the weld notch, where D_1 is the notch depth measured from the plane of the top surface, D_2 is the notch depth taken from the profile line of the weld surface, γ the notch flank angle, β the notch opening angle, and ρ the notch root radius. These definitions make it possible to determine the location and direction of the notch with respect to the weld and the base plate.

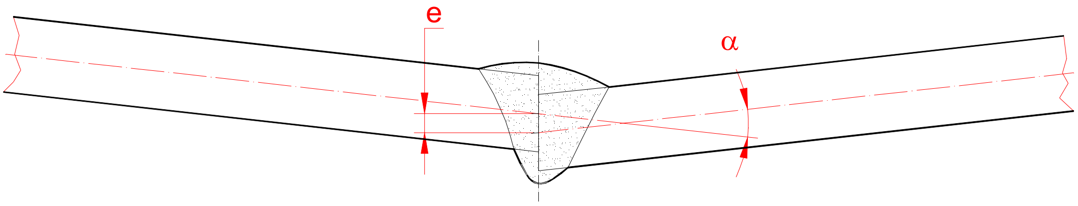

Figure 10: Axial (e) and angular (α) misalignment.

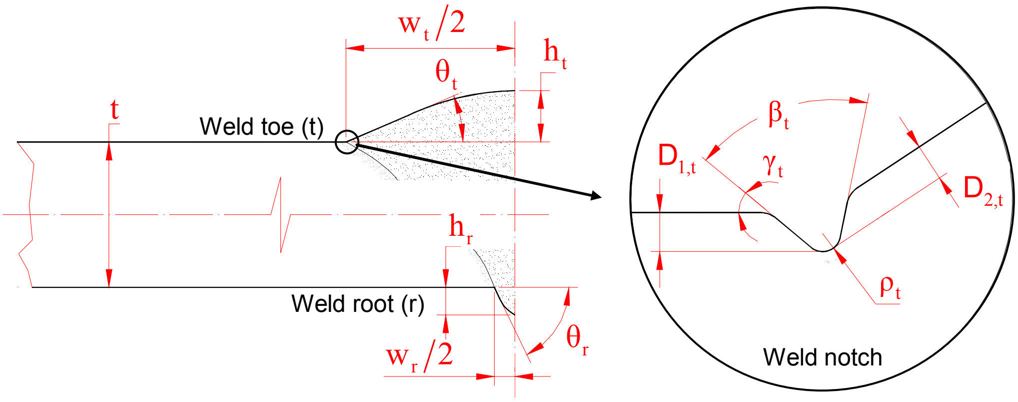

Figure 11: Dimensions of the weld and weld notch: weld width w, weld height h, weld flank angle θ, notch depth D, notch flank angle γ, notch opening angle β, and notch root radius ρ.

2.4 Test arrangements

2.4.1 Joint geometry of welded-plate test specimens

Misalignments

Vertical distances from the horizontal reference line were measured with the dial gauge in six different points along the specimen surface, as shown in Figure 12. Based on these values, the linear lines were defined with the least square method. From these linear lines, the vertical distances H_r and H_l between the middle and the end points of the specimen were calculated. Then, the axial misalignment e of the joint is

$$e=\left|H_l - H_r\right| \tag{1}$$

and the angular misalignment α becomes

$$\alpha=\frac{1}{2}\cdot\left[\arctan\left(2\cdot\frac{H_l}{L}\right)+\arctan\left(2\cdot\frac{H_r}{L}\right)\right], \tag{2}$$

where L is the length of the test specimen.

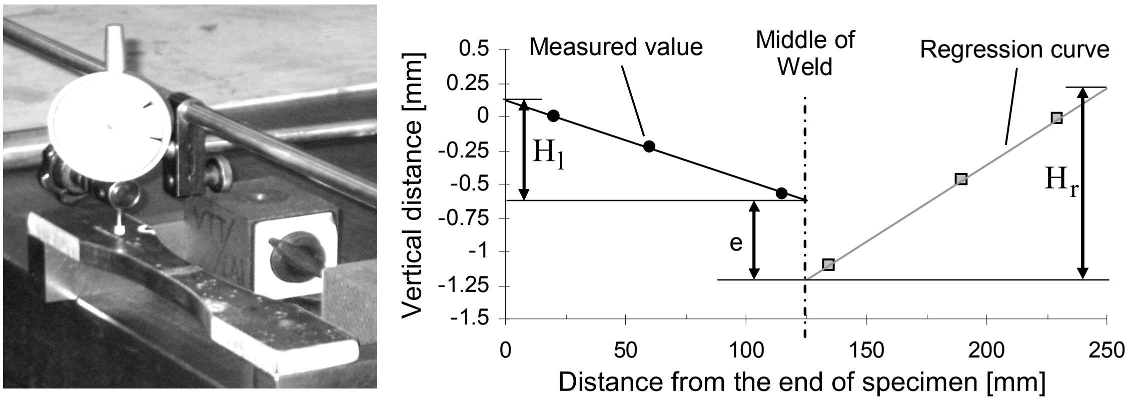

Figure 12: Arrangement to measure axial and angular misalignments.

Weld geometry

The geometry of the weld toe and root sides were analysed using the non-destructive replica technique shown in Figure 13. Before the fatigue tests, the replicas of specimen surfaces were prepared using silicone rubber, which gave resolution down to 1 µm. In Step 1, the surfaces of the weld toe and root were painted with liquid silicon rubber. The rubber hardened within a few minutes. After that, in Step 2, about 1 mm thick slides were cut from the replicas for the macroscopic analysis. Macro photos were taken with two different scales, one from the weld notch and the other from the weld itself. In Step 3, geometrical dimensions were measured from the photos. The numerical values of the weld dimensions, see Figure 11, were determined with the help of the AutoCAD software. The sample size was ten for the geometry of weld and twenty for the geometry of weld notch.

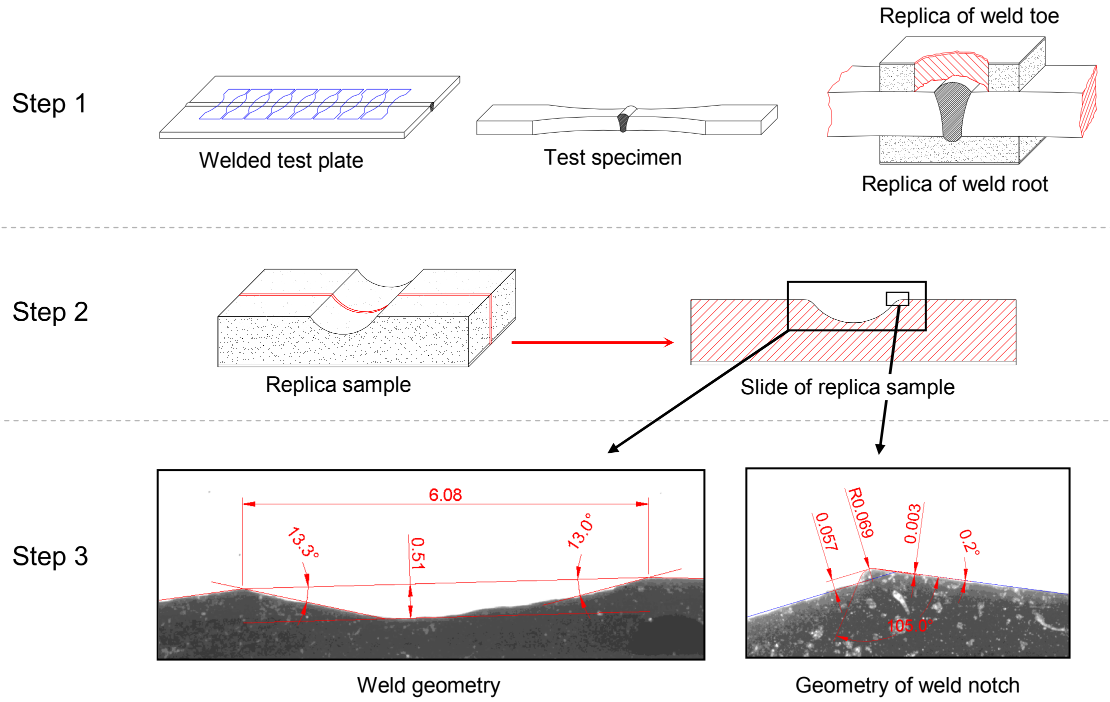

Figure 13: Procedure to measure the weld geometry: Step 1) preparing the replica of weld, Step 2) producing the slides of replica sample, Step 3) macroscopic analysis of the replica.

2.4.2 Mechanical properties of the weld

The study of mechanical properties comprised measurements of hardness and the stress-strain curves. The distributions of the Vickers hardness with 5 kg load, HV5, were measured along the lines in the cross-section of the joints, see Figure 14a, according to the requirement given by the Classification Societies (1996). Additionally, more detailed hardness measurements were taken, as shown in Figure 14b. Hardness measurements were performed in the research laboratory of Ruukki in Finland (Laitinen 2003). Other mechanical properties, such as tensile, bending and Charpy V impact strengths are reported by Laitinen *et al.* (2003).

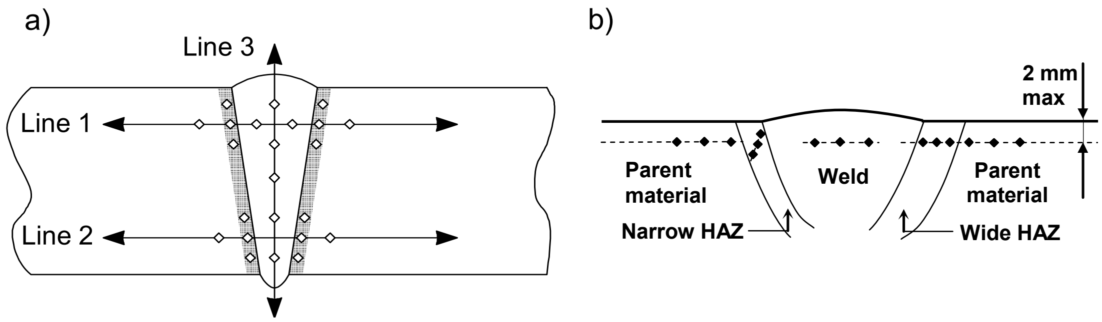

Figure 14: Hardness measurements in the cross-section of the welded joint according to Laitinen (2003).

The monotonic and cyclic stress-strain curves were determined for the parent material and weld metal. Those measurements were also possible for the HAZ metal in the case of the SAW joint. The cyclic stress-strain curves were measured with the miniature specimens using the procedure based on incremental strain range steps linearly first decreasing and then increasing (Landgraf *et al.* 1969), see Figure 15. The strain was measured at the centre line of the specimens using 1 mm long strain gauges. These were positioned on the specimens for the HAZ and weld metal according to the measured hardness distribution, as shown in Figure 15. The measurements carried out in the Laboratory of Engineering Material at TKK are reported in detail by Gribenberg (2003).

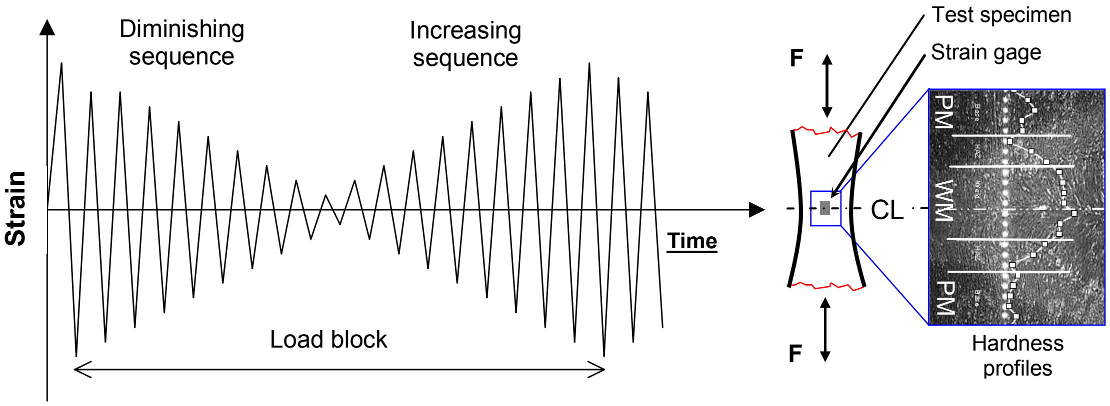

Figure 15: A principal sketch of one load block in the loading history used to determine the cyclic stress-strain curves, adapted from Gribenberg (2003).

The monotonic stress-strain curve was obtained from the first load cycle. The corresponding cyclic stress-strain curve under strain-controlled loading was defined from the saturated stress amplitude. As the total strain contains both the elastic and plastic strains, these two strains often need to be separated. This was achieved with the help of the Ramberg-Osgood equation (Ramberg and Osgood 1943)

$$\frac{\Delta\varepsilon}{2} = \frac{\Delta\sigma}{2 \cdot E} + \left(\frac{\Delta\sigma}{2 \cdot K'} \right)^{1/n'}, \qquad (3)$$

where $\Delta\varepsilon/2$ is the total strain amplitude, $\Delta\sigma/2$ is the total stress amplitude, E is the elastic modulus, n' and K' are the cyclic strain hardening and strength coefficients.

2.4.3 Fatigue tests of weld materials

The object of the tests was to study the fatigue strength of the different material zones in the welded joints. The fatigue resistance was derived from the force-controlled tests with constant amplitude using the miniature test specimens. The tests were performed using cyclic axial tension-compression loading with the load ratio R = -1. The load frequency was 20 Hz and a servo hydraulic testing machine type MTS 858 was used. During these fatigue tests, the number of the load cycle, strain and force were recorded. Strain measurements were taken to observe the point of the macro crack initiation.

The measurement and test arrangements were based on the MTS (Material testing system) standard. Figure 16 shows the general layout of the test system. The test specimen was attached to the special rods fixed to the MTS clamping system. This test arrangement was developed especially to avoid secondary bending of the specimen (Socha 2003). The strain was measured at the narrowest cross-section of the test specimen using the transversal extensometer, type MTS 632.20F-20. The transversal extensometer enabled the measuring of the damage process of the material of interest. During the load cycle, the transverse displacement was measured and the longitudinal total strain was calculated using the Hooke's Law (Socha 2003). Figure 17a shows the measured relationship between the stress and the total strain during one load cycle. The total strain range $\Delta\varepsilon_{tot}$ can be divided into elastic $\Delta\varepsilon_{el}$ and inelastic $\Delta\varepsilon_{ie}$ parts. An example of the recorded inelastic strain range as the function of the load cycle N is given in Figure 17b. The increase of the inelastic strain can be considered as an indication of the material damage due to the fatigue. Therefore, the time history could be divided into two different periods. A stable period was thought to be the time for short crack nucleation

(Socha 2003). The second knuckle point in the time history was considered to be caused by the initiation of macro crack; this point defines the initiation life N_i.

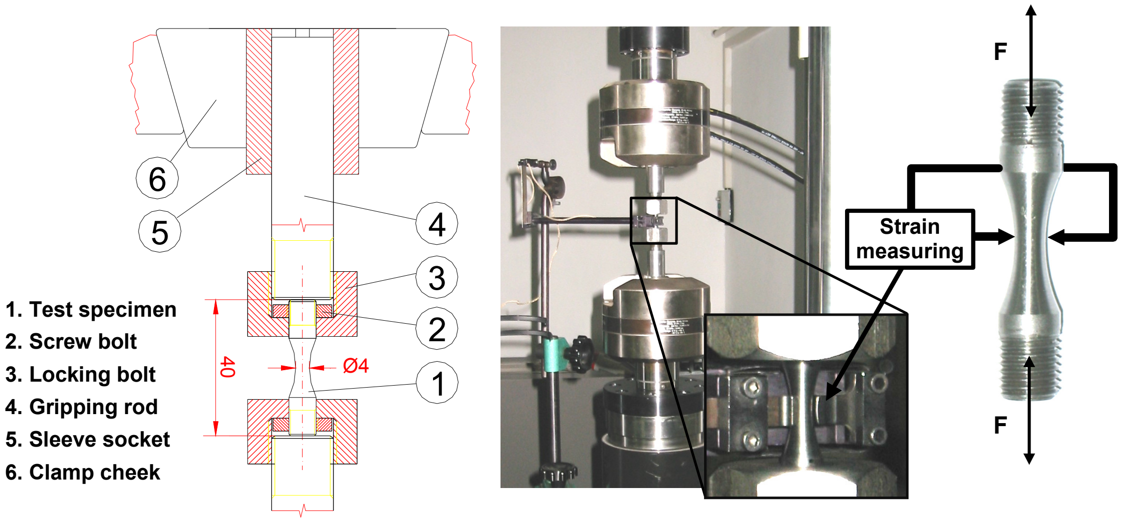

Figure 16: Test arrangement for fatigue tests of weld materials.

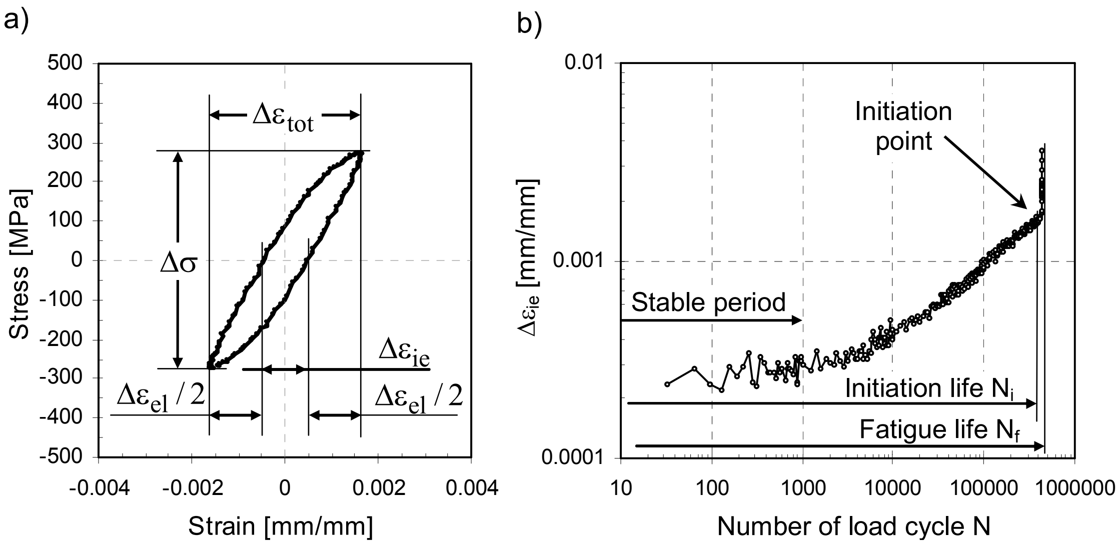

Figure 17: Hysteresis loop during one load cycle (left) and inelastic strain range $\Delta\varepsilon_{ie}$ during cyclic loading (right).

2.4.4 Fatigue tests of welded joints

The object of the testing was to measure the fatigue strength of the welded joints. The macro crack initiation and propagation were of special interest. The condition of the test specimens was ‘as welded’, so the reduction of fatigue strength due to the weld geometry was also included. The welded joints were tested by using tension loading with the load ratio $R = 0$. The fatigue tests were force controlled and the load amplitude was kept constant for each test specimen. The load frequency was between 5 and 20 Hz. The clamping system was rigid without hinges.

During fatigue testing, the force and strain values as well as number of load cycles were measured. The measured data was recorded from selected load cycles representing the whole load cycle range of the test. Figure 18 presents the test arrangement for the strain measurement. The force transducer was placed between the clamping system and the hydraulic cylinder. The axial strain at the narrowest cross-section of the specimen was measured using the extensometer type MTS 632.27F-20. The gauge length of the extensometer was 25 mm. The extensometer was fixed to the toe or root surface with a rubber band. The arrangement for strain measurements was similar to the unloading compliance method (Anderson 2005) used in fracture mechanics.

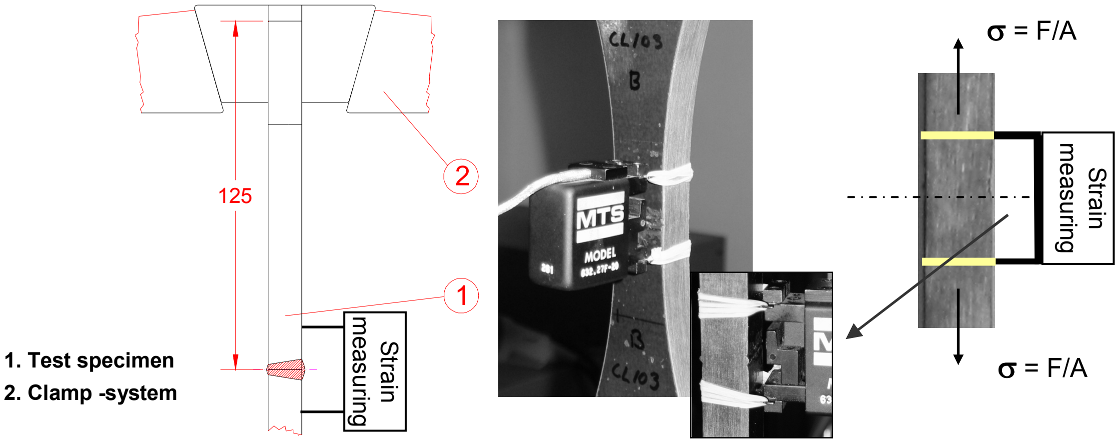

Figure 18: Arrangement of the fatigue test for a welded joint.

Figure 19a shows a measured stress-strain relationship during one load cycle. Based on the measured data, the regression line between the stress σ and the strain ε in the narrowest cross-section of the specimen was derived. Then, the chord modulus E_{CH} is expressed by

$$E_{CH} = \frac{\sigma_{\max} - \sigma_{\min}}{\varepsilon_{\max} - \varepsilon_{\min}} . \qquad (4)$$

The effective cross-section of the specimen is reduced when the macro crack grows; therefore the chord modulus changes. Accordingly, the fatigue damage process is related to the change of the chord modulus ΔE_{CH}

$$\Delta E_{CH} = \left| \frac{E_{CH,0} - E_{CH}}{E_{CH,0}} \right|, \tag{5}$$

where $E_{CH,0}$ is the initial value of the chord modulus after cyclic saturation.

Figure 19b shows an example of the history of the chord modulus change ΔE_{CH} in percentage as the function of the load cycles. The time history can be divided into two different periods separated by the initiation point of the macro crack. This point was defined by the 0.1% change in the value of the chord modulus. Physically, this means that the cracked area in the specimen was approximately 0.24 mm^2 when the initial cross-section area of the specimen was 240 mm^2. After the initiation point, the change of the chord modulus was accelerating due to the growth of the macro crack. The fatigue life N_f is composed of the two parts, i.e. of the initiation time N_i and the propagation time N_p, as presented in Figure 19b.

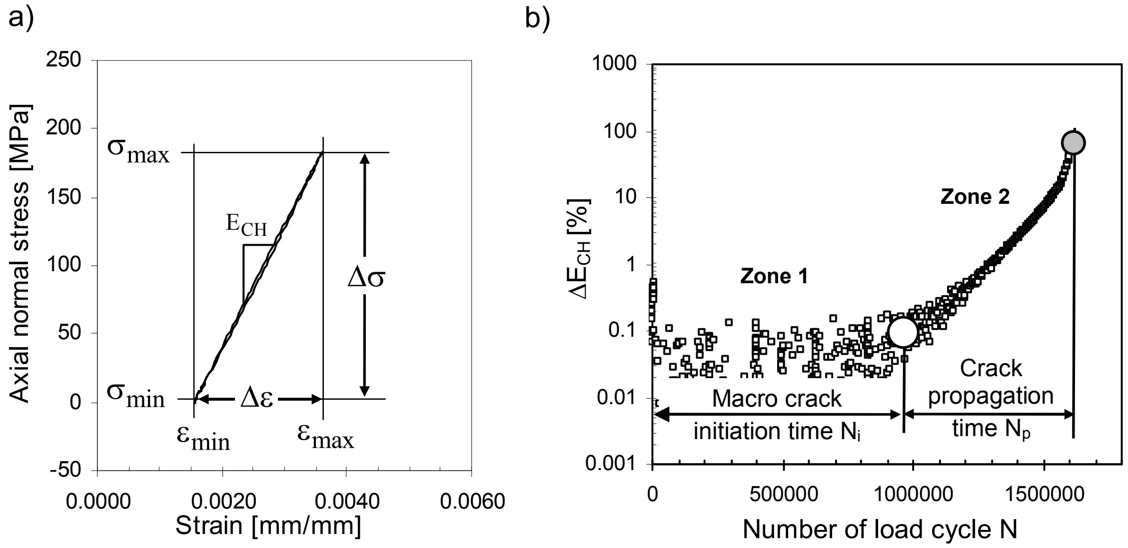

Figure 19: Measured stress-strain during one load cycle (left) and the change of chord modulus in percentage versus load cycles (right).

2.5 Results

2.5.1 Joint geometry

This chapter presents a summary of the geometry measurements for the welded joints, including misalignments and the dimensions of weld bead and notch. The mean value, the standard deviation, as well as the maximum or minimum values, are given. More detailed coverage of the results is given in Appendices A and B.

Misalignments

A summary of the statistical values for the axial and angular misalignments of welded joints are shown in Table 5. The results are given in absolute values to simplify comparison. Details of the misalignment statistics are given in Remes (2003). The values of the axial misalignment between different joints differed slightly. The mean value was almost equal for the SAW, Laser and Hybrid LF joints, varying from 0.20 mm to 0.29 mm. That of the Hybrid MF joint was slightly higher at 0.47 mm. A more remarkable difference was observed for the angular misalignment. The mean and maximum values for the Hybrid LF joint were 0.69° and 0.94°, i.e. significantly higher than those of the other joints with the maximum value about 0.25°.

Table 5: Statistics for axial and angular misalignments of different joints

Welded test specimen	SAW	Laser	Hybrid LF	Hybrid MF
Axial misalignment e [mm]				
Mean value	0.20	0.20	0.29	0.47
Standard deviation	0.11	0.12	0.23	0.05
Maximum value	0.35	0.42	0.69	0.58
Angular misalignment α [deg]				
Mean value	0.21°	0.12°	0.69°	0.18°
Standard deviation	0.02°	0.10°	0.17°	0.02°
Maximum value	0.25°	0.25°	0.94°	0.22°

Geometry of the weld bead

Figure 20 presents examples of macrographs for the different welds. It is clearly seen that the SAW joint has bigger weld when compared to that of the laser-based joints. The smooth weld bead was observed in the case of the Laser and Hybrid LF joints. Additionally, the Laser and Hybrid welded joints have narrow welds and also low heights of both weld toe and root. The Hybrid MF joint has a higher weld toe height than that of the Hybrid LF and Laser joint.

The bead dimensions at the welding side, i.e. weld toe side, for different welds are presented in Table 6. The height of the weld toe side for the SAW joint was 2.3 mm on average, being over four times higher than that of the Hybrid LF joint and over two times higher than that of the Hybrid MF joint. The lowest values of the weld height were observed for the Laser welded joint. Similarly, weld width was significantly larger for the SAW joint (mean 18 mm) than that of the Hybrid LF and Hybrid MF joint (about 6 mm). The width of the Laser joint was about a half of that of the Hybrid joints. The flank angle of the weld toe side for the SAW joint was on average 30°, but for the laser-based joints this varied from 4° to 19°. It is noticeable that the flank angle has large variations in the case of the Laser and Hybrid LF joints.

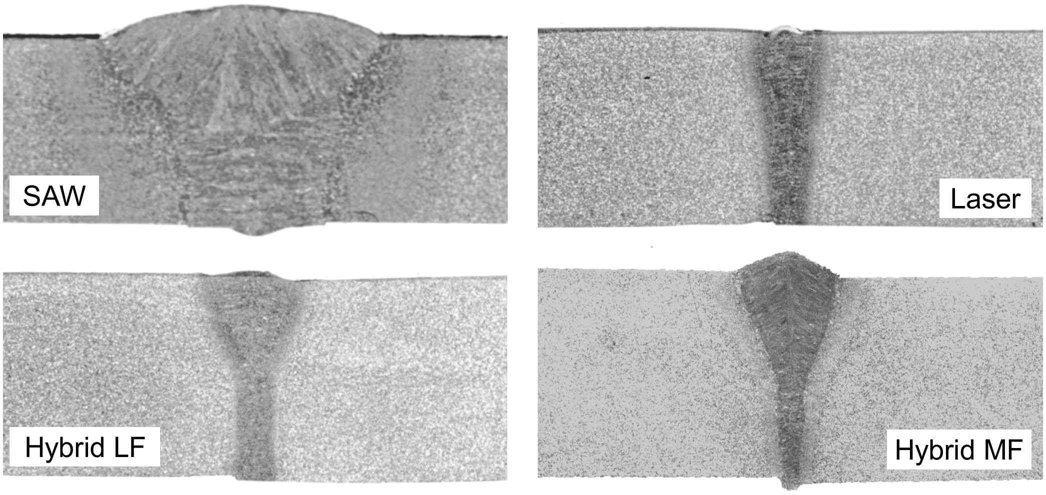

Figure 20: Macrographs of joints welded with different welding methods.

Table 6: Statistics for bead dimensions in the case of the weld toe side

Welded test specimen	SAW	Laser	Hybrid LF	Hybrid MF
Weld height h_t [mm]				
Mean value	2.26	0.06	0.49	0.94
Standard deviation	0.13	0.30	0.16	0.04
Maximum value	2.51	0.36	0.75	1.00
Weld width w_t [mm]				
Mean value	18.11	2.85	5.79	6.43
Standard deviation	0.80	0.46	0.45	0.16
Maximum value	19.15	3.55	6.33	6.67
Weld flank angle θ_t [deg]				
Mean value	29.3°	3.6°	17.0°	18.5°
Standard deviation	2.5°	18.7°	11.4°	1.9°
Maximum value	35.8°	25.1°	43.5°	21.9°

Table 7 presents bead dimensions for weld root sides. The height of the SAW joint had the mean value of 1.4 mm. That of the Laser and Hybrid joints was about two times smaller. The width was almost equal for the Laser and Hybrid joints and the mean values for them were below 2 mm. This value for the SAW joint was significantly larger, about 10 mm. The value of the flank angle for the laser-based joints differed clearly from that of SAW joints. The mean value for the SAW joint was 18°, while with laser-based joints it varied from 39° to 59°. In the case of both Hybrid joints, high values of the maximum were observed.

Table 7: Statistics for bead dimensions in the case of the weld root side

Welded test specimen	SAW	Laser	Hybrid LF	Hybrid MF
Weld height h_r [mm]				
Mean value	1.35	0.53	0.68	0.75
Standard deviation	0.38	0.12	0.56	0.24
Maximum value	1.80	0.71	1.58	1.19
Weld width w_r [mm]				
Mean value	10.01	1.68	1.57	1.89
Standard deviation	0.28	0.13	0.57	0.20
Maximum value	10.42	1.83	2.67	2.19
Weld flank angle θ_r [deg]				
Mean value	18.4°	39.0°	58.7°	48.0°
Standard deviation	5.1°	8.6°	20.6°	11.8°
Maximum value	30.3°	53.7°	91.1°	71.1°

Geometry of the weld notch

The statistical values of notch dimensions at the weld toe side are given in Table 8. The deepest notch was observed for the laser weld. For this joint, the maximum value of the notch depth was about 0.5 mm with a high value of the notch flank angle and a low value of the notch opening angle. Quite a high value of the standard deviation was observed. The notch depth was 0.15 mm or below for the SAW and for both Hybrid joints. On average, the notch root radius was significantly less for the SAW joint than that of the laser-based joints. However, the minimum values for all the joints were almost equal to about 0.03 mm. Therefore, the standard deviation reached a high value in the case of the laser-based joints.

Table 9 presents the statistical values of notch dimensions for the weld root sides. The Hybrid LF joint had the highest value for the notch depth at about 0.2 mm, being only slightly higher than that of the other joints. Similarly, only a small difference was observed in the mean values of the notch flank angle and opening angle between the SAW joint and the laser-based joints. The mean value was between 8° and 18° for the notch flank angle and between 93° and 132° for the opening angle. The notch radius was almost equal at all joints, where the minimum value varied from 0.014 mm to 0.027 mm.

Table 8: Statistics of notch dimensions at the weld toe side

Welded test specimen	SAW	Laser	Hybrid LF	Hybrid MF
Notch depth $D_{1,t}$ [mm]				
Mean value	0.006	0.073	0.018	0.010
Standard deviation	0.006	0.111	0.029	0.009
Maximum value	0.026	0.514	0.096	0.034
Notch depth $D_{2,t}$ [mm]				
Mean value	0.025	0.065	0.045	0.014
Standard deviation	0.018	0.093	0.037	0.013
Maximum value	0.060	0.415	0.145	0.050
Notch flank angle γ_t [deg]				
Mean value	5.8°	25.1°	5.7°	8.5°
Standard deviation	6.7°	15.5°	5.7°	7.0°
Maximum value	27.6°	70.2°	20.3°	24.9°
Notch opening angle β_t [deg]				
Mean value	132.5°	118.6°	139.0°	141.6°
Standard deviation	10.7°	21.9°	19.2°	13.0°
Minimum value	106.9°	60.7°	101.2°	103.4°
Notch radius ρ_t [mm]				
Mean value	0.047	0.395	0.519	0.412
Standard deviation	0.022	0.445	0.619	0.420
Minimum value	0.016	0.042	0.031	0.032

Table 9: Statistics of notch dimensions at weld root side

Welded test specimen	SAW	Laser	Hybrid LF	Hybrid MF
Notch depth $D_{1,r}$ [mm]				
Mean value	0.028	0.026	0.018	0.011
Standard deviation	0.037	0.015	0.021	0.010
Maximum value	0.119	0.063	0.090	0.041
Notch depth $D_{2,r}$ [mm]				
Mean value	0.032	0.047	0.097	0.025
Standard deviation	0.024	0.043	0.069	0.023
Maximum value	0.109	0.188	0.227	0.095
Notch flank angle γ_r [deg]				
Mean value	17.5°	14.0°	7.4°	10.6°
Standard deviation	22.0°	7.3°	10.1°	10.4°
Maximum value	81.7°	29.6°	40.1°	36.5°
Notch opening angle β_r [deg]				
Mean value	132.6°	97.5°	93.2°	109.4°
Standard deviation	22.6°	16.5°	17.0°	12.6°
Minimum value	69.2°	75.4°	55.5°	91.1°
Notch radius ρ_r [mm]				
Mean value	0.175	0.085	0.124	0.182
Standard deviation	0.193	0.062	0.121	0.166
Minimum value	0.023	0.027	0.025	0.014

2.5.2 Mechanical properties of welded joints

Table 10 shows the results of hardness measurements of weld materials for different joints. The peak hardness values of 231 HV5 in the weld metal and 215 HV5 in the HAZ material in the case of the Hybrid LF joints were lower than those of 255 HV5 (weld metal) and 241 HV5 (HAZ material) in the Laser joint. The value of the peak hardness of the Hybrid MF joints for the weld metal and the HAZ was 248 HV5. This indicates that the weld metal and the HAZ of the Laser and Hybrid joints were significantly overmatched compared to the parent material, which had the mean value of 131 HV5 and the standard deviation of 6.1 HV5. The hardness values for the SAW joint with the maximum value of 188 HV5 was higher than that of the parent material, but lower than that of the laser-based joints. Table 10 also presents hardness values close to the weld notch. These were determined from the measured profiles of hardness shown in Figure 21. In the case of the SAW, the hardness values in the notch were slightly lower than the mean value in the HAZ. For the Laser, Hybrid LF and MF joints, hardness at the weld notch was similar to the hardness of the weld zone, but much higher than that of the parent material.

Table 10: Summary of hardness HV5 measurements of different welded joints

Welded test specimen	SAW	Laser	Hybrid LF	Hybrid MF
Weld zone				
Maximum	188	255	231	248
Mean value	175	238	219	234
Standard deviation	9.2	9.3	6.6	11.2
Heat affected zone				
Maximum	173	241	215	248
Toe: Mean value	165	228	207	222
Toe: St.dev.	5.7	13.3	7.0	13.7
Root: Mean value	157	202	187	179
Root: St.dev.	3.1	6.4	16.2	12.2
Weld notch				
Toe: Mean value	153	233	210	229
Root: Mean value	147	225	199	201

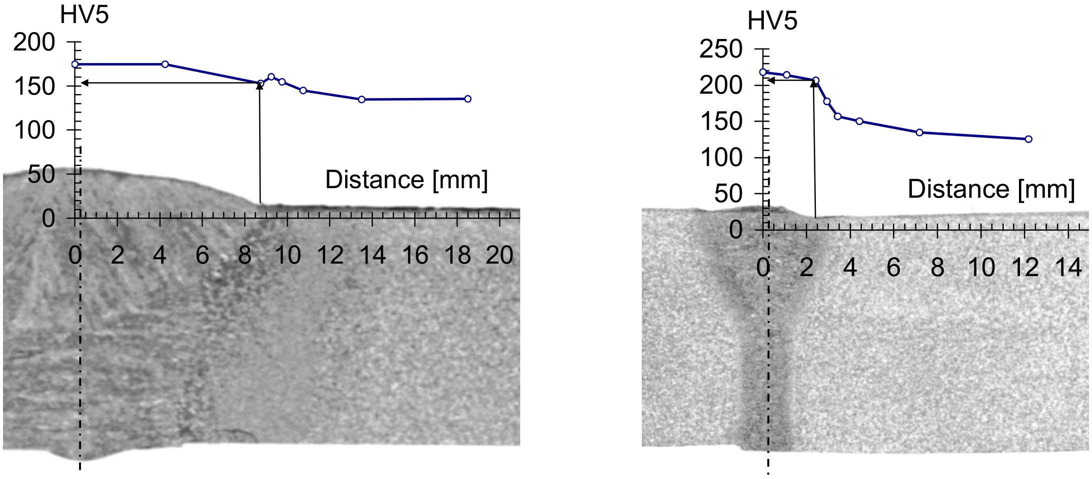

Figure 21: Hardness profiles at weld toe side for SAW and Hybrid LF joints, data gathered from Laitinen (2003).

Figure 22 presents the microstructure of the HAZ for the SAW, Laser and Hybrid LF joints reported by Laitinen *et al.* (2003). It is important to note the difference in the average grain size between different joints. The HAZ of the SAW joint had larger grain size than that of the laser-based joints. Further, it was apparent that smaller inhomogeneous islands of martensite and upper bainite were formed for the HAZ of the Hybrid LF joint than for the HAZ of the Laser joint. Average grain size for all of these complex microstructures was determined by calculating the number of grains that crossed the two perpendicular lines drawn above on the microphotos. Based on this procedure, the average grain size was derived by dividing the total length of the lines by the number of grains. The average grain size for the HAZ of the SAW was 39 μm, which was significantly larger than that of the Laser and Hybrid LF joints at the values of 4.6 μm and 5.1 μm, respectively.

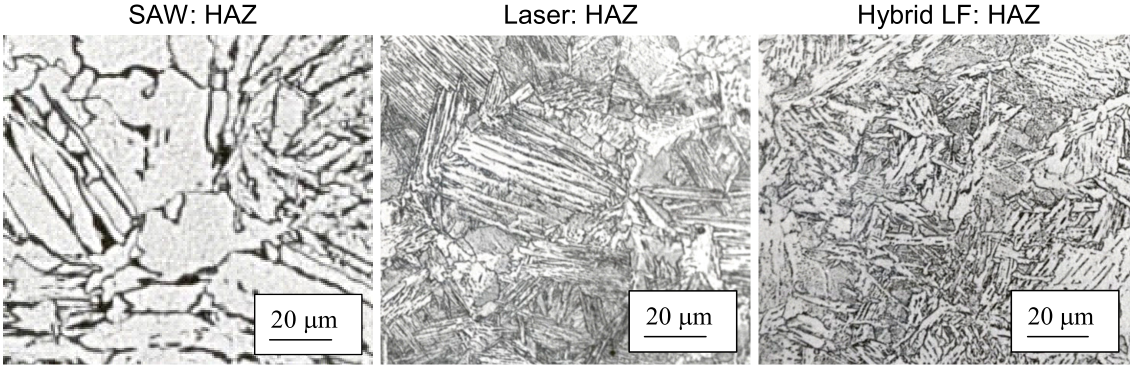

Figure 22: Microstructure in HAZ for SAW, Laser and Hybrid LF joints, figures taken from Laitinen *et al.* (2003).

The interest of the fatigue analysis was focused on the weld notch and on the surrounding material. The stress-strain curves were determined for the weld metal in the case of narrow Laser and Hybrid welds. In the case of a wider SAW joint, the HAZ material was also studied. The monotonic and cyclic stress-strain curves for different joints are shown in Figure 23. Those of the parent material are given as a reference curve. The results show that all the joints had higher yield strength than that of the parent material. Based on the cyclic stress-strain curve, it can be seen that the HAZ material of the SAW joint is slightly stronger than that of the parent material. In the case of the Laser, Hybrid LF and, especially, of the Hybrid MF joints, the cyclic strength exceeded that of the parent material more noticeably. The values of the cyclic strain hardening n' and the strength coefficient K' for the Ramberg-Osgood equation for the different joints are presented in Table 11.

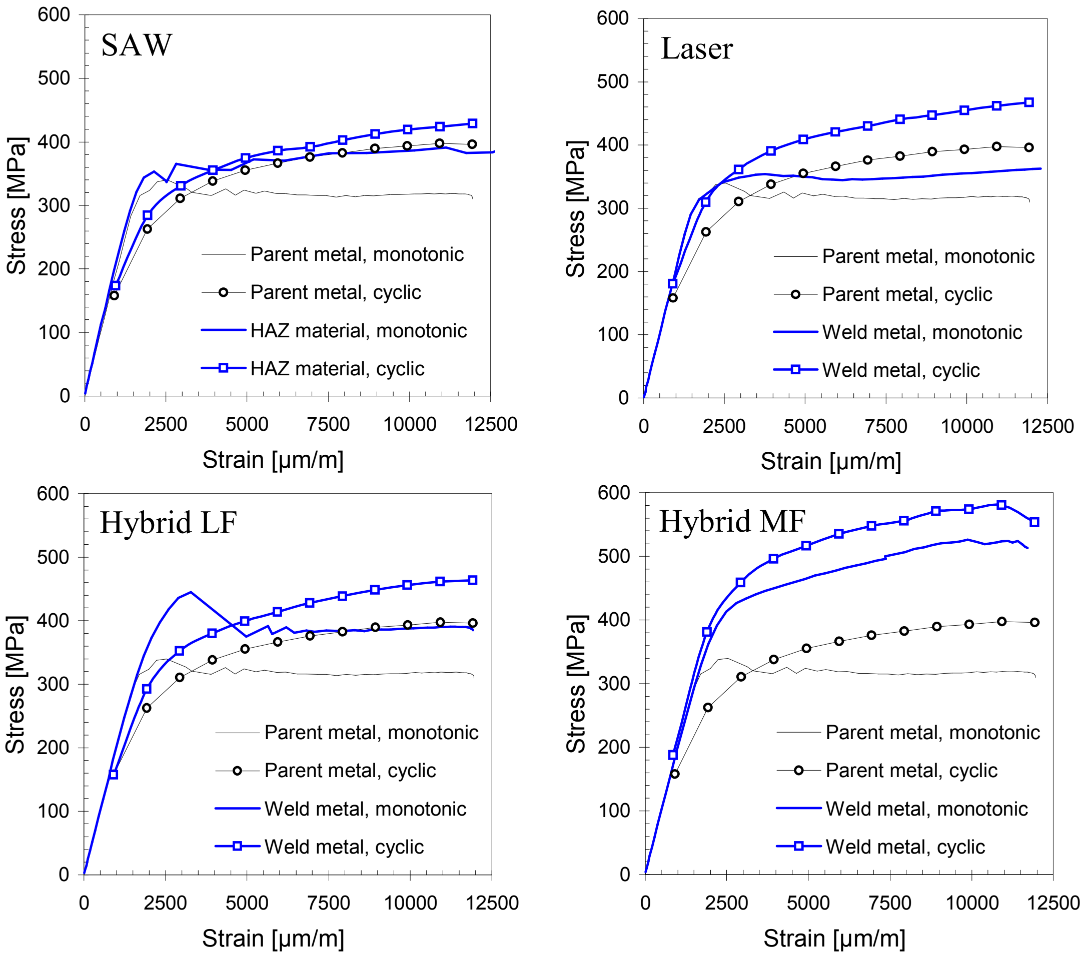

Figure 23: Monotonic and cyclic stress-strain curves of different welded joints, adapted from Gribenberg (2003).

Table 11: The parameters of cyclic stress-strain curves, n' and K', of different joints (Gribenberg 2003).

Welded test Specimen	Material Zone	Ramberg-Osgood parameters n'	K' [MPa]
Base plate	Parent metal	0.143	794
SAW	HAZ	0.136	813
Laser	Weld metal	0.121	823
Hybrid LF	Weld metal	0.144	922
Hybrid MF	Weld metal	0.082	852

2.5.3 Fatigue resistance of weld materials

Fatigue resistance was defined on the basis of the measured initiation life of the macro crack in the miniature specimens; the results for the different material zones and welding methods are presented in Figure 24. The fatigue tests of the parent and weld materials for the SAW and Hybrid LF were carried out using smooth miniature specimens. The fatigue strength of the parent material $\sigma_{a,i}$ was 218 MPa at the crack initiation life of two million load cycles. Comparing that to the values of different weld materials, a 9% higher value for the HAZ of the SAW and a 23-29 % higher value for the HAZ and for the weld metal (WM) of the Hybrid LF were observed, see Table 12. The fatigue tests of the weld materials of the Laser were carried out using micro notched specimens, due to the higher cyclic strength of the weld metal and HAZ compared to the parent metal. Although the specimens were notched, the fatigue strength of these was at least 16% higher than that of the parent material with the smooth specimen. The increase of fatigue strength was observed to correlate with the value of material hardness, see Figure 25.

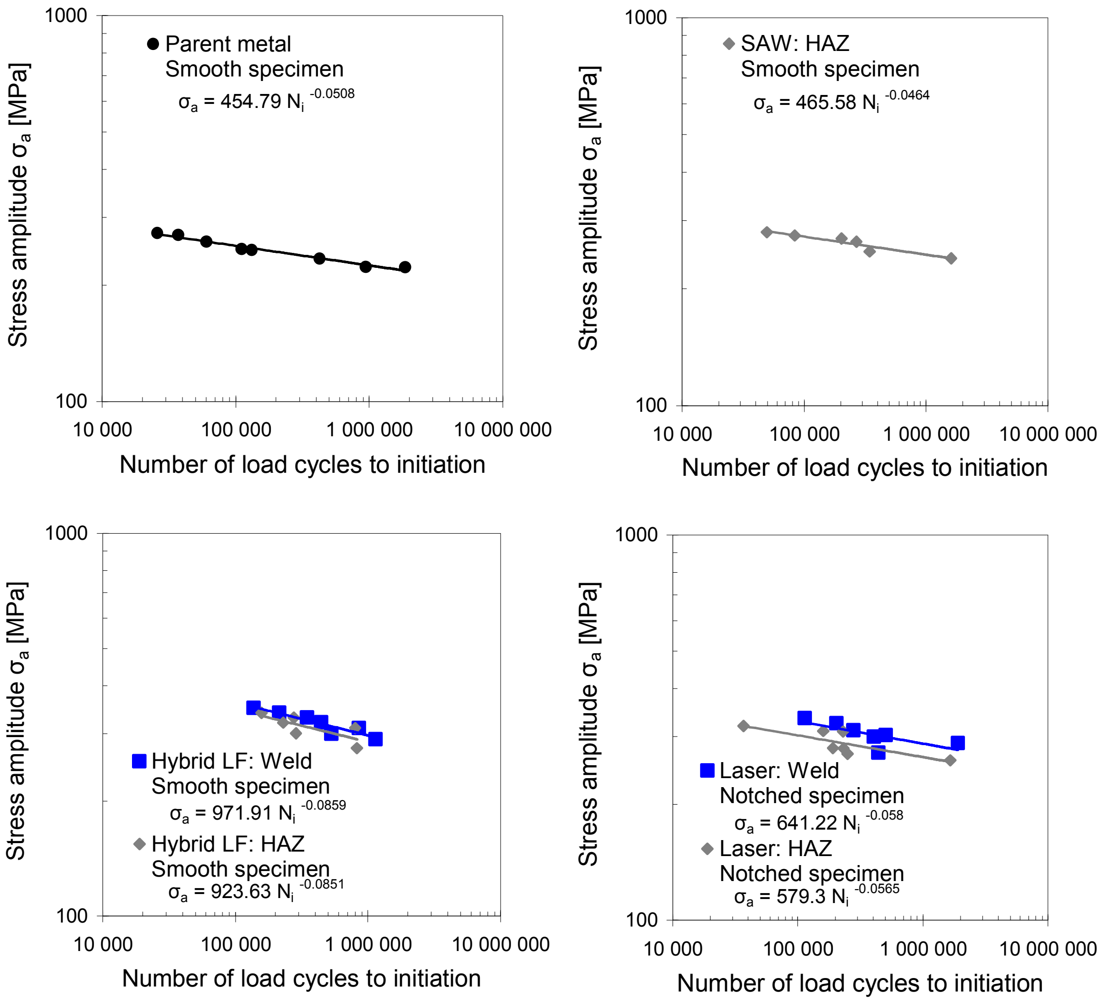

Figure 24: Fatigue resistance based on initiation life with miniature test specimens.

Table 12: Comparison of stress amplitudes at the initiation life of two million load cycles for different weld materials

Welded Sample	Material Zone	Hardness[1] HV5	Test Specimen	Stress amplitude $\sigma_{a,i}$ $\sigma_{a,i}$ [MPa]	Difference [%]
Base plate	Parent metal	131	Smooth	218	Ref. – value
SAW	HAZ	161	Smooth	237	9
Hybrid LF	HAZ	268 [2]	Smooth	269	24
	Weld metal	280 [2]	Smooth	279	28
Laser	HAZ	215	Notched	255	17
	Weld metal	238	Notched	276	27

[1] Mean value of Vickers hardness

[2] The failure initiated about 1 mm from the middle of specimens. Therefore, the results can be considered of lower bound value.

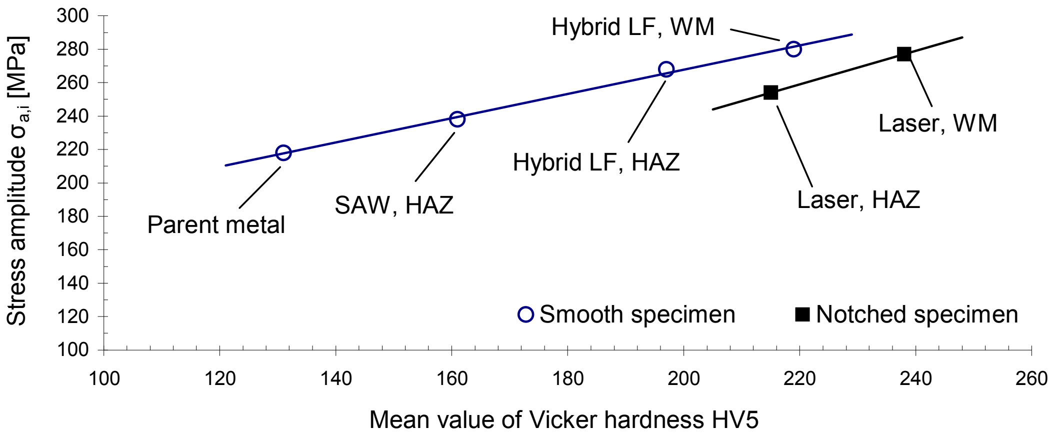

Figure 25: Fatigue strength at $N_i = 2 \cdot 10^6$ versus Vickers hardness.

2.5.4 Fatigue resistance of welded-plate specimens

The fatigue resistances to the macro crack initiation and the final failure were measured in the tests with the welded-plate specimens. Figure 26 shows these resistance curves in the logarithmic scale for the different welding methods. The values of the parameters in the *S*-*N* curves are given in Table 13 for the macro crack initiation and in Table 14 for the final failure. The values are derived from the test results by curve fitting using the least square method. Especially, the obtained values for Hybrid LF weld had statistical uncertainties, because of the scatter caused by limited and varied sample size.

The fatigue strength of the SAW joint was 180 MPa at the fatigue life of two million load cycles, see Table 14. This value has been defined as the mean value of the fatigue strength and the abbreviation $FAT_{50\%}$ has been used. The $FAT_{95\%}$ describes the fatigue strength at the survival probability level of 95% (Hobbacher 2007). The fatigue strength of the Laser welded joint was slightly lower than that of the SAW joint, as Table 14 indicates. For the Hybrid welded joints, the fatigue strength was remarkably higher. The test results showed clearly that high pre-strain due to the angular misalignment in the case of the Hybrid LF with the specimen of Type A reduced the fatigue strength considerably, see Tables 13 and 14. In the tests with the specimen of Type B, this reduction of the strength was avoided.

The initiation life of the macro crack for the SAW and Hybrid MF specimens was about 30-80 % of the total fatigue life. The portion of the initiation life N_i/N_f for the Laser and Hybrid LF specimens was slightly lower, being between 10% - 55%. This portion increased as the function of the fatigue life, but in the case of the Hybrid LF specimen Type A, with the high pre-strain, it had an almost constant value of about 30%.

The slope of the *S-N* curves as the function of the fatigue strength measured by $\Delta\sigma_{i,50\%}$ or by $\text{FAT}_{50\%}$ is presented in Figure 27. The result indicates that the slope initiated from the value of 3 and increased exponentially as the function of the fatigue strength. Especially in the case of Hybrid LF specimen B, the slope values were remarkable high, 44 for the initiation life and 28 for the total life. This may be caused by statistical uncertainty due to limited sample size.

Table 13: Summary of test results of macro crack initiation and its relative portion of fatigue life N_i/N_f in the case of the welded-plate specimen

Welded sample	Test specimen	Failure initiation	Number of sample	Fatigue resistance for initiation		
				Slope m_i	$\Delta\sigma_{i,50\%}$[1]	N_i / N_f
Joint	[End type]	Location	[No.]	[-]	[MPa]	[%]
SAW	A	Toe, root	8	7.9	175	36 – 82
Laser	A, B	Toe, root	6	6.3	155	24 – 48
Hybrid LF	A	Toe	3	3.3	76	26 – 37
	B	Toe (root)	5	44.2	236	10 – 55
Hybrid MF	A	Root	10	12.7	204	39 -71

[1] Stress range at macro crack initiation life of two million load cycles

Table 14: Summary of test results for final failure of the welded-plate specimen

Welded sample	Test specimen	Failure initiation	Number of sample	Fatigue resistance for failure		
				Slope m_f	$\text{FAT}_{50\%}$	$\text{FAT}_{95\%}$[1]
Joint	[End type]	Location	[No.]	[-]	[MPa]	[MPa]
SAW	A	Toe, root	11	5.8	180	172
Laser	A, B	Toe, root	11	5.8	174	154
Hybrid LF	A	Toe	10	3.7	129	107
	B	Toe (root)	5	27.8	238	222
Hybrid MF	A	Root	10	9.6	208	200

[1] FAT at 95% failure probability according to Hobbacher (2007)

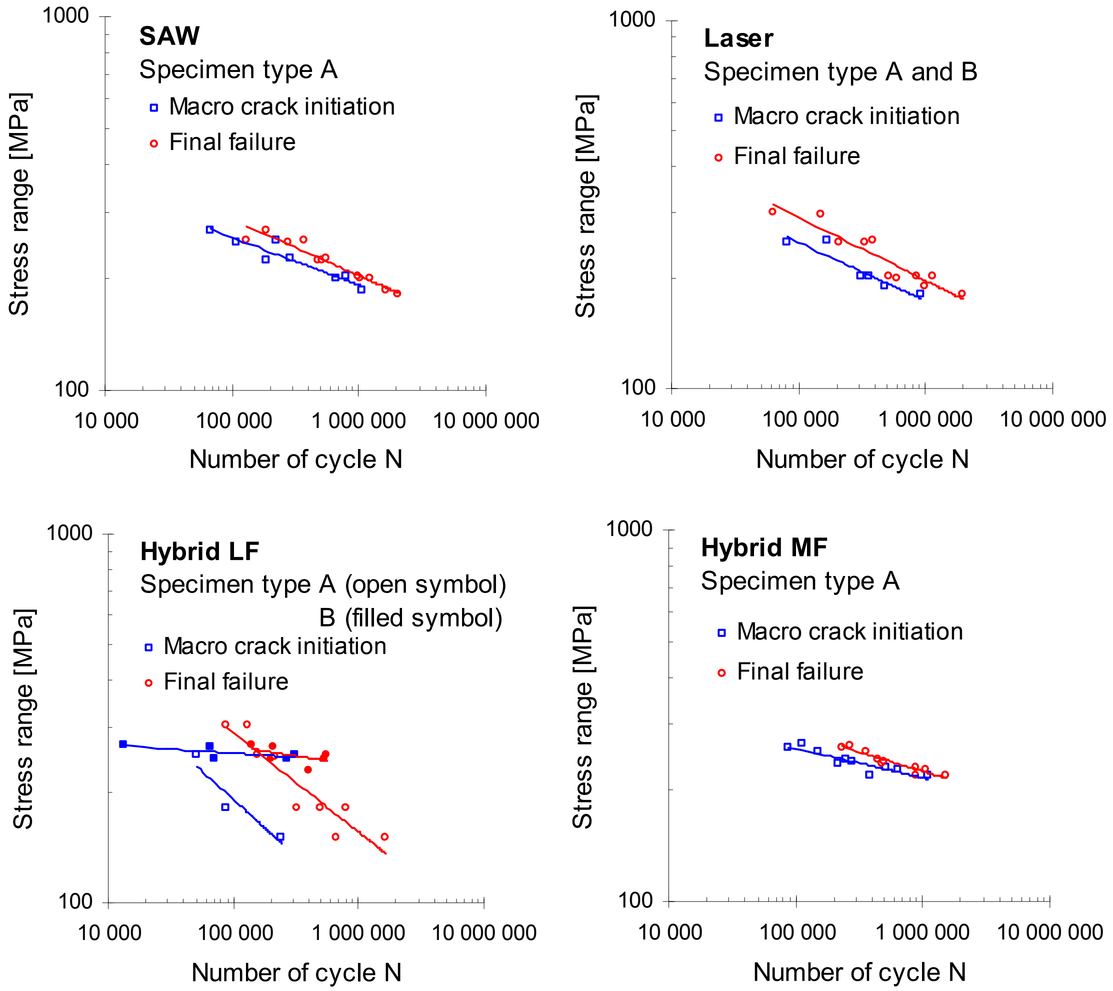

Figure 26: Fatigue resistance based on macro crack initiation and final failure for different welded-plate specimens.

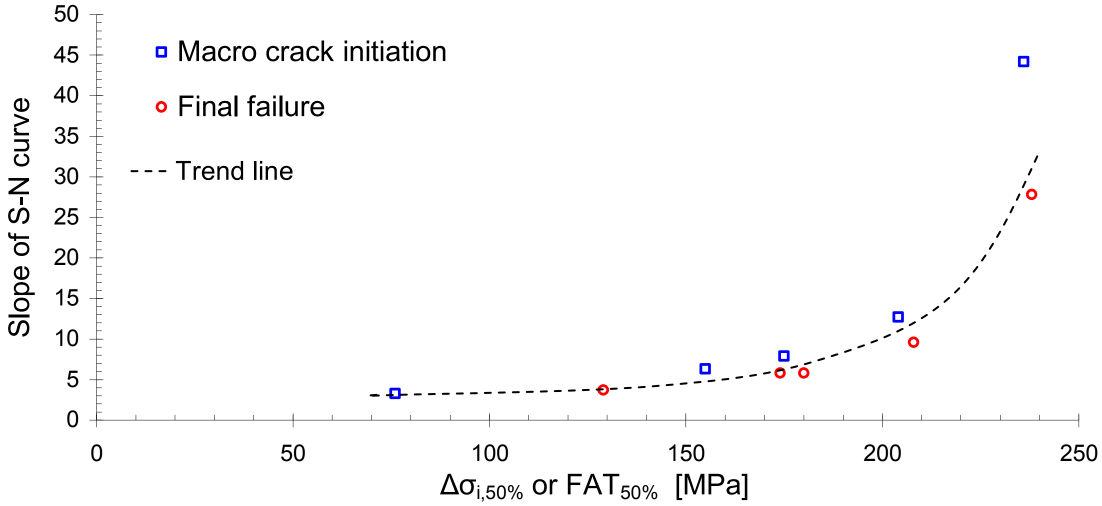

Figure 27: Slope of the *S-N* curve versus the fatigue strength by $\Delta\sigma_{i,50\%}$ or FAT$_{50\%}$. Data was obtained from Tables 13 and 14.

Visual examination of the fatigue cracks revealed the macro crack initiated from the weld notch. The macroscopic study of the fracture surfaces, carried out by Gribenberg (2003), supports this observation. Figure 28 shows the fracture surfaces of the Hybrid LF joints. Comparison of the figures leads to the conclusion that high loading causes more initiation sites of the macro crack (Gribenberg 2003). Even though the specimen contains many initiation sites, only a few of them become predominant during the fatigue damage process. Similar conclusions can be drawn, based on the observations made in the case of the SAW and Laser welded specimens.

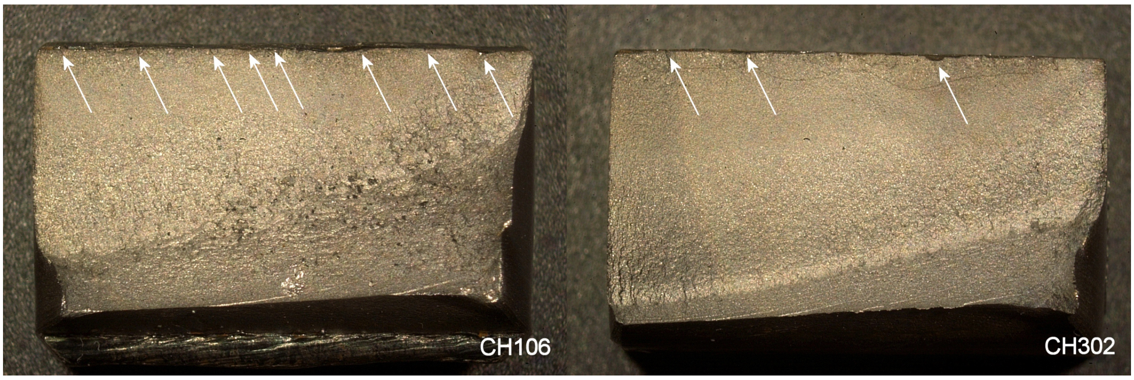

Figure 28: The fracture surfaces of Hybrid LF specimens tested by high (left) and low (right) loading. Arrows show crack initiation sites (Gribenberg 2003).

The Laser and Hybrid welded joints had strong hardness variation at the weld notch, see Figure 21. The Hybrid LF joint was further studied. The macro sample of the surface perpendicular to the crack was repaired, see Figure 29. Both undamaged and damaged specimens for low and high loading were studied. The figure shows that the macro crack was initiated at the borderline of the weld metal and HAZ. The crack growth occurred in the direction of the weld notch in the early phase and followed perpendicular to the surface of the base plate. Thus, the crack propagated first in the HAZ and later in the parent material. No difference in the fracture path between the low and high loading was observed.

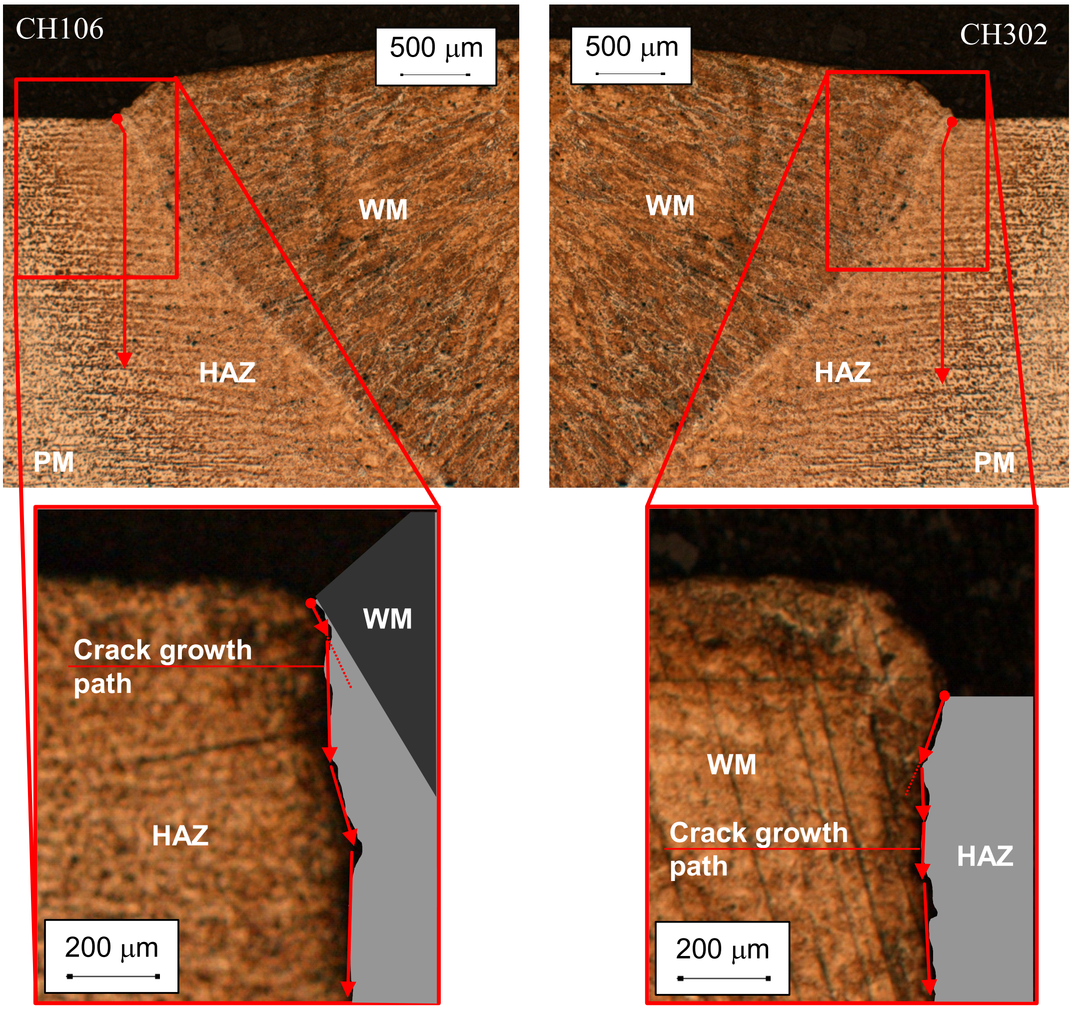

Figure 29: The path of crack growth in Hybrid LF specimens tested by high (left) and low (right) loading. Arrows present the path of crack growth.

2.5.5 Correlation study

Reasons for the variations of the fatigue strength between the different welding methods were studied statistically. The fatigue strength FAT of each joint type was plotted as the function of the joint’s geometrical dimensions and also as the function of the hardness in the HAZ. The mean value was presented by a point and the scatter ranges described by the minimum and maximum values. The ranges for FAT were obtained using the best-fit slope value of each joint. Figure 30 shows the fatigue strength as the function of the axial and angular misalignments. The figure on the left shows poor correlation in the case of the axial misalignment, indicating that it cannot explain the difference in the fatigue strength between different welding methods. The results presented in the figure on the right indicate that the Hybrid LF specimen Type A gave lower fatigue strength as a result of higher angular misalignment. Due to this, Hybrid LF specimen Type A was not included in the following analysis.

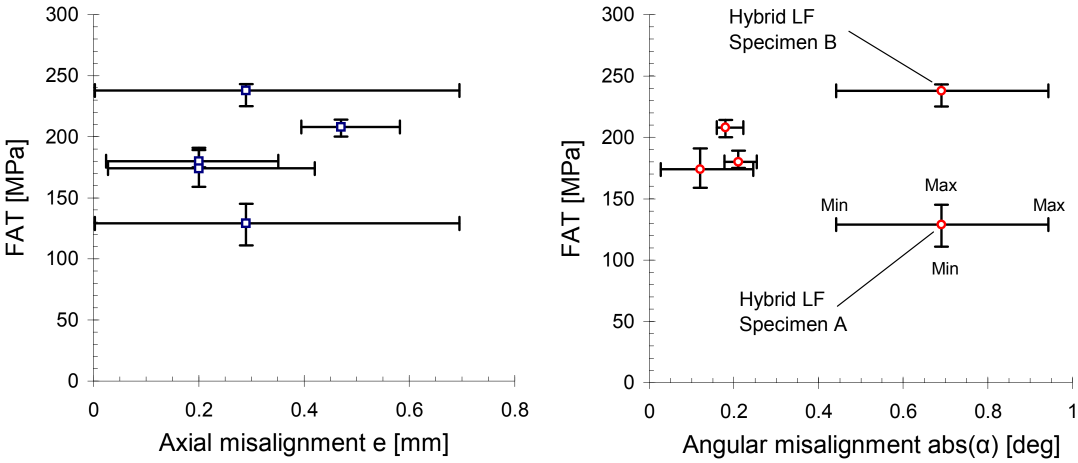

Figure 30: FAT versus axial (left) and angular (right) misalignments with scatter values.

Relations between the fatigue strength and the hardness, as well as between the fatigue strength and the geometrical dimensions of the joints, are shown in Figures 31, 32 and 33. The weld toe and root of the joint were separately studied, taking into account the initiation of the macro crack. Quite clear correlation was identified between the fatigue strength and the hardness and also between the fatigue strength and the radius of the weld notch, see dashed lines in Figures 31 and 33. The notch radius was presented in logarithmic scale to illustrate the small values. The other geometrical parameters, for instance, such as the flank angle of weld, had no clear correlation with the fatigue strength. Similar conclusions can be drawn on the basis of the fatigue strength measured by $\Delta\sigma_{i,50\%}$ instead of $\mathrm{FAT}_{50\%}$.

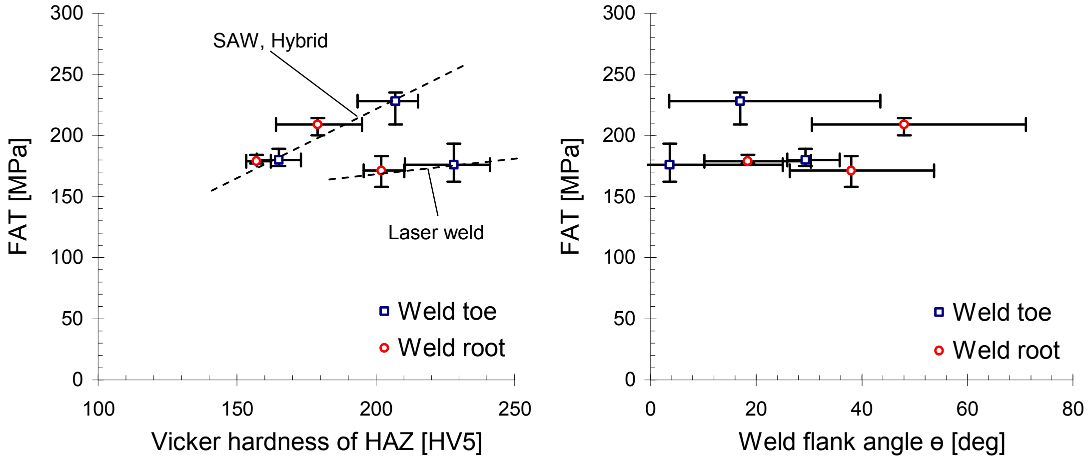

Figure 31: FAT versus Vickers hardness in HAZ and weld flank angle.

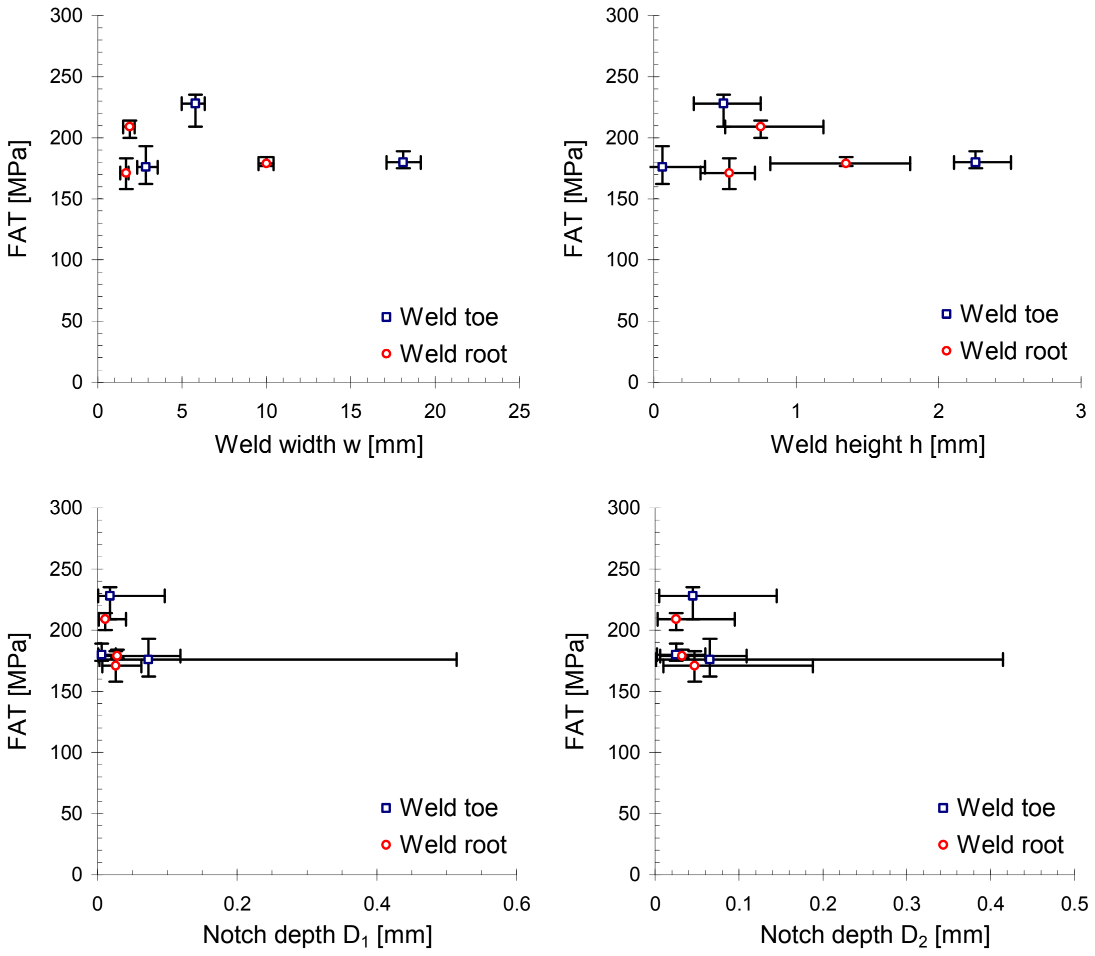

Figure 32: FAT versus weld width, weld height and notch depths.

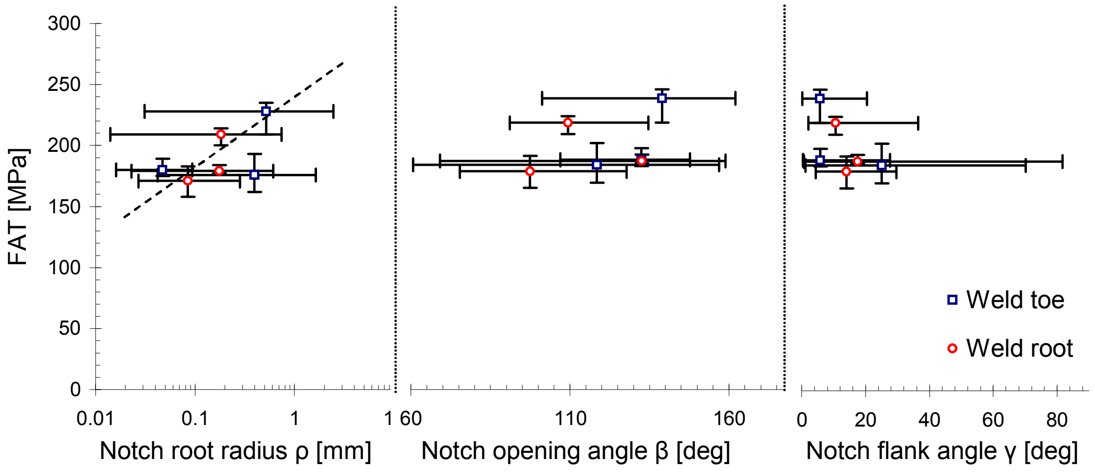

Figure 33: FAT versus notch radius, opening angle and flank angle. The notch radius is presented in logarithmic scale to illustrate small values.

2.5.6 Discussion of test results

Comprehensive fatigue testing with the miniature and welded-plate specimens has been reported. Experimental work also included the measurement of the geometrical and mechanical properties of the tested joints.

The present results show that the angular misalignment of the Hybrid LF joint was significantly higher than that of the other joints. This unexpected result cannot be explained only by the differences in the welding energy, which was the highest for the SAW joint. Hence, the misalignment might also be caused by the welding arrangements and by the clamping system. The angular misalignment of the Hybrid LF joint was on average 0.7°. However, this value is relatively small compared to typical values for arc-welded joints given in the literature (Kendrick 2005). Although the angular misalignment of the Hybrid LF joint was not remarkably high, the clamping mechanism of the test machine without hinges induced static secondary bending and caused significant reduction of the fatigue strength, see Table 14. The values given in the table show that the difference in the fatigue strength between the specimen Types A and B is 52%, which is much higher than 9% calculated using the existing approach by Hobbacher (2007, p. 81). Similar unexpected results in the form of the mean stress have been reported for the arc-welded joints in full-scale structures (Lotsberg *et al.* 2001).

The geometrical dimensions of welded joints may have a considerable effect on local stresses (Anthes *et al.* 1993). Thus, the measured values are compared to those presented in the literature. The measured values of the weld flank angle for the weld toe side are in line with the earlier reported values, varying from 5° to 25° for laser welds (Ring and Dahl 1994) and from 5° to 60° for arc welds (Kendrick 2005). In the case of the weld root side, this dimension for the laser-based joints had the maximum values ranging from 50° to 90°, which significantly differ from the values reported in the literature (Ring and Dahl 1994; Kendrick 2005). However, these high measured values of the flank angle, i.e. the drop-shaped weld bead, showed no significant influence on the fatigue strength, in contrast to the results of the notch stress approach presented in Ring and Dahl (1994). This approach was originally developed for arc welds (Anthes *et al.* 1993) and its application to laser-based joints is questionable due to difference in size of weld beads.

In the present study, the measured maximum values of the notch depths of about 0.2 mm for the Hybrid LF, Hybrid MF and SAW joints are similar to those reported earlier for arc welds (Berge *et al.* 1980), but the variation for arc welds can be significant (Bokalrud and Karlsen 1982; Bell *et al.* 1989; Janosch and Debiez 1998), where up to 1 mm depth has been observed. The measured notch depth of the Laser weld toe was 0.5 mm. This value is closer to the typical value for arc welds.

The present correlation study between the fatigue strength and different geometrical and mechanical properties of the joint provided interesting findings, which are in conflict with the earlier results for arc welds. These earlier results (Petershagen 1990; Gosch and Petershagen 1997; Anthes *et al.* 1994) indicate strong correlation between the fatigue strength and the flank angle, and also with the notch depth. The present results indicate strong correlation between the fatigue strength and the hardness of the material in the welded joint. Additionally, the notch root radius has an effect on the fatigue strength, while the other geometrical dimensions do not.

In the case of the Hybrid LF with the specimen Type A, where the high pre-strain existed and the initiation period was short, the slope of the *S-N* curve had a value of 3 similar to that presented in the literature (Maddox 1991). However, the test results with specimen Type B gave values for the slope of the *S-N* curve, which were over 5. This shows the importance of the pre-strain for the behaviour of macro initiation. This agrees with previous observations (Murakami and Miller 2005), where localized damage, e.g. micro cracking, was observed within a single cycle with high load value.

The fatigue testing with the miniature specimens was aimed at studying macro crack initiation of different weld materials. The transverse extensometer was successfully applied to observe also the short crack nucleation and propagation process in the case of the SAW joint (Remes 2003) in a way similar to that in which the tests with homogeneous parent materials were observed by Socha (2003). However, in the case of the laser-based joints, the narrow material zones caused irregular failures in the smooth test specimens, which made the results unreliable.

On the basis of the experiments, it is difficult to draw sound conclusions from the most important parameters affecting the fatigue strength of laser-welded joints. Therefore, there is a need for theoretical analysis, which would take into account the geometrical and material effects of the joint.

3 NOTCH STRESS AND STRAIN IN A HYBRID WELDED BUTT JOINT

3.1 General

The object of the analysis was to give insight into local stresses and strains in the weld notch of laser joints with narrow HAZ loaded by tension and bending. The analysis concentrated especially on the influence of material inhomogeneity due to strong variation in mechanical properties between different material zones.

In order to clarify the stresses and strains for the different load levels, the elasto-plastic behaviour of the material zones were taken into account in the analysis. A significant plastic deformation might have occurred during the initial load cycle due to the misalignments of the welded joints. With respect to this, the behaviour of the material zones can be described using monotonic stress-strain curves. During the following cycles, the effect of softening or hardening occurred, causing changes in the stress-strain curves, which can be described by the cyclic stress-strain curve. Therefore, the initial and cyclic loadings were covered separately.

The interest of the analysis was focused on the Hybrid LF joint, the geometry of which is presented in Figure 34. The geometrical dimensions of the joint were based on the statistical analysis of the measured values given in Section 2.5.1. The dimensions presented in the figure correspond to the 95% probability level, i.e. the alternatives 1-*P* = 95% and *P* = 95%. The alternative causing higher stress concentration was applied.

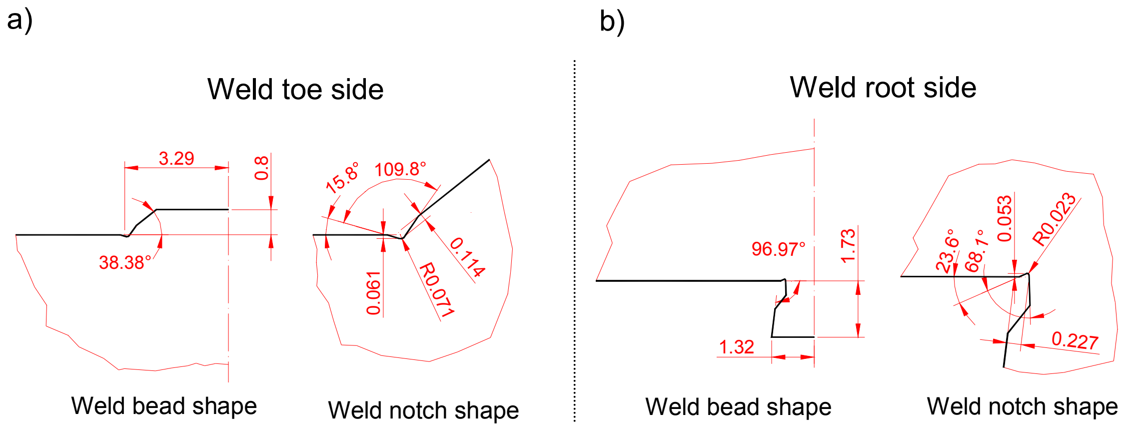

Figure 34: Geometry of the weld bead and notch for the weld toe (left) and the root (right) sides.

3.2 FE analysis

The analysis was carried out with the FEM using ABAQUS Standard 6.1 software. 2D modelling with the assumption of plane stress was applied with material and geometrical nonlinearities. This stress state was appropriate for the modelling of the whole joint. The isotropic hardening model was used.

3.2.1 Modelling of the joint

A sketch of the joint for the FE analysis is shown in Figure 35. Only half of the joint was modelled with the help of boundary conditions at the symmetry plane (Line A). The vertical displacement in the mid node of the loaded end (Point B) was fixed. The tension load was modelled as a nodal force at Point B with the assumption of constant displacement in the x-direction. The misalignments of the joint were separately taken into account by bending loading, which was modelled with the horizontal pressure distributed linearly. In the case of the combined tension and bending loadings, the distributed pressure only was applied. The level of the forces for both load cases was determined by the same nominal stress in the top surface of the joint.

Figure 36 represents the element mesh of the joint, where the eight node elements were used. The maximum element size was 1 mm x 1 mm and at the area of the weld notch that was 0.01 mm x 0.01 mm. The figure also gives an idea of the modelling of the material zones more thoroughly discussed in the next chapter.

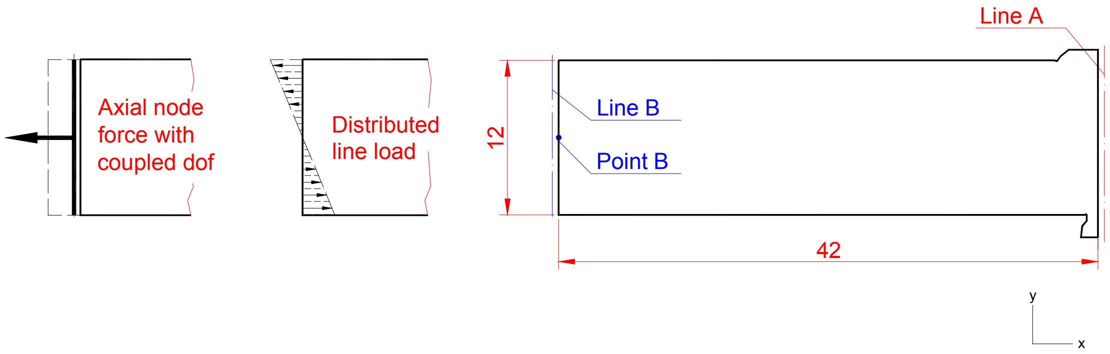

Figure 35. Sketch of the FE model.

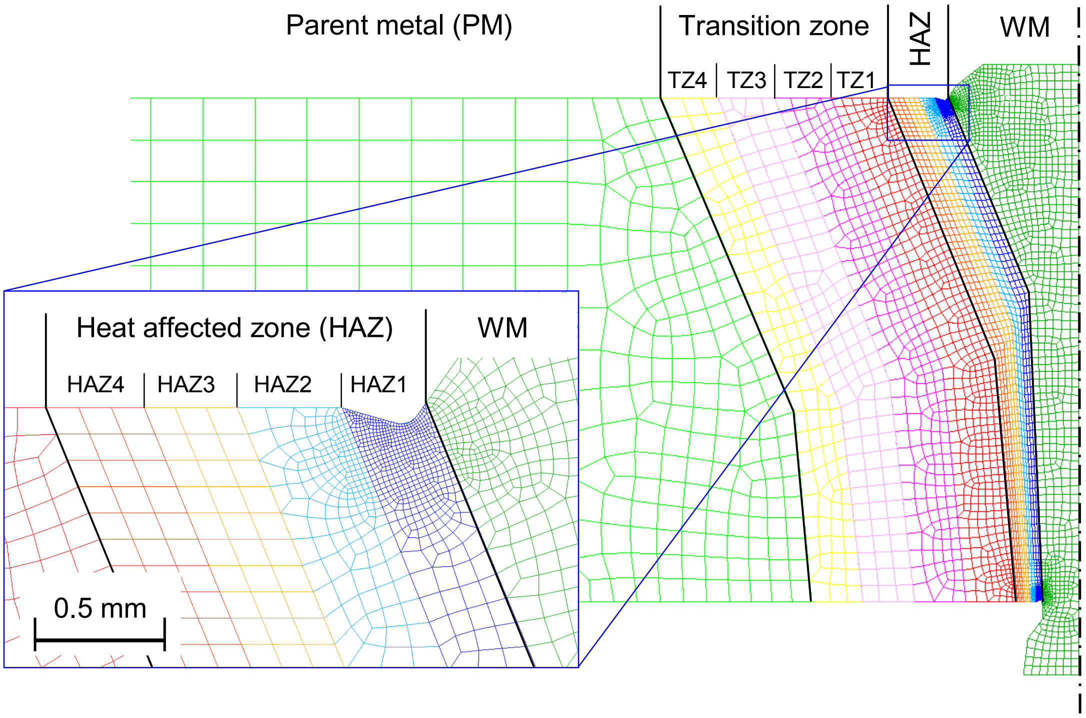

Figure 36. Material zones in the FE model.

3.2.2 Modelling of material zones

The material of the joint was divided into PM, HAZ and WM zones, see Figure 36. An additional one, called the transition zone (TZ), has been defined as well. Exploiting the macrographs of the joint, see Figure 20, the borderlines between the different zones were defined. Based on the hardness distribution, the both HAZ and TZ zones were divided into four sub zones. There the values of the parameters in stress-strain curve (SSC) for elasto-plastic analysis were interpolated from the measured SSC for the parent and the weld metal in the miniature tests. The interpolation was based on the measured hardness distribution over the HAZ and TZ zones. The values of the material parameters for the monotonic and cyclic SSC based on the hardness HV5 are presented in Table 15. The modulus of elasticity E and Poisson's ratio ν are 210 GPa and 0.3, respectively. The FE model including these different material zones was called the inhomogeneous model. For the purposes of comparison, a model of the joint with homogeneous material was also studied. The values of the material parameters there were based on the HAZ1, enabling a comparative study of the effect of the material inhomogeneity on the notch stresses and strains.

Table 15: Material parameters of stress-strain curves (SSC)

Material zone		Vickers Hardness[1]	Monotonic SSC		Cyclic SSC	
			σ_y	E_T	K'	n'
		HV5	[MPa]	[MPa]	[MPa]	[-]
Weld metal	WM	218.0	354.2	1 628	922	0.144
Heat effect zone	HAZ1	207.0	345.7	1 631	906	0.144
	HAZ2	189.0	331.8	1 635	879	0.144
	HAZ3	170.0	317.1	1 640	851	0.143
	HAZ4	152.5	303.6	1 644	826	0.143
Transition zone	TZ1	152.5	303.6	1 644	826	0.143
	TZ2	145.0	297.8	1 646	815	0.143
	TZ3	137.0	291.6	1 648	803	0.143
	TZ4	131.0	287.0	1 650	794	0.143
Parent metal	PM	131.0	287.0	1 650	794	0.143

[1] Calculated mean value from the distribution of measured Vickers hardness HV5.

3.3 Results

3.3.1 Initial load cycle

The deformed shapes of the joint under tension and bending loading are presented in Figure 37. The displacements were logical for these kinds of loadings. The angular deformations versus the nominal stress for the inhomogeneous model are given in Figure 38. In this figure, the permanent deformation was calculated by subtracting the elastic value from the total value. These results correspond to the case where both the tension and the bending loading were applied simultaneously. The total angular deformation was strongly influenced by the ratio of the bending compared to the tension measured with stress at the surface. However, the permanent angular deformation was independent of the bending proportion above 50%. Similar results were observed also for the homogenous model, but the value of the nominal stress causing permanent angular deflection was increased about 20% because the stress-strain curve of HAZ was also used for the base plate.

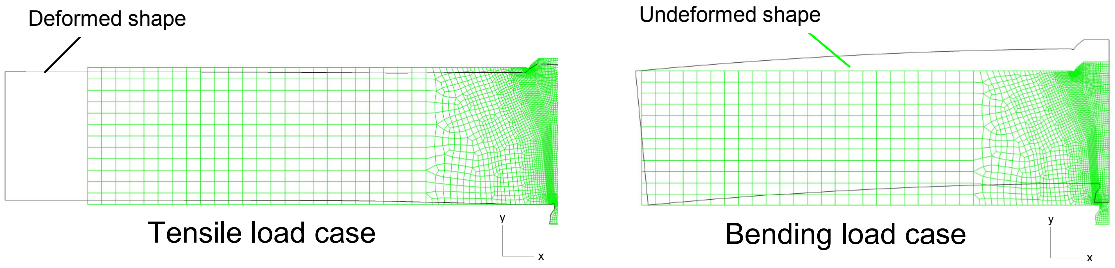

Figure 37. Deformation of the joint under tension and bending loadings with nominal stress of 287 MPa. Magnification factors are 100 and 10, respectively.

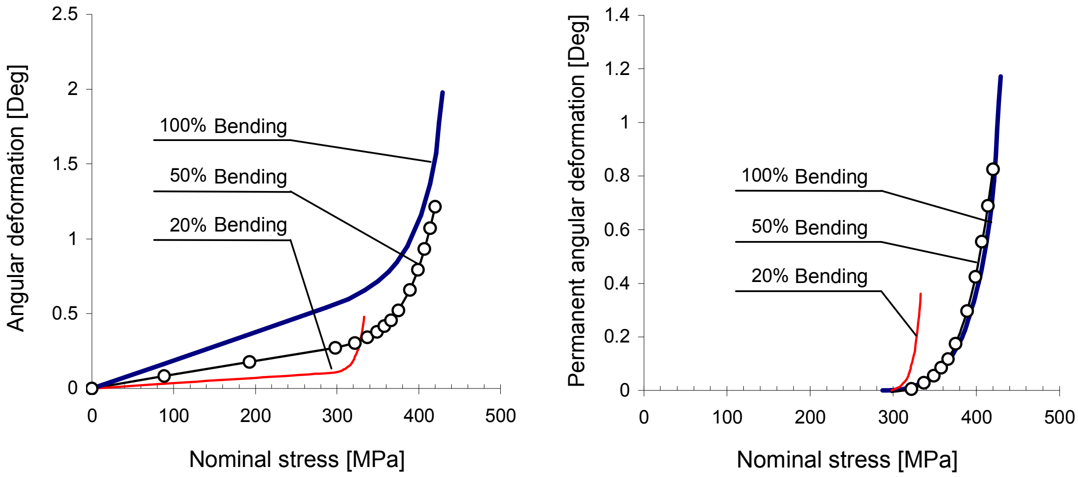

Figure 38. Angular deformations versus applied nominal stress for different bending proportions in the case of the inhomogeneous model.

Figures 39 and 40 give the stress σ_{xx} and the plastic strain $\varepsilon_{xx,pl}$ for the inhomogeneous model. These results correspond to the applied nominal stress level of 287 MPa, which equals the yield stress of the parent material. Figure 40 indicates that the plastic area was larger for the weld notch at the toe side compared to that of the root side, even higher stress and strain values were observed in the weld root side. Thus, the study was focused on the toe area, where the diameter of the plastic zone was about 0.03 mm and 0.1 mm for the nominal stress level of 100 MPa and 200 MPa, respectively. The difference of the local responses in the weld notch between the tension and the bending was minor, see Figure 41. The figure shows the normal stresses and strains versus distance from the weld notch along Path 1 shown in Figure 39. The values in Figure 41 were presented in the logarithmic scales for the different nominal stress levels. The slopes of stress curves outside the plastic area seemed to be independent of the nominal stress. The strain curves in Figure 41 do not show a similar behaviour, but, inside the plastic area, the values increase towards the weld notch. The shape of the strain curves is linear in the logarithmic scale up to the nominal stress of 100 MPa; above that, they are non-linear inside the plastic area.

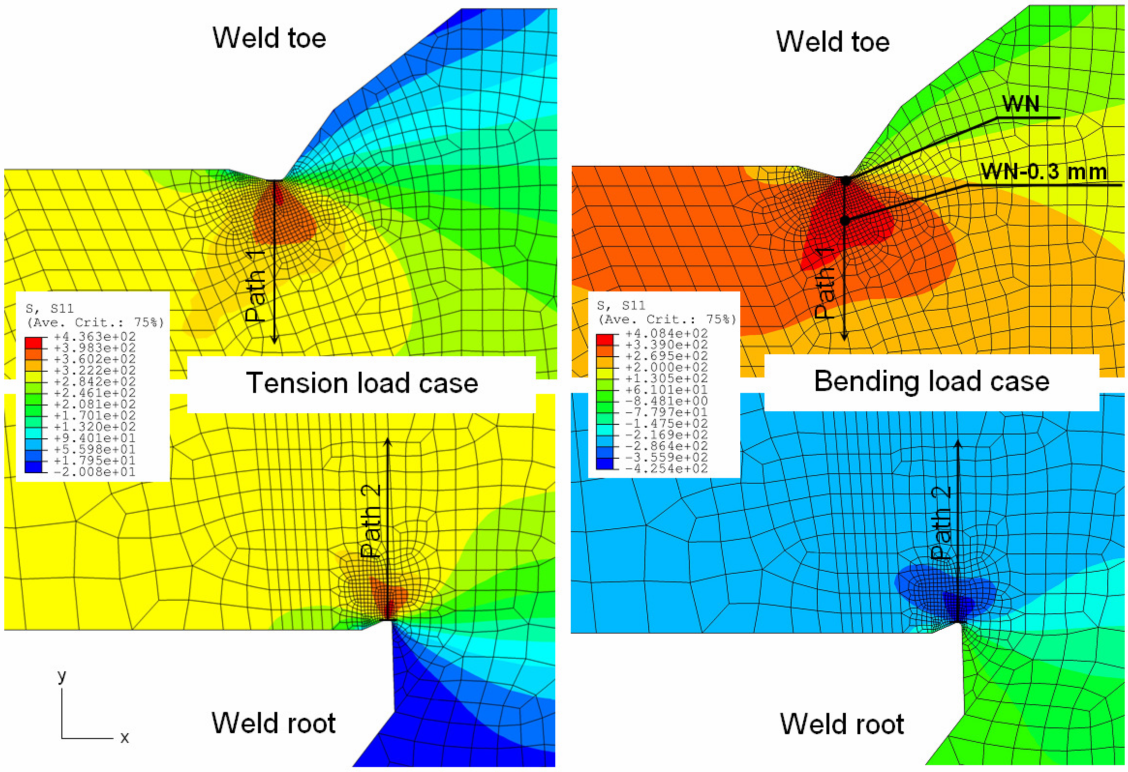

Figure 39. The distribution of normal stress σ_{xx} under tension (left) and bending (right) for applied nominal stress of 287 MPa in the case of the inhomogeneous model.

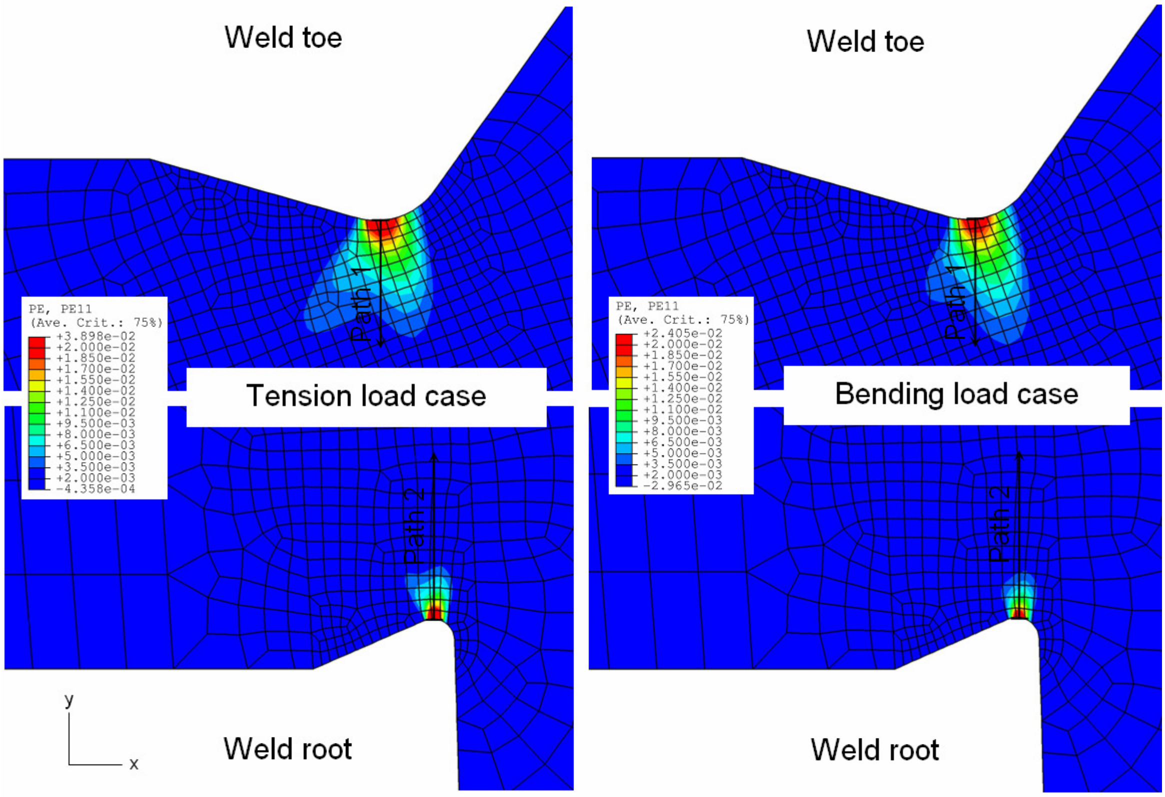

Figure 40. Distribution of plastic strain $\varepsilon_{xx,pl}$ under tension (left) and bending (right) for applied nominal stress of 287 MPa in the case of the inhomogeneous model.

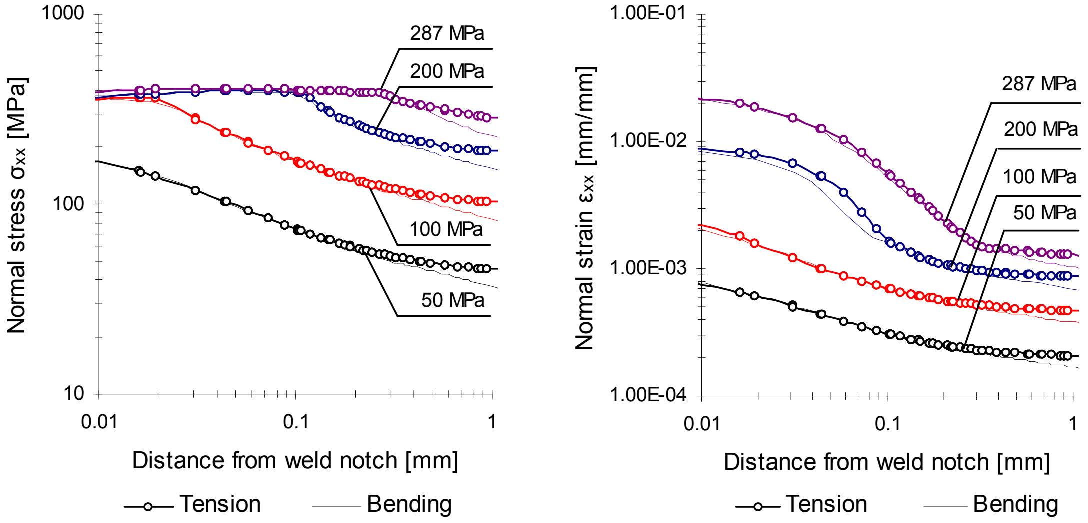

Figure 41. Stress σ_{xx} and total strain ε_{xx} versus distance from weld notch along Path 1 for different nominal stresses levels in the case of the inhomogeneous model.

The influence of the material model of the joint on the notch stresses in the weld notch was studied by comparing the results given by the inhomogeneous and homogeneous cases. The results for the tension and bending loads are shown in Figure 42 for both material models. In this figure, the normal stress σ_{xx} at the weld notch (WN) and below, see Figure 39, are given as the function of the applied nominal stress σ_{nom}. Almost no difference between the results of the inhomogeneous and homogenous material models was observed at the level of the applied nominal stress below the yield stress of parent material $\sigma_{y,\mathrm{PM}}$. Naturally, the homogeneous material model with a higher value of the yield stress $\sigma_{y,\mathrm{HAZ1}}$ made it possible to apply higher tension loading. It is noticeable that, in the bending loading, the applied nominal stress could exceed the yield stress of the parent material.

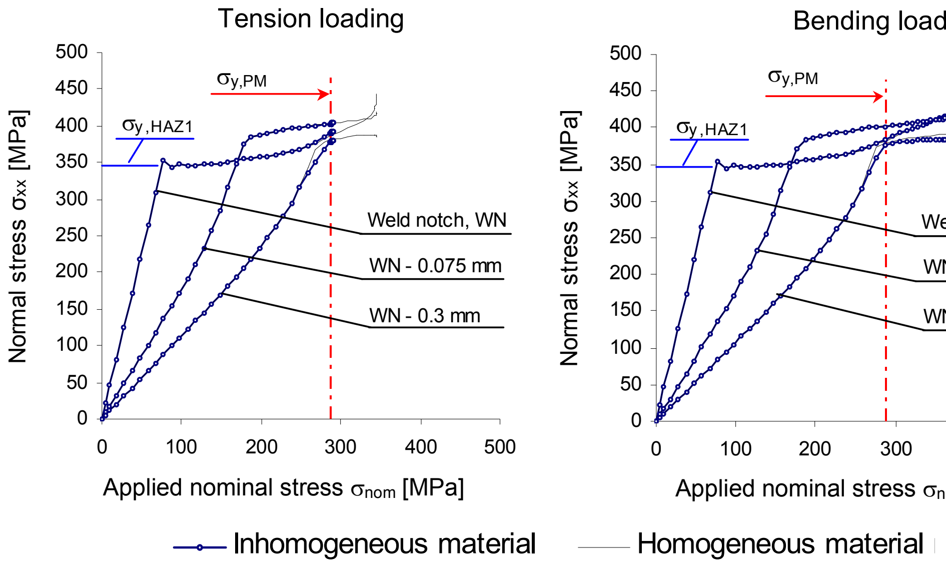

Figure 42. Influence of material models on normal stress σ_{xx} at the weld notch (WN) versus applied nominal stress.

3.3.2 Stabilised cyclic loading

In the case of the inhomogeneous model, the distribution of the amplitudes of normal stress and strain along Path 1 is presented in Figure 43 in the logarithmic scale, where the amplitude of the applied nominal stress is a parameter. The shape of the curves was somewhat similar to that of the previous ones under the initial load cycle. However, under the cyclic loading, the distance from the weld notch did not have such a strong effect on the stress and strain values.

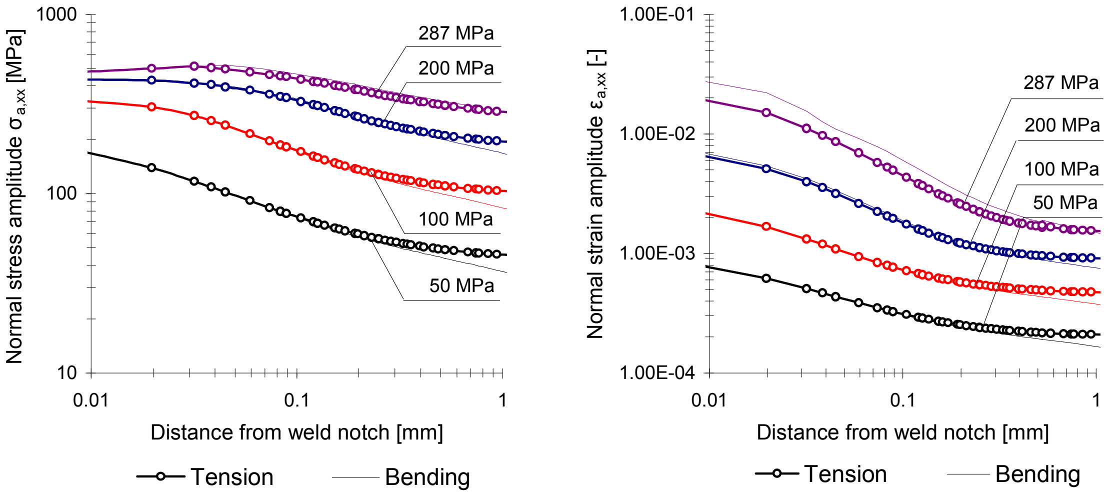

Figure 43. Normal stress $\sigma_{a,xx}$ and strain $\varepsilon_{a,xx}$ amplitudes versus vertical distance from the weld notch for different nominal stress levels in the case of the inhomogeneous model.

The influence of material modelling is presented in Figure 44, where the stress and strain amplitudes versus the applied nominal stress amplitude are given for the tension and bending loading. In Figure 44, the vertical distance from the weld notch at the toe side is given as a parameter. Only a small difference between the values given by the inhomogeneous and homogenous material models was observed in the range of high nominal stress amplitudes, due to the yielding of the parent material in the inhomogeneous case.

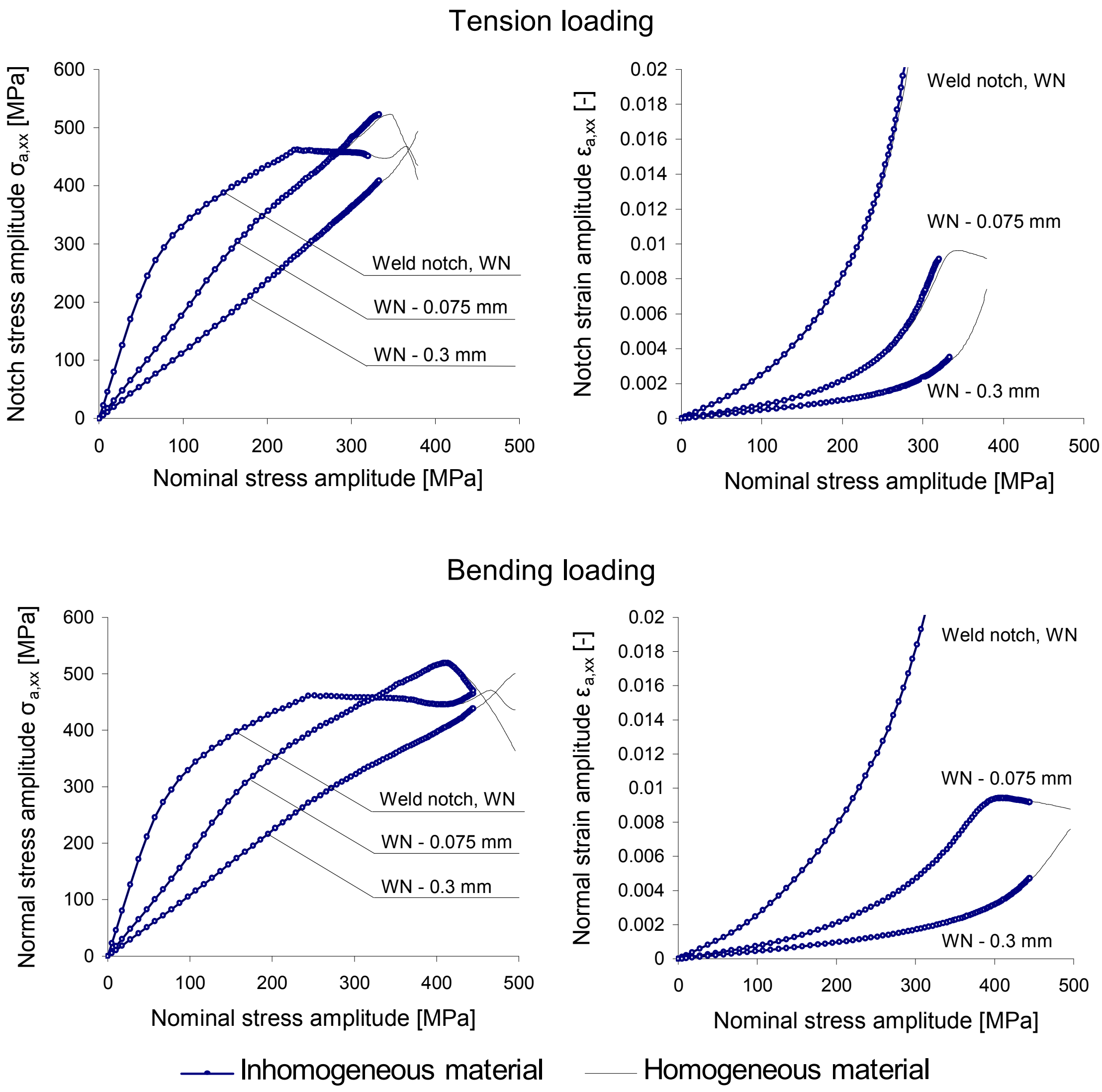

Figure 44. Influence of material models on normal stress $\sigma_{a,xx}$ and strain $\varepsilon_{a,xx}$ amplitudes at the weld notch (WN) versus applied nominal stress amplitude.

3.4 Discussion

The aim of the present elasto-plastic FE analysis was to clarify the effect of the material inhomogeneity on the notch stresses and strains in the case of the hybrid welded joint. The results of the present investigation showed that inhomogeneity is of minor importance for the initial and cyclic loading with applied stress levels below the yield limit of the parent material. Thus, with respect to these results, the use of a stress-strain curve for the HAZ is adequate in the structural analysis of notch stresses and strains. A similar conclusion with respect to the cyclic loading has been reported for fillet arc welds by Fricke *et al.* (1996) and Heo *et al.* (2004).

However, the present investigation revealed that material inhomogeneity of the joint has an important role, when the applied nominal stress exceeds the yield limit of parent material. This situation may occur under the initial load cycle for welded joints with strong misalignments. The initial load cycle defines the mean stress for fatigue strength assessments.

A general aim of the work was to develop the method of the response calculation based on the linear elastic FE analysis with Neuber's rule (1961), thus avoiding the time-consuming elasto–plastic FE analysis. To take into account the yielding of the entire cross-section at the location of the weld notch, Seeger and Heuler (1980) further developed Neuber's rule. Unfortunately, this approach proves difficult to apply when there is partial yielding of the cross-section and inhomogeneous material property. Thus, an idea of a two-step approach for structural analysis based on linear elastic FE analysis will be applied in the following chapters, where the inhomogeneity of the welded joint is taken into account so that, in the first phase, the material properties of the parent material are used and, in the second, those of the HAZ are used.

4 FATIGUE OF WELDED JOINTS

4.1 Assumptions

The experimental results in Chapter 2 indicated that the period of the macro crack initiation can form a significant proportion of the total fatigue life. The process of fatigue failure in welded joints can be divided into two main periods, see Figure 45. As the final failure happens rapidly in late fatigue life, the failure can be considered a separate phenomenon and be excluded. Thus, the total fatigue life N_f is commonly assumed to be composed of the macro crack initiation period N_i and of the propagation period N_p

$$N_f = N_i + N_p \,. \tag{6}$$

Based on this assumption, the fatigue process of welded joints can be described with two separate theoretical models. In these, defining macro crack initiation is estimated through the strain-based approach, while the propagation of the macro crack is modelled with fracture mechanics. The threshold size a_{th} and the critical size a_c of the macro crack determine the application range of the theoretical models.

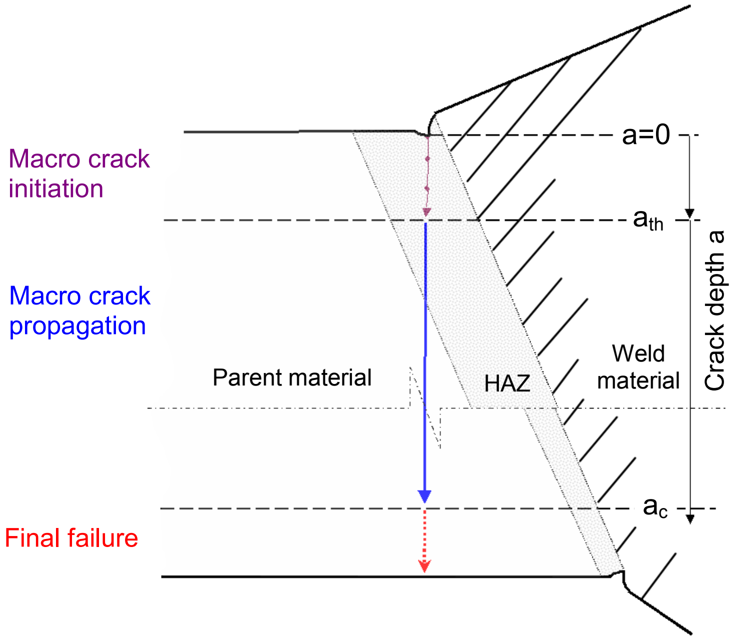

Figure 45: Modelling of fatigue crack growth for welded joints.

In this study, special emphasis was given to the modelling of macro crack initiation process, including the nucleation and the growth of a short crack. The initiation period was assumed to consist of several discrete growth steps denoted with the letter n.

The length of the discrete growth step a_o corresponded to the material microstructure (Kawagoishi *et al.* 2000) and described the damage zone in the weld notch. For each growth step, the number of load cycles N_{in} causing the fracture in the damage zone was calculated using the Coffin-Manson formula. The short crack was increased by length a_o after each step up to the point where the threshold length of macro crack a_{th} was exceeded. Figure 46 presents the principle of the method with references to the chapters, where more-detailed descriptions are given. The structural hot-spot stresses and strains were calculated for the initial geometry of welded joints. To consider the increase of notch stress and strain due to short crack growth, the stress concentrations factor K_t was updated after each growth step. The effective notch stress and strain for fatigue strength assessment were based on the Line Method (Neuber 1968; Taylor 1999), where actual stress distribution is averaged over a certain distance. Additionally, Neuber's rule was applied to estimate the non-linear stresses and strains in the sharp weld notch.

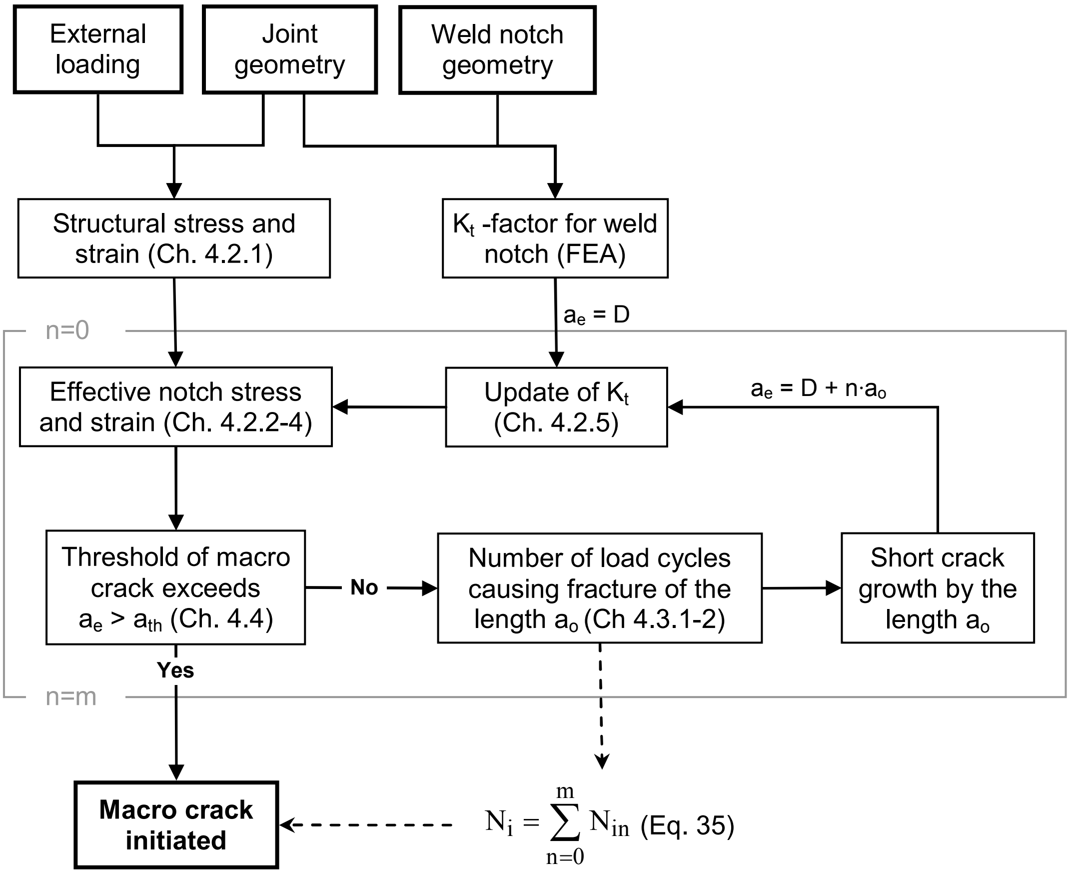

Figure 46: Flow chart of the method used to model the macro crack initiation.

4.2 Response calculation

4.2.1 Structural stress and strain in the weld notch

In this study, the nominal stress σ_{nom} was considered as an external loading for the joint. Based on the classic beam theory, this stress in the elastic regime is expressed by

$$\sigma_{nom} = \frac{F}{A} + \frac{M}{I} y , \tag{7}$$

where F is the applied axial force, M is the applied moment, I is the moment of inertia, A is the area of cross-section, and y is the distance from the neutral axis. In the case of butt joints, the structural stress σ_s, see Figure 47, is the sum of the nominal and secondary bending stress σ_{sb} due to the misalignments described with the help of the magnification factor k_m. Thus, the maximum value of the secondary bending stress at the plate surface due to the axial force is expressed by

$$\sigma_{sb,max} = \frac{F}{A} \cdot \left(k_m - 1\right) . \tag{8}$$

Consequently, the vertical distribution of the normal stress due to the secondary bending can be presented as

$$\sigma_{sb} = \frac{F}{A} \cdot \left(k_m - 1\right) \cdot \frac{2}{t} \cdot y . \tag{9}$$

The parameter k_m takes into account both the angular α and axial e misalignments (Maddox 1991)

$$k_m = 1 + \left(k_{m,\alpha} - 1\right) + \left(k_{m,e} - 1\right) , \tag{10}$$

where $k_{m,\alpha}$ and $k_{m,e}$ are the angular and the axial magnification factors, specified according to Hobbacher (2007) without the elastic straightening of the joint as

$$k_{m,\alpha} = 1 + \lambda_\alpha \cdot \frac{3}{2} \cdot \frac{2 \cdot \alpha \cdot L}{t} , \tag{11}$$

$$k_{m,e} = 1 + \lambda_e \cdot \frac{e}{2 \cdot t} , \tag{12}$$

where the support length L is the distance between the applied force F and the centreline of the joint, see Figure 47, and the parameters λ_α and λ_e take into account the boundary condition at the ends of the joint. For the fixed boundary condition, the parameter λ_α equals 1 and the parameters λ_e equals 6 (Hobbacher 2007).

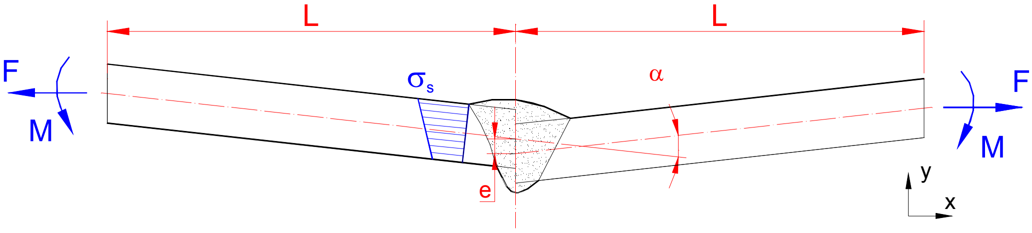

Figure 47: Tension and bending loaded joint having angular and axial misalignments and the corresponding distribution of structural stress in the joint.

The structural stress in the elastic region $\sigma_{s,el}$ for the butt joint is the sum of the nominal and secondary bending stress

$$\sigma_{s,el} = \frac{F}{A} \cdot \left(1 + \left(\left(k_m - 1 \right) \cdot \frac{2}{t} y \right) \right) + \frac{M}{I} \cdot y \,. \tag{13}$$

Assuming linear elastic plane stress material behaviour, the corresponding structural strain $\varepsilon_{s,el}$ according to Hooke's law is

$$\varepsilon_{s,el} = \frac{\sigma_{s,el}}{E} \,. \tag{14}$$

As the loading progresses, the structural stress σ_s exceeds the yield strength, and thus the non-linear relationship between the stress and strain should be considered

$$\sigma_s = f\left(\varepsilon_s \right). \tag{15}$$

Assuming that the cross-section of the beam stays plane, the distribution of the strain is linear and therefore the structural strain ε_s is expressed by

$$\varepsilon_s = \varepsilon_{sf} \cdot \Lambda_f + \varepsilon_{sm} \cdot \Lambda_m = \left[\frac{F}{E \cdot A} \cdot \left(1 + \left(\left(k_m - 1 \right) \cdot \frac{2}{t} y \right) \right) \right] \cdot \Lambda_f + \left[\frac{M}{E \cdot I} \cdot y \right] \cdot \Lambda_m \,, \tag{16}$$

where the load proportion factors Λ_f and Λ_m are obtained from the static equilibrium between the applied loads and the structural strain in the cross-section

$$F = \int_A f(\varepsilon_{sf} \cdot \Lambda_f) \; dy \tag{17}$$

and

$$M = \int_A f(\varepsilon_{sm} \cdot \Lambda_m) \cdot y \; dy \,. \tag{18}$$

If the external moment M equals zero, then, after cyclic tension loading, the residual stresses in the joint reduce the angular misalignment. This effect was taken into account by the permanent plastic moment

$$M_{per} = \int_A \left(\sigma_{s,el} - f(\varepsilon_s)\right) \cdot y \ dy \tag{19}$$

causing reduction of the magnification factor k_m. Thus, the modified magnification factor k_m^* as the function of the moment M_{per} gets

$$k_m^* = \frac{k_m}{\left(k_m - 1\right) \cdot \frac{M_{per}}{M_e} + 1}, \ 0 \le M_{per} \le M_e, \tag{20}$$

where M_e is the elastic moment

$$M_e = \int_A \left(\sigma_{s,el}\right) \cdot y \ dy \,. \tag{21}$$

In the analysis of the laser-welded joints, the stress-strain curve of the parent material was applied for the load proportion factors Λ_f and Λ_m to define the structural strains in the weld notch, i.e. the structural hot-spot strain ε_{hs}. The corresponding structural hot-spot stress σ_{hs} was derived with the help of the stress-strain curve of the HAZ material to take into account roughly the inhomogeneity of the material in the welded joint. This stress σ_{hs} was applied to define the notch stress and strain discussed in Sections 4.2.2, 4.2.3 and 4.2.4.

4.2.2 Notch stress during initial loading

The initial loading of the welded joints can result easily in the notch stresses surpassing the yield stress σ_y of the material. In the case of a sharp notch, its geometry induces internal constraints on the deformation, and thus these strains significantly affect the notch stresses. The maximum notch stress σ_{max} was considered important because it determines the mean stress σ_m for the following cyclic loading, see Figure 48.

Neuber's rule (Neuber 1961) is used to estimate maximum stress σ and strain ε at the notch. Using the structural hot-spot stress σ_{hs} and strain ε_{hs}, Neuber's rule can be rewritten as

$$\sigma \cdot \varepsilon = \sigma_{hs} \cdot \varepsilon_{hs} \cdot K_t^2, \tag{22}$$

where K_t is the linear elastic stress concentration factor

$$K_t = \frac{\sigma}{\sigma_{hs}} \tag{23}$$

defining the ratio between the elastic notch and structural stresses. The strains corresponding to the stresses in Eq. (22) are obtained from the elastic linear hardening stress-strain curve

$$\varepsilon = \frac{\sigma}{E} \text{ when } \sigma < \sigma_y$$
$$\varepsilon = \frac{\sigma_y}{E} + \frac{\sigma - \sigma_y}{E_T} \text{ when } \sigma \geq \sigma_y, \qquad (24)$$

where E_T is the tangent modulus describing material hardening. The notch stress can be solved from Eq. (22) iteratively. In this analysis, the monotonic stress-strain curve of the HAZ material at the weld notch was applied in terms of the equivalent von Mises stress σ_{eq} and strain ε_{eq}. The corresponding maximum principal stress σ_1 and strain ε_1 were calculated using the assumption that the ratio between the von Mises and the principal values stays constant in the elastic (el) and elasto-plastic (pl) regimes (Hoffmann and Seeger 1985)

$$\frac{\sigma_{1,el}}{\sigma_{eq,el}} = \frac{\sigma_{1,pl}}{\sigma_{eq,pl}} \text{ and } \frac{\varepsilon_{1,el}}{\varepsilon_{eq,el}} = \frac{\varepsilon_{1,pl}}{\varepsilon_{eq,pl}}. \qquad (25)$$

Thus, with the help of K_t (Eq. (23)) the maximum principal stress σ_1 and strain ε_1 is expressed by

$$\sigma_1 = \frac{K_{t,\sigma 1}}{K_t} \cdot \sigma \text{ and } \varepsilon_1 = \frac{K_{t,\varepsilon 1}}{K_t} \cdot \varepsilon, \qquad (26)$$

where $K_{t,\sigma 1}$ and $K_{t,\varepsilon 1}$ are the elastic stress and strain concentration factors relating the maximum principal components to the structural stress σ_{hs} and strain ε_{hs}.

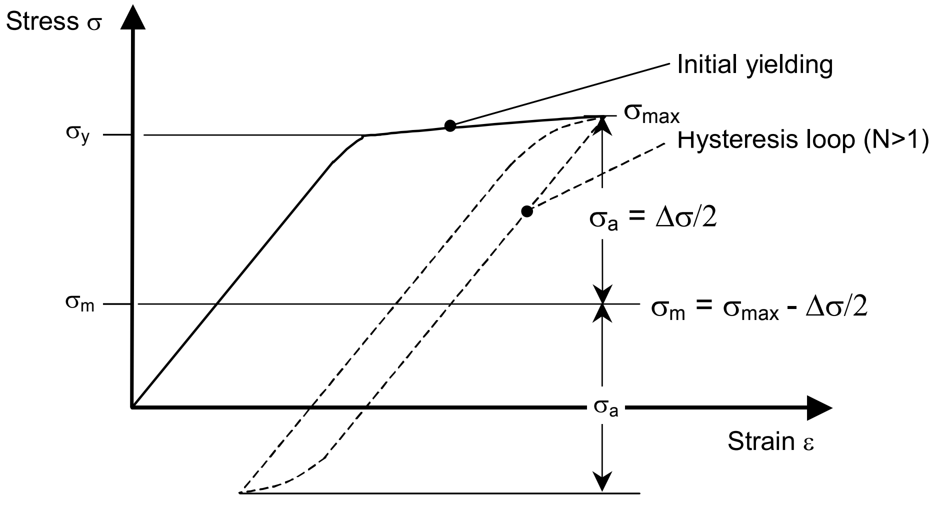

Figure 48: Stress-strain relation of the initial and following cyclic loading.

4.2.3 Notch stress and strain under cyclic loading

During the initial loading, the material behaviour was described by the elastic linear hardening stress-strain curve. Under the following load cycles, the material law is described with the Ramberg-Osgood equation, giving good fit with the cyclic stress-strain curve from the experiments

$$\frac{\Delta\varepsilon}{2}=\frac{\Delta\sigma}{2\cdot E}+\left(\frac{\Delta\sigma}{2\cdot K'}\right)^{1/n'}, \tag{27}$$

where n' and K' are the cyclic strain hardening and strength coefficients. Similarly to the notch strain analysis of the initial loading, the stress-strain curve of the HAZ material was applied. The ranges of the notch stress $\Delta\sigma$ and strain $\Delta\varepsilon$ were calculated using Neuber's rule.

$$\Delta\sigma\cdot\Delta\varepsilon\ =\Delta\sigma_{hs}\cdot\Delta\varepsilon_{hs}\cdot\left(K_t\cdot\frac{k_m^*}{k_m}\right)^2. \tag{28}$$

where the ratio between k_m^* and k_m took into account the straightening of the joint due to the plastic deformation, see Eqs. (10) and (20).

4.2.4 Effective notch stress and strain

A sharp notch based on the measured values was used to define the geometry of the weld notch. At the notch tip, stress and strain gradients are high. Due to this fact, stresses and strains for the fatigue analysis based on the continuous material model must be averaged over a finite volume. The definition of the effective stress σ_e for fatigue is based on the Line Method (Neuber 1968; Taylor 1999), where actual stress distribution is averaged over a certain distance a_o from the notch tip, see Figure 49

$$\sigma_e=\frac{1}{a_o}\cdot\int_0^{a_o}\sigma dy, \tag{29}$$

where the distance a_o is called material characteristic length. A similar procedure was applied for strain.

With a sharp weld notch, it is crucial to determine the value of the characteristic length of the material. This length a_o should correlate with grain size, based on experimental results (Akiniwa *et al.* 1988; Kawagoishi *et al.* 2000). Furthermore, continuum mechanics should be capable of characterising stress and strain distributions inside the length a_o. Several definitions of the material characteristic length suggested are based on material strength properties (Yao *et al.* 1995) and mainly applied to the stress-based approach aimed at estimating the endurance limit of welded joints. Deeper insights into the definition of the characteristic length have been provided through the studies of the formation of micro cracks. Based on their experimental results, Kawagoishi *et al.* (2000) proved that the smallest crack length, the growth rate of which can be measured and described with continuum mechanics, is about three times the averaged grain size d, thus

$$a_o = 3 \cdot d \,. \tag{30}$$

This result is supported by Zhao (2003), who reports that, in the crack tip, microcracking exists mainly inside an area of three times the averaged grain size of the material considered as the damage zone.

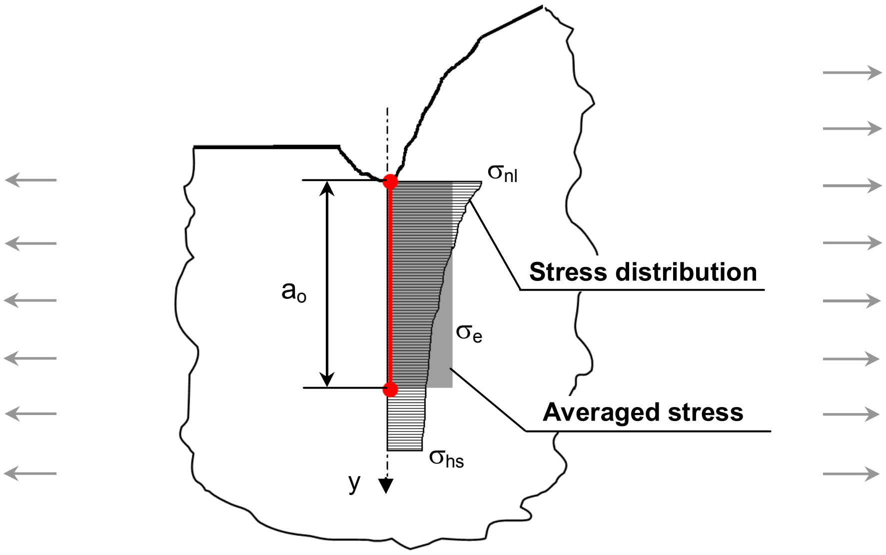

Figure 49: Principle of stress averaging for the Line Method to calculate the effective notch stress.

4.2.5 Increase of notch stress during short crack growth

In the theoretical approach to the macro crack initiation, the short crack propagation was modelled with discrete growth steps up to the length of the threshold value of macro crack a_{th}, see Figure 50. In every discrete growth step, the size of a short crack was increased by the length a_o, affecting the value of the elastic stress concentration factor K_t.

The increase of K_t was calculated using the fracture mechanics approach based on the stress intensity factor ΔK.

For a sharp weld notch, the effective crack depth a_e can be defined as the sum of the actual notch depth D and the total length of the short crack after n steps

$$a_e = D + n \cdot a_o \tag{31}$$

and thus, the stress intensity factor at the step n is expressed by

$$\Delta K = F \cdot \Delta\sigma_{nom} \sqrt{\pi \cdot \left(D + n \cdot a_o\right)}, \tag{32}$$

where F is the geometrical parameter of the weld and crack, see, for example, Hobbacher (2007). The parameter F was considered to be constant from one step to the next, as the short crack differs in scale compared to the weld size. If it is assumed that the increase of the elastic notch stress equals the increase of the stress intensity factor between step n-1 and n, then the stress parameter k_n

$$k_n = \left[\frac{D + (n+1) \cdot a_o}{D + a_o} \right]^{0.5} \tag{33}$$

gives the stress concentration factor K_t^n at the step n

$$K_t^n = k_n \cdot K_t^0, \tag{34}$$

where K_t^0 is stress concentration factor at the step n=0.

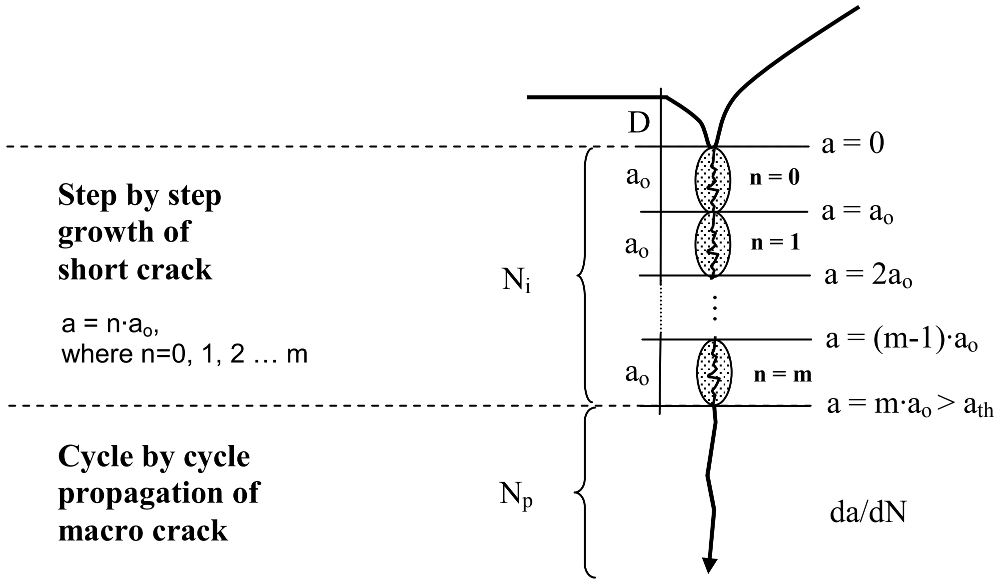

Figure 50: Modelling of short crack propagation by discrete growth steps.

4.3 Macro crack initiation

4.3.1 Damage model for short crack growth

The total time of the macro crack initiation N_i is the sum of the growth steps

$$N_i = \sum_{n=0}^{m} N_{in} \,. \tag{35}$$

where N_{in} is the crack initiation life for the step n, derived from the Coffin-Manson equation (Coffin 1954; Manson 1954) with the mean stress correction based on the damage parameter P_{swt} (Smith *et al.* 1970). The Coffin-Manson equation gives the strain amplitude ε_a as a function of the sum between elastic $\varepsilon_{a,el}$ and plastic $\varepsilon_{a,pl}$ strains

$$\varepsilon_a = \varepsilon_{a,el} + \varepsilon_{a,pl} \,, \tag{36}$$

where the relationship between the strain amplitudes and the initiation life N_{in} gets

$$\varepsilon_{a,el} = \frac{\sigma_a}{E} = \frac{\sigma_f'}{E} \cdot \left(2 \cdot N_{in}\right)^b , \; \varepsilon_{a,pl} = \varepsilon_f' \cdot \left(2 \cdot N_{in}\right)^c . \tag{37a, b}$$

There, the parameters σ_f', ε_f', b and c are the fatigue coefficients based on uniaxial fatigue tests.

The macroscope study in Section 2.5.4 revealed that the tension dominated the initiation failure of the joint, thus the damage parameter P_{swt} is applicable, as noted by Socie and Marquis (2000). This parameter, stated with the help of the maximum principal stress and strain, gets

$$P_{SWT} = \sqrt{\sigma_{max} \cdot \varepsilon_a} \,, \tag{38}$$

where σ_{max} is the maximum value of the notch stress equal to

$$\sigma_{max} = \sigma_m + \sigma_a \,. \tag{39}$$

If the mean stress $\sigma_m = 0$, then, based on Eq. (37a), the maximum stress gets

$$\sigma_{max} = \sigma_a = \sigma_f' \cdot \left(2 \cdot N_{in}\right)^b \tag{40}$$

and the damage parameter P_{swt} as a function of N_{in} can be determined from Eq. (38). As the relation between P_{swt} and N_{in} is independent of the value of mean stress, then the product between the stress σ_{max} and the strain ε_a is also valid in the case of $\sigma_m \neq 0$

$$\sigma_{max} \cdot \varepsilon_a = \left(\frac{\sigma_f'^{\,2}}{E} \cdot \left(2 \cdot N_{in}\right)^{2 \cdot b} + \sigma_f' \cdot \varepsilon_f' \cdot \left(2 \cdot N_{in}\right)^{b+c} \right) . \tag{41}$$

This equation gives the value of the N_{in}, which is substituted to Eq. (35).

4.3.2 Fatigue coefficients based on material hardness

The fatigue coefficients of the Coffin-Manson equation are based on experiments. Unfortunately, it is almost impossible to determine these coefficients experimentally in the case of the narrow laser weld with strongly inhomogeneous material values. Thus, the fatigue coefficients are based on the material hardness, see Roessle and Fatemi (2000) or Lee and Song (2006). Table 16 represents the equations that provide the fatigue coefficients as the function of the Brinell hardness. Based on the data given in Boyer and Gall (1985), the conversion from the Vickers to the Brinell hardness is expressed by

$$HB = 0.9801 \cdot HV^{0.9941}. \tag{42}$$

As the stress and strain variables of Ramberg-Osgood equation (Eq. (3)) are range values, then the strain equals twice the strain amplitude ε_a in the Coffin-Manson equation Eq. (36) with $N_{in} = 0.5$. Thus, the coefficients of the cyclic strain hardening n' and the strength K' in Ramberg-Osgood equation are (Lee and Song 2006)

$$n' = \frac{b}{c} \tag{43}$$

$$K' = \sigma_f' \cdot \left(\varepsilon_f'\right)^{-n'}. \tag{44}$$

Table 16: Hardness-based estimations for the fatigue coefficients of the Coffin-Manson equation (Roessle and Fatemi 2000)

Material parameter	Estimation formula	Unit
Fatigue strength coefficient	$\sigma_f' = 4.25 \cdot HB + 225$	MPa
Fatigue strength exponent	$b = -0.09$	[-]
Fatigue ductility coefficient	$\varepsilon_f' = \frac{1}{E} \cdot \left(0.32 \cdot HB^2 - 487 \cdot HB + 191000\right)$	MPa
Fatigue ductility exponent	$c = -0.56$	[-]

4.4 Macro crack propagation model

Macro crack propagation is based on the linear elastic fracture mechanics. The threshold depth of the macro crack a_{th} is defined by the threshold value of the stress intensity factor ΔK_{th}

$$a_{th} = \frac{1}{\pi}\left(\frac{\Delta K_{th}}{F \cdot \Delta\sigma}\right)^2, \tag{45}$$

where parameter F takes into account stress increase due to the crack and weld geometry. The macro crack propagation is based on the Paris Law (Radaj 1995; Forman *et al.* 1967) and the propagation time N_p is expressed by

$$N_p = \int_{a_{th}}^{a_c} \frac{1-R}{C \cdot \Delta K^n} da\,, \tag{46}$$

where ΔK is the range of the stress intensity factor (Anderson 2005), a_c is the critical crack depth and C, n are material constants defining the rate of crack growth. The effect of the mean stress for the crack propagation is taken into account with the stress ratio R

$$R = \frac{\sigma_{\min}}{\sigma_{\max}}\,. \tag{47}$$

The value of the critical crack depth a_c is based on the ultimate load of the cross-section defined by the limit load theory. According to this, under tensile loading, the final failure occurs when the nominal stress equals the ultimate strength σ_u. Thus, the critical nominal stress for the welded-plate specimen is

$$\sigma_{nom,c} = \sigma_u \cdot \frac{A_e}{A}\,, \tag{48}$$

where A is the initial cross-section and A_e is the effective cross-section, which takes into account the reduction of the cross-section due to the crack propagation. A large macro crack usually tends to obtain a semi-elliptical shape, where the crack length equals two times its depth and then the effective cross-section is expressed by

$$A_e = A - \pi \cdot a^2\,. \tag{49}$$

Now, the critical crack depth for the nominal stress σ_{nom} is obtained by substituting Eq. (49) to Eq. (48) and noting that the nominal stress substitutes the critical one

$$a_c = \sqrt{\frac{A}{\pi} \cdot \left(1 - \frac{\sigma_{nom}}{\sigma_u}\right)} \quad (a_c \le t,\ a_c \le 0.5 \cdot w). \tag{50}$$

It should be noticed that this definition is limited to the crack depth smaller than the plate thickness t and smaller than half the plate width w. Alternatively, the critical crack depth can be determined with the help of the critical stress intensity factor K_c

$$a_c = \frac{1}{\pi}\left(\frac{K_c}{F \cdot \sigma}\right)^2. \tag{51}$$

4.5 Validations

4.5.1 Response

The accuracy of the present response calculation for notch stresses and strains was compared to the results of the elasto-plastic FE analysis, where both material and geometrical nonlinearity was included. Two different validation cases were considered, including the Hybrid LF welded-plate specimen Type B and the notched miniature specimen for the parent material. In the first one, the 2D FE analysis was carried out in a way basically similar to that presented in Chapter 3, but now the modelling of the whole test specimen using the plain strain element was used to focus the analysis on the weld notch. Because of the plane strain assumption, in the present approach the original uniaxial stress-strain curve was modified accordingly, see Dowling (2007), for instance. A sketch of the structural model of the welded-plate specimen is given in Figure 51. The main dimensions and boundary conditions were equal to those during the tests described in Chapter 2. The geometrical dimensions of the joint were obtained from the analysis of the critical weld geometry for the Hybrid LF joint, which is presented in detail in Chapter 7. The FE model included the inhomogeneous material distribution similar to that presented in Section 3.2.2, where both the monotonic and cyclic stress-strain curves are given. In addition, Figure 51 shows the points where the stress and strain were calculated. Point 1 is located in the vertical distance of $3/2 \cdot t$ from the weld notch and points 2 and 3 in the weld notch and below.

Figure 52 presents the results for the welded plate under initial loading. Thus, only stresses were of interest and strains were ignored. The maximum principal stress at the base plate (point 1) and at the vertical distance of 0.05 mm from the notch tip (point 2) was plotted as the function of the applied nominal stress. The results of the analysis indicate that the analytical approach provides a good estimation of the stresses. However, in point 2 the FE analysis took into account the complicated non-linear behaviour of the notch stresses and strains, impossible to be modelled with the present approach.

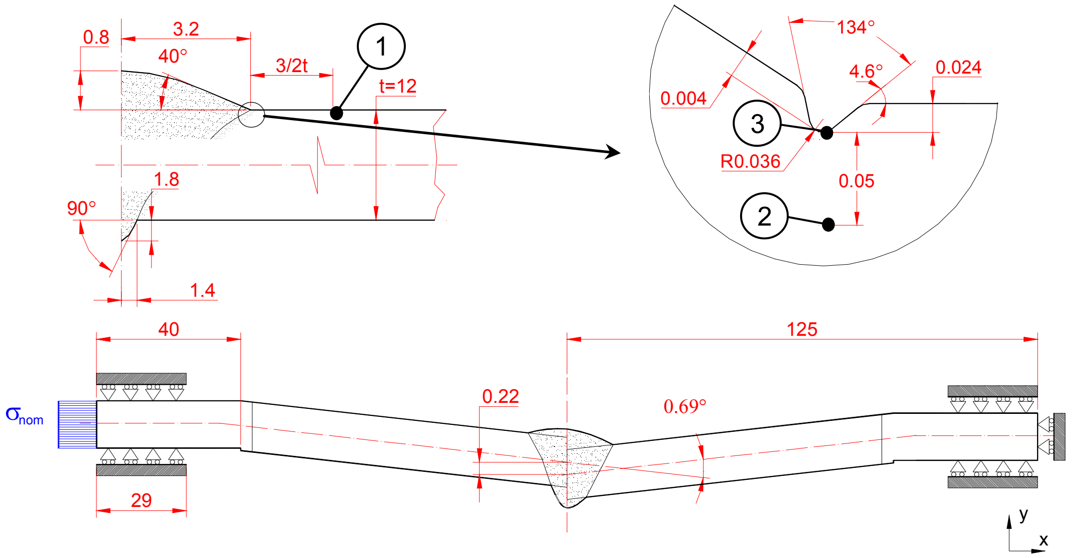

Figure 51. Geometry and boundary conditions of the structural model for Hybrid LF welded-plate specimen Type B. Point 1 in the base plate (PM), points 2 and 3 close to the weld notch (HAZ1) are also presented.

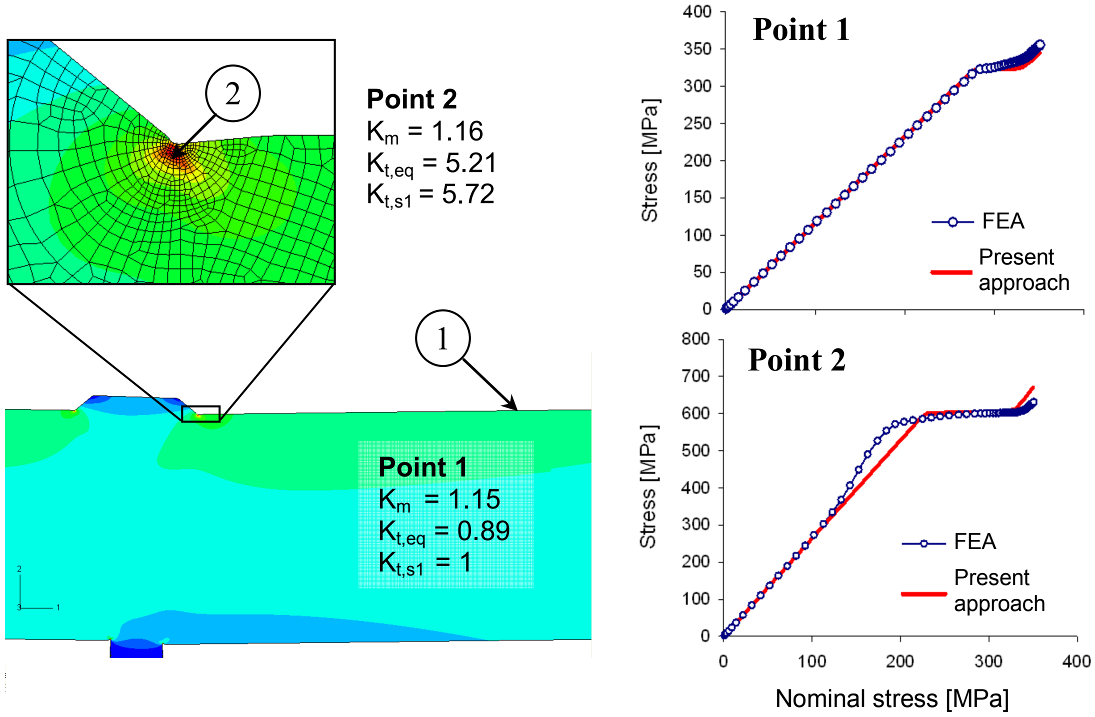

Figure 52. Comparison of the present approach and the elasto-plastic FE analysis of welded-plate specimen. Maximum principal stress at points 1 (PM) and 2 (HAZ1) versus nominal stress under initial loading are given.

Figure 53 presents the results of the welded plate under cyclic loading to illustrate the approach based on the von Mises equivalent stress and strains. The maximum stress and strain range for the notch tip (point 3) was plotted as the function of the applied load. The results of the present approach showed good agreement with those of the FE analysis.

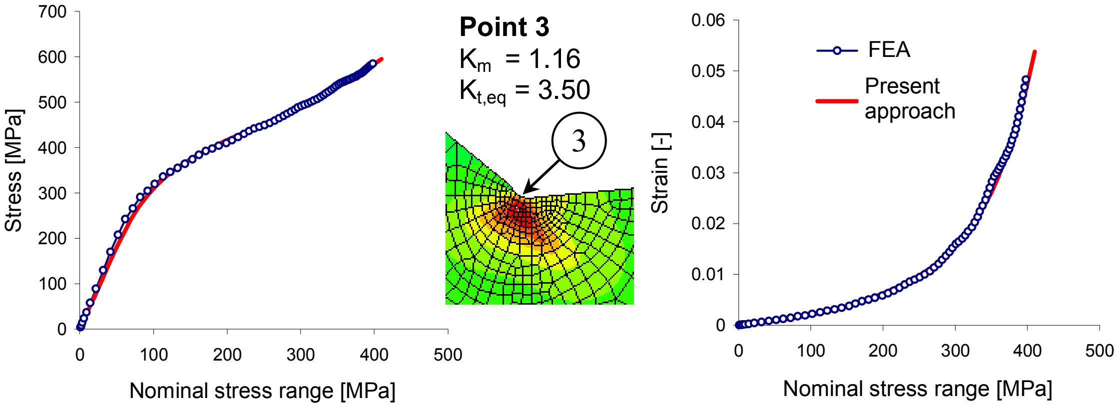

Figure 53. Comparison of the present approach and the elasto-plastic FE analysis of welded-plate specimen. The von Mises stress and strain ranges at point 3 (HAZ1) versus nominal stress range under cyclic loading are given.

The second validation of stresses and strains between the present approach and FE analysis was completed using the geometry of the notched miniature specimen. Figure 54 shows the geometry and boundary conditions. The axisymmetric solid elements were used in FE modelling and only a half model was needed due to symmetry. The cyclic stress-strain curve for the parent material was applied, see Table 15. This case aimed the validation of the response calculation method given in Chapter 4.2 including also the stress and strain averaging to obtain the effective notch stress and strain, see Eq. (29). The averaging was made over a certain distance a_o. Figure 55 presents the effective notch stress and strain versus the nominal stress in the case of a_o = 0.6 mm. In this case, the FE analysis gave $K_t = 0.99$, where the effective notch stress in terms of von Mises stress was divided by the applied nominal stress. The value of the factor K_t was in this case below 1, due to the relatively high value of a_o and due to the use of von Mises stress. A good agreement between the results of the present approach and the FE analysis was observed.

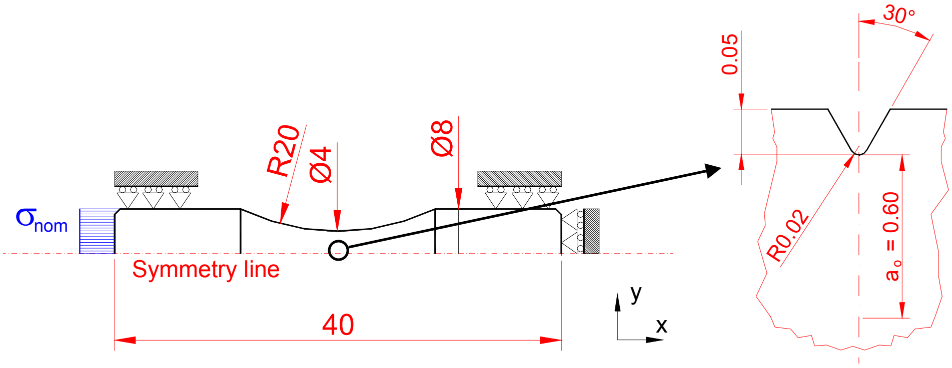

Figure 54. Geometry and boundary conditions for miniature specimen.

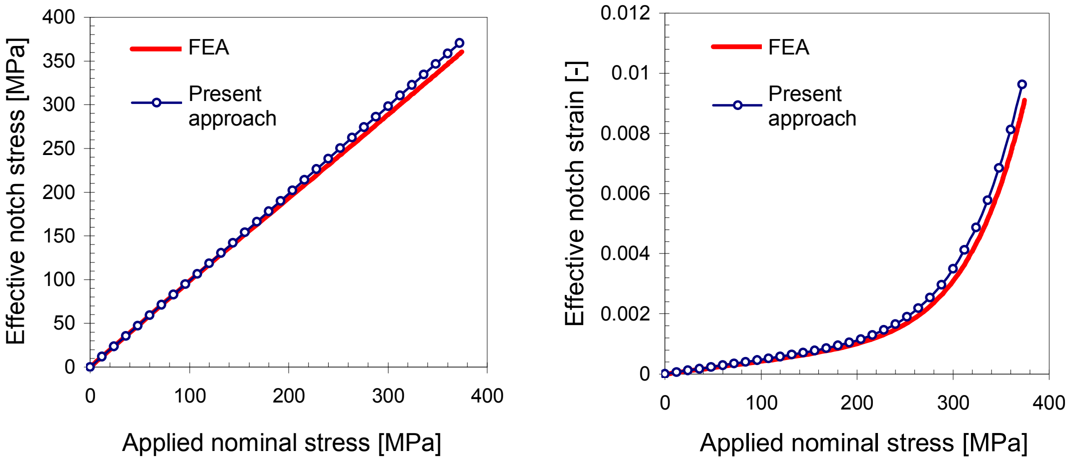

Figure 55: Comparison between the present approach and the elasto-plastic FE analysis for the miniature specimen. Effective notch stress (von Mises) and strain versus applied nominal stress under cyclic loading are shown.

4.5.2 Fatigue resistance based on material hardness

In the present investigation, the fatigue resistance covering the macro crack initiation was described by the Coffin-Manson equation, where the fatigue coefficients were obtained from the empirical formulae based on the material hardness, see Table 16. The validation of this approach for laser-welded joints was based on the results of the fatigue tests with the smooth miniature specimens given in Section 2.5.3. In Figure 56, the predicted life is plotted against that of the measured one in the logarithmic scale. The continuous line shows the complete equivalence of the values between the predicted and the measured. The bounds of the scatter band with a factor of three ($1/3 < N_{mea}/N_{pre} < 3$) are plotted with dashed lines. In the figure, the results for the SAW joint are also given as a reference. In general, the results indicated a good agreement between the predicted and measured life of the test specimens. The scatter band covers 95% of all the points, which is similar to the previous studies where typical parent materials were investigated (Lee and Song 2006). Consequently, the hardness-based approach to determine the fatigue coefficients was considered applicable to the laser-based joints. The test results of the Hybrid LF specimens showed irregular failure where the crack initiated from the borderline between different material zones (WM/HAZ or HAZ/PM). In these cases, the mean values of the material hardness were used.

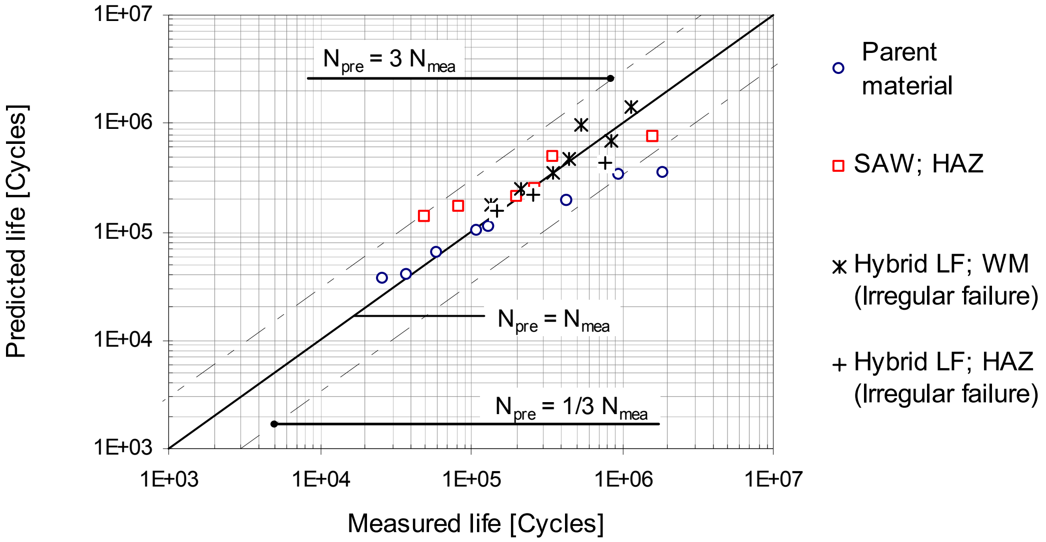

Figure 56: Comparison between the predicted (pre) and measured (mea) values for the macro crack initiation life of smooth miniature specimens.

5 STATISTICAL ANALYSIS

5.1 Outline

The values of the geometrical dimensions of the butt joints had large statistical variation even within one test specimen, depending on the welding method. This variation of the weld geometry should be taken into account in fatigue analyses as the fatigue damage is extremely localised in the welded joints. The flow chart of the statistical analysis is presented in Figure 57. The measured results of the joint geometry presented in Section 2.5.1 gave the initial data to the analysis for the following two tasks:

1. Limit values of joint dimensions
2. Correlation between joints dimensions.

Task 1 included statistical analysis, where best-fitted theoretical distributions were determined for the measured data of weld geometries. These theoretical distributions were used to define the limit values of the geometrical dimensions with certain probability levels. Task 2 consisted of the study to determine regression equations between different geometrical dimensions of the welded joints.

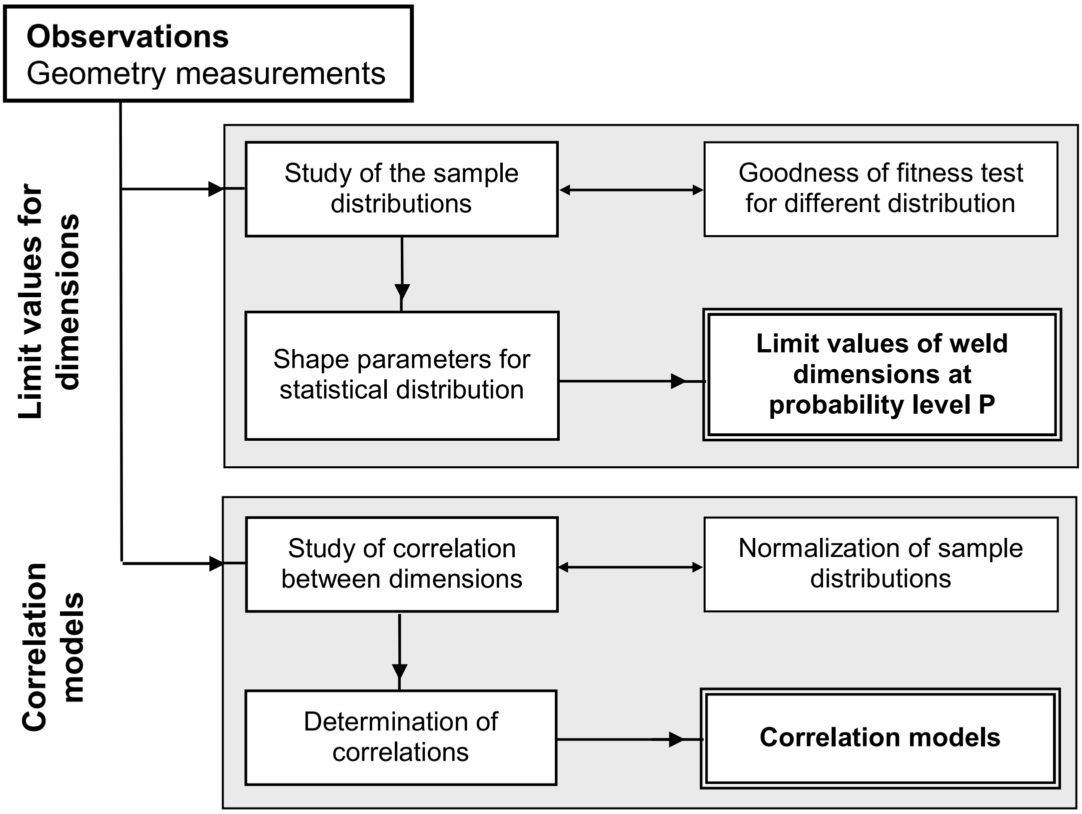

Figure 57: Flow chart of statistical analysis.

5.2 Limit values

The generally available statistical software and self-coded procedures were applied to determine the limit values of joint dimensions at certain probability levels. Statistical distributions such as the Normal, Lognormal, Exponential, Rayleigh and Weibull functions were fitted to the sample histograms and the goodness of the distributions were analysed using the probability plot technique (Filliben 1975; Chambers *et al.* 1983), the Kolmogorov-Smirnov K-S test (Massey 1951), and the Anderson-Darling test (Anderson and Darling 1954). In the probability plot technique, the measured data was plotted against the values from the theoretical distributions. The probability plot correlation coefficient (PPCC), based on the line fitting, shows the goodness of the fit. The probability plot was also used to estimate the parameters of the statistical distributions. In the case of the Weibull distribution with three parameters, the values of these were solved maximising the PPCC. The standard optimisation methods, such as the Quasi-Newton and the Gradient methods were used. The Kolmogorov-Smirnov test gave the largest absolute difference D between the sample and theoretical cumulative distributions. The K-S goodness of the fit test was produced at the significance level of 0.05, and the obtained values of D were compared to the critical value D_c given in the literature (Hoel 1962). The Anderson-Darling test is a modification of the K-S test, giving more weight on the tails of the distribution. This test gives value A^2, which describes the difference of the cumulative distributions.

The limit values for each joint dimension at the certain probability level were calculated from the cumulative distribution with the best fit given by the K-S test. The other two tests were used to support the goodness of the K-S test. The results of the goodness of the fit tests for different distributions are presented in Appendix C. In most cases, the Weibull and Lognormal distribution gave the best results. Based on the best-fit distributions, the mean value, and also the limit values at the 5% and 95% probability levels, was calculated and presented in Tables 17 and 18.

Table 17: Limit values of axial [mm] and angular [deg] misalignments of different joints based on the best-fit distribution

Probability level	SAW		Laser		Hybrid LF		Hybrid MF	
	Axial	Angular	Axial	Angular	Axial	Angular	Axial	Angular
P = 5%	-0.39	-0.25	-0.44	-0.05	-0.15	0.43	0.40	0.16
P = 50%	-0.12	-0.20	0.05	0.12	0.22	0.69	0.47	0.18
P = 95%	0.28	-0.18	0.34	0.28	0.75	0.97	0.57	0.22

Table 18: Limit values of weld dimensions of different joints based on the best-fit distribution

Probability level P	SAW		Laser		Hybrid LF		Hybrid MF	
	Toe	Root	Toe	Root	Toe	Root	Toe	Root
Weld height h [mm]								
P = 5%	2.1	0.7	-0.5	0.3	0.2	0.0	0.9	0.5
P = 50%	2.2	1.4	0.1	0.5	0.5	0.6	0.9	0.7
P = 95%	2.5	1.9	0.5	0.7	0.8	1.8	1.0	1.3
Weld width w [mm]								
P = 5%	16.9	9.5	2.2	1.4	4.9	0.9	6.2	1.5
P = 50%	18.1	10.0	2.8	1.7	5.8	1.4	6.4	1.9
P = 95%	19.5	10.5	3.7	1.9	6.4	2.8	6.7	2.2
Weld flank angle θ [deg]								
P = 5%	26.3	11.2	-31.0	25.4	3.8	23.0	15.6	30.1
P = 50%	28.9	17.9	5.8	38.8	14.5	59.8	18.4	47.2
P = 95%	34.3	27.8	29.7	53.6	40.0	90.4	21.8	69.1
Weld notch depth D_1 [mm]								
P = 5%	0.001	0.002	0.005	0.009	0.001	0.002	0.001	0.002
P = 50%	0.004	0.014	0.037	0.022	0.007	0.010	0.007	0.008
P = 95%	0.017	0.091	0.264	0.057	0.061	0.060	0.032	0.030
Weld notch depth D_2 [mm]								
P = 5%	0.003	0.004	0.004	0.009	0.004	0.014	0.001	0.002
P = 50%	0.021	0.027	0.033	0.034	0.036	0.084	0.010	0.018
P = 95%	0.060	0.080	0.282	0.126	0.121	0.232	0.043	0.076
Notch flank angle γ [deg]								
P = 5%	0.9	0.3	4.9	3.6	0.3	0.1	0.8	0.6
P = 50%	3.9	9.7	22.9	13.2	3.9	3.6	6.8	7.5
P = 95%	17.1	65.4	54.5	27.4	18.0	30.0	23.0	32.4
Notch opening angle β [deg]								
P = 5%	112.3	93.2	80.1	74.6	104.0	62.6	117.6	90.3
P = 50%	133.8	134.4	120.2	95.6	140.8	94.4	143.1	108.7
P = 95%	147.7	165.2	151.0	127.7	167.0	119.0	159.8	131.0
Notch root radius ρ [mm]								
P = 5%	0.019	0.016	0.039	0.024	0.036	0.018	0.047	0.027
P = 50%	0.042	0.099	0.229	0.069	0.272	0.082	0.256	0.126
P = 95%	0.094	0.613	1.334	0.203	2.060	0.379	1.399	0.580

5.3 Correlation between joint dimensions

The correlations between different joint dimensions were studied graphically from scatter diagrams. Additionally, the Pearson correlation number *R* was calculated for each pair of dimensions, see Appendix D. Table 19 represents the minimum and maximum values of the number *R* for the weld dimensions. The calculated value of *R* varied from –0.93 to 0.95, indicating the existence of a significant correlation. Between the axial and angular misalignments, the Pearson correlation number was from –0.72 to 0.45, indicating a weak correlation, see Figure 58.

Table 19: Summary of correlation values between weld dimensions

Welded Joint	Value of Pearson correlation *R* Min	 Max
SAW	-0.93	0.94
Laser	-0.72	0.95
Hybrid LF	-0.69	0.91
Hybrid MF	-0.70	0.86

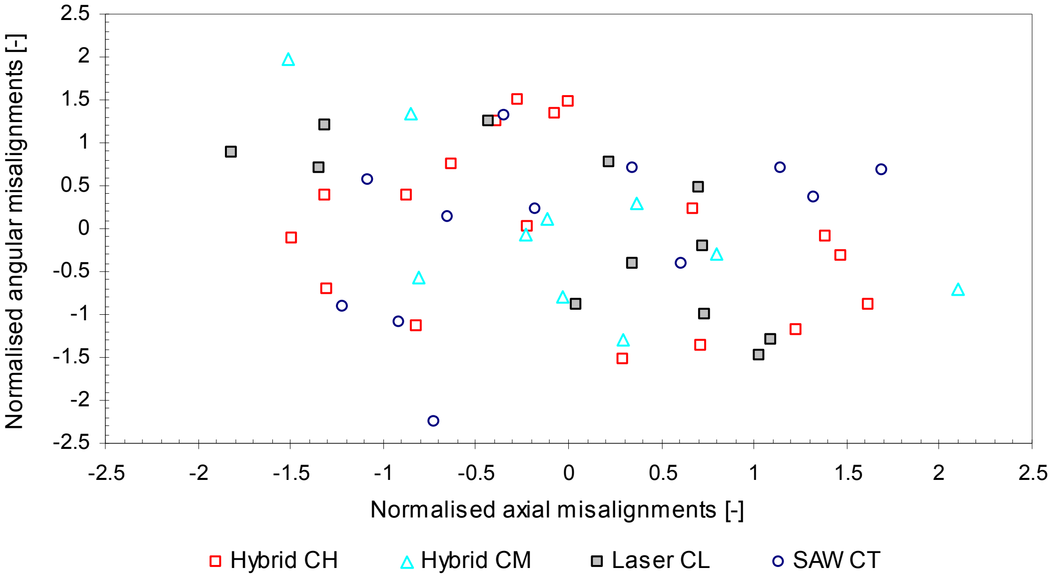

Figure 58: The relation between axial and angular misalignments.

The correlation between weld dimensions appeared statistically significant, as shown in Table 19. Therefore, regression models between the different weld dimensions were required to define the critical weld geometry. A linear regression model was created for each weld dimension as the function of other dimensions. For example, the linear regression model of the weld height h is expressed by

$$h = c_w \cdot w + c_\theta \cdot \theta + c_{D1} \cdot D_1 + c_{D2} \cdot D_2 + c_\gamma \cdot \gamma + c_\beta \cdot \beta + c_\rho \cdot \rho + c\,, \qquad (52)$$

where the parameters c are regression coefficients.

Before the regression analysis, the normality of the sample distribution of the dependent variable was studied using the K-S test. If this sample distribution did not pass the test, a transformed variable was used. The transformation of the variable was carried out with a logarithm, inverse, square, or square root operations. Additionally, the number of the predictors (independent parameters) was kept as low as possible due to limited sample size. The maximum number of the predictors was fixed to four. The best candidates for predictors were selected using stepwise and backward regression methods. The significance of the F-value was the criterion for the analysis. The limit values of the stepwise method were at the significance level of 0.05 for entry and at 0.1 for removal. In the backward regression method, the limit value for the removal was at the significance level of 0.05.

The goodness of the regression models was presented with the Pearson correlation number, giving the correlation between the observed and regression values. The F-value determined as the mean square of the X divided by the mean square of the error was also calculated. Special emphasis was focused on the residual of the regression models. This residual had to be normally distributed and homoscedastic, i.e. it had to have a uniform distribution of residual along the regression line. Additionally, all the observations were considered to be significant, which meant that no remarkable outliers were allowed.

Table 20 represents the minimum and maximum values of the correlation number for the regression models. The numerical values of the other diagnostic values are also given. The statistically significant regression model that can describe 96% of the measured values, i.e. $R^2 = 0.96$, was observed, see Figure 59. Also, the models with low R^2 values were observed. The detailed presentation of the results from the regression analysis is given in Appendix E.

Table 20: Summary of statistical significance of the regression models for geometrical dimensions

Welded	Correlation R^2		F-value		Significance of F	
Joint	Min	Max	Min	Max	Min	Max
SAW	0.23	0.93	5	245	0.0450	< 0.001
Laser	0.24	0.91	6	53	0.0288	< 0.001
Hybrid LF	0.22	0.96	5	440	0.0385	< 0.001
Hybrid MF	0.21	0.77	5	62	0.0430	< 0.001

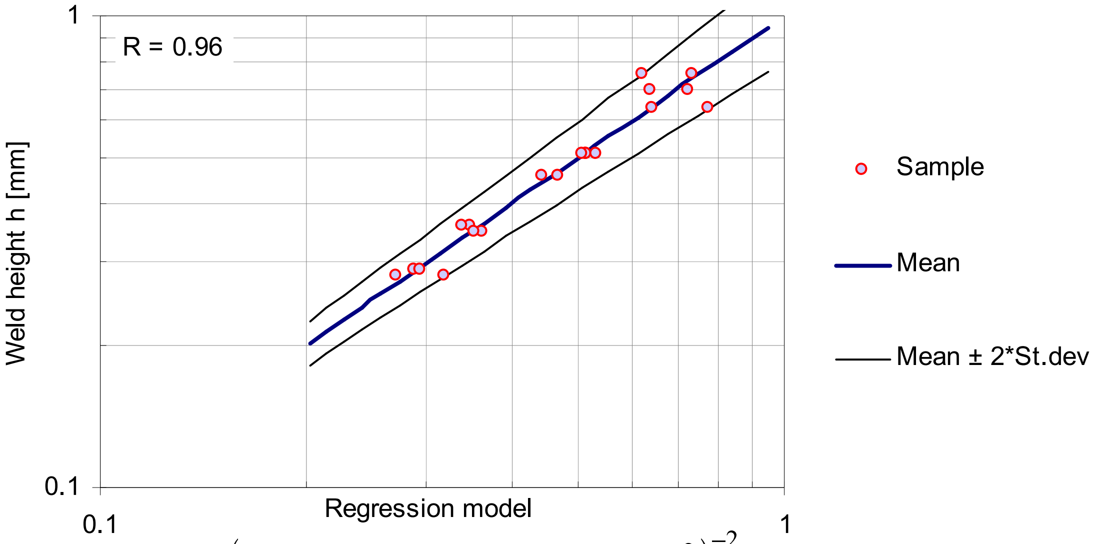

$$h = \left(-0.217 \cdot \ln(\theta) + 0.013 \cdot \gamma - 0.014 \cdot w^2\right)^{-2}$$

Figure 59: Example of the regression model for weld height in the case of Hybrid LF welded joint. Comparison between measured and predicted values is given.

Motivation for the study presented in this chapter was related to the physics of fatigue. Fatigue damage is an extremely localized process that initiates from the most critical geometry of a weld notch. Because of the large statistical variation of the geometry of a weld, the critical weld geometry stays obscure in relation to the stress concentration factor. Solving this problem needs statistical analysis of weld geometry to define the correlation between the dimensions and their limit values. If correlation exists, then the relation between the stress concentration factor and the geometrical dimensions must be determined to define the critical weld geometry. This problem is discussed in next Chapter 6.

6 REGRESSION FORMULA FOR THE STRESS CONCENTRATION FACTOR

To predict the fatigue life of welded joints with the statistically varying weld geometry, knowledge of the relation between weld dimensions and notch stresses is required. This was studied using the linear FE analysis, which included the three different structural models under tension loading, see Figure 60. The influence of the dimensions of the weld bead described by h, w and θ was studied using the model of the welded butt joint without a sharp notch, see Figure 60a. Figure b presents the V-notched plate with the parameters D, β and ρ to analyse the effect of the notch. Here, the notch depth $D = D_1 = D_2$. Additionally, combining these two geometries, Model C was applied to derive the semi-analytical regression formulae of the stress concentration factor K_t. These formulae were needed to determine the critical weld geometry.

The dimensions of the structural models are given in Table 21. The ranges of the values covered at least those of the measured ones presented in Chapter 2. In total, the FE analysis included about 120 different variations of dimensions. The parabolic plane strain elements were used in the structural models, where the minimum size of elements varied from 0.01 mm to 0.05 mm, based on the notch radius ρ. The Young Modulus E of 210 GPa and the Poison ratio ν of 0.3 were used.

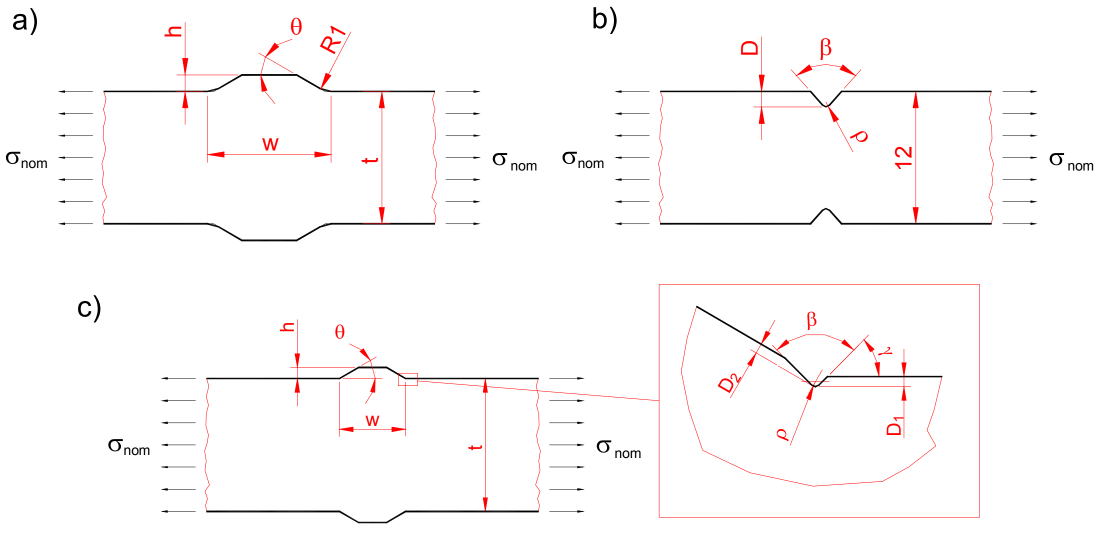

Figure 60: Structural models to define the effects of weld dimensions on notch stresses: a) welded joint without sharp notch, b) V-notched plate and c) butt joint based on the combination of Models A and B.

Table 21: Ranges of dimensions of different structural models [mm and deg]

Reference geometry		Model A	Model B	Model C
Plate thickness	t	12	12	12
Height of weld	h	0.02 – 2.5	-	0.02 – 2.48
Width of weld	w	0.82 – 20	-	0.82 – 19.5
Flank angle of weld	θ	5.18 – 97	-	5.18 – 97
Notch depth	D, D_1, D_2	-	0.05 – 0.60	0.001 – 0.242
Notch flank angle	γ	-	-	0.8 – 54
Notch opening angle	β	-	50 – 170	68 – 173
Notch root radius	ρ	1	0.25, 1.00	0.02 – 1.57

The influence of the dimensions of the weld bead and notch on the notch stresses was studied separately. Figures 61 and 62 present K_t versus the weld width and height for Model A. The other two dimensions were considered as parameters. In the figures, the rectangular boxes indicate the relevant values of K_t, corresponding to the measured joint dimensions. In the case of narrow and low weld bead typical of the Laser and Hybrid welds, the width and height were the most important parameters, while the flank angle had almost no effect. With a wider and higher weld bead typical of the SAW, the flank angle became a more important parameter. The increase of these dimensions gave higher values for K_t, due to the support of the weld.

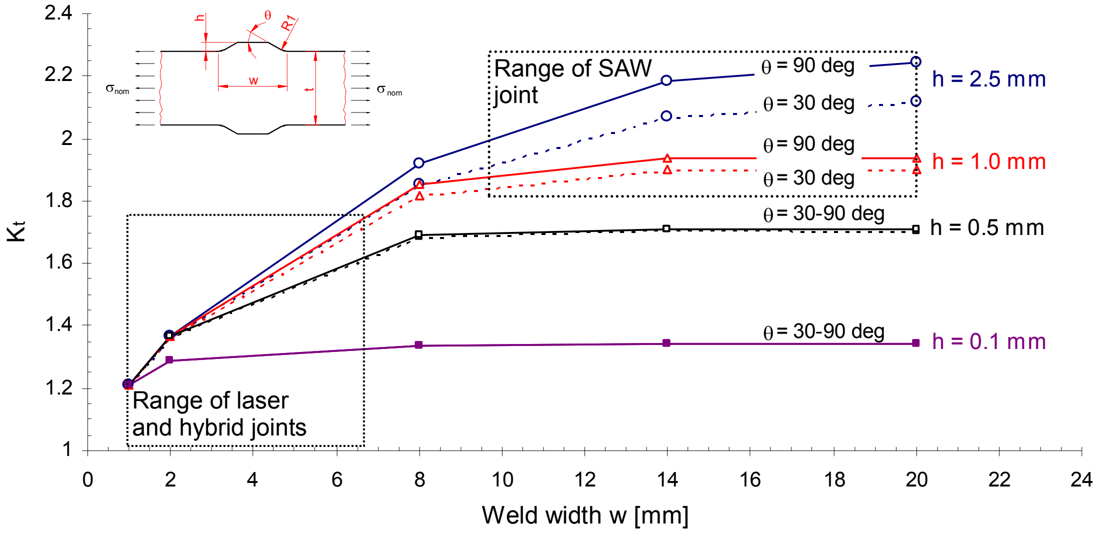

Figure 61: K_t versus weld width w for different weld height h and flank angle θ.

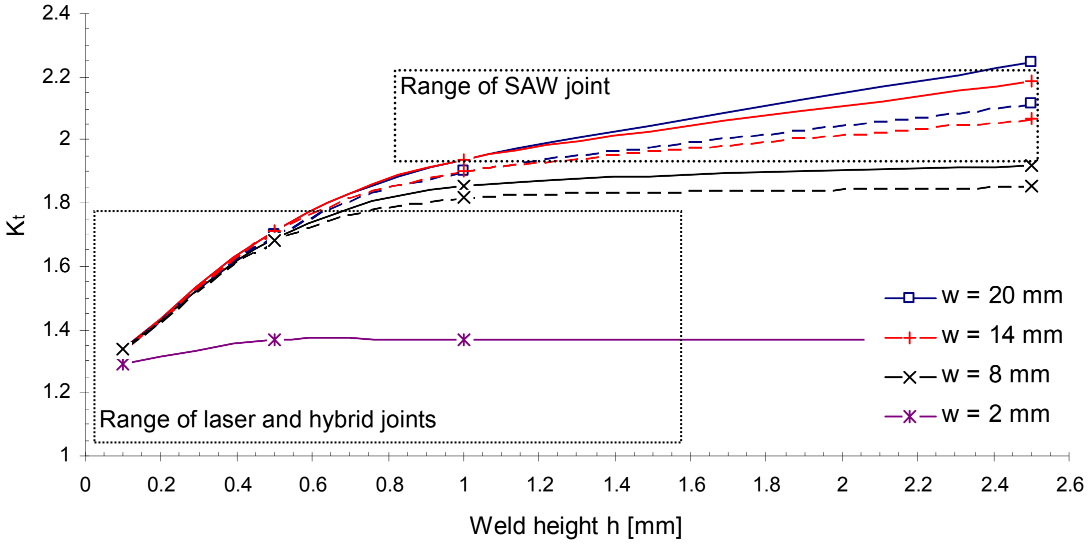

Figure 62: K_t versus weld height *h* for different weld width *w*. The flank angle θ of 30° (dashed line) and 90° (continuous line) are also presented.

The influence of the notch geometry on K_t (Model B) is presented in Figures 63 and 64. In the case of the notch with the opening angle β smaller than 130°, the notch depth *D* and the root radius ρ dominated. When the notch with the constant radius equal to 1 mm was considered, the effect of the notch depth *D* appeared the most important. When the opening angle was smaller than 130°, it had an insignificant effect on K_t. The lower values of the notch radius had a strong effect, but above the value of 0.6 mm the effect was reduced.

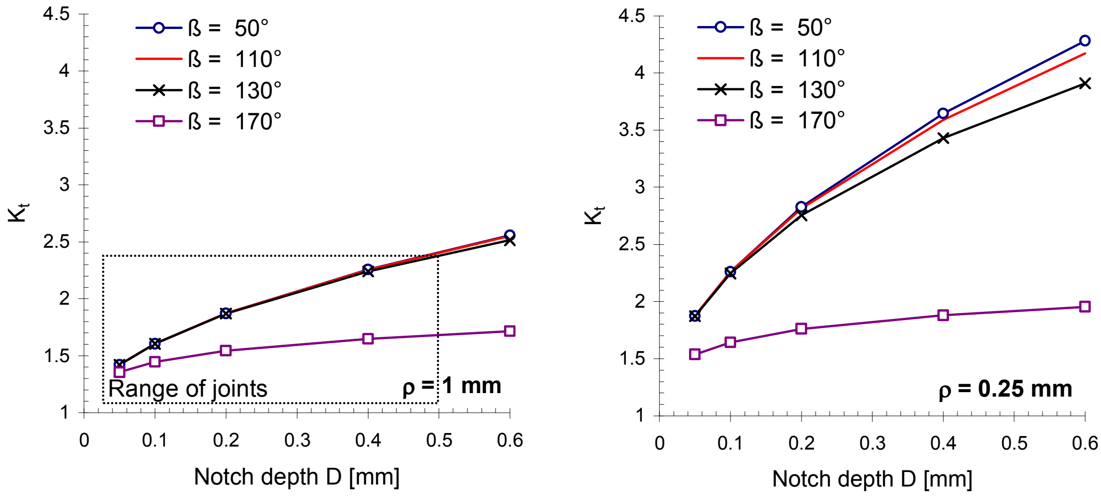

Figure 63: Influence of notch depth *D* on K_t for Model B with notch radius ρ of 1 mm (left) and 0.25 mm (right).

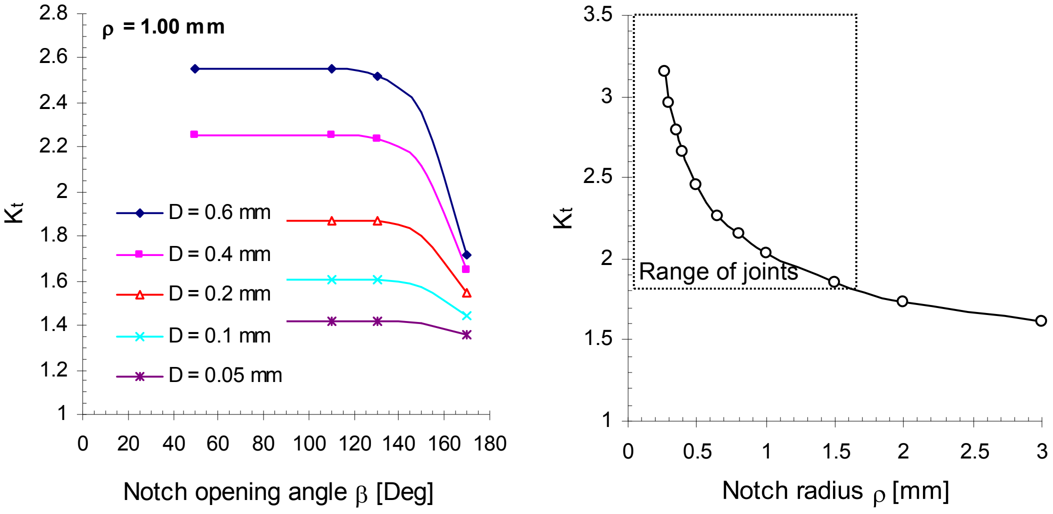

Figure 64: Influence of opening angle β (left) and notch root radius ρ (right) on K_t for Model B.

In summary, the present study showed that the notch depth D has a strong influence on K_t. Inside the range of the measured values of the welded joint, K_t varied from 1 to 2.25 for the notch radius of 1 mm. Correspondingly, the variation of K_t due to the dimensions of the weld bead was 1-1.8 for the Laser and Hybrid joint and 2 - 2.25 for the SAW. The effect of the notch opening angle was weakly negative.

The semi-analytical formula was developed to describe the quantitative influence of the different weld dimensions on K_t. The formula was divided into two parts, covering the effects caused by the weld bead $K_{t,w}$ and by the notch $K_{t,n}$, see Eqs. (53) and (54). The analytical formulae of $K_{t,w}$ and $K_{t,n}$ are based on the literature (Lawrence *et al.* 1981; Yung and Lawrence 1985; Anthes *et al.* 1993) and were further developed with the help of the linear FE analysis, see Appendix F.

The formula for $K_{t,w}$ based on the literature (Anthes *et al.* 1993) was enlarged to also cover the geometry of the laser-based joints. The effects of weld width and height were added and the stress concentration factor $K_{t,w}$ based on the regression analysis is expressed by

$$K_{t,w} = 1 + \left(\frac{h}{t}\right)^{0.30} \cdot \left(\frac{w}{t}\right)^{0.30} \cdot \sin\left(\frac{\theta}{t}\right)^{0.30} \cdot \left(\frac{t}{\rho}\right)^{0.32} . \tag{53}$$

The results given by this formula are compared to those of the FE analysis in Figure 65.

The 10% error bounds are also presented with dashed lines. The present formula showed a good agreement with the FEA results as the correlation between these results was $R = 0.966$.

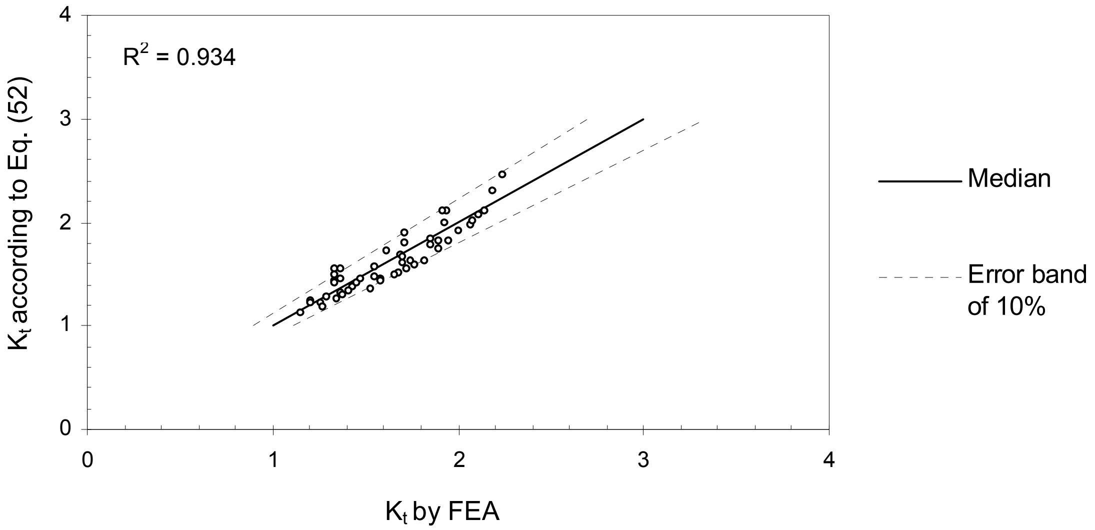

Figure 65: Comparison of K_t obtained by the FEA and by the regression formula Eq. (53) in the case of Model A.

The formula of $K_{t,n}$ is based on the equation developed for U-shaped notches (Lawrence *et al.* 1981). The original formula was further developed to include the effect of the notch opening angle β with the parameter k_β

$$K_{t,n} = 1 + 2 \cdot k_\beta \cdot \left(\frac{D}{\rho}\right)^{0.54}, \tag{54}$$

where k_β is

$$k_\beta = 1 - \left(\frac{\beta}{180°}\right)^{10} \cdot \left(\frac{D}{\rho}\right)^{0.25}. \tag{55}$$

The results of the regression formula for $K_{t,n}$ are compared to those of the FEA in Figure 66. The 5% error bounds are presented with dashed lines. The present formula showed a good agreement with the FEA results, as the correlation was 0.999.

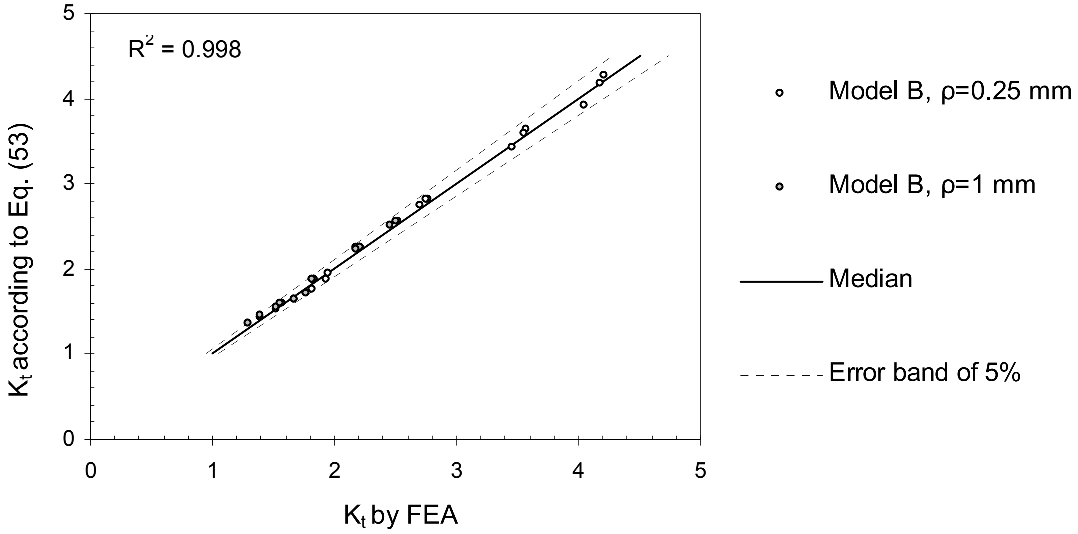

Figure 66: Comparison of K_t obtained by the FEA and by the regression formula Eq. (54) in Model B.

In order to develop the K_t formula including $K_{t,w}$ and $K_{t,n}$, two additional parameters were needed. With help of the regression analysis of the results from the FE analysis, the effective notch radius ρ_e is

$$\rho_e = \rho \cdot \left[1 + 16 \cdot \left(\frac{D_1}{\rho} \right)^{1.12} \right], \tag{56}$$

and, correspondingly, the effective notch opening angle β_e is

$$\beta_e = 180° - \theta - 2 \cdot \gamma \,. \tag{57}$$

These two parameters took into account the cross-correlation between the stress concentration due to the weld bead and notch. Thus, the formula of K_t for welded joints, including sharp notches, is expressed by

$$K_t = K_{t,w}\left(h, w, \theta, \rho_e\right) \cdot K_{t,n}\left(D_1, \beta_e, \rho\right). \tag{58}$$

Figure 67 shows the comparison of K_t by the FEA and by the regression formulas. The results were within 15% error bounds and the correlation number R was 0.99.

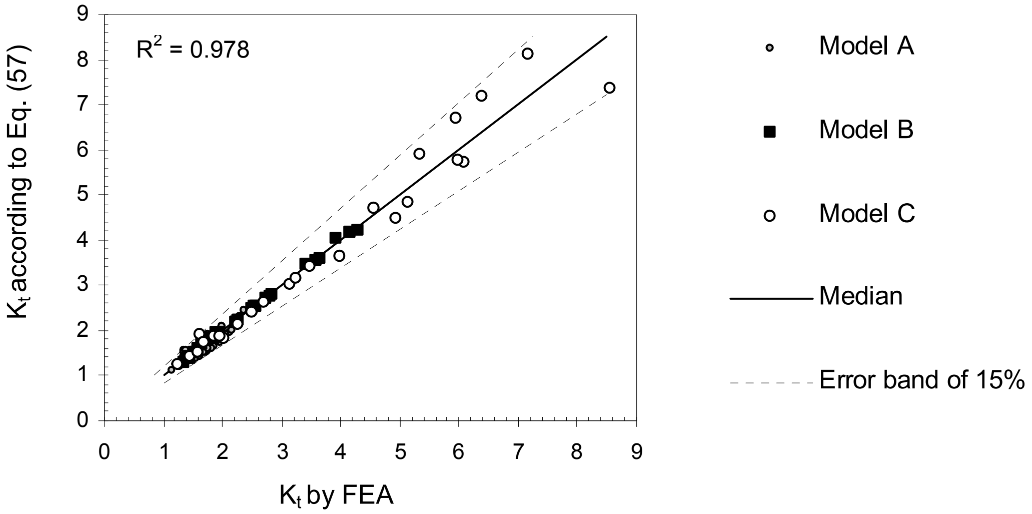

Figure 67: Correlation between the regression formula Eq. (58) and the FEA for different weld geometries given in Table 21.

To predict the fatigue life of welded joints with varying weld geometry requires the determination of the critical weld geometry giving the highest value of the stress concentration factor K_t at the weld notch. When the correlation between the geometrical dimensions occurred, a semi-analytical regression formula for K_t given in Eq. (58) was needed. An important fact was that the formula was also applicable in the case of laser-based joints. The critical geometry for each type of studied weld is given in the next chapter. There the comparison between calculated and measured fatigue lives is also presented.

7 FATIGUE LIFE PREDICTION FOR WELDED BUTT JOINTS

7.1 Outline of theoretical modelling

The life predictions of the macro crack initiation and propagation for the different welded butt joints were calculated using the new theory given in Chapter 4. These results were validated by the measured values presented in Section 2.5. The results from the miniature tests with notched specimens and those from the joint tests with welded-plate specimens were applied to validate macro crack initiation life and the latter tests results also applied to the total fatigue life. In the case of welded-plate specimens, it was required to determine the critical weld geometry for each type studied joint. This geometry was obtained by maximising the stress concentration factor in the space of the measured geometrical dimensions of the weld.

The linear FEM was used to determine the stress and strain distributions at the weld notches. In the analysis, plane strain elements were applied to the welded-plate specimens and correspondingly the axisymmetric solid elements to the miniature specimens. The effect of the axial and angular misalignments was considered separately, using the analytical formulae presented in Chapter 4. The secondary bending stress σ_{sb^*} due to the gripping of the welded-plate specimen was determined with the help of the strain gauge measurements (Remes 2003) and the FE analysis.

According to the experimental observations, the crack initiation in the weld joints was assumed to occur along the borderline between the weld metal and the HAZ, from where the crack propagated through the HAZ to the parent material. Thus, the value of the Vickers Hardness for the HAZ at the weld notch was used to estimate the stress-strain curve and the fatigue strength coefficients.

The propagation life of the macro crack for the welded-plate specimens was estimated on the basis of the linear elastic fracture mechanics, where the stress intensity factors ΔK_I are given in Neyman and Raju (1981; 1983). An elliptical crack was used with material parameters given in British Standard 7608 (1993). The crack growth coefficient C was $3 \cdot 10^{-13}$ Nmm$^{3/2}$ and the crack growth exponent n was equal to 3. The value of the threshold stress intensity factor ΔK_{th} = 240 N/mm$^{3/2}$ was applied according to Radaj (1995). The critical crack length corresponding to the final fracture is based on the limit load theory. According to the measurements, the crack propagation life of miniature specimens was very short, reaching only a few percent of the total fatigue life, and therefore this was not considered.

7.2 Critical weld geometry

The weld geometry varied even inside one welded-plate test specimen, thus the approach to specify the worst weld geometry in relation to fatigue strength was chosen. This critical weld geometry was determined applying an optimisation procedure shown in Figure 68. The critical weld geometry was defined by maximising the value of K_t in Eq. (58), taking into account the macro-support effect of the material for fatigue (Radaj 1990). Thus, this simplified analysis was carried out with the help of the concentration factor K_t based on the fictitious notch radius

$$\rho_f = \rho + 1 \text{ mm.} \tag{59}$$

The constraints of this maximising problem were composed of the limit values of the measured geometrical dimensions and also of the upper and lower bounds of the regression models with 5% and 95% probability, discussed in detail in Chapter 5. An additional constraint for the flank angle was applied

$$\theta \geq \arctan\left(\frac{2 \cdot h}{w}\right). \tag{60}$$

The maximum value of K_t and the corresponding critical weld geometry were calculated iteratively using the gradient-based optimisation method with several initiation points. These results were verified by the genetic algorithm Gallops (Goodman 1996).

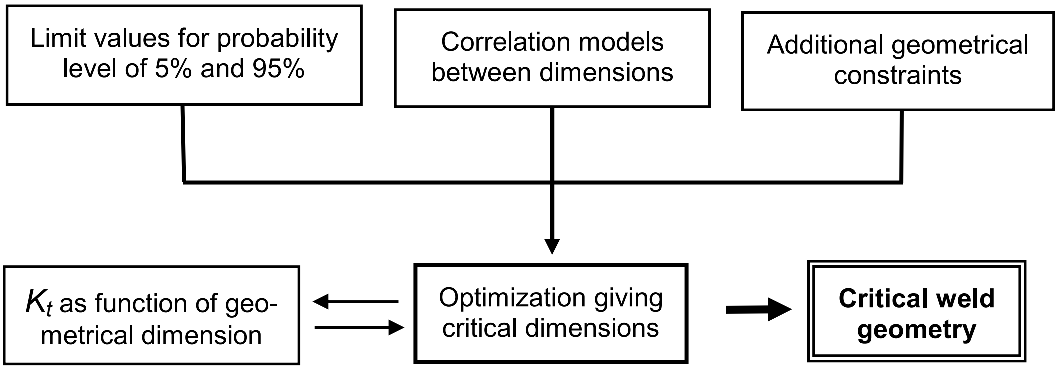

Figure 68: Flow chart of the statistical approach to determine the critical weld geometry.

The results, i.e. solutions to the optimisation problems, are given in Tables 22 and 23 for the weld toe and root sides, and additionally illustrated in Figures 69 and 70. In these tables, the values of $K_{t,c}$, corresponding to the critical weld geometry, are shown. The upper bound $K_{t,max}$, based on the limit values of the geometrical dimensions, is also given. The effects of the correlations between the dimensions were left out. The results indicate that the correlation effects on K_t are small, as the difference between $K_{t,c}$ and $K_{t,max}$ is less than 10%. However, the $K_{t,c}$ based critical weld geometry differed between 10% and 40% from that based on the mean values of the weld dimensions, see Table 24.

Table 22: Dimension of critical weld geometries for the weld toe side

Joint	Value	K_t	h	w	θ	D_1	D_2	γ	β	ρ
SAW	$K_{t,max}$	2.54	2.5	19.5	34.3	0.017	0.060	17.1	112.3	0.019
	$K_{t,c}$	2.48	2.5	17.0	34.3	0.017	0.059	17.1	123.4	0.021
Laser	$K_{t,max}$	2.43	0.5	3.7	29.7	0.264	0.282	54.5	80.1	0.039
	$K_{t,c}$	2.24	0.5	3.7	16.7	0.237	0.198	39.0	101.5	0.139
Hybrid LF	$K_{t,max}$	2.16	0.8	6.4	40.0	0.061	0.121	18.0	104.0	0.036
	$K_{t,c}$	1.96	0.8	6.4	40.0	0.024	0.004	4.6	134.4	0.036
Hybrid MF	$K_{t,max}$	1.95	1.0	6.7	21.8	0.032	0.043	23.0	117.6	0.047
	$K_{t,c}$	1.95	1.0	6.5	21.8	0.032	0.013	23.0	131.1	0.047

Table 23: Dimension of critical weld geometries for the weld root side

Joint	Value	K_t	h	w	θ	D_1	D_2	γ	β	ρ
SAW	$K_{t,max}$	2.54	1.9	10.5	27.8	0.091	0.080	65.4	93.2	0.016
	$K_{t,c}$	2.54	1.9	10.5	27.8	0.091	0.020	57.7	93.2	0.016
Laser	$K_{t,max}$	1.95	0.7	1.9	53.6	0.057	0.126	27.4	74.6	0.024
	$K_{t,c}$	1.95	0.7	1.9	53.6	0.057	0.109	27.4	74.6	0.024
Hybrid LF	$K_{t,max}$	2.33	1.8	2.8	90.4	0.060	0.232	30.0	62.6	0.018
	$K_{t,c}$	2.33	1.8	2.8	90.4	0.060	0.050	25.5	62.6	0.018
Hybrid MF	$K_{t,max}$	1.99	1.3	2.2	69.1	0.030	0.076	32.4	90.3	0.027
	$K_{t,c}$	1.99	1.3	2.2	69.1	0.030	0.011	19.7	90.3	0.036

Table 24: Dimension of weld geometries at 50% probability level

Joint		$K_{t,m}$	h	w	θ	D_1	D_2	γ	β	ρ
SAW	Toe	2.20	2.2	18.1	28.9	0.004	0.021	3.9	133.8	0.042
	Root	1.90	1.4	10.0	17.9	0.014	0.027	9.7	134.4	0.099
Laser	Toe	1.46	0.1	2.8	5.8	0.037	0.033	22.9	120.2	0.229
	Root	1.65	0.5	1.7	38.8	0.022	0.034	13.2	95.6	0.069
Hybrid LF	Toe	1.49	0.5	5.8	14.5	0.007	0.036	3.9	140.8	0.272
	Root	1.60	0.6	1.4	59.8	0.010	0.084	3.6	94.4	0.082
Hybrid MF	Toe	1.64	0.9	6.4	18.4	0.007	0.010	6.8	143.1	0.256
	Root	1.59	0.7	1.9	47.2	0.008	0.018	7.5	108.7	0.126

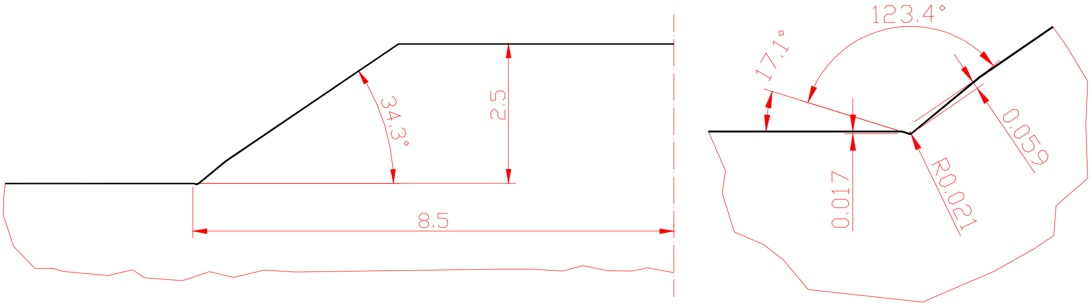

SAW joint

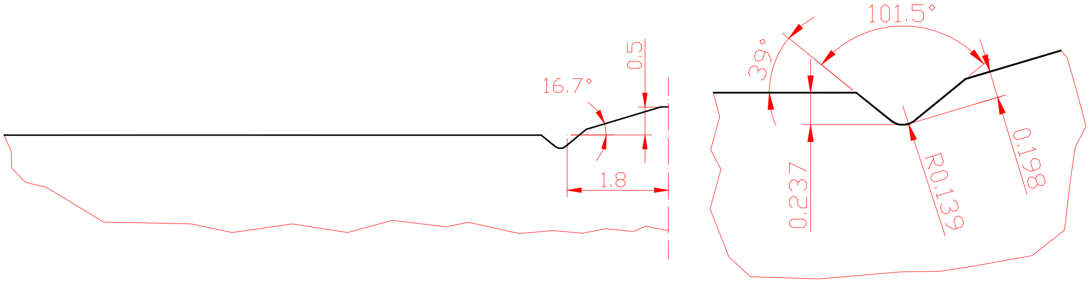

Laser weld

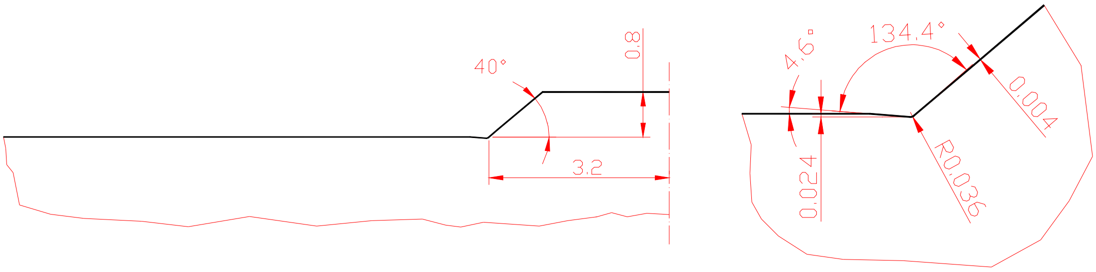

Hybrid LF weld

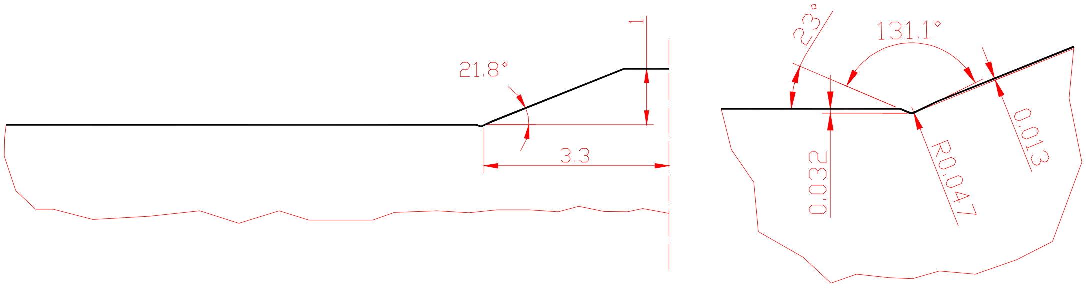

Hybrid MF weld

Figure 69: Critical weld toe geometries for different welds.

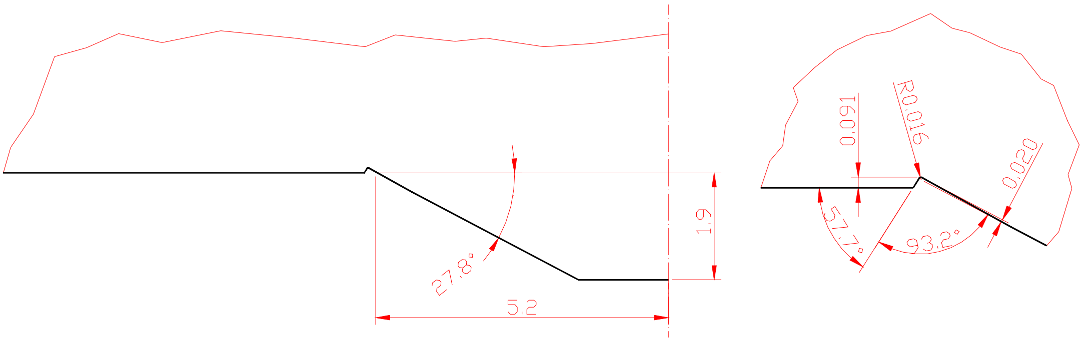

SAW joint

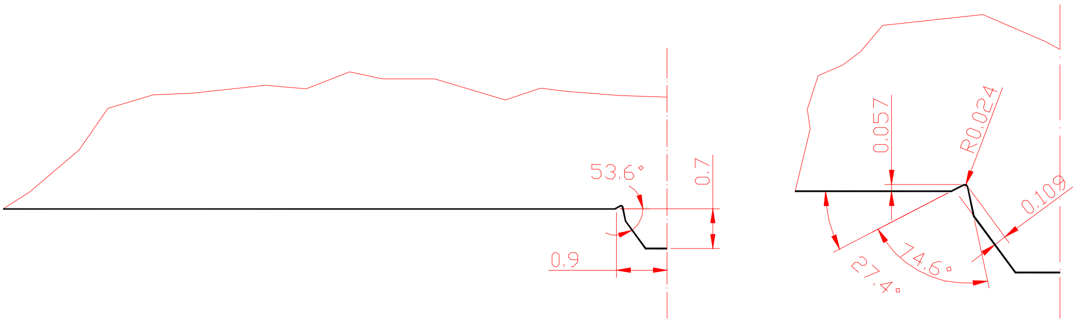

Laser weld

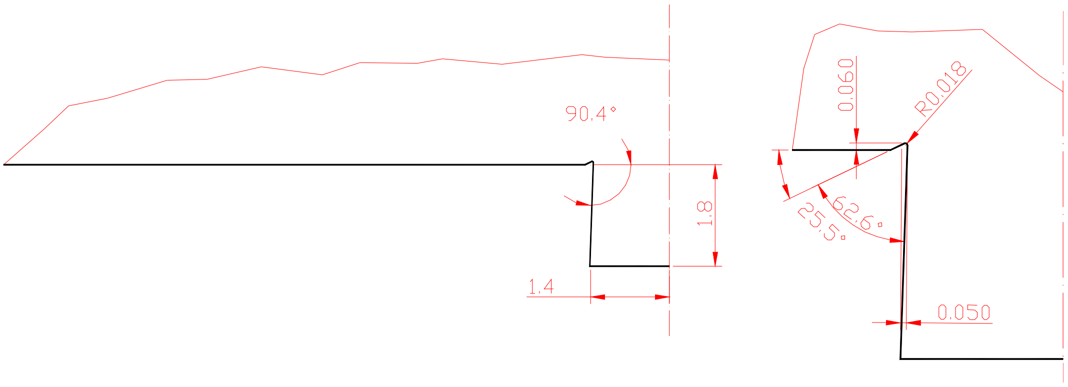

Hybrid LF weld

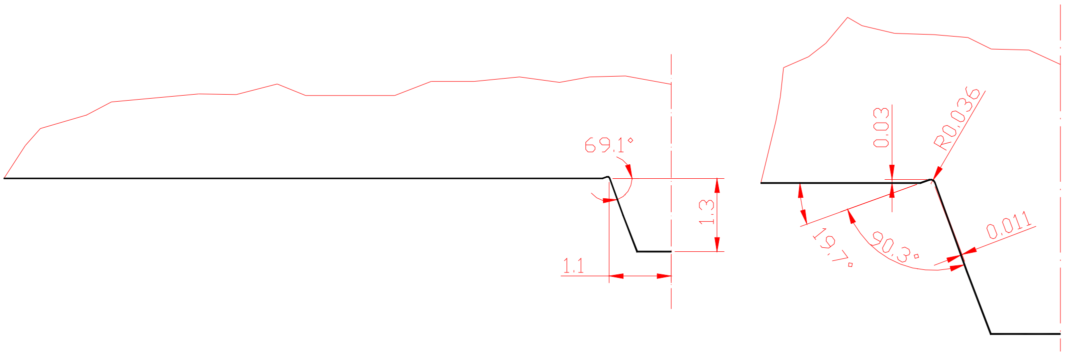

Hybrid MF weld

Figure 70: Critical weld root geometries for different welds.

7.3 Comparison of the calculated and experimental fatigue life

7.3.1 Macro crack initiation

Figure 71 presents the predicted and measured life of the macro crack initiation for the notched miniature specimens. In the figure, the predicted life was plotted against that measured in the logarithmic scale. The continuous line shows the complete equivalence. The bounds of the scatter band with a factor of three are plotted with dashed lines. In the case of the HAZ of Laser weld, the life prediction was calculated using the hardness value equal to 215 HV5 for the HAZ and the mean value between the weld metal and the parent material equals 184 HV5. The latter value concerns the case with the micro notch at the borderline of the HAZ, due to the limited accuracy of the machining. In general, Figure 71 indicates a good correlation between the predicted and measured life, as the scatter band covers 95% of all the points.

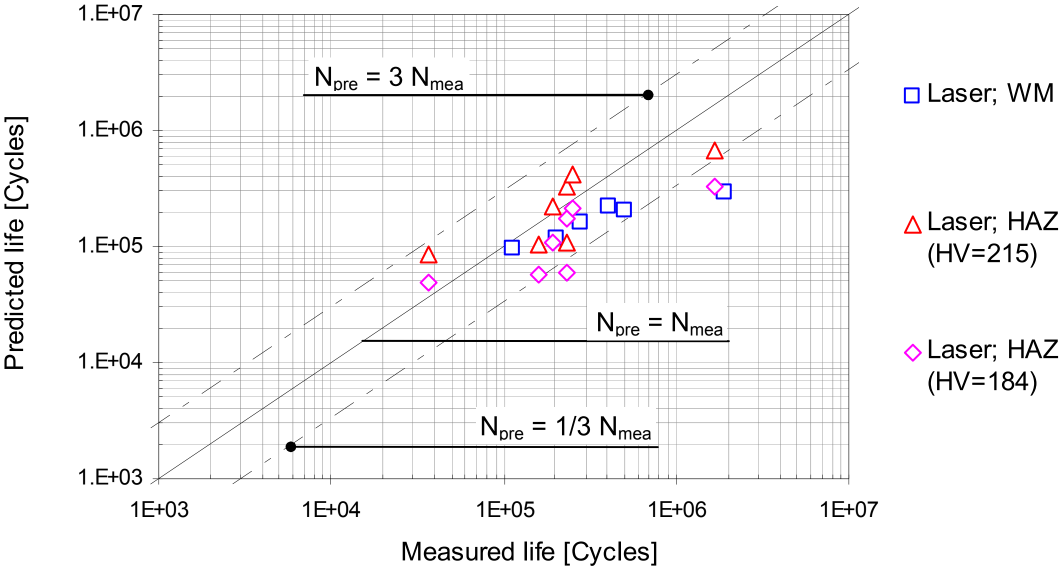

Figure 71: Comparison of the predicted and measured values of the initiation life of a macro crack in the case of notched miniature specimens.

The comparison of the initiation life N_i for the welded-plate specimens, including both Types A and B, is represented in Figure 72. Table 25 presents the numerical values of the loading and the initiation life with the scatter factor s. This factor shows the maximum value of the ratio $N_{i,mea}/N_{i,pre}$ or its inverse. This factor simplifies the comparison. The higher s value indicates a higher discrepancy between the measured and predicted values. In the case of the SAW and the Hybrid MF joints, a good correlation between the predicted and measured life was observed, as the bounds of the scatter band with a factor of 3 covered 90% of the data points. This correlation was only slightly lower than that of the notched miniature specimens. The correlation of the Laser and Hybrid LF welded joints was somewhat lower and the scatter band with a factor of 3 covered 62% of the points. This scatter value transformed to the *S-N* curve gave about 10% difference between the measured and the predicted values in the stress range. Thus, this validation based on the *S-N* curve outlines more clearly the real situation. Figure 73 shows the *S-N* curve of the Laser welded joint, where the difference in the initiation life between the measured and the predicted values was the largest.

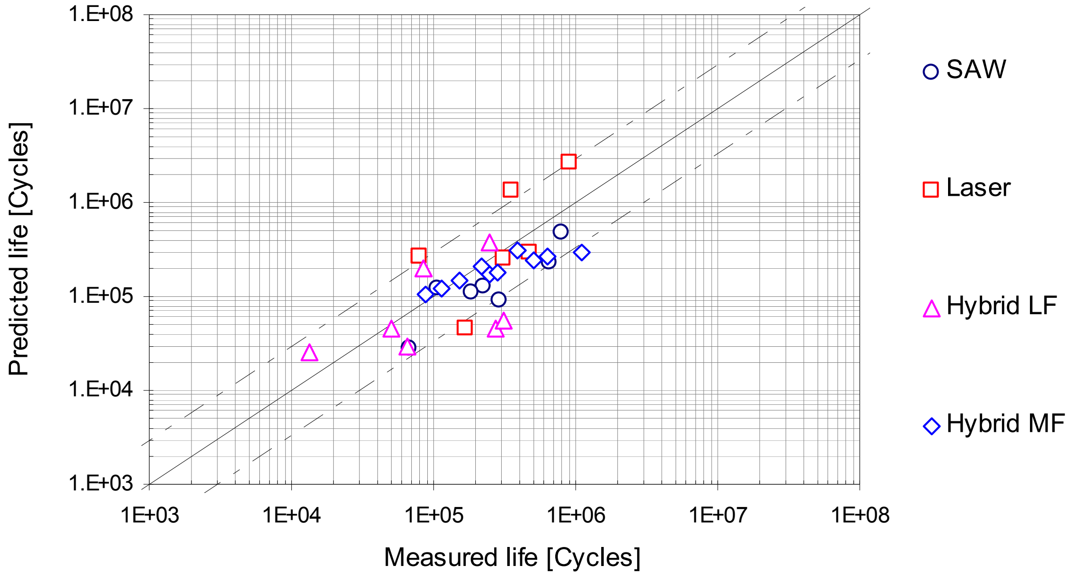

Figure 72: Comparison between the measured and the predicted values of the initiation life of a macro crack in the case of welded-plate specimens.

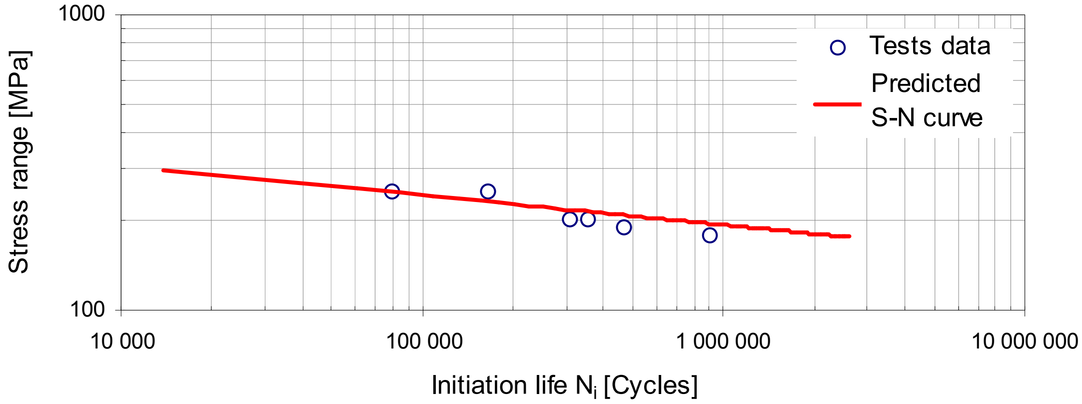

Figure 73: Comparison of the test data and the predicted *S-N* curve of the initiation life N_i of a macro crack in the case of Laser welded-plate specimens.

Table 25: Loading parameters and macro initiation life N_i for the welded-plate specimen

Test specimen		$\Delta\sigma_{nom}$	k_m[1]	σ_{sb^*}	Failure	Initiation life N_i		
Joint	Type	[MPa]	[-]	[MPa]	location	Measured	Predicted	s
SAW	Type A	249	1.00	-52	Toe	106 926	116 054	1.1
	Type A	201	1.00	-47	Toe	798 377	494 567	1.6
	Type A	269	1.05	63	Root	66 907	28 118	2.4
	Type A	252	0.98	-55	Toe	224 550	122 120	1.8
	Type A	200	1.04	63	Root	662 127	231 638	2.9
	Type A	224	1.04	59	Root	187 093	104 592	1.8
	Type A	226	1.05	63	Root	292 013	69 185	4.2
	Type A	184	1.06	63	Root	1 051 716	356 949	2.9
Laser	Type B	179	1.02	0	Root	903 702	3 323 462	3.7
	Type B	190	1.14	0	Toe	473 971	292 684	1.6
	Type B	251	1.11	0	Toe	165 587	46 323	3.6
	Type B	249	0.99	0	Root	80 482	185 190	2.3
	Type B	201	0.98	0	Root	359 896	1 684 118	4.7
	Type B	201	1.09	0	Toe	312 472	255 816	1.2
Hybrid LF	Type A	180	1.30	204	Toe	86 312	241 820	2.8
	Type A	251	1.23	162	Toe	50 141	52 755	1.1
	Type A	150	1.36	274	Toe	244 899	457 900	1.9
	Type B	269	1.29	0	Toe	13 344	28 646	2.1
	Type B	263	1.27	0	Toe	65 309	33 475	2.0
	Type B	247	1.25	0	Toe	270 320	51 610	5.2
	Type B	253	1.17	0	Toe	309 832	64 258	4.8
Hybrid MF	Type A	252	1.03	-49	Root	150 284	169 481	1.1
	Type A	264	1.02	-55	Root	114 385	134 559	1.2
	Type A	242	1.04	-37	Root	248 327	200 325	1.2
	Type A	226	1.04	-40	Root	631 416	303 115	2.1
	Type A	235	1.04	-39	Root	216 319	236 551	1.1
	Type A	218	1.05	-35	Root	388 620	347 717	1.1
	Type A	260	1.06	-29	Root	88 944	118 136	1.3
	Type A	239	1.05	-34	Root	278 631	207 721	1.3
	Type A	218	1.05	-29	Root	1 099 313	340 276	3.2
	Type A	230	1.04	-39	Root	514 335	272 724	1.9

[1] The factor corresponded to the surface where the crack initiated

7.3.2 Total fatigue life

The total fatigue life N_f is composed of the macro crack initiation and propagation life. Figure 74 presents the predicted and the measured values of the propagation life for the welded-plate specimens. In general, the figure indicates a good agreement between the values, as the bounds of the scatter band with a factor of 3 cover all the points.

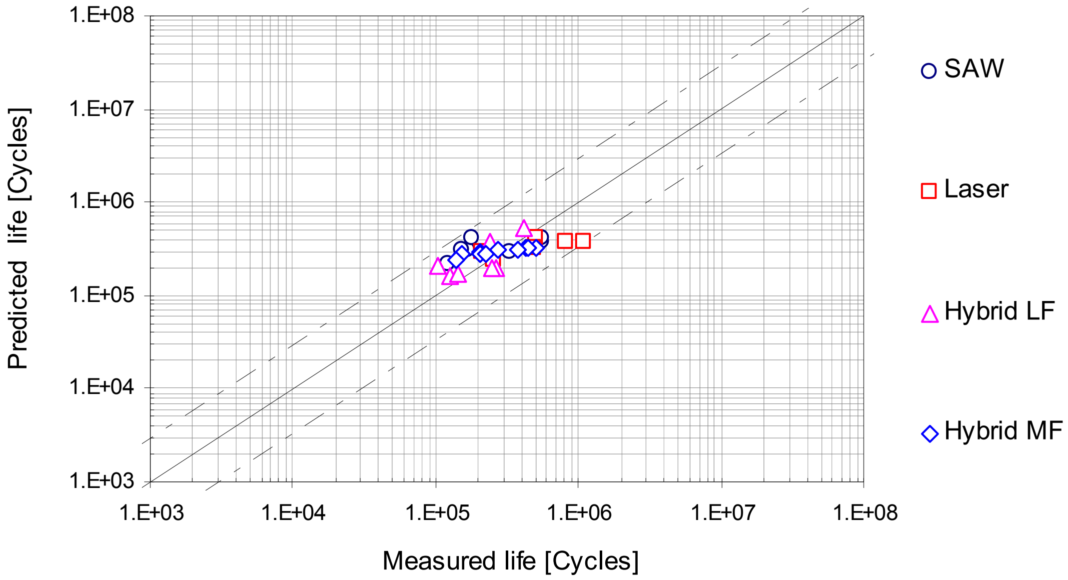

Figure 74: Comparison of the predicted and the measured values of the propagation life of a macro crack in the case of welded-plate specimens.

The total fatigue life of the welded-plate specimens is given in Figure 75, where the bounds of the scatter band with a factor of 3 cover all the points. No significant difference in the correlation was observed due to different joint types or load levels.

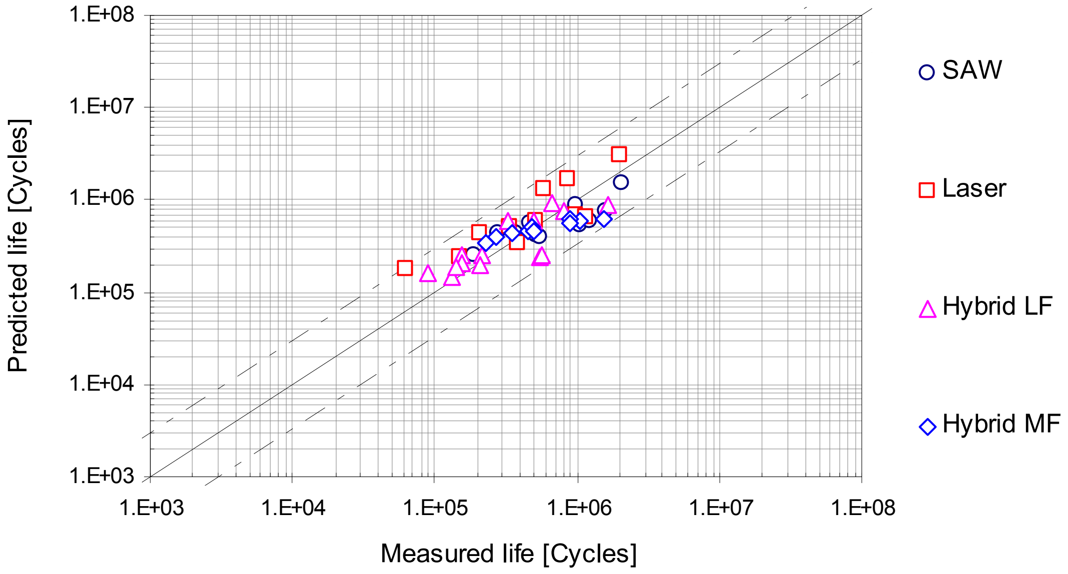

Figure 75: Comparison of the predicted and the measured values for the total fatigue life in the case of welded-plate specimens.

The numerical values of the measured and the predicted fatigue life N_f are represented in Table 26. The last column shows the scatter factor *s* having values from 1.0 to 2.5, which is an indication of excellent correlation. The table gives also the ratio of the initiation N_i and the fatigue life N_f. This ratio shows an increasing trend as the function of the fatigue life N_f both for the measured and the predicted values, see also Figure 76.

Table 26: Comparison of the measured and the predicted total fatigue life N_f for the welded-plate specimen

Test specimen		Failure	Fatigue life N_f		N_i/N_f ration		Scatter
Joint	Type	location	Measured	Predicted	Measured	Predicted	*s*
SAW	Type A	Toe	277 963	429 239	0.38	0.28	1.5
	Type A	Toe	979 349	881 464	0.82	0.54	1.1
	Type A	Root	189 524	249 746	0.35	0.11	1.3
	Type A	Toe	376 019	436 712	0.60	0.29	1.2
	Type A	Root	1 217 355	592 168	0.54	0.38	2.1
	Type A	Root	516 276	411 630	0.36	0.27	1.3
	Type A	Root	549 004	387 382	0.53	0.23	1.4
	Type A	Root	1 611 693	751 116	0.65	0.44	2.1
Laser	Type B	Root	1 982 415	2 989 316	0.46	0.87	1.5
	Type B	Toe	984 909	700 018	0.48	0.42	1.4
	Type B	Toe	380 053	345 657	0.44	0.13	1.1
	Type B	Root	334 617	505 167	0.24	0.52	1.5
	Type B	Root	849 199	1 689 623	0.42	0.81	2.0
	Type B	Toe	1 138 300	639 692	0.27	0.40	1.8
Hybrid LF	Type A	Toe	327 584	584 797	0.26	0.35	1.8
	Type A	Toe	154 927	255 000	0.32	0.18	1.6
	Type A	Toe	662 864	907 740	0.37	0.42	1.4
	Type B	Toe	140 088	187 866	0.10	0.13	1.3
	Type B	Toe	210 665	201 534	0.31	0.15	1.0
	Type B	Toe	539 280	240 881	0.50	0.19	2.2
	Type B	Toe	560 784	252 397	0.55	0.22	2.2
Hybrid MF	Type A	Root	354 052	435 348	0.42	0.34	1.2
	Type A	Root	267 320	394 821	0.43	0.30	1.5
	Type A	Root	451 699	458 980	0.55	0.38	1.0
	Type A	Root	1 057 498	585 575	0.60	0.45	1.8
	Type A	Root	487 091	508 318	0.44	0.41	1.0
	Type A	Root	888 604	630 903	0.44	0.48	1.4
	Type A	Root	229 253	341 895	0.39	0.30	1.5
	Type A	Root	502 035	464 892	0.56	0.39	1.1
	Type A	Root	1 546 593	614 352	0.71	0.48	2.5
	Type A	Root	892 600	548 998	0.58	0.43	1.6

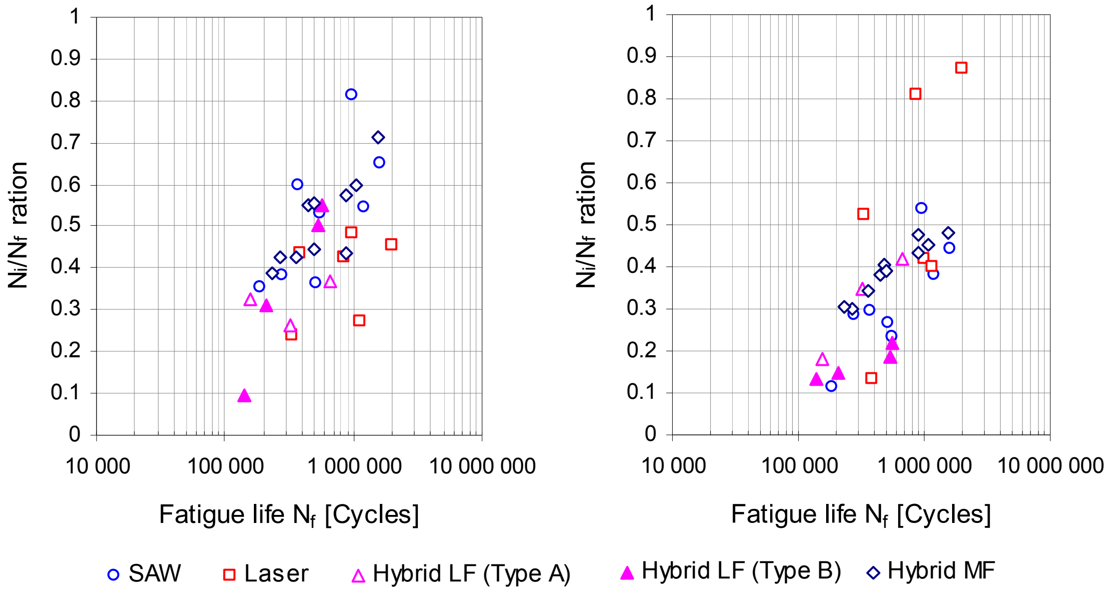

Figure 76: Ratio N_i/N_f versus the measured (left) and the predicted (right) fatigue life.

Figure 77 represents the comparison of the predicted *S-N* curves and the fatigue test results for different welded-plate specimens. Generally, a good agreement between these values was found. The comparison of the fatigue resistance of the Hybrid LF welded specimens between Type A and B reveals the proper prediction of the mean stress effect to obtain a satisfactory correlation. The maximum difference between the predicted and the measured values was observed in the case of the Hybrid LF and MF joints to be close to the endurance limit. The numerical values of the FAT$_{50\%}$ and of the slope of the *S-N* curve determined from the measured and the predicted values are presented in Table 27. The average difference was 10% for the FAT$_{50\%}$. Greater differences were observed in the slope values that were sensitive to the number of the measured points and their scatter.

Table 27: Comparison of the measured and the predicted *S-N* curves for the total fatigue life of the welded-plate specimen

Welded sample	Specimen Type	FAT$_{50\%}$		Slope *m*	
		Measured	Predicted	Measured	Predicted
SAW	A	180	168	5.8	4.1
Laser	A, B	174	186	5.8	7.3
Hybrid LF	A	129	110	3.7	2.5
	B	238	205	27.8	9.6
Hybrid MF	A	208	173	9.6	4.4

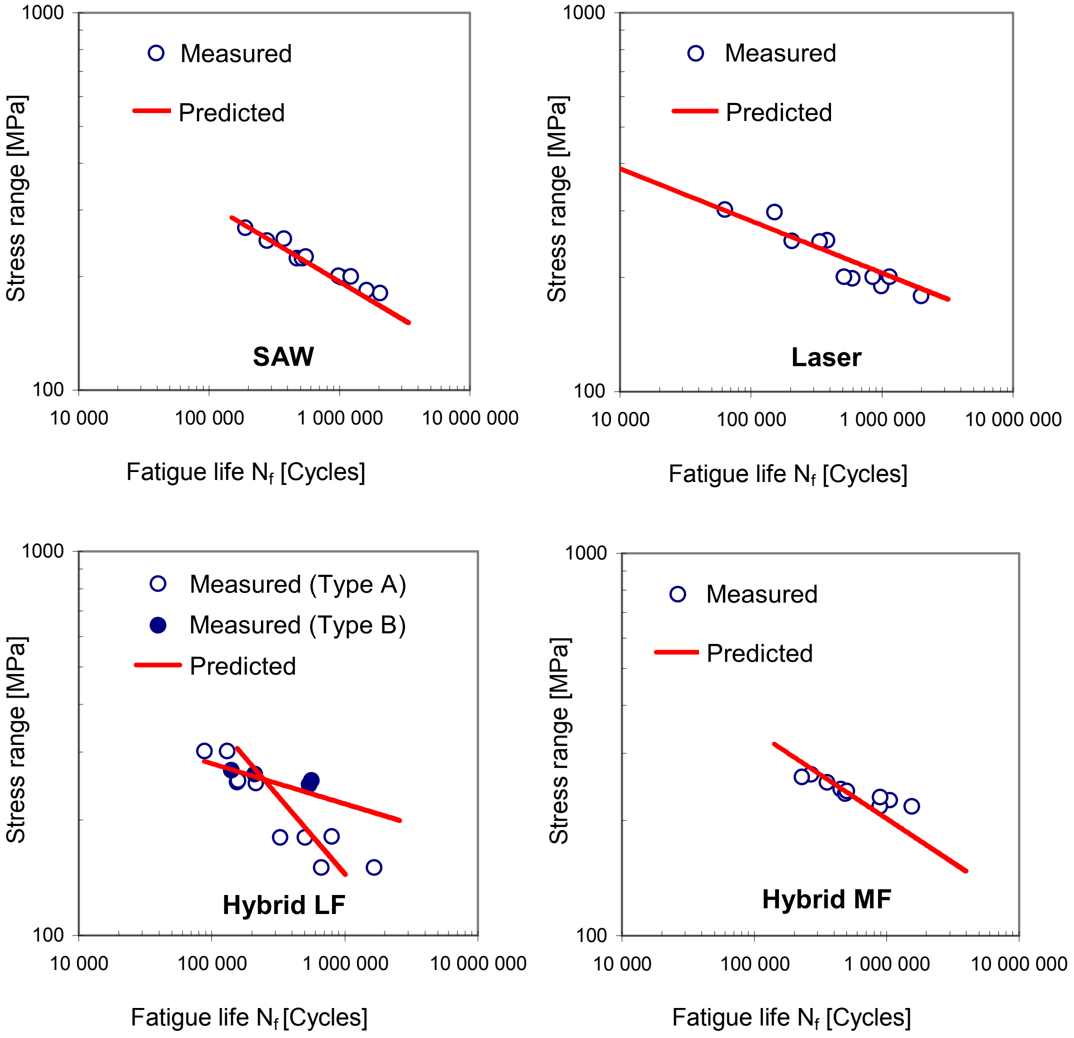

Figure 77: Comparison of the measured fatigue test results and the predicted *S-N* curves for different welded-plate specimens.

7.4 Comparison of the new and the existing strain-based approach

In the present fatigue model, the initiation period was assumed to consist of several discrete growth steps of a short crack up to the threshold size of the macro crack. The length of these discrete growth steps, as well as the averaging distance of the notch stresses and strains, corresponded to the grain size of material microstructure. This approach differs from the existing strain-based approaches to welded joints. In the following, the new and an existing strain-based approach are compared.

In the existing strain-based approach, the macro crack initiation is modelled with one growth step. Additionally, the averaging distance for notch stresses and strains is based on material strength. Taylor (1999) shows that the different existing averaging methods (Siebel and Stieler 1955; Peterson 1959; Neuber 1968) are equivalent to the approach based on the fracture mechanics (El Haddad *et al.* 1979), where the averaging distance a_o is expressed by

$$a_o = \frac{1}{\pi}\left(\frac{\Delta K_{th}}{\Delta \sigma_o}\right)^2 , \tag{61}$$

where $\Delta\sigma_0$ is the fatigue strength at 2 million load cycle for a smooth specimen. In the comparison, the averaging distance was based on the stress intensity factor ΔK_{th} of 240 N/mm$^{3/2}$ and the fatigue strength $\Delta\sigma_0$ obtained from the Coffin-Manson equation, see Eq. (36), ignoring the plastic part due to the low value in the endurance limit.

Figure 78 presents the predicted and the measured values for the macro crack initiation of welded-plate specimens for both approaches. The results of the new approach are copied from Figure 72 to make it easier to compare the approaches. The results produced by the existing approach showed poorer results than the new approach. In the case of the SAW joint, the prediction with the existing approach also gave satisfactory results.

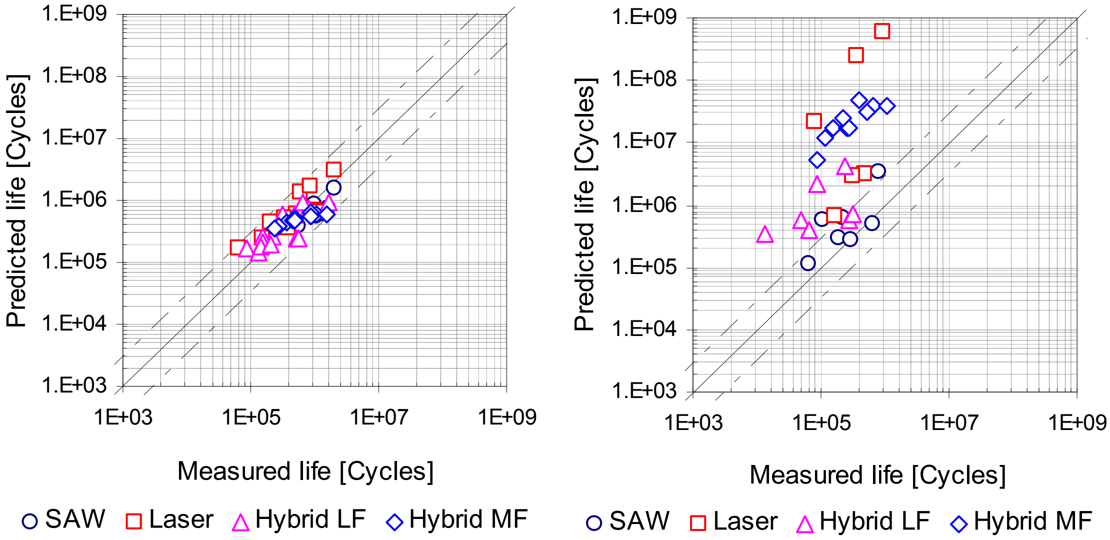

Figure 78: Comparison of the predicted and the measured values for the initiation life of a macro crack in the case of welded-plate specimens using the present (left) and the existing approach (right).

8 SUMMARY AND CONCLUSIONS

8.1 Fatigue strength assessment of laser-based joints

In this work, a new strain-based approach to fatigue strength assessment was developed. Additionally, extensive experimental and theoretical investigations on the fatigue damage processes in laser- and hybrid-welded butt joints were carried out. In the following, the results of general interest are briefly discussed. The focus is on the issues crucial for the theoretical modelling of the fatigue strength of welded joints.

The size of laser weld is significantly smaller than that of arc-welded joints. The results of the present study clearly show that this affects the relation between the geometrical dimensions of the weld and stress concentration factor K_t at the weld notch. For the arc-welded joints, Anthes *et al.* (1993; 1994) show that the weld flank angle of the weld bead has the most important effect on the notch stresses. The results of the present study confirm this for the arc-welded joints. However, the present results for the laser-based joints indicate that the notch depth and its root radius are the most important, while the flank angle has a much lesser effect. The reason for this difference between the arc-welded and laser-based joints can be found in the smaller size of the weld bead. Consequently, in the present work, the existing K_t formula for the arc-welded joints was further developed to be applicable to the laser-based joints also.

The values of geometrical dimensions of welded joints had a large statistical variation. Thus, to predict the actual fatigue life of joints required the determination of the critical weld geometry giving the highest value of the stress concentration factor K_t at the weld notch. Because of the large variation of the weld notch geometry, even in the case of one test specimen, the critical weld geometry remained obscure in relation to the stress concentration factor. The statistical analysis showed the correlation between the notch depth and its radius to be similar to the results reported by Petershagen (1990) for the arc-welded joints. In this work, the correlations between other dimensions were also noticed. However, the results indicate that the correlation between the geometrical dimensions had an insignificant effect on the critical weld geometry, as the stress concentration factors K_t, defined with and without the correlation models, were almost equal. An interesting result was also that the K_t, based on the critical and on the mean weld geometry varied from 10% to 40% for different welded joints. Consequently, this result indicates that the use of the critical weld geometry for fatigue analysis would improve the accuracy of the predictions compared to the existing approach, which is based on the mean geometry suggested by Köttgen *et al.* (1991).

For the laser-based joints, the mechanical properties within the joint varied strongly, complicating the calculation of the notch stresses and strains. This variation, i.e. material inhomogeneity, in the laser and hybrid welds led to radical differences in the strength properties between the weld and parent material. However, the simplified response calculation based on Neuber's rule proved to give sufficiently accurate results when a two-stage approach, based on the structural and local analyses, was applied. The structural analysis, based on the stress-strain curve of the parent material, gave the loading for the weld notch. This loading was applied in the local analysis, where the stress-strain curve of the HAZ close to the weld notch was used.

The results of the advanced fatigue testing proved that the macro crack initiation life formed an essential part of the total fatigue life. Additionally, the difference in the mechanical properties and microstructure of HAZ between the laser-based and arc-welded joints was apparent. Therefore, to obtain a reliable prediction of fatigue life for different welded joints, a new strain-based approach was developed in the present work. There, the initiation period was assumed to consist of several discrete growth steps of the damage up to the threshold of the macro crack. The length of the discrete growth step, as well as the averaging distance of the notch stress and strain, corresponded to the grain size of the material. This differs from the previous studies of welded joints, where the strain-based approach is applied with the assumption of one growth step, see Radaj and Sonsino (1998), for example. Additionally, in the previous studies, the averaging distance is based on the mechanical parameters, such as ultimate strength, hardness or the threshold stress intensity factor of a short crack (Peterson 1959; Neuber 1968; El Haddad *et al.* 1979). The predictions of fatigue life based on the new and on the existing approach showed a significant difference. A considerable improvement between the predicted and measured life was achieved when the averaging distance was based on the averaged grain size defining the smallest crack length, the growth rate of which can be described by the continuum mechanics (Kawagoishi *et al.* 2000). It should be noticed that the other existing approaches have been originally developed for the notch stress approach. Thus, these may be related more to the threshold value of the macro crack propagation and consequently they are not suitable to model the short crack propagation at all. This is especially true in the case of the laser-based joints, due to the fine-grained microstructure. It is generally proven (Dowling 2007) that, in the case of a blunt notch, the existing strain approach based on the stress concentration factor and Neuber's rule gives satisfactory results, due to the fact that the stress gradient inside the threshold length of a macro crack is low. This is not the case with the sharp notch occurring in the welded joints, where the stress gradient is high at the tip of the weld notch. Therefore, in this case, the grain size has to be considered when the effective stress and strain are determined. In the case of small grain size compared to the threshold length of the macro crack, the modelling based on the discrete growth of the short crack was required.

8.2 Conclusions

This work aimed to provide better understanding of the fatigue damage process in the laser-based joints. The main focus was especially on the influence of mechanical and geometrical properties of the weld notch on the macro crack initiation and propagation. In order to reveal the main parameters affecting the fatigue strength, comprehensive experimental and theoretical investigations were carried out for butt-welded steel joints. Based on the results of the present study, several conclusions can be drawn.

In laser-based welding, the high and localised welding energy causes strength overmatching of the weld. This causes material inhomogeneity in the welded joint, which further affects its plastic behaviour and thus the notch stresses and strains. The effect of material inhomogeneity should be taken into account in the response calculation, when nominal stress level exceeds the yield strength of the parent material. Consequently, the response calculation based on Neuber's rule requires a separate structural and local analysis to take into account differences in the stress-strain behaviour of material zones in the welded joint. There, the simplified approach using the stress-strain curves of the base plate and of the weld notch in HAZ can be applied to describe the elasto-plastic behaviour of the joint and thus to define the notch stresses and strains under full or partial yielding of the cross-section.

Since macro crack initiation life forms an essential part of the total fatigue life, it is recommended that the initiation life is always taken into account in the theoretical fatigue analysis of the laser-based butt joints. There, the common approach, dividing the fatigue life into the macro crack initiation and propagation periods, is giving reliable results. However, a new approach is needed to model the macro crack initiation. With a new approach, the hardness-based approach for the fatigue resistance of the material could also be applied for the laser-based and arc-welded joints, as the existing investigations show its applicability to different parent materials. Additionally, because of a sharp weld notch, the averaging of the notch stresses and strains, inside the characteristic length related to material microstructure, is needed. The present study proposes that the chosen averaging length is three times the average grain size; this length is also considered equal to the length of the growth step of a short crack in the analysis. The modelling of the initiation life of the macro crack with several discrete growth steps up to the threshold length of the macro crack is also obligatory due to the fine-grained microstructure in the HAZ, especially in the case of laser-based joints. This approach gives a theoretical basis for the macro crack initiation and thus improves significantly fatigue life predictions for both the laser-based and arc-welded joints compared to the existing approaches. This fact was confirmed with the experimental results.

The results of the advanced fatigue tests, which focused on the fatigue resistance of the welded joints with different material zones, prove that the macro crack initiation life forms an essential part of the total fatigue life, at least for butt joints. Hence, the mechanical properties of the material in the weld notch have also a strong influence on the fatigue resistance. The main material parameters that affect the initiation period of the laser-based joints are material hardness and the averaged grain size at the weld notch. The macro crack initiation life N_i forms an essential part of the total fatigue life N_f and the ratio N_i/N_f strongly increases as a function of the fatigue life. These cause the increase of the slope value m in the S-N curve for the laser-based and also for the high quality arc-welded joints. However, in the case of laser-based joints with high static pre-strain, where the initiation period becomes short, the slope of the *S-N* curve with the value of $m = 3$ is observed, which is similar to that often considered for the arc welds.

The main reason for the different initiation process of fatigue cracks between the laser-based and arc-welded joints is the dissimilar grain size in the HAZ. For the studied steel joints, the averaged grain size of the laser-based joints is about seven times smaller than that of the considered arc-welded joint. Other parameters affecting the fatigue life of laser-based joints are the notch depth and its root radius. The weld flank angle of the laser-based butt joints has a minor influence compared to that of the arc weld with the high support effect of the weld.

8.3 Recommendations for future work

The present study focused on the fatigue resistance of 12 mm thick butt-welded joints in order to concentrate on the weld notch and material effects. The improvement of the theoretical approach can be achieved by 3D analysis of the weld notch instead of the 2D analysis conducted in the present work. This becomes important when single deep defects exist. In fact, further research is needed to acquire more reliable knowledge of other joint types. The higher strength of parent material should also be studied. While the investigation focused on the medium and high cycle range, there nevertheless remains a lack of knowledge concerning the low cycle range, including also the high pre-strain, which is an important matter when structures loaded by sea waves are being considered.

Further research is also needed about the sensitivity of this new approach to the parameters, even though it was explicitly included in the analyses covering several different geometries and load cases. In fact, the significance of the initiation life for the total fatigue life depends on the weld geometry and loading. For instance, in the case of deep weld notch or high pre-strain, the initiation life was observed to be short, and macro crack propagation then dominated. Consequently, the detailed level sensitivity analysis of the new approach should be carried out using specified ranges of geometries of joints and of loads typical for welded structures.

The results of the experimental investigations indicated a potential advantage in the fatigue strength measured with FAT when using hybrid welding. The fatigue strength for hybrid butt joints was above FAT 200, a value significantly higher than that for the typical arc-welded joints, the FAT 100. Actually, the high fatigue strength, about FAT 170, was also measured in the test for the SAW joint with smooth weld geometry, low notch depth and small misalignments. However, it is important to notice, based on the present result, that the reduction of fatigue strength for a hybrid joint, due to a high pre-strain, was significant. Therefore, to reveal the true advantage of hybrid welding for fatigue strength in practice, further research on loads and welding distortions caused during fabrication, as well as on the effect of variable amplitude loading, is required and recommended.

REFERENCES

Akiniwa, Y.; Tanaka, K.; Matsui, E. 1988. Statistical characteristics of propagation of small fatigue cracks in smooth specimens of aluminium alloy 2024-T3. Materials Science & Engineering A: Structural Materials: Properties, Microstructure and Processing. Vol. v A104. p. 105-115.

Anderson, T. L. 2005. Fracture mechanics: fundamentals and applications. 3. ed. Boca Raton, Taylor & Francis. 621 p.

Anderson, T. W.; Darling, D. A. 1954. A Test of Goodness of Fit. Journal of the American Statistical Association. Vol. 49:268. p. 765-769.

Anthes, R. J.; Köttgen, V. B.; Seeger, T. 1993. Notch shape factors of butt joints and double-T joints. Schweisen und Schneiden. Vol. 45:12. p. 685-688.

Anthes, R. J.; Köttgen, V. B.; Seeger, T. 1994. Effect of the weld geometry on the fatigue strength of butt and double-T joints. Schweisen und Schneiden. Vol. 46:9. p. 433-436.

Bell, R.; Vosikovsky, O.; Bain, S. A. 1989. Significance of weld toe undercuts in the fatigue of steel plate T-joints. International Journal of Fatigue. Vol. 11:1. p. 3-11.

Berge, S.; Eide, O. I.; Moe, E. T. 1980. Fatigue crack initiation in weldments of a C-MN steel. In: Proceedings of European offshore steel research seminar. The Welding Institute. Cambridge: Abington.

Bokalrud, T.; Karlsen, A.; 1982. Control of the fatigue failure in ship hull by ultrasonic inspection. Norwegian Maritime Research. No. 1. p. 9.

Boyer, H. E.; Gall, T. L. 1985. Metals handbook. Metals Park, OH: ASM. 1500 p.

BS-7608. 1993. Code of practice for fatigue design and assessment of steel structures. London: British Standards Institution. 96 p.

Caccese, V.; Blomquist, P.A.; Berube, K.A.; Webber, S.R.; Orozco, N.J. 2006. Effect of weld geometric profile on fatigue life of cruciform welds made by laser/GMAW processes. Marine Structures. Vol. 19:1. p. 1-22.

Cai, C. Q.; Shin, C. S. 2005. A normalized area-compliance method for monitoring surface crack development in a cylindrical rod. International Journal of Fatigue. Vol. 27:7. p. 801-809.

Chambers, J. M.; Cleveland, W. S.; Kleiner, B.; Tukey, P. A. 1983. Graphical Methods for Data Analysis. Beaumont, California: Wadsworth.

Classification Societies. 1996. Requirements for the approval of CO2 laser welding procedures. Lloyd's Register of Shipping, Registro Italiano Navale, Germanischer Lloyd, Bureau veritas, Det Norske Veritas.

Classification Society. 2006. Qualification and approval of hybrid laser-arc welding in shipbuilding. Guidelines No. 19. Det Norske Veritas.

Coffin, L. F. 1954. A study of the effect of cyclic thermal stresses on a ductile metal. Transactions of ASME. Vol. 76:6. p. 931 - 950.

Cui, W. 2002. A state-of-the-art review on fatigue life prediction methods for metal structures. Journal of Marine Science and Technology. Vol. 7:1. p. 43-56.

Dahl, W.; Reinhold, P. 1996. Experimentelle Ermittlung und rechnerische Überprüfung der Dauerfestigkeit praxisnah hergestellter Laserstrahlschweißverbindungen verschiedener Geometrien (Experimental determination and numerical checks of the fatigue strength of laser beam welded joints of different geometries). Forschungsbericht P262. Düsseldorf: Studiengesellschaft Stahlanwendung.

Dowling, N. E. 2007. Mechanical behavior of materials: engineering methods for deformation, fracture, and fatigue. 3rd ed. Upper Saddle River, New Jersey: Prentice Hall. 773 p.

El Haddad, M. H.; Smith, K. N.; Topper, T. H. 1979. Fatigue crack propagation of short cracks. Journal of Engineering Materials and Technology, Transactions of the ASME. Vol. 101:1. p. 42-46.

Fatemi A.; Yang, L. 1998. Cumulative fatigue damage and life prediction theories: a survey of the state of the art for homogeneous materials. International Journal of Fatigue. Vol. 20:1. p. 9-34.

Filliben, J. J. 1975. The Probability Plot Correlation Coefficient Test for Normality. Technometrics. Vol. 17:1. p. 111-117.

Forman, R. G.; Kearney, V. E.; Engle, R. M. 1967. Numerical analysis of crack propagation in cyclic loaded structures. Journal of Basic Engineering. Transactions of the ASME. Vol. 89. p. 459.

Fricke, W.; Pohl, S.; Weydling, C. 1996. Zur Anwendung des Kerbgrundkonzeptes auf Schweißverbindungen - Teil 2: nichtlineare Berechnung und Erfassung zufallsbehafteter Einflußgrößen (Application of the cyclic strain approach to welded joints - part 2: nonlinear computations and stochastic influence parameters). Schiffbauforschung. Vol. 35:2.

Glinka, G. 1985. Calculation of inelastic notch-tip strain-stress histories under cyclic loading. Engineering Fracture Mechanics. Vol. 22:5. p. 839-854.

Goodman, E. D. 1995. Gallops: The Genetic Algorithm Optimized for Portability and Parallelism System. Michigan State University.

Gosch, T.; Petershagen, H. 1997. Influence of undercuts on the fatigue strength of butt welds. Schweissen und Schneiden. Vol. 49:3. p. E44-E46.

Goto, M. 1994. Statistical investigation of the behavior of small cracks and fatigue life in carbon steels with different ferrite grain sizes. Fatigue and Fracture of Engineering Materials & Structures. Vol. 17:6. p. 635-649.

Goto, M.; Nisitani, H. 1994. Fatigue life prediction of heat-treated carbon steels and low alloy steels based on a small crack growth law. Fatigue and Fracture of Engineering Materials & Structures. Vol. 17:2. p. 171-185.

Gripenberg, H. 2003. A Study of Submerged Arc, Laser and Hybrid Weld Properties, Residual Stresses, CSS-Curves and Fractography. Espoo, Finland: Helsinki University of Technology, Laboratory of Engineering Materials. Research report TKK-MTR-2/03. 67 p.

Heo, J.-H.; Kang, J.-K.; Kim, Y.; Yoo, I.-S.; Kim, K.-S.; Urm, H.-S. 2004. A study on the design guidance for low cycle fatigue in ship structures. In: Keil, H.; Lehmann, E. Proceedings of 9th International Symposium on Practical Design of Ships and Other Floating Structures. Luebeck-Travemuende, Germany. 12-17.9.2004. Hamburg: Schiffbautechnische Gesellschaft. p. 782-789.

Herbert, S. 2004. Laser-hybrid welding of ship. Welding Journal. Vol. 83:6. p. 39-43.

Hobbacher, A. / IIW Joint Working Group XIII-XV. 2007. Recommendations for fatigue design of welded joints and components. IIW document XIII-2151-07 / XV-1254-07. Paris, France. 149 p.

Hou, C.-Y.; Charng, J.-J. 1997. Models for the estimation of weldment fatigue crack initiation life. International Journal of Fatigue. Vol. 19:7. p. 537-541.

Hoel, P. G. 1962. Introduction to mathematical statistics. New York: John Wiley & Sons. 427 p.

Hoffmann, M.; Seeger, T. 1985. Generalized method for estimating multiaxial elastic-plastic notch stresses and strains. Journal of Engineering Materials and Technology, Transactions of the ASME. Vol. 107: 4. p. 250-260.

Janosch, J. J.; Debiez, S. 1998. Influence of the shape of undercut on the fatigue strength of fillet welded assemblies - application of the local approach. Welding in the World. Vol. 41:4. p. 350-360.

Kahl, A. 2000. Eine Werft verändert sich-neue Strukturen, neue Methoden. In: proceeding of “Sondertagung Schweißen im Schffbau und Ingenieurbau“ (A shipyard in change – new structures, new methods. In proceedings of Special congress of welding in shipbuilding and civil engineering). Hamburg, Germany: Germanischer Lloyd.

Kawagoishi, N.; Chen, Q.; Nisitani, H. 2000. Significance of the small crack growth law and its practical application. Metallurgical and materials transactions A: Physical Metallurgy and Materials Science. Vol. 31:8 p. 2005-2013.

Kendrick, A. / SSC. 2005. The effect of fabrication tolerances on fatigue life of welded joints. Research report SSC-436. 2005. Ship Structure Committee. Ontario, Canada: BMT Fleet Technology Ltd.

Köttgen, V. B.; Olivier, R.; Seeger, T. 1991. Schwingfestigkeitsanlayse für Schweißverbindungen auf der Grundlage örtlicher Beanspruchungen (Fatigue analysis of welded connections based on local stresses). In: DVS-Report No 133, DVS-Verlag, Düsseldorf. English translation in IIW-document XIII-1408-91/XV-802-92. International Institute of Welding.

Kristensen, J., K. 1996. Laser welding in ship building. Proceeding of IIW Shipbuilding Seminar. Odence, Denmark.

Kujala, P.; Socha, G.; Koli, K.; Toivonen T. 1999. Characteristics of stake laser welded joints. In: Kujanpää, V.; Ion, J. Proceedings 7th Nordic Conference in Laser Processing of Materials. Lappeenranta, Finland 1999. Lappeenranta: Lappeenranta University of Technology. p. 120-133.

Laitinen, R. 2003. Results of the hardness tests no. 580/01, 622/01, 468/02, 583/02, 226/03. Raahe, Finland: Ruukki.

Laitinen, R.; Kujala P.; Remes H.; Nielsen, S. E. 2003. CO2-laser MAG Weldability of Laser Cutting LASER RAEX Steels, Hull Structural Steel Grade A and High Strength Formable Steel OPTIM RAEX 700 MC. In: Halmøy, E. Proceedings 9th Conference on Laser Materials Processing in the Nordic Countries. Trondheim, Norway. 4-6.8. 2003. Trondheim: Norwegian University of Technology. p. 51-62.

Laitinen, R.; Martikainen, J.; Kauppila, J.; Saastamoinen, T.; Porter, D. 1999 Laser weldability of RAEX LASER grades and two other structural steels. In: Kujanpää, V.; Ion, J. Proceedings 7th Nordic Conference in Laser Processing of Materials. Lappeenranta, Finland 1999. Lappeenranta: Lappeenranta University of Technology. p. 239–251.

Landgraf, R. W.; Morrow, J.-D.; Endo, T. 1969. Determination of the cyclic stress-strain curve. Journal of Materials. Vol. 4:1. p. 176-188.

Lawrence F. V.; Mattos, R. J.; Higashide, Y.; Burk, J. D. 1978. Estimating the fatigue crack initiation life of welds. ATSM STP648, Fatigue testing of weldments. Philadelphia: ATSM. p. 134-158.

Lawrence F. V.; Ho, N. J.; Mazumdar, P. K. 1981. Predicting the fatigue resistance of welds. Annual Review of Materials Science. Vol. 11. p. 401-425.

Lee, K.-S.; Song, J.-H. 2006. Estimation methods for strain-life fatigue properties from hardness. International Journal of Fatigue. Vol. 28:4. p. 386-400.

Lotsberg, I.; Askheim, D. Ø.; Haavi, T.; Maddox, S. J. 2001. Full scale testing of side longitudinals in FPSOs. In: Langen, I.; Yao, T.; Koo, J; Knapp, R. H.; Chung, J. S. The Proceedings of the Eleventh (2001) International Offshore and Polar Engineering Conference. Stavanger, Norway. 17-22. 6. 2001. Cupertino, California: International Society of Offshore and Polar Engineers. Vol. IV. p. 67-72.

Maddox, S. J. 1991. Fatigue strength of welded structures. Cambridge: Abington.

Manson, S. S. 1954. Behaviour of materials under conditions of thermal stress. Heat transfer symposium. University of Michigan, Engineering Research Institute and NACA TN2933. p. 9-74.

Mattos, R. J.; Lawrence, F. V. 1977. Estimation of the fatigue crack initiation life in weld using low cycle fatigue concepts. SAE SP-424.Warrendale: SAE.

Massey, F. J. 1951. The Kolmogorov-Smirnov Test for Goodness of Fit. Journal of the American Statistical Association. Vol. 46:253. p. 68-78.

Meyer Werft. 2000. SN testing of laser-hybrid butt welds. Unpublished research report MT70-F00262. Marintek SINTEF group.

Miller, A. K.; Obabueki, A. O.; Lee, C.-H.; Tanaka, T. G.; Lee, S.-B. 1987. Unified model for fatigue crack initiation and growth, with emphasis on short-crack behavior, crack closure effects, variable-temperature fatigue and creep-fatigue interaction. Materials Science & Engineering A: Structural Materials: Properties, Microstructure and Processing. Vol. A103:1. 1988. p. 71-93.

Morrow, J.D. 1965. Cyclic plastic strain energy and fatigue of metals. ASTM STP 378. Philadelphia: ASTM. p. 45-87.

Müller, R.; Koczera, S. 2003. Shipyard uses laser-GMAW hybrid welding to achieve one-sided welding: New system “reforms” prefabrication in shipbuilding. Fabricators & Manufacturers Association Intl. [Electronic journal]. 20.11.2003. [Cited 26.4.2007.] Available at: www.thefabricator.com.

Murakami, Y.; Miller, K. J. 2005. What is fatigue damage? A view point from the observation of low cycle fatigue process. International Journal of Fatigue. Vol. 27:8. p. 991-1005.

Neuber, H. 1961. Theory of stress concentration for shear-strained prismatic bodies with arbitrary nonlinear stress-strain law. Journal of Applied Mechanics. Transactions of ASME. Vol. 28. p. 544-550.

Neuber, H. 1968. Über die Berücksichtigung der Spannungskonzentration bei Festigkeitsberechnungen (On the consideration of stress concentrations in strength analyses). Konstruktion 20:7, p. 245-251.

Newman, J. C. Jr.; Raju, I. S. 1981. Empirical stress-intensity factor equation for the surface crack. Engineering Fracture Mechanics. Vol. 15:1-2. p. 185-192.

Newman, J. C. Jr.; Raju, I. S. 1983. Stress-intensity factor equations for cracks in three-dimensional finite bodies. American Society for Testing and Materials, Special Technical Publications 791. p. 238-265.

Newman, J. C. Jr.; Phillips, E. P.; Swain, M. H. 1999. Fatigue life prediction methodology using small crack theory. International Journal of Fatigue. Vol. 21:2. p. 109 - 119.

Nguyen, N. T.; Wahab, M. A. 1996. The effect of undercut and residual stresses on fatigue behaviour of misaligned butt joints. Engineering Fracture Mechanics. Vol. 55:3. p. 453-469.

Nguyen, T. N.; Wahab, M. A. 1995. A theoretical study of the effect of weld geometry parameters on fatigue crack propagation life. Engineering Fracture Mechanics. Vol. 51:1. p. 1-18.

Nguyen, T. N.; Wahab, M. A. 1998. The effect of weld geometry and residual stresses on the fatigue of welded joints under combined loading. Journal of Materials Processing Technology. Vol. 77:1-3. p. 201-208.

Nisitani, H. 1981. Unifying treatment of fatigue crack growth laws in small, large and non-propagating cracks. American Society of Mechanical Engineers, Applied Mechanics Division, AMD. Vol. 47. p. 151-166.

Otegui, J.L.; Mohaupt, U.H.; Burns, D.J. 1991. Effect of weld process on early growth of fatigue cracks in steel T joints. International Journal of Fatigue. Vol. 13:1. p. 45-58.

Paris, P.; Erdogan, F. 1963. A critical analysis of crack propagation laws. Journal of Basic Engineering. Vol. 85. p. 528–534.

Peeker, E.; Niemi, E. 1999. Fatigue crack propagation model based on a local strain approach. Journal of Constructional Steel Research Vol:49. p. 139–155.

Petershagen, H. 1986. The influence of undercut on the fatigue strength of welds - supplementary remarks to IIS/IIW Doc. XIII-1120-84. IIS/IIW Document XIII-WG4-30-86.

Petershagen, H. 1990. The influence of undercut on the fatigue strength of welds: A literature survey. Welding in the World. Vol. 28:7-8. p. 114-125.

Peterson, R. E. 1959. Notch sensitivity. In: Sines, G.; Waisman, J. L.; Metal Fatigue. New York: McGraw Hill. p. 293-306.

Peterson R. E. 1974. Stress concentration factors: charts and relations useful in making strength calculations for machine parts and structural elements. 2nd ed. New York: Wiley. 317 p.

Radaj, D. 1990. Design and analysis of fatigue-resistant welded structures. Cambridge: Abington Publishing. 378 p.

Radaj, D. 1995. Ermüdungsfestigkeit – Grundlagen für Leichtbau: Maschinen- and Stahlbau (Fatigue strength – Fundamentals for light weight design: mechanical and structural engineering). Berlin: Springer.

Radaj, D.; Sonsino, C. M. 1998. Fatigue assessment of welded joints by local approaches. Cambridge: Abington. 416 p.

Radaj, D.; Sonsino, C.M.; Flade, D. 1998. Prediction of service fatigue strength of a welded tubular joint on the basis of the notch strain approach. International Journal of Fatigue. Vol: 20:6. p. 471-480.

Ramberg, W.; Osgood, W. R. 1943. Description of stress-strain curves by three parameters. Technical Report No. 902, NACA.

Remes, H. 2003. Fatigue tests of $C0_2$-laser, $C0_2$-laser hybrid and submerged arc welded butt joint of RAEX S275 LASER and NVA. Espoo, Finland: Helsinki University of Technology, Ship Laboratory. Research Report M-278, Vol. 1 and 2. 97+201 p.

Remes, H.; Socha, G. 2003. Fatigue tests of $C0_2$-laser, $C0_2$-laser hybrid and submerged arc welded material of RAEX S275 LASER. Espoo, Finland: Helsinki University of Technology, Ship Laboratory. Research Report M-277, Vol. 1 and 2. 169+327 p.

Ring, M.; Dahl, W. 1994. Fatigue properties of laser-beam weldments on the high-strength steels. Steel Research. Vol. 65:11. p. 505-510.

Roessle, M.L.; Fatemi, A. 2000 Strain-controlled fatigue properties of steels and some simple approximations. International Journal of Fatigue.Vol. 22:6. p. 495-511.

Roland, F.; Manzon, L.; Kujala, P.; Brede, M.; Weitzenböck, J. 2004. Advanced joining techniques in European shipbuilding. Journal of Ship Production. Vol. 20:3. p. 200-210.

Seeger, T.; Heuler, P. 1980. Generalized application of Neuber's rule. Journal of Testing and Evaluation. Vol. 8:4. p. 199-204.

Siebel, E.; Stieler, M. 1955. Ungleichförmige Spanungsverteilung bei schwingender Beanspruchung (Non-uniform stress distribution during cyclic loading). VDI-Zeitschrift. Vol. 97:5. p. 121 - 126.

Smith, K. N.; Watson, P.; Topper, T. H. 1970. Stress- strain function for the fatigue of metals. Journal of Materials. Vol. 5:4. p. 767-778.

Socha, G. 2003. Experimental investigations of fatigue cracks nucleation, growth and coalescence in structural steel. International Journal of Fatigue. Vol. 25:2. p 139-147.

Socha, G. 2004. Prediction of the fatigue life on the basis of damage progress rate curves. International Journal of Fatigue. Vol. 26:4. p. 339-347.

Socie, D. F.; Marquis, G. B. 2000. Multiaxial fatigue. Warrendale (PA): Society of Automotive Engineers. 484 p.

Sonsino, C.M. 1995. Multiaxial fatigue of welded joints under in-phase and out-of-phase local strains and stresses. International Journal of Fatigue. Vol. 17:1. p. 55 - 70.

Tamminen, T.; Remes, H. 2003. Fatigue tests of laser, laser hybrid and arc welded butt and T-joints of RAEX S275 LASER, RAEX 420MC LASER, RAEX 700 OPTIM, GL-A36TM and NVA steels. Espoo, Finland: Helsinki University of Technology, Ship Laboratory. Research Report M-284. 453 p.

Taylor, D. 1999. Geometrical effects in fatigue: a unifying theoretical model. International Journal of Fatigue. Vol. 21:5. p. 413-420.

Tokaji, K.; Ogawa, T.; Harada, Y. 1986. Evaluation on limitation of linear elastic fracture mechanics for small fatigue cracks under rotating bending. Zairyo/Journal of the Society of Materials Science. Vol. 35:391. p. 394-400. (In Japanese)

Wahab, M. A.; Alam, M. S. 2004. The significance of weld imperfections and surface peening on fatigue crack propagation life of butt-welded joints. Journal of Materials Processing Technology. Vol. 153-154:1-3. p. 931-937.

Weichel, F.; Petershagen, H. 1995. Fatigue strength of laserwelded structural steels with thicknesses between 8 and 20 mm. IIW Document XIII-1590-95. Germany: University of Hamburg.

Weldingh, J.; Kristensen, J. K. 2003. Hybrid YAG-laser/MAG welding quality and stability. In: Halmøy, E. Proceedings 9th Conference on Laser Materials Processing in the Nordic Countries. Trondheim, Norway. 4-6.8.2003. Trondheim: Norwegian University of Technology. p. 15–24.

Yao, W.; Xia, K.; Gu, Y. 1995. On the fatigue notch factor, K_f. International Journal of Fatigue. Vol. 17:4. p. 245-251.

Yung, J. Y.; Lawrence, F. V. 1985. Analytical and graphical aids for the fatigue design of weldments. Fatigue Fracture Engineering Materials and Structures. Vol. 8:3. p. 223-241.

Zhao, Y. 2003. Size evolution of the surface short fatigue cracks of 1Cr18Ni9Ti weld metal. Journal of Materials Science and Technology. Vol. 19:2. p. 129-132.

Zhixue, W. 2001. Short fatigue crack parameters describing the lifetime of unnotched steel specimens. International Journal of Fatigue. Vol. 23:4. p. 363-369.

Appendix A Measured values for geometrical dimensions of weld

The geometries of the weld toe and root sides were analysed using a non-destructive replica technique. The replicas of specimen surfaces were prepared using silicone rubber. Macro photos were taken from 1 mm thick slides of the replicas to define the geometrical dimensions of the weld and weld notch. These are given in Figure A1. The geometry of the weld is defined with three geometrical dimensions: the weld width w, the weld height h and the flank angle of weld θ. Subscripts t and r refer to the weld toe and root sides, respectively. Five dimensions were used to describe the geometry of the weld notch, where D_1 is the notch depth measured from the plane of the top surface, D_2 is the notch depth taken from the profile line of the weld surface, γ the notch flank angle, β the notch opening angle, and ρ the notch root radius. The measured values for different welded joints are presented in Tables A1-A4. The first column in the tables specifies the sample index, where the first two letters describe the joint type and the next three numbers identify the test specimen. The last number in the index represents the number of the replica samples.

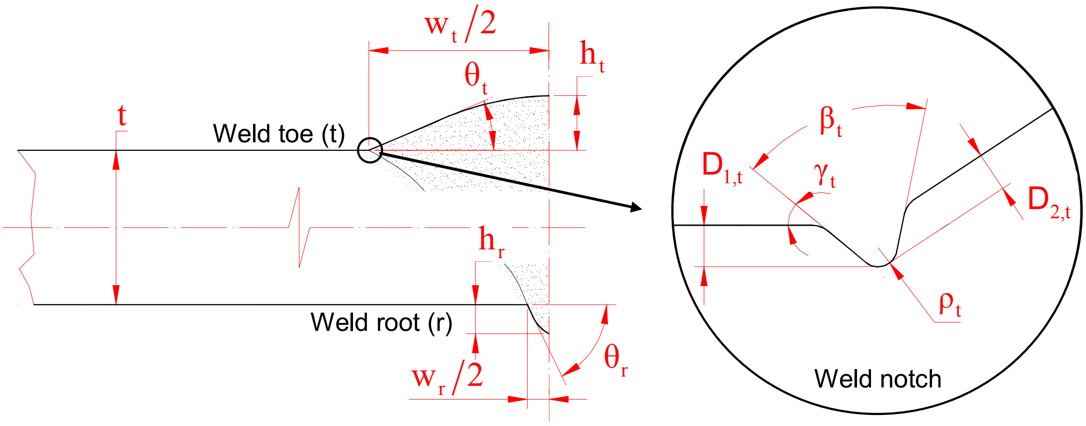

Figure A1: Dimensions of the weld and weld notch: weld width w, weld height h, weld flank angle θ, notch depth D, notch flank angle γ, notch opening angle β, and notch root radius ρ.

Table A1: Weld toe dimensions for the SAW joint

Test	Weld dimensions			Weld notch dimensions				
sample [Index]	h_t [mm]	w_t [mm]	θ_t [Deg]	$D_{1,t}$ [mm]	$D_{2,t}$ [mm]	γ_t [Deg]	β_t [Deg]	ρ_t [mm]
CT207_1	2.22	19.07	26.7	0.006	0.025	4.3	121.8	0.016
			27.3	0.008	0.043	3.8	130.2	0.040
CT207_2	2.26	18.83	30.2	0.001	0.030	3.4	127.6	0.025
			29.0	0.001	0.006	2.1	136.8	0.031
CT207_3	2.24	19.15	31.6	0.003	0.027	5.5	131.2	0.018
			35.8	0.001	0.020	0.4	136.7	0.057
CT207_4	2.25	19.04	30.4	0.001	0.006	1.5	146.3	0.031
			27.7	0.006	0.008	3.5	147.7	0.077
CT209_1	2.46	17.62	29.1	0.005	0.036	6.9	131.2	0.044
			28.1	0.006	0.009	3.5	137.2	0.041
CT209_2	2.51	17.63	26.3	0.012	0.005	27.6	112.0	0.049
			25.9	0.005	0.015	4.0	136.4	0.050
CT210_1	2.11	17.72	27.5	0.004	0.010	3.4	138.0	0.039
			28.2	0.003	0.037	2.4	119.5	0.022
CT210_2	2.11	17.82	32.9	0.004	0.018	1.6	141.9	0.039
			28.6	0.008	0.058	6.3	135.7	0.047
CT210_3	2.21	17.12	28.9	0.008	0.002	8.2	139.6	0.068
			29.4	0.002	0.033	2.9	143.4	0.094
CT210_4	2.23	17.12	30.5	0.026	0.060	21.0	130.6	0.089
			32.9	0.005	0.043	3.8	106.9	0.055

Table A2: Weld root dimensions for the SAW joint

Test	Weld dimensions			Weld notch dimensions				
sample [Index]	h_r [mm]	w_r [mm]	θ_r [Deg]	$D_{1,r}$ [mm]	$D_{2,r}$ [mm]	γ_r [Deg]	β_r [Deg]	ρ_r [mm]
CT207_1	0.82	9.73	14.3	0.011	0.038	3.6	143.3	0.439
			14.0	0.038	0.046	20.5	133.3	0.080
CT207_2	0.82	9.94	14.1	0.002	0.010	0.6	150.7	0.069
			15.3	0.003	0.017	4.9	140.0	0.038
CT207_3	1.07	9.54	15.2	0.119	0.109	60.8	92.6	0.027
			14.7	0.009	0.043	3.2	130.6	0.035
CT207_4	1.04	9.65	20.7	0.005	0.050	10.0	133.6	0.133
			20.8	0.015	0.030	13.0	122.2	0.023
CT209_1	1.31	10.42	23.0	0.007	0.056	6.5	148.4	0.479
			27.0	0.009	0.020	3.4	154.5	0.614
CT209_2	1.49	10.29	16.3	0.109	0.030	54.3	98.6	0.171
			10.2	0.007	0.026	4.8	157.8	0.063
CT210_1	1.68	10.17	17.1	0.012	0.009	10.4	140.8	0.142
			15.5	0.010	0.008	8.5	158.9	0.574
CT210_2	1.73	10.21	15.8	0.016	0.034	8.5	135.8	0.149
			15.9	0.009	0.018	16.6	141.2	0.116
CT210_3	1.80	9.97	21.5	0.049	0.006	16.1	132.8	0.033
			22.0	0.013	0.006	18.9	126.9	0.028
CT210_4	1.76	10.16	30.3	0.102	0.050	81.7	69.2	0.027
			24.8	0.009	0.036	3.0	141.7	0.259

Table A3: Weld toe dimensions for the Laser joint

Test sample [Index]	Weld dimensions			Weld notch dimensions				
	h_t [mm]	w_t [mm]	θ_t [Deg]	$D_{1,t}$ [mm]	$D_{2,t}$ [mm]	γ_t [Deg]	β_t [Deg]	ρ_t [mm]
CL108_1	-0.11	2.44	-11.1	0.009	0.026	24.4	130.6	0.070
			3.6	0.003	0.022	1.2	101.9	0.059
CL108_2	-0.12	2.33	-32.0	0.070	0.023	18.6	138.1	0.858
			-19.4	0.067	0.029	21.9	133.2	0.169
CL108_3	-0.39	3.55	15.9	0.032	0.020	29.7	116.3	0.156
			20.6	0.015	0.041	34.6	78.1	0.042
CL108_4	-0.45	3.37	7.4	0.148	0.195	47.0	93.5	0.581
			25.0	0.117	0.086	28.0	116.3	0.682
CL303_1	0.33	2.44	18.1	0.083	0.044	10.1	135.4	1.350
			12.4	0.013	0.020	20.0	128.6	0.205
CL303_2	0.27	2.46	-3.1	0.039	0.038	14.8	124.9	0.324
			-14.9	0.030	0.070	3.1	133.6	0.093
CL303_3	0.21	3.22	-18.2	0.102	0.070	34.1	125.8	0.248
			-31.9	0.016	0.033	10.5	156.9	0.123
CL303_4	0.15	3.30	24.4	0.026	0.006	28.6	107.0	0.105
			18.4	0.069	0.056	28.5	124.0	0.586
CL304_1	0.36	2.92	17.3	0.063	0.103	35.3	116.3	1.635
			5.8	0.514	0.415	70.2	60.7	0.414
CL304_2	0.34	2.46	9.4	0.008	0.001	18.7	127.5	0.105
			25.1	0.027	0.006	23.7	123.9	0.091

Table A4: Weld root dimensions for the Laser joint

Test sample [Index]	Weld dimensions			Weld notch dimensions				
	h_r [mm]	w_r [mm]	θ_r [Deg]	$D_{1,r}$ [mm]	$D_{2,r}$ [mm]	γ_r [Deg]	β_r [Deg]	ρ_r [mm]
CL108_1	0.49	1.83	26.4	0.017	0.117	4.8	92.3	0.027
			42.3	0.017	0.017	15.6	119.7	0.037
CL108_2	0.48	1.66	43.6	0.039	0.033	13.7	89.4	0.068
			27.0	0.020	0.054	23.8	75.4	0.032
CL108_3	0.48	1.74	37.1	0.016	0.188	10.7	90.2	0.069
			49.2	0.052	0.058	29.6	80.5	0.122
CL108_4	0.46	1.75	44.2	0.035	0.094	4.4	78.7	0.141
			49.6	0.011	0.045	7.0	100.8	0.033
CL303_1	0.61	1.73	31.8	0.018	0.042	11.5	90.9	0.061
			34.5	0.034	0.062	4.5	97.6	0.031
CL303_2	0.65	1.66	36.9	0.009	0.013	19.2	100.0	0.069
			32.0	0.007	0.013	18.9	118.4	0.030
CL303_3	0.71	1.70	28.9	0.016	0.019	6.2	126.5	0.078
			44.1	0.022	0.044	17.2	80.9	0.110
CL303_4	0.68	1.60	44.1	0.030	0.023	15.1	91.3	0.062
			42.2	0.063	0.010	12.1	97.7	0.060
CL304_1	0.41	1.76	53.7	0.025	0.032	22.8	95.5	0.117
			51.6	0.024	0.041	16.6	77.3	0.099
CL304_2	0.33	1.33	27.2	0.042	0.015	20.4	118.3	0.282
			33.6	0.018	0.020	5.0	127.8	0.179

Table A5: Weld toe dimensions for the Hybrid LF joint

Test sample [Index]	Weld dimensions			Weld notch dimensions				
	h_t [mm]	w_t [mm]	θ_t [Deg]	$D_{1,t}$ [mm]	$D_{2,t}$ [mm]	γ_t [Deg]	β_t [Deg]	ρ_t [mm]
CH108_1	0.29	5.23	9.3	0.069	0.030	20.3	159.8	1.492
			7.9	0.006	0.012	2.1	162.1	0.357
CH108_2	0.36	4.98	9.4	0.007	0.006	7.0	156.7	0.205
			3.5	0.088	0.077	11.7	161.8	2.457
CH108_3	0.35	5.41	34.4	0.003	0.038	2.8	131.8	0.093
			26.4	0.001	0.145	0.2	117.3	0.457
CH108_4	0.28	5.49	15.1	0.002	0.052	3.1	143.2	0.410
			37.5	0.004	0.125	0.3	132.9	0.368
CH306_1	0.75	6.33	15.4	0.007	0.022	8.3	146.3	1.179
			13.3	0.003	0.065	0.8	152.4	0.157
CH306_2	0.70	5.99	3.9	0.013	0.066	4.6	140.7	0.708
			16.1	0.096	0.040	15.6	154.4	0.290
CH306_3	0.51	6.07	9.7	0.022	0.025	9.7	138.5	0.579
			7.5	0.007	0.005	12.9	140.3	0.119
CH306_4	0.64	6.22	23.1	0.009	0.036	3.7	123.2	0.112
			43.5	0.001	0.035	2.5	101.2	0.033
CH307_1	0.46	6.05	14.3	0.003	0.057	0.2	105.0	0.069
			27.1	0.003	0.038	3.6	108.9	0.031
CH307_2	0.51	6.08	9.2	0.005	0.012	2.4	145.1	0.121
			13.0	0.008	0.015	1.2	159.1	1.153

Table A6: Weld root dimensions for the Hybrid LF joint

Test sample [Index]	Weld dimensions			Weld notch dimensions				
	h_r [mm]	w_r [mm]	θ_r [Deg]	$D_{1,r}$ [mm]	$D_{2,r}$ [mm]	γ_r [Deg]	β_r [Deg]	ρ_r [mm]
CH108_1	1.58	2.67	86.6	0.004	0.124	0.6	87.7	0.191
			67.3	0.003	0.138	1.3	78.3	0.469
CH108_2	1.51	2.34	67.3	0.002	0.167	0.3	93.8	0.150
			58.4	0.005	0.133	0.9	117.9	0.061
CH108_3	0.99	1.56	23.1	0.026	0.105	4.4	114.5	0.227
			27.9	0.013	0.028	2.7	107.4	0.026
CH108_4	1.14	1.97	21.3	0.005	0.015	25.6	96.9	0.058
			47.4	0.041	0.098	13.8	76.2	0.106
CH306_1	0.20	1.47	57.5	0.031	0.198	40.1	55.5	0.044
			59.7	0.090	0.013	9.2	118.4	0.299
CH306_2	0.14	1.31	55.7	0.010	0.227	3.9	91.4	0.044
			79.7	0.011	0.040	4.1	98.3	0.130
CH306_3	0.16	1.18	88.6	0.020	0.217	17.6	89.7	0.039
			61.1	0.014	0.119	2.4	80.0	0.172
CH306_4	0.25	0.99	74.2	0.005	0.074	4.1	93.1	0.045
			60.0	0.028	0.018	2.9	83.7	0.032
CH307_1	0.51	1.19	52.5	0.002	0.024	1.7	106.7	0.025
			91.1	0.005	0.097	1.3	66.4	0.045
CH307_2	0.32	0.97	62.0	0.008	0.092	3.7	94.7	0.027
			32.8	0.030	0.019	7.1	113.4	0.297

Table A7: Weld toe dimensions for the Hybrid MF joint

Test sample [Index]	Weld dimensions			Weld notch dimensions				
	h_t [mm]	w_t [mm]	θ_t [Deg]	$D_{1,t}$ [mm]	$D_{2,t}$ [mm]	γ_t [Deg]	β_t [Deg]	ρ_t [mm]
CM107_1	0.90	6.34	21.9	0.003	0.009	5.6	148.0	0.896
			15.9	0.006	0.016	5.4	139.7	1.599
CM107_2	0.86	6.41	18.9	0.002	0.006	2.7	161.2	0.422
			19.7	0.003	0.009	2.1	148.4	0.950
CM108_1	0.99	6.22	17.1	0.011	0.010	2.7	150.3	0.178
			16.5	0.002	0.008	5.3	129.1	0.057
CM108_2	0.93	6.21	17.2	0.014	0.001	14.0	136.9	0.212
			19.0	0.005	0.008	5.9	147.9	0.162
CM108_3	0.94	6.55	20.6	0.030	0.042	16.7	139.7	0.776
			18.5	0.034	0.050	18.0	128.8	0.344
CM108_4	0.93	6.62	19.8	0.003	0.019	2.6	137.8	0.328
			21.4	0.011	0.017	20.5	125.2	0.102
CM108_1	0.91	6.28	20.6	0.015	0.001	8.0	151.0	0.366
			19.7	0.010	0.003	12.2	150.0	0.123
CM110_2	0.95	6.45	16.7	0.004	0.001	11.0	148.8	0.137
			17.0	0.011	0.011	2.0	156.3	0.213
CM110_3	1.00	6.59	19.7	0.015	0.017	6.2	150.5	0.203
			15.8	0.009	0.034	2.9	139.5	1.046
CM110_4	0.97	6.67	18.2	0.012	0.014	24.9	103.4	0.032
			16.3	0.001	0.007	0.9	139.2	0.091

Table A8: Weld root dimensions for the Hybrid MF joint

Test sample [Index]	Weld dimensions			Weld notch dimensions				
	h_r [mm]	w_r [mm]	θ_r [Deg]	$D_{1,r}$ [mm]	$D_{2,r}$ [mm]	γ_r [Deg]	β_r [Deg]	ρ_r [mm]
CM107_1	1.02	2.19	71.1	0.009	0.014	3.8	112.1	0.201
			57.8	0.006	0.011	3.4	99.5	0.187
CM107_2	1.19	2.01	41.1	0.007	0.004	14.0	119.1	0.060
			45.2	0.002	0.025	2.1	100.7	0.254
CM108_1	0.60	1.64	63.1	0.002	0.003	13.6	112.8	0.043
			54.6	0.002	0.004	5.5	94.1	0.074
CM108_2	0.63	1.83	50.4	0.023	0.068	8.8	94.1	0.316
			33.1	0.012	0.029	24.2	119.9	0.068
CM108_3	0.97	1.99	38.0	0.021	0.040	36.5	94.7	0.014
			31.5	0.010	0.034	7.8	112.8	0.201
CM108_4	0.89	2.03	51.3	0.008	0.014	4.2	99.4	0.096
			67.1	0.004	0.010	7.6	116.1	0.372
CM108_1	0.60	1.50	42.3	0.008	0.009	2.9	91.1	0.152
			45.7	0.041	0.032	30.0	110.5	0.057
CM110_2	0.58	1.83	56.4	0.005	0.048	3.4	94.1	0.082
			56.9	0.007	0.021	4.5	134.6	0.210
CM110_3	0.52	1.80	47.4	0.010	0.006	27.1	116.8	0.046
			34.0	0.005	0.016	3.3	119.4	0.166
CM110_4	0.5	2.04	30.6	0.024	0.095	3.3	117.1	0.742
			42.9	0.008	0.021	5.2	128.1	0.291

Appendix B Empirical cumulative distributions for geometrical dimensions

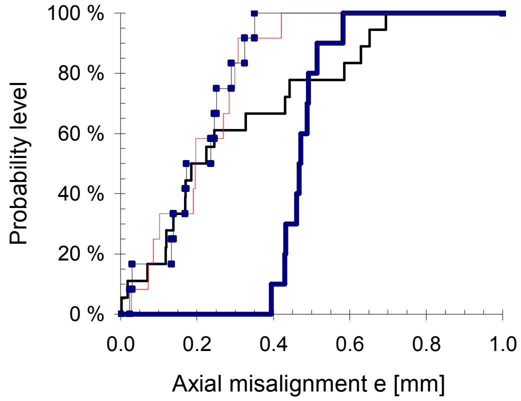

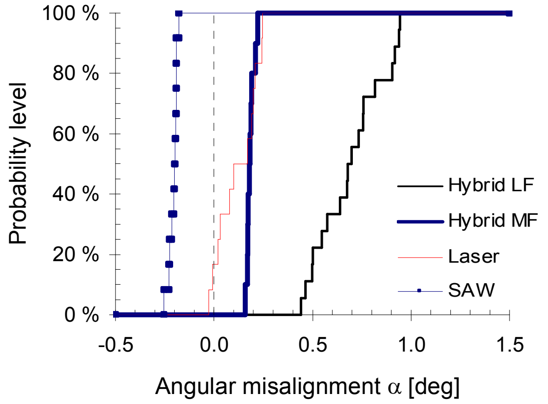

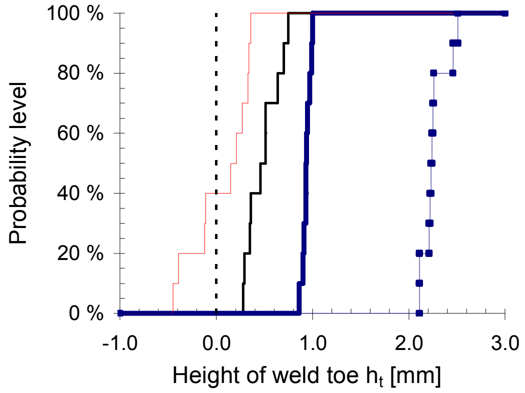

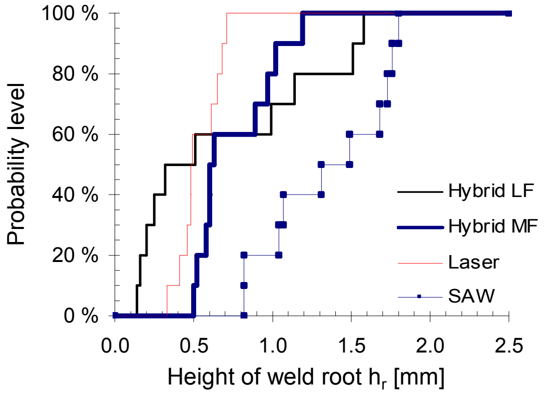

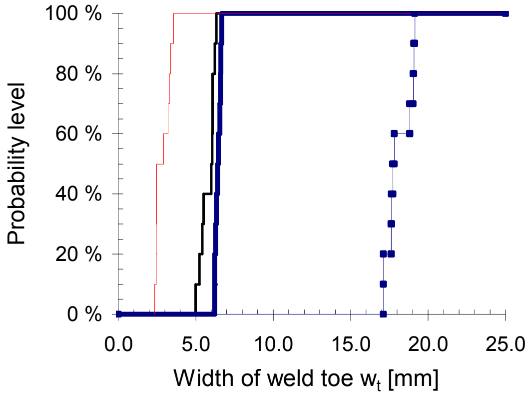

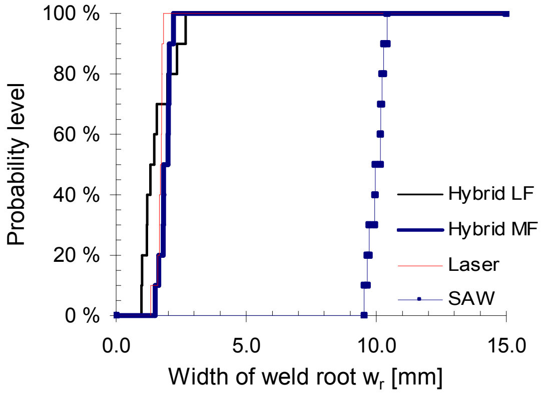

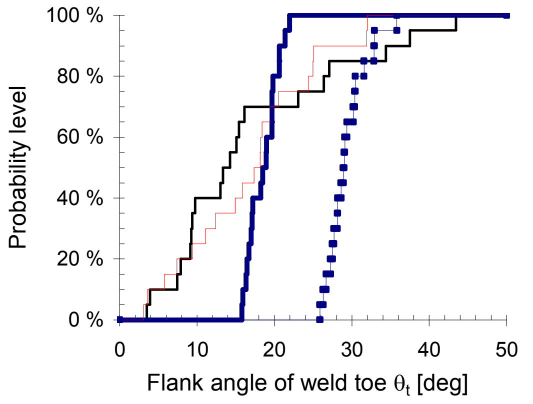
Probability level
100 %
80 %
60 %
40 %
20 %
0 %
0
10
20
30
40
50
Flank angle of weld toe θ_t [deg]

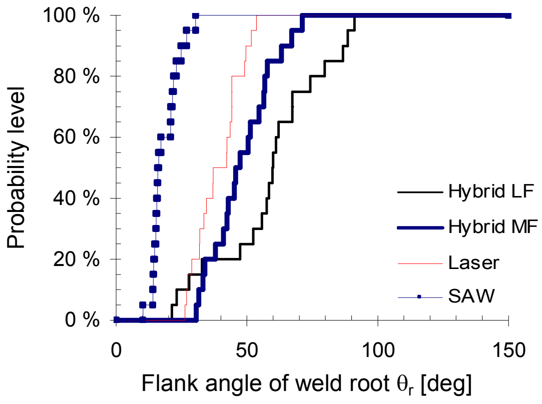
Probability level
100 %
80 %
60 %
40 %
20 %
0 %
0
50
100
150
Flank angle of weld root θ_r [deg]
Hybrid LF
Hybrid MF
Laser
SAW

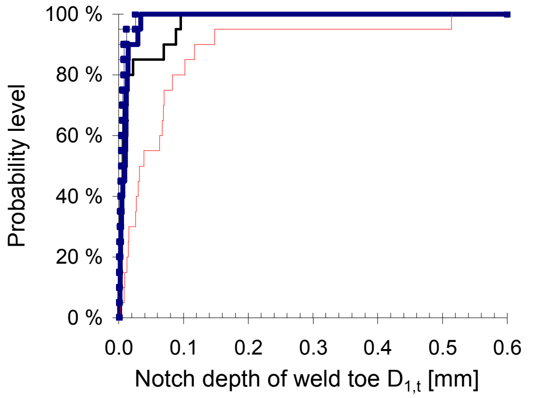
Probability level
100 %
80 %
60 %
40 %
20 %
0 %
0.0
0.1
0.2
0.3
0.4
0.5
0.6
Notch depth of weld toe $D_{1,t}$ [mm]

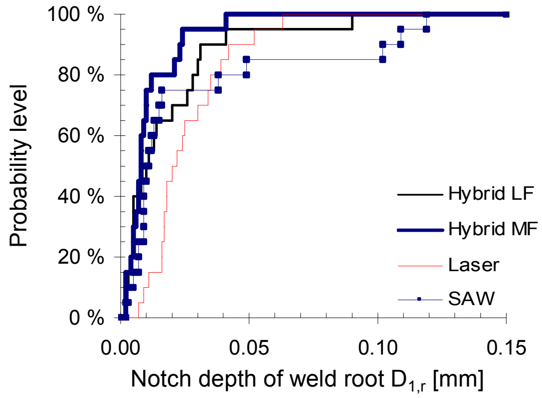
Probability level
100 %
80 %
60 %
40 %
20 %
0 %
0.00
0.05
0.10
0.15
Notch depth of weld root $D_{1,r}$ [mm]
Hybrid LF
Hybrid MF
Laser
SAW

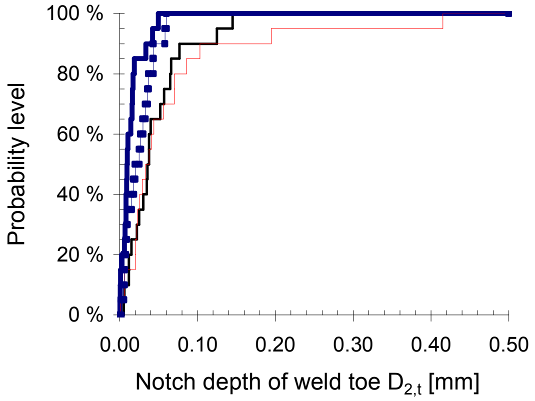
Probability level
100 %
80 %
60 %
40 %
20 %
0 %
0.00
0.10
0.20
0.30
0.40
0.50
Notch depth of weld toe $D_{2,t}$ [mm]

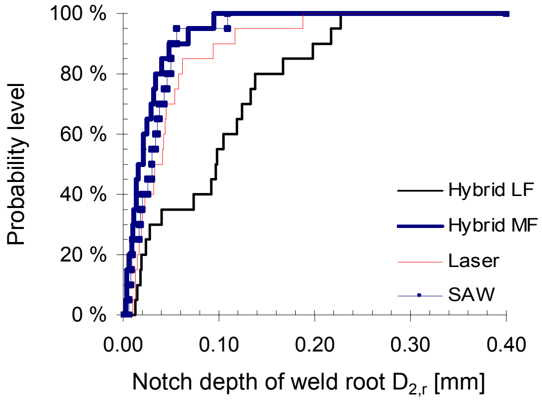
Probability level
100 %
80 %
60 %
40 %
20 %
0 %
0.00
0.10
0.20
0.30
0.40
Notch depth of weld root $D_{2,r}$ [mm]
Hybrid LF
Hybrid MF
Laser
SAW

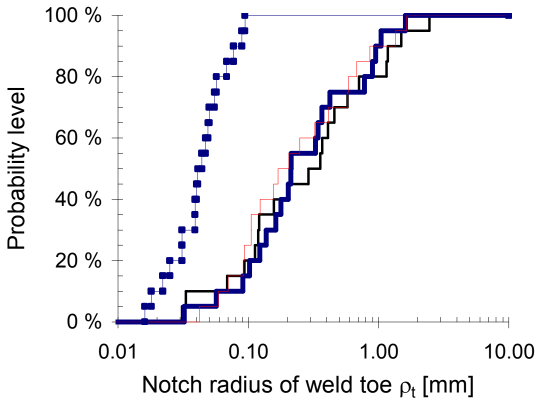
100 %
80 %
60 %
40 %
20 %
0 %
Probability level
0.01
0.10
1.00
10.00
Notch radius of weld toe ρ_t [mm]

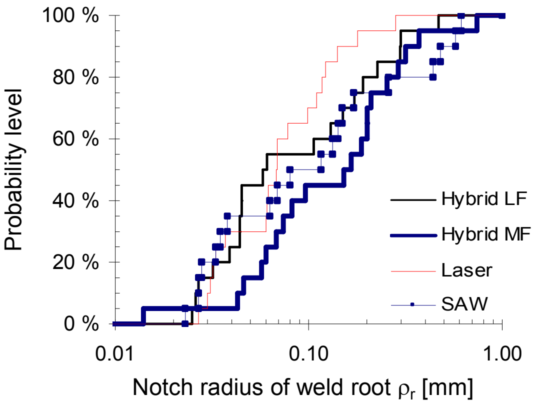
100 %
80 %
60 %
40 %
20 %
0 %
Probability level
0.01
0.10
1.00
Notch radius of weld root ρ_r [mm]
Hybrid LF
Hybrid MF
Laser
SAW

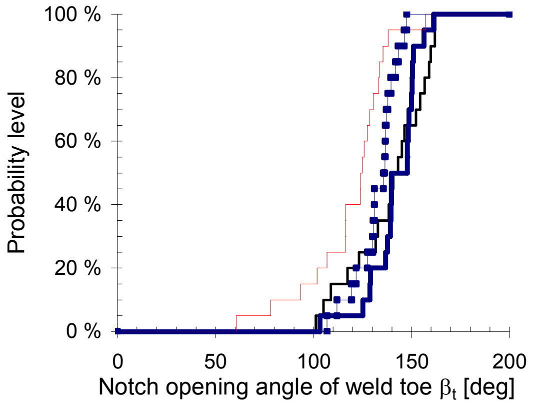
100 %
80 %
60 %
40 %
20 %
0 %
Probability level
0
50
100
150
200
Notch opening angle of weld toe β_t [deg]

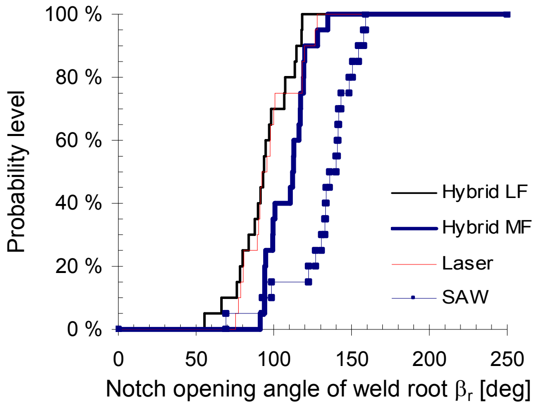
100 %
80 %
60 %
40 %
20 %
0 %
Probability level
0
50
100
150
200
250
Notch opening angle of weld root β_r [deg]
Hybrid LF
Hybrid MF
Laser
SAW

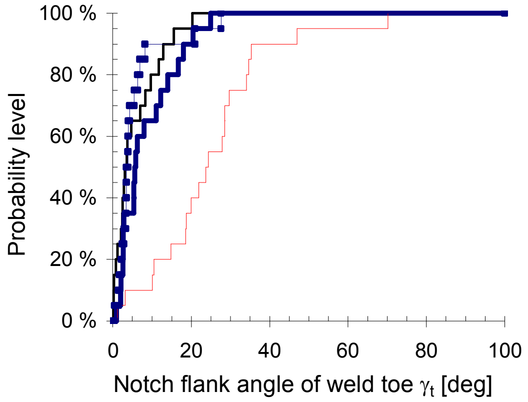
100 %
80 %
60 %
40 %
20 %
0 %
Probability level
0
20
40
60
80
100
Notch flank angle of weld toe γ_t [deg]

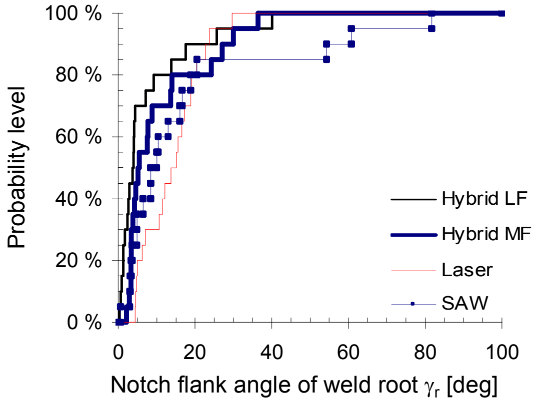
100 %
80 %
60 %
40 %
20 %
0 %
Probability level
0
20
40
60
80
100
Notch flank angle of weld root γ_r [deg]
Hybrid LF
Hybrid MF
Laser
SAW

Appendix C Results of goodness of fit test for geometrical dimensions

Table C1: Parameters of fitted distributions and goodness test results for axial mis-alignments

Joint type	Distribution	Parameters of distribution			Goodness test results			Note
Type		Location	Scale	Shape	A^2	*D*	PPCC	
SAW	Normal	-0.10	0.21	-	0.376	0.161	0.964	
	Lognormal	-	-	-	-	-	-	Rejected
	Exponential	-0.40	0.27	-	0.786	0.180	0.890	
	Rayleigh	-0.49	0.44	-	0.251	0.135	0.979	
	Weibull	-0.47	0.42	1.90	0.242	0.133	0.979	Best-fit
Laser	Normal	0.02	0.24	-	0.605	0.182	0.942	
	Lognormal	-	-	-	-	-	-	Rejected
	Exponential	-0.45	0.36	-	2.589	0.400	0.144	Rejected
	Rayleigh	-0.45	0.52	-	1.033	0.232	0.904	
	Weibull	-8.74	8.86	44.84	0.385	0.170	0.964	Best-fit
Hybrid LF	Normal	0.24	0.28	-	0.307	0.112	0.977	
	Lognormal	-	-	-	-	-	-	Rejected
	Exponential	-0.20	0.37	-	1.784	0.263	0.796	Rejected
	Rayleigh	-0.28	0.60	-	0.241	0.100	0.978	Best-fit
	Weibull	-0.43	0.77	2.65	0.242	0.104	0.982	
Hybrid MF	Normal	0.47	0.05	-	0.257	0.158	0.976	
	Lognormal	-0.75	0.11	-	0.212	0.140	0.985	
	Exponential	0.39	0.07	-	1.156	0.323	0.876	Rejected
	Rayleigh	0.37	0.11	-	0.228	0.148	0.984	
	Weibull	0.38	0.10	1.78	0.258	0.158	0.985	Best-fit

Table C2: Parameters of fitted distributions and goodness test results for angular mis-alignments

Joint type	Distribution	Parameters of distribution			Goodness test results			Note
Type		Location	Scale	Shape	A^2	*D*	PPCC	
SAW	Normal	-0.21	0.02	-	0.545	0.216	0.949	
	Lognormal	-	-	-	-	-	-	Rejected
	Exponential	-0.30	0.06	-	6.631	0.597	-	Rejected
	Rayleigh	-0.30	0.09	-	2.276	0.346	-	Rejected
	Weibull	-1.95	1.75	100.00	0.313	0.173	0.984	Best-fit
Laser	Normal	0.12	0.10	-	0.450	0.185	0.957	
	Lognormal	-	-	-	-	-	-	Rejected
	Exponential	-0.05	0.14	-	1.639	0.292	0.641	
	Rayleigh	-0.06	0.21	-	0.559	0.209	0.944	
	Weibull	-0.26	0.42	4.36	0.430	0.176	0.962	Best-fit
Hybrid LF	Normal	0.69	0.17	-	0.319	0.118	0.974	
	Lognormal	-0.39	0.25	-	0.336	0.115	0.974	
	Exponential	0.40	0.24	-	2.559	0.302	0.684	Rejected
	Rayleigh	0.38	0.36	-	0.342	0.110	0.971	Best-fit
	Weibull	0.23	0.52	3.06	0.289	0.113	0.978	
Hybrid MF	Normal	0.18	0.02	-	0.382	0.188	0.961	
	Lognormal	-1.70	0.10	-	0.302	0.169	0.972	
	Exponential	0.15	0.03	-	1.590	0.379	0.826	Rejected
	Rayleigh	0.15	0.04	-	0.238	0.161	0.981	
	Weibull	0.16	0.03	1.40	0.204	0.132	0.987	Best-fit

Table C3: Parameters of fitted distributions and goodness test results for weld toe high h_t

Joint type	Distribution	Parameters of distribution			Goodness test results			Note
Type		Location	Scale	Shape	A^2	D	PPCC	
SAW	Normal	2.26	0.13	-	0.758	0.300	0.919	
	Lognormal	0.81	0.06	-	0.709	0.290	0.925	
	Exponential	2.10	0.15	-	0.765	0.312	0.931	
	Rayleigh	2.02	0.27	-	0.598	0.262	0.940	Rejected
	Weibull	2.10	0.18	1.29	0.696	0.221	0.949	Best-fit
Laser	Normal	0.06	0.31	-	0.577	0.217	0.933	
	Lognormal	-	-	-	-	-	-	Rejected
	Exponential	-0.47	0.42	-	1.791	0.368	0.452	Rejected
	Rayleigh	-0.47	0.61	-	1.261	0.253	0.899	
	Weibull	-16.37	16.56	67.19	0.454	0.172	0.955	Best-fit
Hybrid LF	Normal	0.49	0.17	-	0.304	0.171	0.967	
	Lognormal	-0.78	0.36	-	0.271	0.152	0.971	
	Exponential	0.25	0.21	-	0.562	0.225	0.893	
	Rayleigh	0.17	0.36	-	0.248	0.152	0.976	
	Weibull	0.15	0.38	2.11	0.249	0.153	0.976	Best-fit
Hybrid MF	Normal	0.94	0.04	-	0.156	0.125	0.989	
	Lognormal	-0.06	0.05	-	0.162	0.133	0.987	
	Exponential	0.80	0.10	-	4.046	0.536	-	Rejected
	Rayleigh	0.86	0.09	-	0.561	0.165	0.973	
	Weibull	0.73	0.23	5.62	0.160	0.112	0.991	Best-fit

Table C4: Parameters of fitted distributions and goodness test results for weld root high h_r

Joint type	Distribution	Parameters of distribution			Goodness test results			Note
Type		Location	Scale	Shape	A^2	D	PPCC	
SAW	Normal	2.26	0.13	-	0.758	0.300	0.919	
	Lognormal	0.81	0.06	-	0.709	0.290	0.925	
	Exponential	2.10	0.15	-	0.765	0.312	0.931	
	Rayleigh	2.02	0.27	-	0.598	0.262	0.940	
	Weibull	2.10	0.18	1.29	0.696	0.221	0.949	Best-fit
Laser	Normal	0.06	0.31	-	0.577	0.217	0.933	
	Lognormal	-	-	-	-	-	-	Rejected
	Exponential	-0.47	0.42	-	1.791	0.368	0.452	Rejected
	Rayleigh	-0.47	0.61	-	1.261	0.253	0.899	
	Weibull	-16.37	16.56	67.19	0.454	0.172	0.955	Best-fit
Hybrid LF	Normal	0.49	0.17	-	0.304	0.171	0.967	
	Lognormal	-0.78	0.36	-	0.271	0.152	0.971	
	Exponential	0.25	0.21	-	0.562	0.225	0.893	
	Rayleigh	0.17	0.36	-	0.248	0.152	0.976	
	Weibull	0.15	0.38	2.11	0.249	0.153	0.976	Best-fit
Hybrid MF	Normal	0.94	0.04	-	0.156	0.125	0.989	
	Lognormal	-0.06	0.05	-	0.162	0.133	0.987	
	Exponential	0.80	0.10	-	4.046	0.536	-	Rejected
	Rayleigh	0.86	0.09	-	0.561	0.165	0.973	
	Weibull	0.73	0.23	5.62	0.160	0.112	0.991	Best-fit

Table C5: Parameters of fitted distributions and goodness test results for weld toe width w_t

Joint type	Distribution	Parameters of distribution			Goodness test results			Note
Type		Location	Scale	Shape	A^2	D	PPCC	
SAW	Normal	18.11	0.82	-	0.682	0.239	0.925	
	Lognormal	2.90	0.05	-	0.666	0.233	0.927	
	Exponential	17.10	0.94	-	1.007	0.242	0.841	
	Rayleigh	16.64	1.68	-	0.636	0.218	0.927	
	Weibull	16.22	2.14	2.64	0.669	0.228	0.931	Best-fit
Laser	Normal	2.85	0.47	-	0.744	0.294	0.923	
	Lognormal	1.03	0.16	-	0.756	0.293	0.922	
	Exponential	2.30	0.53	-	0.681	0.239	0.891	
	Rayleigh	1.99	0.98	-	0.748	0.294	0.937	
	Weibull	2.02	0.95	1.93	0.749	0.294	0.937	Best-fit
Hybrid LF	Normal	5.79	0.47	-	0.556	0.270	0.946	
	Lognormal	1.75	0.08	-	0.580	0.277	0.943	
	Exponential	4.90	0.70	-	1.996	0.389	0.347	Rejected
	Rayleigh	4.96	0.94	-	1.069	0.299	0.917	
	Weibull	-3.01	9.00	23.18	0.454	0.239	0.963	Best-fit
Hybrid MF	Normal	6.43	0.17	-	0.273	0.154	0.970	
	Lognormal	1.86	0.03	-	0.274	0.155	0.970	
	Exponential	6.20	0.21	-	0.677	0.231	0.848	
	Rayleigh	6.12	0.36	-	0.300	0.163	0.967	
	Weibull	5.97	0.52	3.06	0.257	0.151	0.973	Best-fit

Table C6: Parameters of fitted distributions and goodness test results for weld root width w_r

Joint type	Distribution	Parameters of distribution			Goodness test results			Note
Type		Location	Scale	Shape	A^2	D	PPCC	
SAW	Normal	10.01	0.29	-	0.276	0.198	0.976	
	Lognormal	2.30	0.03	-	0.285	0.201	0.975	
	Exponential	9.50	0.42	-	1.405	0.348	0.668	Rejected
	Rayleigh	9.46	0.62	-	0.442	0.217	0.960	
	Weibull	8.61	1.51	5.48	0.227	0.182	0.981	Best-fit
Laser	Normal	1.68	0.14	-	0.806	0.254	0.892	
	Lognormal	0.51	0.09	-	0.953	0.272	0.870	
	Exponential	1.30	0.27	-	4.105	0.576	-	Rejected
	Rayleigh	1.30	0.39	-	1.648	0.366	0.655	Rejected
	Weibull	0.00	1.73	15.22	0.502	0.207	0.939	Best-fit
Hybrid LF	Normal	1.57	0.58	-	0.484	0.203	0.944	
	Lognormal	0.39	0.35	-	0.285	0.139	0.970	
	Exponential	0.96	0.63	-	0.392	0.158	0.979	
	Rayleigh	0.47	1.25	-	0.330	0.166	0.973	
	Weibull	0.81	0.84	1.29	0.201	0.120	0.985	Best-fit
Hybrid MF	Normal	1.89	0.21	-	0.317	0.192	0.974	
	Lognormal	0.63	0.11	-	0.370	0.199	0.965	
	Exponential	1.40	0.37	-	2.776	0.461	-	Rejected
	Rayleigh	1.49	0.45	-	0.782	0.213	0.948	
	Weibull	0.00	1.97	10.73	0.254	0.166	0.984	Best-fit

Table C7: Parameters of fitted distributions and goodness test results for flank angle of weld toe θ_t

Joint type	Distribution	Parameters of distribution			Goodness test results			Note
Type		Location	Scale	Shape	A^2	D	PPCC	
SAW	Normal	29.34	2.49	-	0.439	0.148	0.966	
	Lognormal	3.38	0.08	-	0.320	0.132	0.977	
	Exponential	25.00	3.61	-	2.931	0.314	0.849	Rejected
	Rayleigh	24.55	5.43	-	0.215	0.108	0.989	
	Weibull	25.75	4.01	1.44	0.166	0.083	0.995	Best-fit
Laser	Normal	3.63	18.74	-	0.719	0.150	0.952	
	Lognormal	-	-	-	-	-	-	Rejected
	Exponential	-35.00	28.59	-	4.905	0.391	-	Rejected
	Rayleigh	-35.00	42.61	-	1.298	0.210	0.907	
	Weibull	-210.06	221.62	13.91	0.463	0.129	0.970	Best-fit
Hybrid LF	Normal	16.97	11.37	-	0.937	0.230	0.941	
	Lognormal	2.62	0.69	-	0.271	0.107	0.984	
	Exponential	3.00	13.22	-	0.603	0.186	0.967	
	Rayleigh	3.00	17.56	-	2.885	0.272	0.876	Rejected
	Weibull	2.14	16.31	1.30	0.304	0.142	0.985	Best-fit
Hybrid MF	Normal	18.52	1.88	-	0.394	0.163	0.977	
	Lognormal	2.91	0.10	-	0.407	0.157	0.977	
	Exponential	15.00	2.79	-	3.380	0.285	0.656	Rejected
	Rayleigh	14.95	4.06	-	0.393	0.141	0.979	
	Weibull	13.95	5.15	2.62	0.348	0.148	0.982	Best-fit

Table C8: Parameters of fitted distributions and goodness test results for flank angle of weld root θ_r

Joint type	Distribution	Parameters of distribution			Goodness test results			Note
Type		Location	Scale	Shape	A^2	D	PPCC	
SAW	Normal	18.43	5.10	-	0.774	0.214	0.959	
	Lognormal	2.88	0.27	-	0.561	0.181	0.974	
	Exponential	10.00	7.09	-	2.688	0.379	0.858	Rejected
	Rayleigh	8.74	10.99	-	0.560	0.175	0.979	
	Weibull	10.19	9.30	1.66	1.028	0.160	0.983	Best-fit
Laser	Normal	38.99	8.62	-	0.393	0.146	0.976	
	Lognormal	3.64	0.23	-	0.443	0.176	0.972	
	Exponential	25.00	11.57	-	2.158	0.274	0.768	Rejected
	Rayleigh	22.71	18.48	-	0.450	0.172	0.974	
	Weibull	16.25	25.55	2.89	0.357	0.149	0.980	Best-fit
Hybrid LF	Normal	58.70	20.57	-	0.440	0.142	0.973	
	Lognormal	4.00	0.43	-	1.053	0.221	0.934	
	Exponential	20.00	30.15	-	3.833	0.410	0.534	Rejected
	Rayleigh	20.62	43.21	-	1.319	0.183	0.955	
	Weibull	-32.41	99.04	5.11	0.380	0.123	0.977	Best-fit
Hybrid MF	Normal	48.02	11.80	-	0.189	0.083	0.987	
	Lognormal	3.84	0.25	-	0.200	0.097	0.987	
	Exponential	30.00	15.42	-	1.587	0.262	0.857	Rejected
	Rayleigh	25.35	25.73	-	0.173	0.093	0.991	
	Weibull	21.39	30.14	2.39	0.147	0.083	0.993	Best-fit

Table C9: Parameters of fitted distributions and goodness test results for notch depth D_1 at weld toe

Joint type	Distribution	Parameters of distribution			Goodness test results			Note
Type		Location	Scale	Shape	A^2	D	PPCC	
SAW	Normal	0.01	0.01	-	1.618	0.243	0.838	Rejected
	Lognormal	-5.52	0.89	-	0.624	0.147	0.964	Best-fit
	Exponential	0.00	0.01	-	0.652	0.155	0.953	
	Rayleigh	0.00	0.01	-	3.583	0.280	0.827	Rejected
	Weibull	0.00	0.01	1.02	0.668	0.157	0.951	
Laser	Normal	0.07	0.11	-	2.887	0.266	0.734	Rejected
	Lognormal	-3.29	1.19	-	0.197	0.120	0.991	Best-fit
	Exponential	0.00	0.09	-	1.463	0.210	0.877	
	Rayleigh	0.00	0.11	-	10.91	0.422	0.681	Rejected
	Weibull	0.00	0.05	0.63	1.155	0.208	0.960	
Hybrid LF	Normal	0.02	0.03	-	3.880	0.368	0.758	Rejected
	Lognormal	-4.96	1.31	-	0.667	0.174	0.958	Best-fit
	Exponential	0.00	0.02	-	5.179	0.431	0.877	Rejected
	Rayleigh	0.00	0.03	-	24.86	0.646	0.684	Rejected
	Weibull	0.00	0.01	0.60	1.238	0.197	0.926	
Hybrid MF	Normal	0.01	0.01	-	1.192	0.192	0.902	
	Lognormal	-4.98	0.93	-	0.421	0.167	0.980	Best-fit
	Exponential	0.00	0.01	-	0.354	0.134	0.972	
	Rayleigh	0.00	0.01	-	3.462	0.262	0.886	Rejected
	Weibull	0.00	0.01	1.12	0.384	0.134	0.971	

Table C10: Parameters of fitted distributions and goodness test results for notch depth D_1 at weld root

Joint type	Distribution	Parameters of distribution			Goodness test results			Note
Type		Location	Scale	Shape	A^2	D	PPCC	
SAW	Normal	0.03	0.04	-	3.242	0.373	0.801	Rejected
	Lognormal	-4.26	1.14	-	0.852	0.206	0.955	Best-fit
	Exponential	0.00	0.03	-	2.568	0.363	0.914	Rejected
	Rayleigh	0.00	0.04	-	16.12	0.599	0.746	Rejected
	Weibull	0.00	0.02	0.74	1.279	0.231	0.933	
Laser	Normal	0.03	0.01	-	0.692	0.170	0.953	
	Lognormal	-3.81	0.57	-	0.209	0.132	0.991	Best-fit
	Exponential	0.00	0.02	-	3.209	0.376	0.845	Rejected
	Rayleigh	0.00	0.03	-	0.432	0.145	0.980	
	Weibull	0.00	0.03	1.82	0.357	0.134	0.986	
Hybrid LF	Normal	0.02	0.02	-	1.705	0.224	0.841	
	Lognormal	-4.56	1.06	-	0.289	0.157	0.984	Best-fit
	Exponential	0.00	0.02	-	0.628	0.180	0.964	
	Rayleigh	0.00	0.02	-	7.691	0.369	0.799	Rejected
	Weibull	0.00	0.02	0.82	0.541	0.158	0.983	
Hybrid MF	Normal	0.01	0.01	-	1.663	0.279	0.875	Rejected
	Lognormal	-4.86	0.83	-	0.397	0.129	0.977	Best-fit
	Exponential	0.00	0.01	-	0.564	0.155	0.980	
	Rayleigh	0.00	0.01	-	3.578	0.339	0.869	Rejected
	Weibull	0.00	0.01	1.09	0.670	0.167	0.976	

Table C11: Parameters of fitted distributions and goodness test results for notch depth D_2 at weld toe

Joint type	Distribution	Parameters of distribution			Goodness test results			Note
Type		Location	Scale	Shape	A^2	D	PPCC	
SAW	Normal	0.02	0.02	-	0.460	0.145	0.966	
	Lognormal	-4.04	0.94	-	0.467	0.146	0.970	
	Exponential	0.00	0.02	-	0.968	0.179	0.913	
	Rayleigh	0.00	0.03	-	1.849	0.246	0.956	Rejected
	Weibull	0.00	0.03	1.40	0.320	0.135	0.981	Best-fit
Laser	Normal	0.07	0.09	-	2.781	0.280	0.767	Rejected
	Lognormal	-3.41	1.30	-	0.499	0.200	0.967	
	Exponential	0.00	0.08	-	1.349	0.224	0.911	
	Rayleigh	0.00	0.09	-	10.56	0.452	0.715	Rejected
	Weibull	0.00	0.05	0.66	1.042	0.263	0.980	Rejected
Hybrid LF	Normal	0.05	0.04	-	0.965	0.204	0.922	
	Lognormal	-3.44	0.91	-	0.310	0.137	0.982	
	Exponential	0.00	0.04	-	0.656	0.156	0.976	
	Rayleigh	0.00	0.06	-	2.293	0.258	0.912	Rejected
	Weibull	0.00	0.05	1.20	0.238	0.105	0.984	Best-fit
Hybrid MF	Normal	0.01	0.01	-	1.364	0.217	0.902	
	Lognormal	-4.80	1.24	-	0.763	0.199	0.954	
	Exponential	0.00	0.01	-	0.440	0.132	0.978	
	Rayleigh	0.00	0.02	-	5.077	0.306	0.871	Rejected
	Weibull	0.00	0.01	1.02	0.389	0.132	0.978	Best-fit

Table C12: Parameters of fitted distributions and goodness test results for notch depth D_2 at weld root

Joint type	Distribution	Parameters of distribution			Goodness test results			Note
Type		Location	Scale	Shape	A^2	D	PPCC	
SAW	Normal	0.03	0.02	-	0.675	0.140	0.921	
	Lognormal	-3.72	0.81	-	0.492	0.152	0.973	
	Exponential	0.00	0.03	-	1.209	0.188	0.950	
	Rayleigh	0.00	0.04	-	1.369	0.189	0.923	
	Weibull	0.00	0.04	1.35	0.316	0.107	0.972	Best-fit
Laser	Normal	0.05	0.04	-	1.555	0.218	0.868	
	Lognormal	-3.37	0.79	-	0.237	0.104	0.986	
	Exponential	0.00	0.05	-	0.574	0.155	0.985	
	Rayleigh	0.00	0.06	-	3.338	0.273	0.862	Rejected
	Weibull	0.00	0.05	1.07	0.652	0.166	0.981	Best-fit
Hybrid LF	Normal	0.10	0.07	-	0.499	0.147	0.963	
	Lognormal	-2.68	0.96	-	0.919	0.220	0.946	
	Exponential	0.00	0.09	-	1.253	0.257	0.889	Rejected
	Rayleigh	0.00	0.12	-	2.237	0.246	0.952	Rejected
	Weibull	0.00	0.11	1.44	0.714	0.168	0.971	Best-fit
Hybrid MF	Normal	0.03	0.02	-	1.110	0.171	0.906	
	Lognormal	-4.08	0.96	-	0.158	0.089	0.991	
	Exponential	0.00	0.02	-	0.178	0.082	0.996	
	Rayleigh	0.00	0.03	-	3.788	0.289	0.884	Rejected
	Weibull	0.00	0.03	1.04	0.222	0.098	0.995	Best-fit

Table C13: Parameters of fitted distributions and goodness test results for notch flank angle γ at weld toe

Joint type	Distribution	Parameters of distribution			Goodness test results			Note
Type		Location	Scale	Shape	A^2	D	PPCC	
SAW	Normal	5.81	6.68	-	3.000	0.290	0.784	Rejected
	Lognormal	1.35	0.90	-	0.650	0.155	0.961	
	Exponential	0.00	6.29	-	1.257	0.206	0.928	
	Rayleigh	0.00	7.75	-	6.622	0.437	0.764	Rejected
	Weibull	0.39	4.98	0.80	1.318	0.203	0.946	Best-fit
Laser	Normal	25.15	15.50	-	0.467	0.156	0.957	
	Lognormal	2.96	0.92	-	1.314	0.235	0.903	Rejected
	Exponential	0.00	21.28	-	2.568	0.332	0.864	Rejected
	Rayleigh	0.00	29.46	-	0.574	0.138	0.964	
	Weibull	0.00	28.41	1.69	0.462	0.137	0.974	Best-fit
Hybrid LF	Normal	5.65	5.70	-	1.121	0.232	0.923	Rejected
	Lognormal	1.07	1.38	-	0.451	0.153	0.970	
	Exponential	0.00	5.92	-	0.335	0.133	0.989	
	Rayleigh	0.00	7.56	-	7.230	0.384	0.876	Rejected
	Weibull	0.00	5.71	0.96	0.250	0.115	0.988	Best-fit
Hybrid MF	Normal	8.48	7.02	-	1.002	0.227	0.936	
	Lognormal	1.78	0.92	-	0.333	0.137	0.982	
	Exponential	0.00	8.09	-	0.594	0.166	0.970	
	Rayleigh	0.00	10.71	-	3.398	0.314	0.920	Rejected
	Weibull	0.00	9.18	1.20	0.363	0.134	0.985	Best-fit

Table C14: Parameters of fitted distributions and goodness test results for notch flank angle γ at weld root

Joint type	Distribution	Parameters of distribution			Goodness test results			Note
Type		Location	Scale	Shape	A^2	D	PPCC	
SAW	Normal	17.47	21.99	-	2.568	0.295	0.827	Rejected
	Lognormal	2.24	1.17	-	0.285	0.115	0.982	
	Exponential	0.00	20.11	-	1.154	0.211	0.947	
	Rayleigh	0.00	24.45	-	10.85	0.434	0.776	Rejected
	Weibull	0.00	15.69	0.77	0.691	0.195	0.970	Best-fit
Laser	Normal	13.96	7.28	-	0.309	0.130	0.977	
	Lognormal	2.48	0.61	-	0.705	0.151	0.958	
	Exponential	0.00	11.09	-	3.625	0.325	0.678	Rejected
	Rayleigh	0.02	15.81	-	0.358	0.122	0.987	
	Weibull	0.00	15.83	2.00	0.357	0.122	0.987	Best-fit
Hybrid LF	Normal	7.39	10.05	-	2.432	0.317	0.822	Rejected
	Lognormal	1.29	1.26	-	0.179	0.138	0.993	
	Exponential	0.00	8.93	-	1.608	0.311	0.951	Rejected
	Rayleigh	0.00	10.64	-	12.90	0.543	0.760	Rejected
	Weibull	0.00	6.10	0.69	0.625	0.150	0.993	Best-fit
Hybrid MF	Normal	10.55	10.42	-	2.082	0.267	0.870	Rejected
	Lognormal	1.96	0.88	-	0.752	0.166	0.955	
	Exponential	0.03	10.82	-	0.982	0.183	0.968	
	Rayleigh	0.00	13.82	-	6.813	0.404	0.850	Rejected
	Weibull	0.00	10.86	1.00	0.987	0.183	0.968	Best-fit

Table C15: Parameters of fitted distributions and goodness test results for notch opening angle β at weld toe

Joint type	Distribution	Parameters of distribution			Goodness test results			Note
Type		Location	Scale	Shape	A^2	D	PPCC	
SAW	Normal	132.54	10.72	-	0.570	0.165	0.963	
	Lognormal	4.88	0.08	-	0.722	0.182	0.951	
	Exponential	100.00	22.16	-	8.509	0.512	-	Rejected
	Rayleigh	100.00	33.85	-	2.032	0.299	0.719	Rejected
	Weibull	0.00	137.16	14.86	0.267	0.123	0.987	Best-fit
Laser	Normal	118.64	21.88	-	0.851	0.208	0.947	
	Lognormal	4.76	0.22	-	1.357	0.250	0.903	Rejected
	Exponential	60.00	40.78	-	7.792	0.499	-	Rejected
	Rayleigh	60.00	61.85	-	2.269	0.314	0.790	Rejected
	Weibull	0.00	127.28	6.42	0.628	0.179	0.966	Best-fit
Hybrid LF	Normal	139.03	19.23	-	0.536	0.138	0.961	
	Lognormal	4.92	0.15	-	0.721	0.166	0.949	
	Exponential	100.00	29.14	-	4.656	0.414	-	Rejected
	Rayleigh	100.00	43.26	-	1.197	0.196	0.921	
	Weibull	0.00	146.97	8.59	0.328	0.101	0.978	Best-fit
Hybrid MF	Normal	141.60	12.97	-	0.737	0.186	0.942	
	Lognormal	4.95	0.10	-	0.943	0.187	0.919	
	Exponential	100.00	27.86	-	9.324	0.545	-	Rejected
	Rayleigh	100.00	42.81	-	2.700	0.325	0.580	Rejected
	Weibull	0.00	147.09	13.25	0.469	0.159	0.973	Best-fit

Table C16: Parameters of fitted distributions and goodness test results for notch opening angle β at weld root

Joint type	Distribution	Parameters of distribution			Goodness test results			Note
Type		Location	Scale	Shape	A^2	D	PPCC	
SAW	Normal	132.65	22.62	-	1.112	0.215	0.920	
	Lognormal	4.87	0.20	-	1.673	0.254	0.875	Rejected
	Exponential	65.00	45.33	-	9.062	0.567	-	Rejected
	Rayleigh	65.00	69.91	-	2.801	0.343	0.610	Rejected
	Weibull	0.00	141.54	7.10	0.744	0.182	0.950	Best-fit
Laser	Normal	97.46	16.53	-	0.692	0.170	0.957	
	Lognormal	4.57	0.17	-	0.516	0.145	0.968	
	Exponential	70.00	22.79	-	2.547	0.322	0.803	Rejected
	Rayleigh	66.32	35.33	-	0.437	0.136	0.972	
	Weibull	67.23	34.30	1.93	0.426	0.135	0.972	Best-fit
Hybrid LF	Normal	93.21	17.00	-	0.217	0.086	0.985	
	Lognormal	4.52	0.20	-	0.350	0.112	0.969	
	Exponential	50.00	31.07	-	6.476	0.469	-	Rejected
	Rayleigh	50.00	46.38	-	0.908	0.184	0.909	
	Weibull	0.00	100.08	6.32	0.224	0.109	0.990	Best-fit
Hybrid MF	Normal	109.35	12.58	-	0.613	0.155	0.966	
	Lognormal	4.69	0.12	-	0.670	0.158	0.965	
	Exponential	90.00	16.35	-	1.968	0.315	0.815	Rejected
	Rayleigh	85.71	26.82	-	0.723	0.174	0.969	
	Weibull	80.00	33.16	2.54	0.623	0.155	0.972	Best-fit

Table C17: Parameters of fitted distributions and goodness test results for notch radius ρ at weld toe

Joint type	Distribution	Parameters of distribution			Goodness test results			Note
Type		Location	Scale	Shape	A^2	D	PPCC	
SAW	Normal	0.05	0.02	-	0.431	0.138	0.970	
	Lognormal	-3.18	0.49	-	0.215	0.144	0.987	Best-fit
	Exponential	0.00	0.04	-	4.721	0.375	0.566	Rejected
	Rayleigh	0.00	0.05	-	0.220	0.106	0.987	
	Weibull	0.00	0.05	2.25	0.261	0.113	0.985	
Laser	Normal	0.39	0.44	-	1.778	0.229	0.872	
	Lognormal	-1.47	1.07	-	0.327	0.119	0.982	Best-fit
	Exponential	0.00	0.44	-	0.758	0.178	0.979	
	Rayleigh	0.00	0.54	-	8.888	0.416	0.826	Rejected
	Weibull	0.00	0.38	0.85	0.537	0.143	0.986	
Hybrid LF	Normal	0.52	0.62	-	1.722	0.240	0.867	Rejected
	Lognormal	-1.30	1.23	-	0.170	0.095	0.990	Best-fit
	Exponential	0.00	0.59	-	0.765	0.167	0.979	
	Rayleigh	0.00	0.72	-	9.718	0.376	0.812	Rejected
	Weibull	0.00	0.48	0.79	0.295	0.108	0.995	
Hybrid MF	Normal	0.41	0.42	-	1.627	0.243	0.891	Rejected
	Lognormal	-1.36	1.03	-	0.216	0.121	0.990	Best-fit
	Exponential	0.00	0.43	-	0.448	0.162	0.984	
	Rayleigh	0.00	0.55	-	6.592	0.410	0.855	Rejected
	Weibull	0.00	0.41	0.95	0.435	0.138	0.985	

Table C18: Parameters of fitted distributions and goodness test results for notch radius ρ at weld root

Joint type	Distribution	Parameters of distribution			Goodness test results			Note
Type		Location	Scale	Shape	A^2	D	PPCC	
SAW	Normal	0.17	0.19	-	1.962	0.258	0.874	Rejected
	Lognormal	-2.32	1.11	-	0.516	0.155	0.963	Best-fit
	Exponential	0.00	0.19	-	0.911	0.168	0.957	
	Rayleigh	0.00	0.24	-	9.929	0.393	0.829	Rejected
	Weibull	0.00	0.17	0.90	0.641	0.151	0.957	
Laser	Normal	0.09	0.06	-	1.100	0.204	0.900	
	Lognormal	-2.67	0.65	-	0.370	0.130	0.977	Best-fit
	Exponential	0.02	0.07	-	0.339	0.146	0.992	
	Rayleigh	0.00	0.10	-	1.356	0.241	0.921	Rejected
	Weibull	0.00	0.09	1.39	0.577	0.159	0.975	
Hybrid LF	Normal	0.12	0.12	-	1.447	0.250	0.894	Rejected
	Lognormal	-2.50	0.93	-	0.640	0.191	0.963	Best-fit
	Exponential	0.00	0.13	-	0.689	0.177	0.990	
	Rayleigh	0.00	0.16	-	5.979	0.420	0.870	Rejected
	Weibull	0.00	0.13	1.00	0.690	0.178	0.990	
Hybrid MF	Normal	0.18	0.17	-	1.131	0.182	0.886	
	Lognormal	-2.07	0.93	-	0.297	0.131	0.985	Best-fit
	Exponential	0.01	0.17	-	0.313	0.116	0.981	
	Rayleigh	0.00	0.23	-	3.059	0.294	0.871	Rejected
	Weibull	0.00	0.19	1.08	0.373	0.131	0.977	

Appendix D Pearson correlation number between geometrical dimensions

Table D1: Weld toe dimensions for the SAW joint

Dimension		h_t	w_t	θ_t	$D_{1,t}$	$D_{2,t}$	γ_t	β_t
Weld height	h_t							
Weld width	w_t	-0.11						
Weld flange angle	θ_t	0.48	-0.54					
Notch depth	$D_{1,t}$	-0.12	-0.23	-0.19				
Notch depth	$D_{2,t}$	0.29	-0.26	0.17	0.41			
Notch flange angle	γ_t	-0.15	0.00	-0.27	0.78	0.12		
Notch opening angle	β_t	-0.06	-0.22	0.05	-0.21	-0.34	-0.42	
Notch root radius	ρ_t	-0.32	-0.46	0.09	0.47	0.15	0.31	0.28

Table D2: Weld root dimensions for the SAW joint

Dimension		h_r	w_r	θ_r	$D_{1,r}$	$D_{2,r}$	γ_r	β_r
Weld height	h_r							
Weld width	w_r	0.60						
Weld flange angle	θ_r	0.82	0.25					
Notch depth	$D_{1,r}$	-0.05	0.13	0.16				
Notch depth	$D_{2,r}$	0.10	0.42	0.03	0.54			
Notch flange angle	γ_r	0.07	0.12	0.30	0.94	0.49		
Notch opening angle	β_r	-0.19	-0.24	-0.34	-0.87	-0.52	-0.93	
Notch root radius	ρ_r	0.01	-0.22	0.20	-0.28	-0.10	-0.32	0.48

Table D3: Weld toe dimensions for the Laser joint

Dimension		h_t	w_t	θ_t	$D_{1,t}$	$D_{2,t}$	γ_t	β_t
Weld height	h_t							
Weld width	w_t	-0.46						
Weld flange angle	θ_t	0.92	-0.44					
Notch depth	$D_{1,t}$	0.04	0.44	0.03				
Notch depth	$D_{2,t}$	0.07	0.37	0.05	0.95			
Notch flange angle	γ_t	0.27	0.35	0.27	0.78	0.78		
Notch opening angle	β_t	-0.41	0.09	-0.48	-0.61	-0.67	-0.72	
Notch root radius	ρ_t	0.17	0.42	0.18	0.20	0.21	0.14	0.06

Table D4: Weld root dimensions for the Laser joint

Dimension		h_r	w_r	θ_r	$D_{1,r}$	$D_{2,r}$	γ_r	β_r
Weld height	h_r							
Weld width	w_r	0.26						
Weld flange angle	θ_r	0.73	-0.12					
Notch depth	$D_{1,r}$	0.24	-0.09	0.26				
Notch depth	$D_{2,r}$	0.21	0.12	-0.08	-0.11			
Notch flange angle	γ_r	0.19	0.35	0.24	0.19	-0.28		
Notch opening angle	β_r	-0.46	-0.28	-0.39	-0.26	-0.43	-0.25	
Notch root radius	ρ_r	-0.06	-0.06	-0.01	0.34	-0.16	0.17	0.20

Table D5: Weld toe dimensions for the Hybrid LF joint

Dimension		h_t	w_t	θ_t	$D_{1,t}$	$D_{2,t}$	γ_t	β_t
Weld height	h_t							
Weld width	w_t	0.83						
Weld flange angle	θ_t	0.86	0.61					
Notch depth	$D_{1,t}$	-0.52	-0.59	-0.34				
Notch depth	$D_{2,t}$	0.36	0.25	0.36	0.01			
Notch flange angle	γ_t	-0.65	-0.64	-0.42	0.78	-0.32		
Notch opening angle	β_t	-0.69	-0.56	-0.68	0.47	-0.30	0.45	
Notch root radius	ρ_t	-0.47	-0.29	-0.43	0.61	0.11	0.47	0.54

Table D6: Weld root dimensions for the Hybrid LF joint

Dimension		h_r	w_r	θ_r	$D_{1,r}$	$D_{2,r}$	γ_r	β_r
Weld height	h_r							
Weld width	w_r	0.91						
Weld flange angle	θ_r	0.50	0.36					
Notch depth	$D_{1,r}$	-0.32	-0.43	-0.18				
Notch depth	$D_{2,r}$	0.58	0.46	0.39	-0.24			
Notch flange angle	γ_r	-0.24	-0.34	-0.21	0.29	0.19		
Notch opening angle	β_r	-0.13	-0.05	-0.43	0.19	-0.45	-0.39	
Notch root radius	ρ_r	0.30	0.21	-0.06	0.29	-0.07	-0.20	0.16

Table D7: Weld toe dimensions for the Hybrid MF joint

Dimension		h_t	w_t	θ_t	$D_{1,t}$	$D_{2,t}$	γ_t	β_t
Weld height	h_t							
Weld width	w_t	0.26						
Weld flange angle	θ_t	-0.03	-0.47					
Notch depth	$D_{1,t}$	0.33	0.27	0.19				
Notch depth	$D_{2,t}$	0.18	0.42	0.05	0.72			
Notch flange angle	γ_t	0.15	0.18	0.28	0.58	0.30		
Notch opening angle	β_t	-0.03	-0.43	0.08	-0.23	-0.33	-0.70	
Notch root radius	ρ_t	-0.25	-0.22	-0.04	-0.02	0.31	-0.26	0.16

Table D8: Weld root dimensions for the Hybrid MF joint

Dimension		h_r	w_r	θ_r	$D_{1,r}$	$D_{2,r}$	γ_r	β_r
Weld height	h_r							
Weld width	w_r	0.60						
Weld flange angle	θ_r	0.86	0.43					
Notch depth	$D_{1,r}$	-0.42	-0.34	-0.33				
Notch depth	$D_{2,r}$	-0.39	-0.23	-0.40	0.58			
Notch flange angle	γ_r	-0.35	-0.39	-0.25	0.55	0.00		
Notch opening angle	β_r	-0.15	0.12	-0.11	-0.04	-0.10	0.03	
Notch root radius	ρ_r	-0.09	0.00	-0.14	0.16	0.64	-0.48	0.22

Appendix E Correlation models for geometrical dimensions

Table E1: Regression models for weld toe dimensions of the SAW joint

Regression model							St. dev of residual
Variable							
h^{-2}	= 3.083E-01 +	-3.777E-03 $\cdot\ \theta$					1.856E-02
w^{-2}	= 5.312E-03 +	-1.146E+00 $\cdot\ \theta^{-2}$	+	1.613E-04 $\cdot \ln(D_1)$			1.748E-04
θ^{-2}	= -1.541E-03 +	2.733E-03 $\cdot\ h^{-2}$	+	1.533E-04 $\cdot\ w$	+	1.071E-04 $\cdot \ln(D_1)$	9.853E-05
$D_1^{0.5}$	= 1.848E-02 +	2.353E-02 $\cdot\ \gamma^{0.5}$					1.798E-02
$\ln(\gamma)$	= 3.060E+00 +	-1.068E-01 $\cdot\ \theta$	+	2.051E+01 $\cdot\ D_1^{0.5}$			4.866E-01
$\ln(\rho)$	= 1.985E+00 +	-2.849E-01 $\cdot\ w$					4.353E-01

Table E2: Statistical significance of regression models for weld toe dimensions of the SAW joint

Dimensions		Correlation R^2	F-value	Significance of F
Weld height	h_t	0.20	4.6	0.045
Weld width	w_t	0.57	24.0	0.000
Weld flange angle	θ_t	0.72	45.4	0.000
Notch depth	$D_{1,t}$	0.66	35.6	0.000
Notch flange angle	γ_t	0.71	44.2	0.000
Notch root radius	ρ_t	0.21	4.9	0.040

Table E3: Regression models for weld root dimensions of the SAW joint

Regression model							St. dev of residual
Variable							
h	= -8.801E+00 +	6.595E-01 $\cdot\ w$	+	1.094E+00 $\cdot \ln(\theta)$	+	1.341E-01 $\cdot\ D_1^{-0.25}$	9.973E-02
w	= 1.215E+01 +	1.108E+00 $\cdot\ h$	+	-1.165E+00 $\cdot \ln(\theta)$	+	-2.933E-02 $\cdot\ D_1^{-0.5}$	1.280E-01
$\ln(\theta)$	= 7.250E+00 +	8.116E-01 $\cdot\ h$	+	-5.120E-01 $\cdot\ w$	+	-1.143E-01 $\cdot\ D_1^{-0.25}$	8.592E-02
$\ln(D_1)$	= -6.139E+00 +	8.371E-01 $\cdot \ln(\gamma)$					5.772E-01
$D_2^{0.5}$	= 3.499E-01 +	-1.372E-03 $\cdot\ \beta$					5.618E-02
$\mathrm{Ln}(\gamma)$	= 6.018E+00 +	8.858E-01 $\cdot \ln(D_1)$					5.938E-01
β^2	= 2.028E+04 +	-1.975E+02 $\cdot\ \gamma$	+	7.177E+03 $\cdot\ \rho$			1.945E+03
$\ln(\rho)$	= -4.443E+00 +	1.176E-04 $\cdot\ \beta^2$					9.168E-01

Table E4: Statistical significance of regression models for weld root dimensions of the SAW joint

Dimensions		Correlation R^2	F-value	Significance of F
Weld height	h_r	0.93	245.1	0.000
Weld width	w_r	0.80	71.0	0.000
Weld flange angle	θ_r	0.90	158.2	0.000
Notch depth	$D_{1,r}$	0.74	51.6	0.000
Notch depth	$D_{2,r}$	0.23	5.5	0.031
Notch flange angle	γ_r	0.74	51.6	0.000
Notch opening angle	β_r	0.87	117.2	0.000
Notch root radius	ρ_r	0.32	8.4	0.010

Table E5: Regression models for weld toe dimensions of the Laser joint

Regression model Variable					St. dev of residual
$(h+1)^2$	= 1.104E+00 +	2.807E-02 · θ			2.439E-01
w	= 5.867E+00 +	-2.215E-01 · $(\theta+100)^{0.5}$ +	2.350E-01 · ln(D_1)		3.029E-01
$(\theta+100)^{0.5}$	= 9.962E+00 +	2.967E+00 · h			3.688E-01
$D_1^{\ 0.5}$	= 2.464E-01 +	1.225E+00 · D_2	+ -4.134E-02 · $\rho^{-0.5}$		4.630E-02
$D_2^{\ 0.5}$	= 3.093E-02 +	8.185E-01 · $D_1^{\ 0.5}$			6.552E-02
γ^2	= 1.949E+03 +	8.752E+03 · D_2	+ -1.399E+01 · β		3.200E+02
β^2	= 4.154E+04 +	-2.106E+03 · $(\theta+100)^{0.5}$ +	-3.116E+00 · γ	+ -1.257E+03 · $\rho^{-0.5}$	2.155E+03
$\rho^{-0.5}$	= 1.973E+00 +	-8.338E-01 · ln(D_1)	+ -1.975E-02 · β		6.497E-01

Table E6: Statistical significance of regression models for weld toe dimensions of the Laser joint

Dimensions		Correlation R^2	F-value	Significance of F
Weld height	h_t	0.82	83.7	0.000
Weld width	w_t	0.57	23.6	0.000
Weld flange angle	θ_t	0.85	103.0	0.000
Notch depth	$D_{1,t}$	0.90	162.7	0.000
Notch depth	$D_{2,t}$	0.77	60.5	0.000
Notch flange angle	γ_t	0.91	192.9	0.000
Notch opening angle	β_t	0.79	69.3	0.000
Notch root radius	ρ_t	0.69	39.5	0.000

Table E7: Regression models for weld root dimensions of the Laser joint

Regression model Variable				St. dev of residual
h	= -4.392E-01 +	3.228E-01 · w	+ 1.098E-02 · θ	7.094E-02
θ	= 2.801E+01 +	5.726E+01 · h	+ -6.854E+00 · w^2	5.142E+00
ln(D_2)	= 6.026E-01 +	-4.569E-02 · γ	+ -3.421E-02 · β	5.367E-01
β^{-2}	= 1.570E-04 +	-1.212E-05 · $D_2^{\ -0.5}$	+ 1.893E-06 · γ	2.348E-05

Table E8: Statistical significance of regression models for weld root dimensions of the Laser joint

Dimensions		Correlation R^2	F-value	Significance of F
Weld height	h_r	0.66	35.3	0.000
Weld flange angle	θ_r	0.64	32.6	0.000
Notch depth	$D_{2,r}$	0.54	20.9	0.000
Notch opening angle	β_r	0.56	23.4	0.000

Table E9: Regression models for weld toe dimensions of the Hybrid LF joint

Variable	Regression model				St. dev of residual
$h^{-0.5}$	= 2.473E+00 +	-1.432E-02 $\cdot\, w^2$	+ -2.168E-01 $\cdot \ln(\theta)$	+ 1.302E-02 $\cdot\, \gamma$	5.139E-02
w^2	= 5.901E+01 +	-1.692E+01 $\cdot\, h^{-0.5}$			2.678E+00
$\ln(\theta)$	= 6.767E+00 +	-3.063E+00 $\cdot\, h^{-0.5}$	+ 2.110E-01 $\cdot\, \gamma$		2.646E-01
$\ln(D_1)$	= -7.494E+00 +	1.519E-01 $\cdot\, \gamma$	+ 8.500E-05 $\cdot\, \beta^2$		6.616E-01
γ	= 2.314E+01 +	-7.048E+00 $\cdot \ln(D_1^{-0.5})$			3.331E+00
β^2	= 1.506E+04 +	-2.537E+03 $\cdot \ln(D_2)$	+ 3.154E+03 $\cdot \ln(\rho)$		2.865E+03
$\ln(\rho)$	= -6.923E+00 +	5.740E-01 $\cdot \ln(D_2)$	+ 5.462E-02 $\cdot\, \beta$		7.233E-01

Table E10: Statistical significance of regression models for weld toe dimensions of the Hybrid LF joint

Dimensions		Correlation R^2	F-value	Significance of F
Weld height	h_t	0.96	440.2	0.000
Weld width	w_t	0.73	48.3	0.000
Weld flange angle	θ_t	0.85	105.2	0.000
Notch depth	$D_{1,t}$	0.75	52.9	0.000
Notch flange angle	γ_t	0.66	34.7	0.000
Notch opening angle	β_t	0.69	39.8	0.000
Notch root radius	ρ_t	0.65	34.1	0.000

Table E11: Regression models for weld root dimensions of the Hybrid LF joint

Variable	Regression model				St. dev of residual
$(h+1)^{-0.5}$	= 1.027E+00 +	-1.452E-01 $\cdot\, w$	+ -5.570E-01 $\cdot\, D_2$	+ 1.438E-02 $\cdot\, \rho^{-0.5}$	4.879E-02
w^{-1}	= 8.700E-01 +	-3.067E-01 $\cdot\, h$	+ 2.878E+00 $\cdot\, D_1$		1.018E-01
θ	= 1.278E+02 +	-8.633E+01 $\cdot\, (h+1)^{-0.5}$			1.762E+01
$\ln(D_1)$	= -5.277E+00 +	5.567E-01 $\cdot \ln(\gamma)$	+ 8.500E-05 $\cdot\, \beta$		7.960E-01
$D_2^{0.5}$	= 9.894E-01 +	-5.595E-01 $\cdot\, (h+1)^{-0.5}$	+ -2.708E-03 $\cdot\, \beta$		8.140E-02
$\ln(\gamma)$	= 4.860E+00 +	7.837E-01 $\cdot \ln(D_1)$			9.444E-01
β	= 1.123E+02 +	-6.602E+01 $\cdot\, D_2^{0.5}$			1.505E+01

Table E12: Statistical significance of regression models for weld root dimensions of the Hybrid LF joint

Dimensions		Correlation R^2	F-value	Significance of F
Weld height	h_r	0.84	96.5	0.000
Weld width	w_r	0.79	68.0	0.000
Weld flange angle	θ_r	0.29	7.4	0.014
Notch depth	$D_{1,r}$	0.44	13.9	0.002
Notch depth	$D_{2,r}$	0.54	21.1	0.000
Notch flange angle	γ_r	0.44	13.9	0.002
Notch opening angle	β_r	0.22	5.0	0.038

Table E13: Regression models for weld toe dimensions of the Hybrid MF joint

Regression model		St. dev of
Variable		Residual
w	$= 6.842E{+}00 + -3.801E{-}02 \cdot \theta + 1.807E{+}00 \cdot D_2^{0.5} + -7.696E{-}02 \cdot \ln(\rho)$	9.973E-02
θ	$= 5.344E{+}01 + -5.427E{+}00 \cdot w$	1.658E+00
$D_1^{0.5}$	$= 2.988E{-}02 + 1.552E{+}00 \cdot D_2 + 2.248E{-}02 \cdot \ln(\gamma)$	2.476E-02
$D_2^{0.5}$	$= 7.118E{-}02 + 3.479E{+}00 \cdot D_1$	4.488E-02
$\ln(\gamma)$	$= 8.546E{+}00 + 5.593E{-}01 \cdot \ln(D_1) + -2.814E{-}02 \cdot \beta$	5.963E-01
β^2	$= 2.308E{+}04 + -3.385E{+}02 \cdot \gamma$	2.545E+03
$\rho^{-0.5}$	$= -6.346E{+}00 + 2.795E{+}00 \cdot w + -5.859E{+}01 \cdot D_2 + -6.055E{-}02 \cdot \beta$	6.033E-01

Table E14: Statistical significance of regression models for weld toe dimensions of the Hybrid MF joint

Dimensions		Correlation R^2	F-value	Significance of F
Weld width	w_t	0.63	31.0	0.000
Weld flange angle	θ_t	0.23	5.2	0.035
Notch depth	$D_{1,t}$	0.63	31.2	0.000
Notch depth	$D_{2,t}$	0.32	8.4	0.010
Notch flange angle	γ_t	0.58	24.5	0.000
Notch opening angle	β_t	0.47	15.7	0.001
Notch root radius	ρ_t	0.74	51.7	0.000

Table E15: Regression models for weld root dimensions of the Hybrid MF joint

Regression model		St. dev of
Variable		residual
$h^{-0.5}$	$= 1.821E{+}00 + -1.306E{-}02 \cdot \theta$	8.328E-02
w	$= 1.507E{+}00 + 5.054E{-}01 \cdot h$	1.618E-01
θ	$= 1.188E{+}02 + -5.927E{+}01 \cdot h^{-0.5}$	5.611E+00
$\ln(D_1)$	$= -1.319E{+}00 + 5.999E{-}01 \cdot \ln(D_2) + -2.688E{+}00 \cdot \gamma^{-0.5}$	4.944E-01
$D_2^{0.5}$	$= 3.220E{-}01 + 4.352E{-}02 \cdot \ln(D_1) + 1.874E{-}01 \cdot \rho$	4.284E-02
$\ln(\gamma)$	$= 3.743E{-}01 + 4.301E{-}01 \cdot \ln(D_1) + 2.011E{-}02 \cdot \beta + -7.133E{-}01 \cdot \ln(\rho)$	4.398E-01
$\ln(\rho)$	$= 1.332E{+}00 + 5.126E{-}01 \cdot \ln(D_1) + -8.671E{-}02 \cdot \gamma$	4.943E-01

Table E16: Statistical significance of regression models for weld root dimensions of the Hybrid MF joint

Dimensions		Correlation R^2	F-value	Significance of F
Weld height	h_r	0.77	61.6	0.000
Weld width	w_r	0.36	9.9	0.005
Weld flange angle	θ_r	0.77	61.6	0.000
Notch depth	$D_{1,r}$	0.64	32.3	0.000
Notch depth	$D_{2,r}$	0.59	26.4	0.000
Notch flange angle	γ_r	0.75	53.3	0.000
Notch root radius	ρ_r	0.72	45.7	0.000

Appendix F Parametric study of geometrical dimensions using the FEA

Model A: welded joint without sharp notch

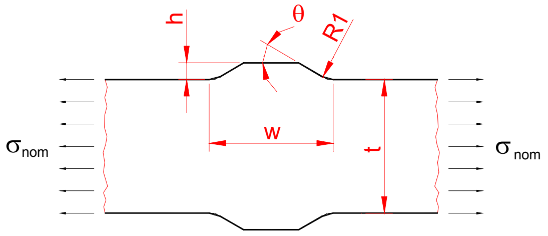

Plain strain element
E = 210 GPA
ν = 0.3

Figure F1: Geometry and material data of the structural model A. Thickness t and weld notch radius were 12 mm and 1 mm. The height h, width w and flank angle θ were varied.

Table F1: Results for the FE-model A

Model id.	t [mm]	h [mm]	w [mm]	θ [°]	ρ [mm]	K_t
A_01	12	2.50	20	90	1	2.24
A_02	12	1.00	20	90	1	1.94
A_03	12	0.50	20	90	1	1.71
A_04	12	0.10	20	90	1	1.34
A_05	12	2.50	14	90	1	2.18
A_06	12	1.00	14	90	1	1.94
A_07	12	0.50	14	90	1	1.71
A_08	12	0.10	14	90	1	1.34
A_09	12	2.50	8	90	1	1.92
A_10	12	1.00	8	90	1	1.85
A_11	12	0.50	8	90	1	1.69
A_12	12	0.10	8	90	1	1.34
A_13	12	1.00	2	90	1	1.37
A_14	12	0.50	2	90	1	1.37
A_15	12	0.10	2	90	1	1.29
A_16	12	0.13	1	90	1	1.21
A_17	12	0.10	1	90	1	1.21
A_18	12	2.50	20	30	1	2.12
A_19	12	1.00	20	30	1	1.90
A_20	12	0.50	20	30	1	1.70
A_21	12	0.10	20	30	1	1.34
A_22	12	2.50	14	30	1	2.07
A_23	12	1.00	14	30	1	1.90
A_24	12	0.50	14	30	1	1.70
A_25	12	2.15	8	30	1	1.86
A_26	12	1.00	8	30	1	1.82
A_27	12	0.50	8	30	1	1.68
A_28	12	0.42	2	30	1	1.36

Table F1: Results for the FE-model A (continued)

Model id.	t [mm]	h [mm]	w [mm]	θ [°]	ρ [mm]	K_t
A_29	12	0.80	6.58	38.4	1	1.77
A_30	12	0.46	5.76	14.1	1	1.53
A_31	12	0.26	5.06	5.2	1	1.26
A_32	12	1.73	2.64	97.0	1	1.62
A_33	12	0.52	1.46	55.4	1	1.43
A_34	12	0.16	0.82	31.7	1	1.27
A_35	12	1.01	6.72	21.8	1	1.72
A_36	12	0.94	6.44	18.4	1	1.66
A_37	12	0.87	6.16	15.6	1	1.59
A_38	12	1.20	2.24	69.5	1	1.55
A_39	12	0.71	1.88	46.6	1	1.46
A_40	12	0.42	1.56	31.3	1	1.38
A_41	12	0.62	3.68	32.7	1	1.58
A_42	12	0.02	2.82	14.9	1	1.15
A_43	12	0.76	1.92	54.5	1	1.48
A_44	12	0.52	1.68	38.1	1	1.41
A_45	12	0.35	1.46	26.6	1	1.35
A_46	12	2.48	19.50	33.6	1	2.15
A_47	12	2.26	18.10	29.3	1	2.08
A_48	12	2.05	16.80	25.4	1	2.01
A_49	12	2.07	10.50	27.8	1	1.95
A_50	12	1.30	10.00	17.8	1	1.75
A_51	12	0.81	9.54	11.4	1	1.55

Model B: V-notched plate

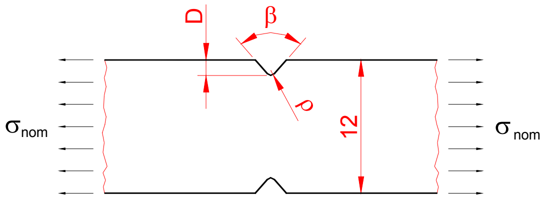

Plain strain element
E = 210 GPA
ν = 0.3

Figure F2: Geometry and material data of the structural model B. Thickness *t* was 12 mm and notch depth *D*, notch flank angle *β* and notch radius *ρ* were varied.

Table F2: Results for the FE-model B

Model id.	*t* [mm]	*D* [mm]	*β* [°]	*ρ* [mm]	K_t
B_01	12	0.05	50	1	1.42
B_02	12	0.10	50	1	1.61
B_03	12	0.20	50	1	1.87
B_04	12	0.40	50	1	2.26
B_05	12	0.60	50	1	2.56
B_06	12	0.05	110	1	1.42
B_07	12	0.10	110	1	1.61
B_08	12	0.20	110	1	1.87
B_09	12	0.40	110	1	2.26
B_10	12	0.60	110	1	2.55
B_11	12	0.05	130	1	1.42
B_12	12	0.10	130	1	1.61
B_13	12	0.20	130	1	1.87
B_14	12	0.40	130	1	2.24
B_15	12	0.60	130	1	2.52
B_16	12	0.05	170	1	1.36
B_17	12	0.10	170	1	1.45
B_18	12	0.20	170	1	1.54
B_19	12	0.40	170	1	1.65
B_20	12	0.60	170	1	1.72
B_21	12	0.05	50	0.25	1.87
B_22	12	0.10	50	0.25	2.26
B_23	12	0.20	50	0.25	2.83
B_24	12	0.40	50	0.25	3.65
B_25	12	0.60	50	0.25	4.28

Table F2: Results for the FE-model B (continued)

Model id.	t [mm]	D [mm]	β [°]	ρ [mm]	K_t
B_26	12	0.05	110	0.25	1.87
B_27	12	0.10	110	0.25	2.26
B_28	12	0.20	110	0.25	2.82
B_29	12	0.40	110	0.25	3.59
B_30	12	0.60	110	0.25	4.17
B_31	12	0.05	130	0.25	1.87
B_32	12	0.10	130	0.25	2.25
B_33	12	0.20	130	0.25	2.76
B_34	12	0.40	130	0.25	3.43
B_35	12	0.60	130	0.25	3.91
B_36	12	0.05	170	0.25	1.54
B_37	12	0.10	170	0.25	1.64
B_38	12	0.20	170	0.25	1.76
B_39	12	0.40	170	0.25	1.88
B_40	12	0.60	170	0.25	1.95

Model C: Welded butt joint

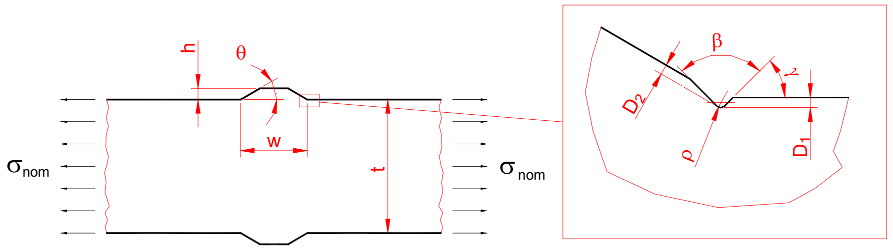

Plain strain element
E = 210 GPA
ν = 0.3

Figure F3: Geometry and material data of the structural model C. Thickness t was 12 mm and all weld dimensions were varied: weld width w, weld high h, weld flank angle θ, notch depth D, notch flank angle γ, notch opening angle β, notch root radius ρ.

Table F3: Results for the FE-model C; dimensions in mm and deg

Id.	t	h	w	θ	D_1	D_2	γ	β	ρ	K_t
C_01	12	0.80	6.58	38.4	0.061	0.114	15.8	109.8	0.071	4.95
C_02	12	0.46	5.76	14.1	0.009	0.035	4.0	137.7	0.334	2.04
C_03	12	0.26	5.06	5.2	0.001	0.011	1.0	172.7	1.567	1.26
C_04	12	1.73	2.64	97.0	0.053	0.227	23.6	68.1	0.023	6.38
C_05	12	0.52	1.46	55.4	0.011	0.079	4.4	91.7	0.089	2.71
C_06	12	0.16	0.82	31.7	0.003	0.028	0.8	123.5	0.341	1.47
C_07	12	1.01	6.72	21.8	0.026	0.038	21.4	121.3	0.072	3.98
C_08	12	0.94	6.44	18.4	0.007	0.010	6.5	141.0	0.288	2.25
C_09	12	0.87	6.16	15.6	0.002	0.003	2.0	163.9	1.156	1.58
C_10	12	1.20	2.24	69.5	0.028	0.068	29.2	90.0	0.037	4.56
C_11	12	0.71	1.88	46.6	0.008	0.018	7.5	108.6	0.134	2.52
C_12	12	0.42	1.56	31.3	0.002	0.005	1.9	131.2	0.484	1.59
C_13	12	0.62	3.68	32.7	0.242	0.212	54.4	86.4	0.059	5.94
C_14	12	0.02	2.82	14.9	0.040	0.040	21.4	116.7	0.262	1.64
C_15	12	0.76	1.92	54.5	0.053	0.125	27.7	72.8	0.024	5.33
C_16	12	0.52	1.68	38.1	0.022	0.035	12.4	96.1	0.069	3.15
C_17	12	0.35	1.46	26.6	0.009	0.010	5.5	126.8	0.202	1.85
C_18	12	2.48	19.50	33.6	0.016	0.058	17.3	115.7	0.020	8.55
C_19	12	2.26	18.10	29.3	0.004	0.020	3.8	132.1	0.042	5.14
C_20	12	2.05	16.80	25.4	0.001	0.007	0.8	150.9	0.088	3.50
C_21	12	2.07	10.50	27.8	0.088	0.077	54.0	99.0	0.027	7.16
C_22	12	1.30	10.00	17.8	0.017	0.026	10.9	130.8	0.117	3.26
C_23	12	0.81	9.54	11.4	0.003	0.009	2.2	172.7	0.510	1.68
C_24	12	1.00	6.00	30.0	0.100	0.100	25.0	90.0	0.050	6.08
C_25	12	1.00	6.00	30.0	0.100	0.100	45.0	90.0	0.050	6.00
C_26	12	0.08	6.00	45.0	0.080	0.140	15.0	100.0	1.000	1.97

ISBN 978-951-22-9189-2
ISBN 978-951-22-9190-8 (PDF)
ISSN 1795-2239
ISSN 1795-4584 (PDF)